

DISSERTATION

Mechanical Reliability of Open Through Silicon Via Structures for Integrated Circuits

ausgeführt zum Zwecke der Erlangung des akademischen Grades
eines Doktors der technischen Wissenschaften

eingereicht an der Technischen Universität Wien
Fakultät für Elektrotechnik und Informationstechnik

von

Santo Papaleo

Lange Gasse 24/17
1080 Wien, Österreich
Matr. Nr. 1329523

geboren am 11 August 1988 in Novara, Italien

Wien, im Dezember 2016

Ai miei Zii

Science is the belief in the ignorance of experts

RICHARD FEYNMAN

Kurzfassung

Seit Kurzem hat die Halbleiterindustrie signifikante Anstrengungen in Richtung der Einführung von über Speicher und Logik Anwendungen hinausgehender zusätzlicher Funktionalität unternommen, welche auch als "More-than-Moore" Integration bekannt ist. Diese Art der Integration, allgemein mit drei dimensionaler Die/Halbleiterscheiben-Stapelung assoziiert, wird mittels Siliziumdurchkontaktierungstechnologie realisiert, welche eine vertikale, elektrische Kontaktierung zwischen Systemen erlaubt, geringen Energieverbrauch, dichte Bauteilpackung und reduzierte RC-Verzögerung ermöglicht. Die Implementierung und Fertigung dieser 3D Strukturen resultiert in vielen herausfordernden Zuverlässigkeitsproblemen. Daher muss die Zuverlässigkeit jeder Komponente des Gerätes sorgfältig analysiert werden. In dieser Arbeit wird die Zuverlässigkeit in Bezug auf die mechanische Stabilität von gefüllten (hohlen) TSVs basierend auf Wolfram-Metallisierung betrachtet. Die unterschiedlichen Aspekte welche die mechanische Stabilität von TSVs beeinflussen werden untersucht und neue Modelle implementiert.

Die Finite Elemente Methode (FEM) ist ein numerisches Verfahren das häufig in der Halbleitermodellierung zur Unterstützung der Entwicklung von neuen Bauteilen und Prozessen verwendet wird. Die mechanische Analyse der hohlen TSVs ist in einer kommerziellen FEM Software implementiert, welche unterschiedliche Schemata, Materialien und mechanische Modelle einsetzt.

Während des Stapelns von 3D integrierten Schaltungen können Bauteile wie die hohlen TSVs unbeabsichtigt externen Kräften ausgesetzt werden die zu einem Versagen der Struktur führen. Durch die Simulation einer externen Kraft, die auf einen hohlen TSV wirkt, können kritische Areale identifiziert werden in denen ein mechanisches Versagen am wahrscheinlichsten ist. Die höchste Wahrscheinlichkeit eines Versagens durch Materialbruch oder Delamination ist an den Ecken des TSV-Bodens aufzufinden. Nachfolgend wurden die kritischen Areale lokalisiert und eine Delaminationsanalyse für die Materialgrenzflächen der Multilagenstruktur am TSV-Boden durchgeführt. Die Delaminationsvorhersage wird durch die Energiefreisetzungsrate während der Delaminationspropagation beschrieben. Wenn die Energiefreisetzungsrate einen kritischen Wert überschreitet propagiert die Delamination. Bedingungen wie die Lagendicke, angewandte Kraft und der Reststress der involvierten Materiallagen werden variiert um zu untersuchen, welche Faktoren die Wahrscheinlichkeit einer Delaminationsfortpflanzung zu erhöhen. SiO_2/W wurde als die kritischste Grenzfläche indentifiziert. Wenn für die Wolfram-Lage ein hoher Wert an intrinsischer Zugspannung angenommen wurde, wurden hohe Energiefreisetzungsraten erzielt.

Dünne Metallfilme, unter Verwendung von Complementary Metal-Oxide-Semiconductor (CMOS) Fertigungstechniken, enthalten für Gewöhnlich Reststress, der die Leistung und die Zuverlässigkeit von ICs beeinflusst. Hohe intrinsische Stresswerte, im Speziellen in der leitenden Wolfram Lage des offenen TSVs, erhöhen die Wahrscheinlichkeit eines delaminationsinduzierten Fehlers. Daher ist ein Modell zur Vorhersage des Stressaufbaus in dünnen Metallfilmen während des Abscheidungsprocesses implementiert worden. Das Model wird unter Verwendung von Messdaten für mehrere Materialien kalibriert und wird zur Untersuchung der Filmstressentwicklung während des Filmwachstums an einer ausgebogten Oberfläche verwendet. Während der TSV-Fabrikation bildet sich eine ausgebogte Oberfläche entlang der TSV-Seitenwand auf Grund des verwendeten reaktiven Ionentiepenätzprozesses. Dünnefilme die auf einer ausgebogten Oberfläche wachsen entwickeln im Vergleich zu ebenen Proben einen geringeren intrinsischen Stress. Daher kann der intrinsische Stress, durch die Kontrolle der Prozessparameter während des Ätzens, im Film minimiert werden.

Abstract

Recently, the semiconductor industry has been investing significant effort towards introducing more functionality to applications beyond memory and logic, referred to as “More-than-Moore” integration. This type of integration, commonly associated with three dimensional (3D) die/wafer stacking, is realized using a through-silicon via (TSV) technology, which allows for a vertical electrical contact between systems, enabling low power consumption, dense device packing, and reduced RC delays. The implementation and fabrication of the 3D structure results in many challenging reliability issues. Therefore, the reliability of every component of the device must be thoroughly analyzed. In this work the reliability related to the mechanical stability of lined (open) TSVs, based on the W metalization technology, is considered. The different aspects which impact the mechanical stability of the TSV interconnects are examined and new models are implemented.

The finite element method (FEM) is a numerical method frequently used in semiconductor modeling to support the development of new devices and processes. The mechanical analysis of open TSVs is implemented in a commercial FEM software, where different simulation schemes, materials, and mechanical models are employed.

During 3D integrated circuit (IC) stacking devices such as open TSVs can be subjected to unintentional extra forces leading to a failure of the structure. By simulating an external force acting on an open TSV critical areas can be identified, where a mechanical failure is most likely. The highest probability of a failure due to material cracking or delamination is found at the corner of the TSV bottom. Subsequently the critical areas are localized and a delamination analysis is performed for the material interfaces of the multilayer structure at the TSV bottom. Delamination prediction is formulated by using the energy release rate generated during delamination propagation. If the energy release rate exceeds a critical value delamination propagates. Conditions such as the thicknesses of the layers, applied forces, and residual stresses of the involved material layers are varied to investigate which factor increase the probability of delamination propagation. SiO_2/W is found to be the most critical interface; when the W layer is assumed to carry a large value of intrinsic tensile stress, high values of energy release rate are obtained.

Thin metal films, deposited using complementary metal-oxide-semiconductor (CMOS) fabrication techniques, usually contain residual stresses, which affect the performance and reliability of the IC. High values of intrinsic stress, in particular in the W conducting layer of the open TSV, increase the probability of delamination-induced failure. Therefore, a model is implemented to predict the stress build-up in thin metal film during the deposition process. The model is calibrated by using measured data for several materials and is used to investigate the film stress evolution during film growth on a scalloped surface. During TSV fabrication, due to the deep reactive ion etching process used, a scalloped surface is formed along the TSV sidewall. Thin films grown on a scalloped surface develop a smaller intrinsic stress when compared to flat samples. Therefore, by controlling the process parameters during etching the intrinsic stress in the film can be minimized.

Riassunto

Recentemente, l'industria dei semiconduttori ha affrontato notevoli sforzi nell'introduzione di più funzionalità al di là di memorie e dispositivi logici. Questo approccio è chiamato "more than Moore" integrazione. Questo tipo di integrazione, generalmente associata all'impilamento di die e wafer nelle tre dimensioni (3D), è realizzata usando la tecnologia di fori passanti su wafers di silicio (inglese Through Silicon Vias (TSVs)), che permette il collegamento elettrico verticale tra sistemi, permettendo bassi consumi energetici, densi imballaggi di dispositivi, e una riduzione del ritardo RC. L'implementazione e la fabbricazione di strutture tridimensionali hanno diversi importanti problemi di affidabilità da affrontare. L'affidabilità di ogni componente del dispositivo dev'essere dettagliatamente analizzata. In questo lavoro viene considerata l'affidabilità riguardante la stabilità meccanica di lined (open) TSVs, che utilizza come materiale conduttore il tungsteno. Vengono esaminati i diversi aspetti che impattano la stabilità meccanica di interconnessioni TSV e sono implementati nuovi modelli.

Il metodo ad elementi finiti (FEM) è un metodo numerico frequentemente utilizzato nella modellizzazione di semiconduttori; per descrivere, analizzare, e sviluppare nuovi dispositivi e processi. L'analisi meccanica di open TSVs è stata implementata con un software commerciale FEM, dove sono utilizzati differenti schemi di simulazione, materiali e modelli meccanici.

Durante l'impilamento di circuiti integrati nelle tre dimensioni, dispositivi elettronici come ad esempio open TSVs possono essere soggetti ad involontarie forze esterne portando al fallimento della struttura. Simulando una forza esterna agente su un open TSV, possono essere identificate delle aree critiche, in cui la possibilità che si verifichi un fallimento meccanico è molto alta. La più alta probabilità di fallimento a causa di rottura del materiale o delaminazione è stata trovata all'angolo inferiore del TSV. Successivamente aver localizzato le aree critiche, è stata svolta un'analisi sulla delaminazione per le interfacce presenti nel multistrato alla base del TSV. Le previsioni sulla delaminazione sono formulate utilizzando il tasso di rilascio d'energia generato durante la propagazione della delaminazione. Se il tasso di energia rilasciata supera un critico valore, la delaminazione propaga. Condizioni come lo spessore degli strati del materiale, forze applicate, e stress residui dei materiali utilizzati, sono stati variati per investigare i fattori responsabili dell'aumentano della probabilità di propagazione della delaminazione. SiO₂/W si è rilevata l'interfaccia più critica; quando il tungsteno è ipotizzato con alti valori di stress interno di trazione, sono stati ottenuti alti valori di tasso di rilascio d'energia.

Strati metallici sottili, depositati usando le tecniche di fabbricazione complementary metal-oxide-semiconductor (CMOS), esibiscono stress residui, che influiscono sulle performance e l'affidabilità dei circuiti integrati. Alti valori di stress intrinseco, in particolare nel materiale tungsteno conduttore nelle open TSVs, aumentano la probabilità di fallimento dovuto alla delaminazione. È stato dunque implementato un modello che permette di simulare la formazione di stress intrinseco in film sottili durante i processi di deposizione. Il modello è calibrato usando dati sperimentali di diversi materiali ed è utilizzato per investigare l'evoluzione dello stress in film durante la crescita su una superficie ondulata. Durante il processo di produzione delle TSVs, vengono utilizzati processi di attacco chimico e lungo le pareti del TSV si forma una superficie ondulata. Gli strati sottili cresciuti su una superficie dalla forma ondulata sviluppano uno stress interno inferiore rispetto a crescite su campioni piatti. Per cui, controllando i parametri utilizzati durante l'attacco chimico lo stress interno dei film può essere minimizzato.

Acknowledgement

Firstly, I would like to express my gratitude to my supervisor Prof. Hajdin Cerić for the support of my Ph.D. study and related research. I'm very glad that he gave me the possibility to be part of his Christian Doppler Laboratory for Reliability Issues in Microelectronics.

I want, as well, to thank Prof. Siegfried Selberherr for his patience and help during my years at the institute.

I would like to thank Prof. Olivier Thomas that accepted to take part in the examining committee on such short notice.

Thanks to all the people of the Institute of Microelectronics. Thanks to them I had an enjoyable time at the institute.

Many thanks to Gerhard Rzepa, Wolfhard ZISSER, and Thomas Windbacher for translating the discussed abstract into German!

I am grateful to Raffaele Coppeta for having informed me about the Ph.D. position, honestly grazie, I will appreciate it forever!

I am very glad for having met the beautiful person of Thomas Windbacher, he gave me many suggestions about ALL kind of topics! Grazie bello!

I am really grateful to Lado Filipovic! Grazie and again grazie! I appreciated his patience and his accuracy. All his various suggestions, discussions, comments, and proof-reading helped me a lot to improve my work. Grazie Lado!

Words cannot express my gratitude to Dipl.-Ing. Dr. Techn. Wolfhard ZISSER. I have found the many scientific discussions with him very important and fundamental. He has been my Austrian reference for any problem. Also I enjoyed our spare time at Karlsplatz, I will never forget these moments. Danke for having made my time in Austria easier and more enjoyable.

Furthermore, I had the good fortune to meet interesting people outside the institute. They gave me the possibility to fully experience the perfect and beautiful Vienna. I thank my initial flatmates, Marta and Renate, who warmly welcomed me and introduced me to Vienna, and I thank my current flatmates, Caroline and Venus, I had an enjoyable time in the flat with them. I thank Alessio, Arbi, Alberto, and Ornella, for helping me to survive in Vienna; I thank Giuseppe (small), Giuseppe (big), Gretel, Francesco (urologist), Malcolm, Marco (urologist), Paolo, and Valerio who have made me proud in these years to be an Italian abroad. All of them gave me the possibilities to rest and take a break from my studies, therefore thanks to all you.

Thanks to Micheal, Ilaria, Chino, Esther, Samy, Elisa, Simone, Nicola, and Cisco who encouraged me to take this adventure and later visited me in Vienna. Grazie amici!

I am thankful to Gino. He never complained or reproached my absence. Thanks puledro!

Starting this challenge in the first place was the "fault" of Marta C., Bobbio, and Benny who strongly pushed me. I express my deepest gratitude to them!

Many thanks to Marco and Silvia, sincere FRIENDS who have always been present in these years. I miss our time together in Lange Gasse and I am really sorry if I messed up your life!:) Thanks to them I will have beautiful memories of Vienna.

Thanks to Nino and Marianna. Grazie mille per avermi sempre incoraggiato, motivato, e spinto in questa esperienza. Avevate ragione in tutto, grazie!

I am really grateful to my parents, my sister and my grandmother. Grazie a mia mamma, che in questi tre anni mi ha sempre calorosamente cercato e riaccolto a casa come un re. Grazie a mio padre che mi ha sempre appoggiato, creduto e spinto nelle

mie scelte. Grazie a mia sorella che mi ha fatto sempre sentire importante. Grazie a mia nonna, per avermi sempre dimostrato il suo affetto anche se siamo sempre stati distanti. Grazie per il vostro aiuto, se sono diventato quello che sono è stato solo grazie a voi. Ve ne sarò sempre grato.

As last, but not least, I want to thank Martina, my love. She never complained for the time that I did not dedicate to her, she rather always helped and encouraged me. I will be grateful to her forever. Abbiamo silenziosamente sofferto la distanza, ma forse (speriamo) è finalmente arrivato il tempo di stare insieme. Grazie per avermi aspettato per così tanto tempo.

Contents

Contents	xix
List of Abbreviations	xxi
List of Symbols	xxiii
List of Figures	xxxi
List of Tables	xxxiii
1 Introduction	1
1.1 Integrated Circuits	1
1.2 Interconnect Structures	3
1.2.1 2D Integrated Circuit	4
1.2.2 2.5D and 3D Integrated Circuit	5
1.3 Through Silicon Vias	6
1.3.1 TSV Fabrication	7
1.3.2 TSV Metalization	9
1.3.3 Current and Future TSV Applications	10
1.4 Reliability of Interconnect Structures	11
1.5 FEM Approach for Reliability	13
1.6 Outline of the Thesis	14
2 Overview of Solid Mechanics and the Finite Element Method	15
2.1 Continuum Mechanics	15
2.1.1 Deformation and Strain	15
2.1.2 Stress	19
2.1.3 Constitutive Laws	22
2.1.3.1 Elasticity	24
2.2 Plane Strain and Plane Stress	25
2.2.1 Plane Strain	25
2.2.2 Plane Stress	26
2.3 Source of Residual Stress in Thin Films	26
2.3.1 Intrinsic Stress	26
2.3.2 Thermal Strain and Thermal Stress	26
2.4 Virtual Work	27
2.5 Fracture Mechanics	28
2.6 FEM	29
2.6.1 Weighted Residual Method	30
2.6.2 Weak Formulation	35

2.6.3	Spatial Discretization	36
2.7	FEM for Solid Mechanics	37
3	Stress Evolution during 3D IC Stacking using Open TSVs	41
3.1	Stress Generation during 3D IC Stacking	41
3.2	Nanoindentation	41
3.3	FEM Approach	44
3.3.1	Simulation Setup	44
3.3.2	Plasticity Simulation	46
3.4	Results and Discussions	47
3.5	Summary	51
4	Fracture Mechanics and Delamination in Open TSVs	53
4.1	Basis of Fracture Mechanics	53
4.1.1	Crack-Tip Field	53
4.1.2	Delamination	57
4.2	Energy Release Rate	60
4.2.1	Failure Criterion	62
4.3	Energy Release Rate Calculation	63
4.3.1	J -Integral	63
4.3.2	Regression Analysis	64
4.4	Delamination Prediction at TSV Bottom	64
4.4.1	Studied System	65
4.4.2	Approach	65
4.4.3	Results	67
4.4.3.1	Residual Stress Analysis	67
4.4.3.2	Thickness Analysis	71
4.4.3.3	Force Analysis	74
4.4.4	Discussion	76
4.5	Experimental Analysis	77
4.5.1	Experiment - Four Point Bend Technique	77
4.5.2	Simulation	79
4.5.3	Simulation Results	80
4.5.4	Discussion	83
4.6	Comparison between J -Integral and Regression Analysis	83
4.6.1	Structure	83
4.6.2	Results and Discussion	83
4.7	Summary	85
5	Simulation of Intrinsic Stress Build-Up in Thin Metal Films	87
5.1	Introduction	87
5.2	Theoretical Background	88
5.2.1	Volmer-Weber Growth	88
5.2.2	DRIE Scallop Formation	90
5.3	Volmer-Weber Model for Thin Films	91
5.3.1	Geometry	91
5.3.2	First Step: Compressive Stress	92
5.3.3	Second Step: Island Coalescence Process	93
5.3.4	Third Step: Thickening	94

5.4	Results	97
5.4.1	Low Adatom Mobility Analysis	97
5.4.1.1	Sample Description	97
5.4.1.2	Island Nucleation and Expansion	98
5.4.1.3	Island Coalescence and Grain Formation	99
5.4.1.4	Effects of the Island Shapes	101
5.4.1.5	Influence of Scallops	102
5.4.1.6	Effects of the Scallop Geometry (Width & Height)	104
5.4.1.7	Overtaking of Grains	106
5.4.2	High Adatom Mobility Analysis	107
5.4.2.1	Temperature Effects	107
5.4.2.2	Growth Rate Effects	108
5.5	Summary	110
6	Summary and Outlook	113
A	Kolosov-Muskhelishvili Formulas	117
A.1	Airy Stress Function	117
A.2	Analytic Function and Complex Variable	117
A.3	Complex Representation of the Airy Stress Function	118
A.4	Stress and Displacement described by Airy Stress Function	119
B	Westergaard Approach	123
	Bibliography	125

List of Abbreviations

IC	Integrated Circuit
FEOL	Front End Of the Line
BEOL	Back End Of the Line
2D	Two-Dimensional
3D	Three-Dimensional
MCM	Multi-Chip Module
SOC	System-On-Chip
SiP	System-in Package
CSP	Chip-Scale Package
TSV	Through Silicon Via
CMOS	Complementary Metal-Oxide-Semiconductor
DRIE	Deep Reactive Ion Etching
CVD	Chemical Vapor Deposition
PVD	Physical Vapor Deposition
ECD	Electro Chemical Deposition
CTE	Coefficient of Thermal Expansion
DRAM	Dynamic Random-Access Memory
NAND	Negative AND
DDR4	Double Data Rate-4
MEMS	Microelectromechanical Systems
FEM	Finite Element Method
FEA	Finite Element Analysis
PDE	Partial Differential Equation
4PB	Four Point Bend
DRIE	Deep Reactive Ion Etching
V-W	Volmer-Weber

List of Symbols

Overview of Solid Mechanics and Finite Element Method

X_i	Lagrangian Cartesian Coordinates, $i=1,2,3$
x_i	Eulerian Cartesian Coordinates, $i=1,2,3$
\mathbf{u}	Displacement Field
l_{ij}	Lagrange Infinitesimal Strain Tensor
$\varepsilon_{ij}, \boldsymbol{\varepsilon}$	Eulerian Infinitesimal Strain Tensor
\mathbf{t}	Stress Vector
$\boldsymbol{\sigma}$	Cauchy Stress Tensor
τ_{ij}	Shear Stress Components
F	Body Force
b	Force per Unit of Mass
ρ	Density of a Body
σ_{mises}	Von Mises Effective Stress
$\boldsymbol{\varepsilon}_e$	Elastic Strain Tensor
$\boldsymbol{\varepsilon}_p$	Plastic Strain Tensor
\mathbf{C}	Elasticity Tensor
\mathbf{M}	Compliance Tensor
λ	Lamé Constant
E	Young's Modulus
ν	Poisson's Ratio
μ	Shear Modulus
α	Coefficient of Thermal Expansion
$\delta \mathbf{u}$	Virtual Displacement
$\delta \varepsilon_{ij}$	Virtual Strain Components

Stress Evolution during 3D IC Stacking using Open TSVs

p_m	Pressure of an Indenter
-------	-------------------------

Y	Uniaxial Compressive Yield Stress of a Sample
a	Contact Area between Indenter and Sample
E^*	Reduced Modulus
R	Radius of an Indenter
P	Applied Load by Indenter
d	Penetration Depth in a Sample
Q_p	Plastic Potential
I_1	First Invariant of Cauchy Stress Tensor
J_2	Second Invariant of Cauchy Stress Tensor
J_3	Third Invariant of Cauchy Stress Tensor
$\dot{\epsilon}_p$	Plastic Strain Tensor Increment
$\dot{\epsilon}_{pe}$	Effective Plastic Strain Rate
F_y	Yield Function
σ_{ys0}	Initial Yield Stress
E_{Tiso}	Isotropic Tangent Modulus

Fracture Mechanics and Delamination in Open TSV

Z_I	Westergaard Function
K_I, K_{II}, K_{III}	Stress Intensity Factors for mode I, II, and III, respectively
ϕ	Airy Stress Function
ε	Bimaterial Constant
G	Energy Release Rate
G_c	Critical Energy Release Rate
Π	Total Potential Energy
U	Total Strain Energy
W	Strain Energy Density
V	Potential of External Force
γ	Fracture Surface Energy
J	J -Integral

Simulation of Intrinsic Stress Build-Up in Thin Metal Films

R	Radius Parameter
R_i	Initial Radius of the Island
R_{fr}	Frozen-In Radius

h_f	Film Thickness
f	Surface Stress
ΔP	Laplace Pressure
γ_s	Surface Energy
γ_{gb}	Grain Boundary Energy
h_{gb}	Grain Boundary Height
v_g	Deposition Rate
v_{gb}	Grain Boundary Velocity
μ_s	Surface Chemical Potential
μ_{gb}	Grain Boundary Chemical Potential
N_{gb}	Number of Atoms Moving from the Surface to Grain Boundary
D	Atom Diffusivity
a	Height of an Atomic Step
C_s	Fractional Coverage of Adatoms
σ_T	Tensile Stress
σ_C	Compressive Stress
Ω	Atomic Volume
r	Island Radius at the Coalescence Point
L	Grain Size
w_s	Width of the Scallop
h_s	Height of the Scallop

List of Figures

1.1	Schematic representation of an IC. The FEOL indicates all those wafer processing steps since the wafer enters production. It includes all the films needed to form transistors, capacitors, resistors and local interconnects. BEOL are all those process steps used for forming global interconnections.	3
1.2	Interconnect evolution: (a) The 2D interconnect structure (long interchip connections between logic and memory). (b) The SOC configuration (Larger die with issues regarding process, design and time to market). (c) The 3D stacked Si (Shortest interconnects between functions).	4
1.3	In (a) different discrete devices with their own packages interconnected using a circuit board. (b) The SiP configuration, where multiple dies and/or CSP are all connected on a common substrate.	5
1.4	(a) Indicates the 2.5D IC architecture and (b) the 3D IC architecture.	5
1.5	Process steps for Via First, Via Middle, and Via Last. For Via First and Via Middle, the TSV etching proceeds from the top of the wafer, where BEOL devices are located. Only in the Via Last process does the TSV etching initiate from the back of the wafer and the FEOL metals are used as an etch-stop layer	7
1.6	Simplified TSV fabrication steps. The first processing step is the hole generation through the Si, the second processing step is the TSV isolation line deposition, the third processing step is the building of the TSV barrier layer, and the fourth processing is the metal fill process for filled TSV (bottom) or the metal linear deposition (top). Further steps include wafer thinning and backside processing, not depicted here.	8
1.7	Channel crack in a thin film lying on top of a substrate. In this example the substrate and the interface are intact.	11
1.8	Interface crack between two materials. This phenomenon is also known as delamination.	12
1.9	Ratcheting. The picture on the left indicates the structure before metal deformation. The picture on the right denotes the deformed structure after many thermal cycles.	12
1.10	Schematic representation of the electromigration phenomenon. The conducting electrons transfer the momentum to the metal ions. This causes the gradual movement of ions and the formation of voids and consequently hillocks in the conductor material.	13
1.11	Due to a high stress the voids form and can increase in size leading to an open circuit failure.	13
1.12	Discretized domain and the corresponding elements and nodes.	14

2.1	Coordinate system. At the reference configuration $t = 0$ the body B is undeformed. The body b is deformed at time $t > 0$. X_1, X_2 and X_3 refer to the material coordinates at $t = 0$. x_1, x_2 and x_3 are spatial coordinates at $t > 0$. \mathbf{u} indicates the displacement vector.	16
2.2	Schematic representation of a body subjected to a force $\Delta \mathbf{F}$	20
2.3	Stress components on an infinitesimal cube.	21
2.4	Example of stress-strain curve for a ductile material.	23
2.5	Polycrystalline material.	23
2.6	Atom movements in elastic and slip deformation.	24
2.7	Piecewise linear hat-functions	37
2.8	An unformed body (left) and a deformed body (right).	38
3.1	(a) A sample of load displacement curve. (b) An indenter penetrating in to a sample.	42
3.2	Examples of load-displacement (P - d) curves for different material responses and properties. The pop-in event in (e) indicates cracking or delamination.	43
3.3	Two-dimensional representation of a TSV structure and an indenter. The dashed line indicates the axis of symmetry. Only a quarter of the system is represented. Al is shown in yellow, W in black, SiO_2 in orange, and Si in red. The multilayer consists of different materials. The indenter is spatially external to the TSV (the via height and width of the TSV in the figure do not represent the real size, under consideration).	45
3.4	Stress-strain curve showing the elastic part before reaching the σ_{ys0} . At σ_{ys0} the plastic deformation begins.	47
3.5	FEM result, illustrating the displacement (μm) of the indenter inside of the TSV. The displacement peaks at about $3 \mu\text{m}$	48
3.6	The loading part of the nanoindentation process is plotted and it illustrates a comparison between the FEM simulation and experimental data.	49
3.7	This image depicts normalized Von Mises stress development in the TSV. Two physical regions with high mechanical stress can be identified. The first is located in the TSV area above the indenter and the second is at the corner of the TSV. This perspective of the structure differs from Figure 3.3 in order to highlight those areas with a high concentration of mechanical stress.	50
3.8	Normalized Von Mises stress versus displacement into surface.	50
4.1	The three crack opening modes. (a) indicates mode I (opening), (b) mode II (sliding) and (c) mode III (tearing).	54
4.2	Coordinate at the crack-tip.	54
4.3	Tip of a bimaterial crack.	57
4.4	Example of crack advance in two-dimensional.	61
4.5	A possible (arbitrary) path around the crack-tip for the J -integral.	63
4.6	Schematic of the Open TSV geometry under consideration. The open TSV is integrated in the silicon of the wafer. The alternating layers with different thickness are located at the bottom. There are the interfaces where a failure of the device due to delamination is expected.	65
4.7	Schematic representation of the studied system. In the inset the path Γ for the J integral calculation is shown. The variable a indicates the crack length and w the width of the layer.	66

4.8	The energy release rate G for different initial stresses (Al) and crack lengths in the interface Ti/Al. Simulation conditions were $\sigma_{\text{Ti}}=-50$ MPa, $h_{\text{Ti}}=0.15$ μm , and $h_{\text{Al}}=0.5$ μm	67
4.9	The energy release rate G for different initial stresses (Ti) and crack lengths in the interface Ti/Al. Simulation conditions were $\sigma_{\text{Al}}=-100$ MPa, $h_{\text{Ti}}=0.15$ μm , and $h_{\text{Al}}=0.5$ μm	68
4.10	The energy release rate G for different initial stresses (SiO_2) and crack lengths in the interface Si/ SiO_2 . Simulation conditions were $h_{\text{Si}}=5$ μm , and $h_{\text{SiO}_2}=1.4$ μm	68
4.11	The energy release rate G for different initial stresses (W) and crack lengths in the interface SiO_2/W . Simulation conditions were $\sigma_{\text{SiO}_2}=-100$ MPa, $h_{\text{W}}=0.1$ μm and $h_{\text{SiO}_2}=0.4$ μm	69
4.12	The energy release rate G for different initial stresses (SiO_2) and crack lengths in the interface SiO_2/W . Simulation conditions were $\sigma_{\text{W}}=1.25$ GPa, $h_{\text{SiO}_2}=0.4$ μm , and $h_{\text{W}}=0.1$ μm	69
4.13	The energy release rate G for different initial stresses (TiN) and crack lengths in the interface SiO_2/TiN . Simulation conditions were $\sigma_{\text{SiO}_2}=-100$ MPa, $h_{\text{SiO}_2}=1$ μm , and $h_{\text{TiN}}=0.15$ μm	70
4.14	The energy release rate G for different initial stresses (SiO_2) and crack lengths in the interface SiO_2/TiN . Simulation conditions were $\sigma_{\text{TiN}}=-50$ MPa, $h_{\text{SiO}_2}=1$ μm , and $h_{\text{TiN}}=0.15$ μm	70
4.15	The energy release rate G for different thicknesses (W) and crack lengths in the SiO_2/W interface. Simulation conditions were $\sigma_{\text{SiO}_2}=-100$ MPa, $\sigma_{\text{W}}=1.25$ GPa, and $h_{\text{SiO}_2}=0.4$ μm	71
4.16	The energy release rate G for different thicknesses (SiO_2) and crack lengths in the SiO_2/W interface. Simulation conditions were $\sigma_{\text{SiO}_2}=-100$ MPa, $\sigma_{\text{W}}=1.25$ GPa, and $h_{\text{W}}=0.1$ μm	72
4.17	The energy release rate G for different thicknesses (TiN) and crack lengths in the SiO_2/TiN interface. Simulation conditions were $\sigma_{\text{SiO}_2}=-100$ MPa, $\sigma_{\text{TiN}}=-50$ MPa, and $h_{\text{SiO}_2}=1$ μm	72
4.18	The energy release rate G for different thicknesses (Al) and crack lengths in the Ti/Al interface. Simulation conditions were $\sigma_{\text{Ti}}=-50$ MPa, $\sigma_{\text{Al}}=-100$ MPa, and $h_{\text{Ti}}=0.15$ μm	73
4.19	The energy release rate G for different thicknesses (SiO_2) and crack lengths in the Si/ SiO_2 interface. Simulation conditions were $\sigma_{\text{SiO}_2}=-100$ MPa and $h_{\text{Si}}=5$ μm	73
4.20	The energy release rate G for different force and crack lengths in the SiO_2/W interface. Simulation conditions were $\sigma_{\text{SiO}_2}=-100$ MPa, $\sigma_{\text{W}}=1.25$ GPa, $h_{\text{SiO}_2}=0.4$ μm , and $h_{\text{W}}=0.1$ μm	74
4.21	The G for different forces and crack lengths in the Si/ SiO_2 interface. Simulation conditions were $\sigma_{\text{SiO}_2}=-100$ MPa, $h_{\text{SiO}_2}=1.4$ μm , and $h_{\text{Si}}=5$ μm	74
4.22	The G for different forces and crack lengths in the SiO_2/TiN interface. Simulation conditions were $\sigma_{\text{SiO}_2}=-100$ MPa, $\sigma_{\text{TiN}}=-100$ MPa, $h_{\text{SiO}_2}=1$ μm , and $h_{\text{Ti}}=0.15$ μm	75
4.23	The G for different forces and crack lengths in the Ti/Al interface. Simulation conditions were $\sigma_{\text{Ti}}=-50$ MPa, $\sigma_{\text{Al}}=-100$ MPa, $h_{\text{Ti}}=0.1$ μm , and $h_{\text{Al}}=0.5$ μm	75
4.24	Schematic representation of the studied system. On the top a force (F) was applied, and at the bottom two fixed points were used as bearings.	77

4.25	Experimental results for Sample 1 and Sample 2. The gray area indicates the steady state region where delamination appears.	78
4.26	Experimental results for Sample 3, Sample 4, and Sample 5. The gray area indicates the steady state region where delamination appears.	79
4.27	FEM simulation of the 4PB test. The legend indicates the Von Mises Stress (10^6 N/m ²). Due to the boundary condition the stress development in the bottom layer can be observed. In the inset a zoomed-in section of the crack, with the mesh used is shown.	80
4.28	Example of the obtained FEM results compared with the stresses calculated using (4.40). Here σ_{xx} as a function of r is shown.	80
4.29	Example of the obtained FEM results compared with the stresses calculated using (4.40). Here τ_{xy} as a function of r is shown.	81
4.30	G obtained from FEM simulations. Crack length in the range from 1 mm to 10 mm was simulated.	81
4.31	G obtained from FEM simulations. The crack length in the range from 1 mm to 10 mm was simulated.	82
4.32	Structure used for a comparison between the two methods.	84
4.33	G values obtained using the J -Integral method and the linear regression method. Crack lengths in the range from 0.1 mm to 0.9 mm were simulated. The percentage of variation between the two methods is reported.	84
5.1	Three steps of the V-W growth process. (a) indicates the nucleation of the islands where compressive stress occurs, (b) indicates the coalescence process where the islands impinge upon each other, and (c)-(d) is the thickening process where a homogeneous film is formed. The properties of the deposited material distinguish two kinds of microstructure, Type 1 (for low adatom mobility materials) or Type 2 (for high adatom mobility materials).	89
5.2	Stress evolution during the deposition process for both kinds of materials.	89
5.3	(a) A schematic illustration of the DRIE process, where a passivation layer protects the sidewalls during the subsequent etching cycle. (b) Etched trench structure after 8 deposition/etch cycles.	90
5.4	Half-cylindrical islands which lie on the substrate.	92
5.5	Schematic diagram of the impingement of the islands is shown. The dashed lines indicate the island before the coalescence process and the solid lines depict the homogeneous film (after the coalescence of the islands).	92
5.6	$h_{gb,i}$ during film growth.	94
5.7	Behavior of v_{gb} as a function of thickness for different v_g	95
5.8	σ_{xx} (in GPa) during the initial nucleation of W isolated islands. Development of compressive stress is observable at the W islands.	98
5.9	Behavior of the compressive stress due to the Laplace pressure for different grain sizes before coalescence. For all the samples $R_{fr}=10$ nm was assumed.	98
5.10	Behavior of the compressive stress for different values of R_{fr}	99
5.11	$\langle\sigma_{xx}\rangle$ dependence on film thickness for different grain size during V-W growth. After the coalescence, the stress becomes tensile and constant.	100
5.12	Normalized $\langle\sigma_{xx}\rangle \times h_f$ for different grain size during growth.	100
5.13	Distributions of σ_{xx} stress (GPa) at the point of coalescence for three different samples are shown.	101
5.14	Normalized average stress as a function of film thickness measured for the three different samples is shown. As the films thicken, their stress reach a steady value. All the stresses are normalized at the steady value.	101

5.15	Normalized $\langle \sigma_{xx} \rangle$ distribution in a scalloped structure ($h_s=0.1 \mu\text{m}$ and $w_s=1 \mu\text{m}$) for three different film thicknesses ($\sim 0 \text{ nm}$ (a), 200 nm (b), and 400 nm (c)).	103
5.16	Normalized average stress as a function of film thickness measured for different samples. In (a) the height of the scallops was varied, keeping constant the width of $0.75 \mu\text{m}$. In (b) the height of $0.1 \mu\text{m}$ was fixed and the width of the scallops was varied.	105
5.17	Normalized average stress as a function of film thickness measured for different samples. In (a) the height of the scallops was varied, keeping constant the width of $1 \mu\text{m}$. In (b) the height of $0.2 \mu\text{m}$ was fixed and the width of the scallops was varied.	105
5.18	Normalized average stress as a function of film thickness measured for different samples. In (a) the height of the scallops was varied, keeping constant the width of $1.25 \mu\text{m}$. In (b) the height of $0.3 \mu\text{m}$ was fixed and the width of the scallops was varied.	105
5.19	Schematic representation of grain overtaking. As the film thickness increases the grain which grows between scallops (indicated in red) is overtaken by the neighboring grains.	106
5.20	The crossed data points are the experimental data from [1, 2], and the lines are the results of the FEM simulations.	107
5.21	Average stress obtained from FEM simulations for different deposition temperatures.	108
5.22	The crossed data points are the experimental data from [3] and the lines represent the FEM simulations.	109
5.23	Average stress measured from FEM simulations for different thicknesses is shown.	109

List of Tables

1.1	Evolution in the number of transistors implemented within a single IC.	2
4.1	Thickness of layers employed.	66
4.2	Critical values G_c for the considered interface.	66
4.3	Summary of the conditions for delamination propagation.	77
4.4	Geometry of the samples used in the simulation study. The thickness h_2 includes the thickness of the adhesive. The comments indicate the type of deposition process and the presence or absence of the Ti layer.	78
4.5	G_c values measured from experimental data and calculated using FEM simulations. The G_c values calculated for Sample 3, Sample 4, and 5 are in good agreement with the experimentally measured G_c values.	82
5.1	Parameters used for the simulations. The value $(2\gamma_s - \gamma_{gb})$ was used as fitting parameter.	100

1

Introduction

Since the invention of integrated circuits many advancements in processing technologies have been achieved. Electronic devices are used daily and therefore they have enormously impacted our lives and life without them would be unfathomable. Thus, the reliability issues connected to newly developed devices are of great technical and economic interest.

1.1 Integrated Circuits

Integrated circuits (ICs) are an integral component of electronic devices such as computers, mobile phones, and other digital home appliances. ICs are simply very advanced electric circuits consisting of active and passive components. The most frequently implemented passive components are resistors and capacitors while the active components are diodes and transistors. Each component has a specific task to perform and they all have to work together to make the circuit perform as desired. Resistors are used to adjust signal levels, to limit current flow, bias active elements, and terminate transmission lines. Capacitors permit to temporarily store electrical energy in an electric field. Diodes allow current flow in only one direction and transistors are used to amplify or switch electronic signals and electrical power. These components are interconnected together by a single or multilevel metalization on a piece of single crystal silicon (Si) [4]. ICs range in complexity from simple logic modules to entire microcomputers, incorporating millions of components.

The first semiconductor-based electronic devices were constructed in 1947 for applications in medicine, military and other areas [4, 5, 6]. The first transistors were connected together with traces of metal that implemented different circuit functions. At that time these semiconductor devices could perform better than vacuum tubes or other electromechanical components. However, the real revolution was possible only with the development of the planar process which enabled the integration of multiple interconnect devices on one chip [4, 6].

Since their invention in 1959, ICs had a fast evolution. The first IC was composed of a few devices per chip, whereas now a typical IC has billions devices per chip, fabricated with a geometry size measured in nanometers [7]. In 1965, Gordon Moore made the important empirical observation that the number of components which fit on a single IC has doubled every year since their invention [8]. Subsequently, in 1975, looking forward to the next decade, he changed his prediction to a doubling every two years [9]. This technology revolution was supported by the exponential improvements of all the digital components, from processing speed and storage capacity to networking bandwidth and speed. The device miniaturization became strongly dependent on the process technology. The process technology and the number of transistors employed during the years are presented in the **Table 1.1** [10, 11].

ICs are fabricated by chemically or physically modifying the surface of a circular single-crystal Si called substrate (wafer). The build area of the IC is defined as a die.

Name	Description	Year	Number of transistors
SSI	small-scale integration	1964	1 to 10
MSI	medium-scale integration	1968	10 to 500
LSI	large-scale integration	1971	500 to 20 000
VLSI	very large-scale integration	1980	20 000 to 1 000 000
ULSI	ultra large-scale integration	1984	1 000 000 and more

Table 1.1: Evolution in the number of transistors implemented within a single IC.

To reduce the fabrication costs a large number of dies are processed on a single substrate and subsequently diced (die cutting). When a single die is packaged, it is then referred to as a chip. A single-crystal Si wafer is generally used as the base of ICs. Si is used because of its excellent electrical and physical properties fundamental for microelectronic devices compared to other semiconductor materials [12].

The IC is built by applying different chemical and mechanical processing steps on desired areas of the wafer. The basic processes employed to construct a device are:

- **Deposition:** chemical or physical deposition processes are used to deposit a film of material onto a substrate or on top of a previously deposited layer.
- **Etching:** implemented when a material or materials from the surface need to be removed. The etching process acts selectively, by coating surface areas that are to be protected, and leaving other areas exposed for etching. Two main categories of etching processes are available: chemical etching and dry plasma etching.
- **Ion Implantation:** different techniques are used to introduce dopant impurities into a wafer. Usually an electrical field can be used to accelerate ionized particles into a specific area of the wafer. This step is usually followed by diffusion in order to ensure proper distribution of the implanted dopant through the wafer depth
- **Patterning:** refers to the photolithography process. This process is used to transfer geometric shapes to the surface of the wafer by using a mask to specify patterns.

In ICs, the electrical devices (capacitors, transistors, resistors, etc.) are built by applying the above described processes. All these steps are employed during IC fabrication and they are repeated until all the IC is completed. The manufacturing of an IC can require hundreds of processing steps.

Two different fabrication stages during IC manufacturing are defined, referred to as the Front End Of the Line (FEOL) and the Back End Of the Line (BEOL) [13]. These two stages have a very significant difference and therefore the semiconductor industry uses this terminology as a way to differentiate the stages of semiconductor processing. FEOL refers to all the wafer processing steps of the initial stages of the IC processing. In this stage transistors, capacitors, resistors, and local interconnects are manufactured. Local interconnects are simple metal conductors, but at this stage they are used only as local connectors between various devices; therefore, these processes do not include the deposition of metal interconnect layer necessary to connect all the devices of the FEOL process. On the other hand, BEOL are all the processing steps required for the formation of the metal interconnects where the electrical devices get interconnect wiring on the wafer (cf. **Figure 1.1**) [13]. The first function of BEOL is to connect all the devices created during the FEOL processes. The components processed in the BEOL stage are contacts, insulating layers, metal levels, and bonding sites for chip-to-chip-package connections.

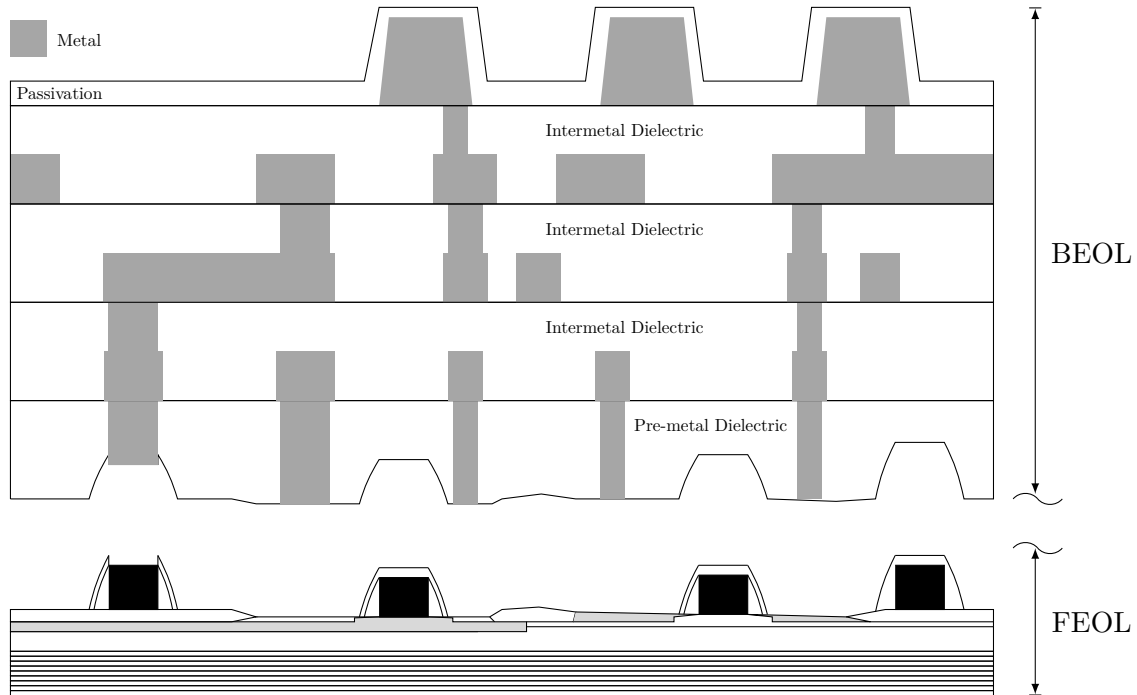


Figure 1.1: Schematic representation of an IC. The FEOL indicates all those wafer processing steps since the wafer enters production. It includes all the films needed to form transistors, capacitors, resistors and local interconnects. BEOL are all those process steps used for forming global interconnections.

Essentially, FEOL refers to the manipulation of the silicon wafer in order to generate all the desired devices, while BEOL refers to the addition of metal layers on top of the wafer, used to complete all necessary device connections.

FEOL and BEOL stages are intensively studied in order to increase and maintain the performance of the IC necessary to continue device development.

The final stage of IC fabrication is the packaging. This last step is necessary because the ICs are small, fragile, susceptible to environmental damage and difficult to handle by the users. Ceramic and plastic are most commonly used materials used for the packaging technology. Plastic materials are preferred due to the lower cost compared to ceramics. A wide variety of IC packages are available for different IC architectures. This stage is the last assembly process before testing and shipping devices to the customers.

1.2 Interconnect Structures

Because of the necessity to minimize the chip level features, the number of transistors per unit of area in IC continues to increase. All of the IC components must be electrically connected in order to provide the proper functionality. Over the years, different IC architectures were developed to maintain the miniaturization path.

Since the invention of the IC, the important role of the interconnects was already clear. With the increased complexity of the electronic devices the number of interconnects increased exponentially. At the beginning the connection of the electronic devices was difficult, expensive and unreliable. Through IC downscaling the transistor delay improved unlike the delay of caused by interconnect.

An evolution from two-dimensional (2D) to three-dimensional (3D) circuit fabrication was necessary in order to avoid efficiency problems [14] (c.f. **Figure 1.2**).

1.2.1 2D Integrated Circuit

The 2D IC approach consists of connecting different discrete devices with their packages using a printed circuit board (mechanical support with conductive tracks) (cf. **Figure 1.3** (a)). The leading microelectronics companies always struggle to increase performance and to integrate most advanced technologies in order to increase competitiveness of their products. The 2D integration of different technologies is an advantage for the device performance, but a continued demand leads to the requirement of a large and bulky circuit board. In the circuit board, the signal propagation is slow due to the extra length of the circuit, thereby hindering the performance.

In 2D ICs the dies can also be directly connected by wire bonding (cf. **Figure 1.2** (a)). This connection technology has significant limitations in terms of area and performance because it suffers from large interconnect lengths as well as an interconnect bandwidth bottleneck. To increase performance of 2D ICs continued research and development is a necessity [14].

The beginning of the 1990s was the time for the advent of Multi-Chip Modules (MCMs), where digital-only dies were mounted on the same package substrate [15].

The next step was the System-On-Chip (SOC) technology where all discrete devices were implemented on a single die [16]. This mixed-technology design was innovative but it led to an increase in the chip area and as a consequence to transmission delays (cf. **Figure 1.2** (b)). In addition the SOC technology needs different and complex process and these aspects have obviously fostered the development and success of a new architecture.

The System-in-Package (SiP) was the new technology available at the start of the 2000s (c.f. **Figure 1.3** (b)) able to overcome the size problem of the SOC technology [17]. Here multiple dies and/or Chip-Scale Package (CSP) devices are mounted and are all connected on a common substrate. Therefore all the components are built in a single package. Unlike SOC technology, SiP permits analog, digital, and radio frequency dies to be included in the same package.

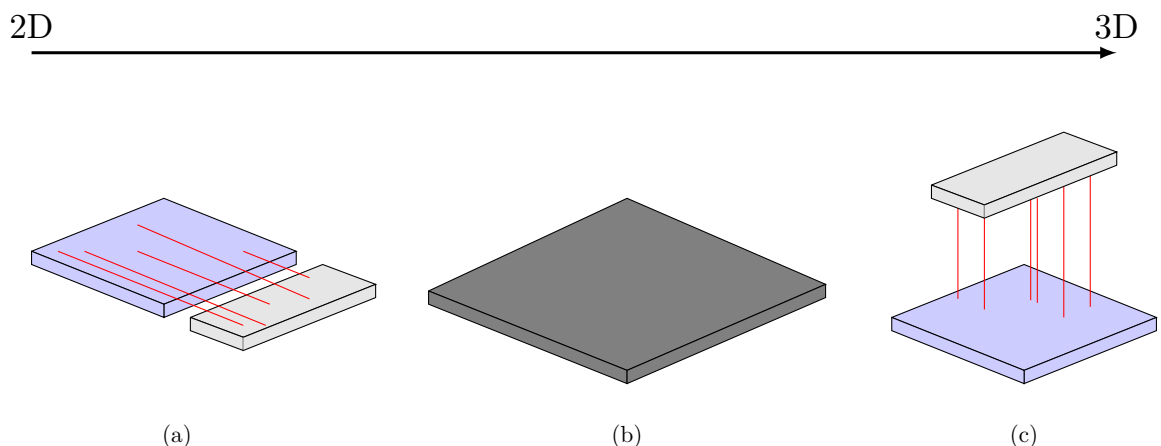


Figure 1.2: Interconnect evolution: (a) The 2D interconnect structure (long interchip connections between logic and memory). (b) The SOC configuration (Larger die with issues regarding process, design and time to market). (c) The 3D stacked Si (Shortest interconnects between functions).

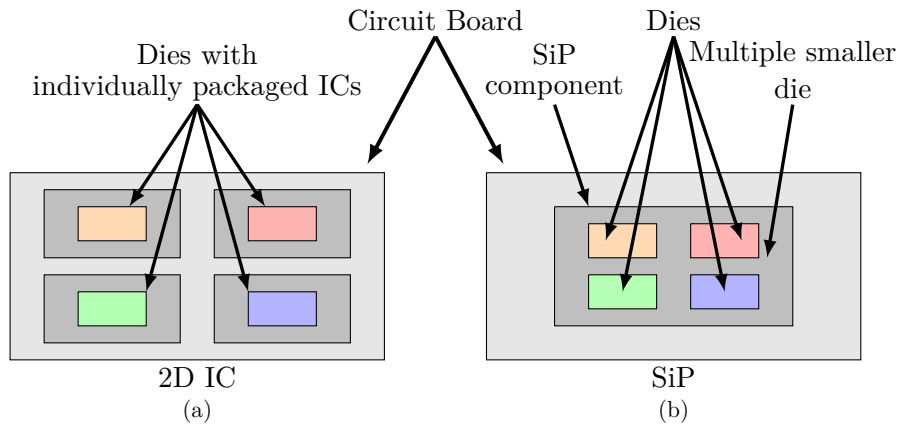


Figure 1.3: In (a) different discrete devices with their own packages interconnected using a circuit board. (b) The SiP configuration, where multiple dies and/or CSP are all connected on a common substrate.

All the single dies can be fabricated using the most appropriate technology process and subsequently integrated in the package.

1.2.2 2.5D and 3D Integrated Circuit

By using the third dimension, the large number of long interconnects, needed in 2D structures, are replaced by vertical interconnects which have maintained, and even increased, the performance of the device. The vertical direction is used to stack and connect the logic gates using Through Silicon Vias (TSVs) [14, 18, 19]. The TSV is effectively a conductor connecting the top and bottom of a silicon substrate of the stacked dies. The conductor is electrically insulated from the substrate by a dielectric layer and its function is to connect the metal wires of the stacked dies. The dies are connected by employing solder bumps. Bumps are interconnections which enable the face-to-face electrical connection between two devices. TSVs and bumps are used in 2.5D and 3D IC architectures [14, 20].

To explain the 2.5D IC architecture we refer to the 2D IC/SiP. The main difference between these two configuration is that, for the 2.5D IC/SiP an interposer is used between the SiP substrate and the dies (c.f. **Figure 1.4** (a)). TSVs are placed in the interposer connecting the metalization layers on its upper and lower surfaces. The interposer is an electrical interface used for the electrical routing one socket or connection to another and is composed of multiple wiring layers (redistribution layers) and TSVs. In the interposer the choice of the materials to use has to take into account the electrical, mechanical, thermal,

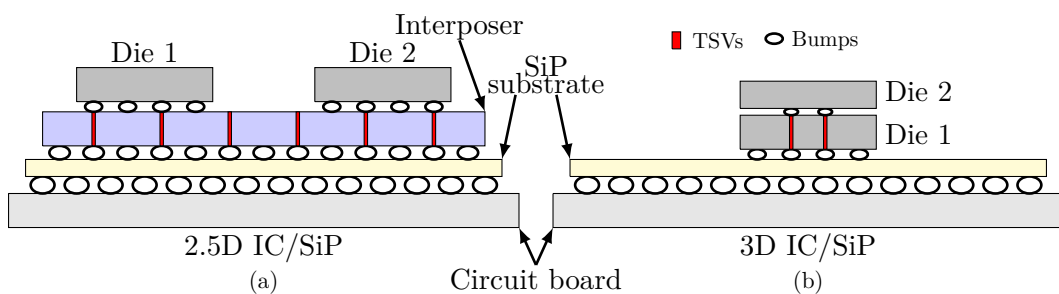


Figure 1.4: (a) Indicates the 2.5D IC architecture and (b) the 3D IC architecture.

and physical properties, as well as the cost of device. Glass, organic materials, and Si are widely used as interposer materials [14]. The 2.5D IC/SiP technology leads to an increase in capacity and performance, and thereby also to usage of smaller dies. A disadvantage of this integration is a significantly increased operation complexity. The idea behind the 3D IC/SiP architecture is to mount dies on top of each other (c.f. **Figure 1.4** (b)). The individual die can theoretically be very thin and therefore it would be possible to mount large dies on top of each other. By employing TSVs the upper die can electrically communicate with the lower die and the SiP substrate.

The development of the 3D TSV architecture depends on the progress of several technologies. All 3D IC fabrication processes comprise three basic steps [14, 18]:

- **Thinning of the layer:** coarse or fine grinding processes are used for wafer thinning. The wafer can be thinned to thickness as low as 50 μm . The exact process depends greatly on the technology used.
- **TSV creation:** the connection has to be created and isolated through the silicon substrate and subsequently filled with a conductor material. The size of the TSV depends on the intended freedom of access to the layer and on the desired architecture.
- **Alignment and bonding:** several technologies are necessary to align and bond die to wafer or wafer to wafer.

These three processing steps are described in more detail in **Section 1.3.1**.

A further distinction arises at the chip fabrication stage during which the via is formed. Three different approaches are industrially defined. In the Via First or Via Last technology the vias are fabricated before or after tier bonding, respectively, (tier is a structure comprising one or more IC die) and in the Via Middle technology, the vias are fabricated after the FEOL processes but before the BEOL interconnect metalization. The choice of approach depends on the device architecture. Via Middle is the preferred manufacturing approach for 3D IC applications because it is the least cost-intensive one. Via Last technology is mainly used for complementary metal-oxide-semiconductor (CMOS) image sensors and Via First technology has limitations mainly due to the via resistance [14]. In **Figure 1.5** the three technologies are schematically depicted.

3D system integration is the key to the realization of the “More than Moore” system fabrication where SiP and vertical integrations enable heterogeneous integration of different technologies [21].

1.3 Through Silicon Vias

3D integration, which enhances the performance of the IC by reducing the chip area and reducing the RC delay is made possible by TSVs. Stacking ICs and densely interconnecting them vertically gives several benefits [18].

One benefit is due to the heterogeneous functionalities including processing, sensing, memory, and data transmission which can be incorporated in a single die using TSVs. This opens new opportunities for efficient system integration. Dies can be built in different process technologies from different vendors and can be bonded at the later stage by a third party.

A second benefit is the capability of integration of incompatible technologies, leading to advantages in performance and form factor. In particular, the trend of smart technologies, including smart-watches, phones, and tablets need increasing functionality in a decreasing

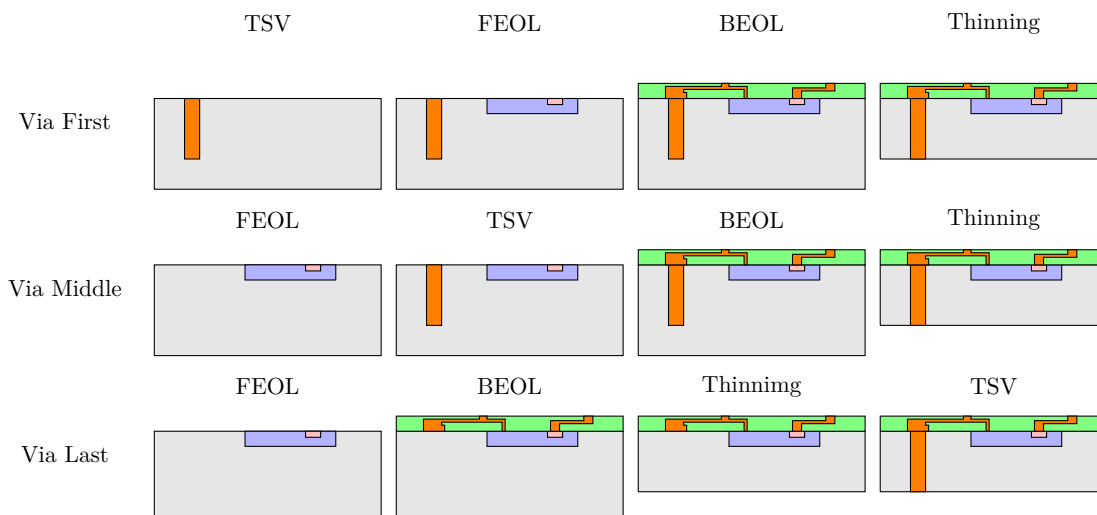


Figure 1.5: Process steps for Via First, Via Middle, and Via Last. For Via First and Via Middle, the TSV etching proceeds from the top of the wafer, where BEOL devices are located. Only in the Via Last process does the TSV etching initiate from the back of the wafer and the FEOL metals are used as an etch-stop layer

amount of space. Only by stacking can this combination of dense packing and increased functionality be enabled.

A third benefit lies 3D structure geometry itself. In a 3D structure the average wiring length is shorter than in a 2D structure and therefore the signal paths between dies is shorter, making the circuit faster. This contributes to a power decrease and a faster data transmission.

Another important benefit is related to the production cost, the chip stacking enables more cost-efficient integration.

1.3.1 TSV Fabrication

Stacking dies in 3D using TSVs as interconnects results in a variety of different advantages as detailed above. However, in order to fabricate 3D TSVs many separate processing steps are necessary. In the following, a simplified TSV fabrication procedure is described.

The **first processing step** is the formation of a via hole through the Si wafer. The via is created by etching the Si until a desired depth is reached, usually marked by an etch-stop layer. Due to the vertical scheme of CMOS fabrication, the etching may need to proceed through different layers such as resist, oxide, or BEOL metals, prior to reaching the wafer surface. These layers can complicate the etching processes, resulting in the mechanical failure of the device. Most frequently the Si hole is realized using a Deep Reactive Ion Etching (DRIE) sequence, but other etching processes, such as ion-enhanced plasma etching, or laser drilling can also be used to generate deep holes inside silicon. During the via hole etching the control and regulation of different parameters such as sidewall tapering angle, sidewall roughness and scalloping, defect generation, etc. is necessary [22, 23]. The DRIE technique is frequently also referred to as the Bosch process due to its introduction by Bosch in the mid 1990s [24]. In this etching process the sidewall passivation deposition and an ion-enhanced chemical etch process are applied in sequence for several cycles, producing an anisotropic and highly vertical structure. During the passivation process, a polymer is deposited on the Si surface. Subsequently, during the etching process, the

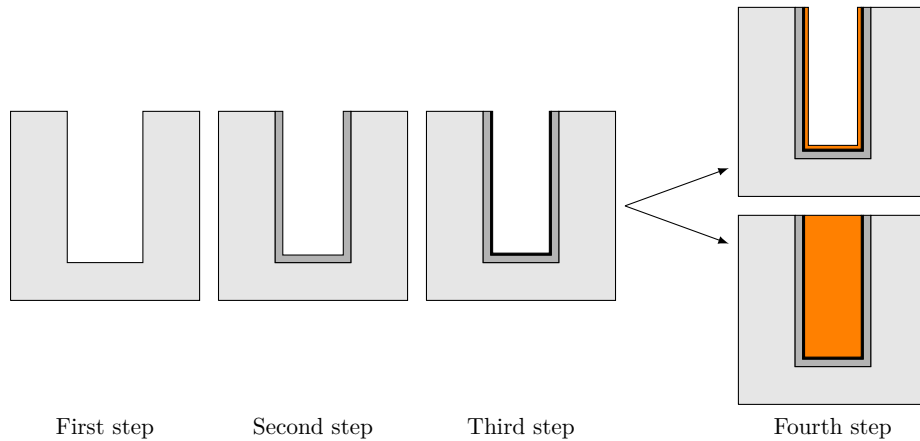


Figure 1.6: Simplified TSV fabrication steps. The **first processing step** is the hole generation through the Si, the **second processing step** is the TSV isolation line deposition, the **third processing step** is the building of the TSV barrier layer, and the **fourth processing** is the metal fill process for filled TSV (bottom) or the metal linear deposition (top). Further steps include wafer thinning and backside processing, not depicted here.

polymer at the bottom surface of the hole is easily removed using physical etching with accelerated ions, while the polymer at the via sidewall protects the hole sidewall. Unfortunately, this technique produces a particular local feature on the sidewall, made up of a series of small ridges, known as “scallops” which can lead to mechanical problems for the next deposition processes. The reduction of the sidewall roughness is required in order to enable a good coverage of the successive deposited materials; therefore, some companies are bringing to the market a TSV etch process referred to as scallop-free [14]. The polymers deposited during the passivation layer need to be carefully and fully removed before the next processing step can proceed.

The **second processing step** is the deposition of an isolation liner. The TSV conductive metal layer requires an isolation from the Si because the TSV should exhibit low leakage current, sufficiently large breakdown voltage, and a low parasitic capacitance. There are several methods by which the isolation materials can be deposited, such as using spray spin coating. For Via Middle and Via Last technologies, the processing temperature during deposition is limited so as to not affect the reliability of the FEOL devices. Therefore, low to mid-temperature deposition processes must be used. The materials used most frequently for isolation liner are oxide or nitride, deposited by low temperature chemical vapor deposition (CVD) or physical vapor deposition (PVD) [22].

The **third processing step** is the deposition of the TSV barrier layer. A high quality pinhole-free barrier layer is required in order to avoid the migration of metal into the Si. Tantalum and titanium nitride (TiN) are frequently used as a barrier materials. These materials also aid in the adhesion between the TSV metal and the line layer. CVD and PVD are the frequently used deposition processes, while CVD is preferred for barrier layer deposition [22].

The **fourth processing step** is the metal deposition or fill process. In this process a conductive material is used to fill the via holes. The materials utilized for this step are described in **Section 1.3.2**. Two different approaches are possible: filled or lined (open) TSVs. The unfilled configuration is favored when, due to the thermal expansion between adjoining materials, the fabrication of the TSV can induce thermal stress which degrades the performance of the device. The unfilled configuration allows for the metal lining to

expand towards the center of the TSV limiting critical stress in the structure [25]. An added reliability concern of filled TSV is copper pumping, which had adverse affects on the stress in the structure and its reliability in addition to the reliability of adjacent circuit elements, such as transistors [26].

The **fifth and final processing step** involves the deposition of the oxide and nitride passivation layers, followed by wafer thinning and backside processing.

Once the TSV fabrication is completed the dies or the interposer layer have to be bonded together in pairs. The bonding requires a perfect alignment, where TSVs must be correctly placed to establish the electrical connection between dies and/or interposer layer. Any offset may result in increased local stresses and degraded performance.

The TSV geometry differ slightly for 3D IC and 2.5D interposer applications. Usually, for 3D IC applications TSVs have a small dimension, 1-5 μm in diameter and 10-50 μm in depth. For Si interposers, TSVs are bigger with diameters of 10 μm or more and depths of 50-100 μm or more [14].

In **Figure 1.6** the process steps are illustrated.

1.3.2 TSV Metalization

Copper (Cu) and tungsten (W) are the materials most frequently employed as metalization in the TSV structures. For Via First technology poly-silicon can be employed as well. The frequently used materials with their features are listed below:

- **Cu:** the use of the Cu derives from the previously used single and dual-damascene Cu plating during BEOL processing. Before performing the actual filling a Cu-seed deposition process is required to obtain a continuous Cu seed layer in high aspect ratio TSV structures. The Cu filling process is realized using electrochemical deposition (ECD). The Cu-TSV structure requires a "superfilling" of the etched holes to ensure that no voids have formed. After the Cu deposition, the Cu is annealed in order to avoid a volumetric expansion (Cu extrusion) during further thermal processing steps [14, 22]. For Cu-filled TSVs with small sizes and high aspect ratios CVD deposition is used. For larger and deeper TSV the electro chemical deposition process is commonly employed [27]. For Via Last technology the integration and reliability concerns related to the TSV can be minimized by using the open TSV configuration [28]. Cu is mostly used because of the ease of fabricating high-aspect ratio TSV, for better electromigration compared to W, and it is comparatively low resistivity which makes it suitable for fast switching.
- **W:** this material has a smaller mismatch of thermal expansion coefficient with Si when compared to Cu and thus a smaller variation in stress with temperature. However, due to the deposition process the W develops a very large residual stress causing significant stress in the Si and limiting the thickness of the deposited W layers. CVD is employed to fill narrow TSV structures with large aspect ratios. The thickness of the W layer can be controlled by using the unfilled TSV configuration. Open W-lined TSVs are used and are available in the market for sensor signals, such as for image sensors. This structure provides an advantage regarding the geometric aspect, leaving a larger free area for the sensing functionality [29].
- **Poly-Silicon:** due to the compatibility problems with the FEOL process Cu and W TSVs are not suitable for Via First technology. Poly-Silicon is used as a TSV fill and only a linear barrier is required. This approach is applicable only for high-impedance TSV interconnects due to the high resistivity of the poly-silicon [22].

The choice of material also depends on the geometric dimensions of the TSV. The coefficient of thermal expansion (CTE) mismatch between the TSV metalization and the surrounding Si is a cause of thermal stress in the surrounding Si, causing reliability issues for the TSV structure and surrounding devices, when subject to different thermal loads. Since TSV stresses increase as the TSV diameter increases, the choice of the metal for TSVs can be determined by the required depth and aspect ratio of TSVs demanded for a specific architecture.

1.3.3 Current and Future TSV Applications

The application of TSVs can be split into two main areas [18]:

1. The first application area is where the device form factor is required and the 3D IC technology can also bring advantage in performance.
2. The second application area is where high performance computing is required, and therefore 3D TSV technology permits higher clock rates, lower power dissipation, and higher integration technology. TSVs are used as components for CMOS image sensors, dynamic random-access memory (DRAM) and negative AND (NAND), processors, and other logic devices.

CMOS image sensors are the one of the first devices to use 3D integration in high volume manufacturing. Since 2007-2008, Toshiba, Aptina, ST Microelectronics, and other companies have commercialized CMOS image sensors which implement TSVs. The use of TSVs resulted in an increased lateral compactness permitting the design of miniature devices [30]. This advantage led to a wide implementation of CMOS image sensors in cellular phones and tablets. Usually, a Via Last technology is used for the processing of TSVs within the fabrication of CMOS image sensors. An Austrian sensors manufacturer, ams AG developed Open TSV structure for CMOS image sensors. This open TSV technology allowed for an electrical connection between a thinned wafer on top and a CMOS image sensor, bonded to the bottom [29]. The bottom and top wafers are electrically connected by TSVs. In this application the use of open TSVs results an improved thermal behavior compared to filled TSVs.

In order to increase the performance of DRAM a shrinking of the dimensions while maintaining a sufficient amount of capacitance in a memory cell and low level of leakage current is required. In 2014 Samsung started the mass production of double data rate-4 (DDR4) registered dual n-line memory modules which use the 3D TSV packaging technology [30]. In the future, Samsung plans to continue to work on improving 3D TSV technologies in order to create even higher density DRAM modules supporting the transition from DDR3 to DDR4.

In 2015 Toshiba announced the development of the first stacked NAND flash memories utilizing TSVs [31]. NAND are flash memories which enable the largest bit density among solid-state memory devices. The application of TSV technology in this device produces an increase in the speed of reading and writing data while reducing the power consumption.

Micron Technology (memory manufacturer) and Intel (CPU manufacturer) have jointly built a new breed of integrated architectures based on 3D chip packaging [30]. TSVs are used in order to resolve many problems regarding the mismatch in the clock speed between CPUs and memory.

Microelectromechanical systems (MEMS) can also incorporate TSVs. MEMS are mainly used for microsensors and microactuators where piezo-capacitive components are used to measure a physical phenomenon and convert it to an electrical signal. Usually

the signal level is low and noise sensitive TSVs can be employed to reduce the parasitic capacitance. Since 2011, ST Microelectronics began to replace traditional wiring with short TSVs in MEMS devices such as smart sensors and multi-axis inertial modules [30].

The continued demand for electronic devices having a more compact form factor, more versatility, higher performance and lower power consumption will lead to further innovation and continues development of 3D technology.

1.4 Reliability of Interconnect Structures

In microelectronics, interconnect structures bear the task of electrically connecting several components of an IC. It is evident that, along with the reliability of the device themselves, the reliability of the interconnect structures must be thoroughly investigated in order to limit the probability of IC or chip failure. By definition, reliability is the probability that a device, operating under defined conditions, will continue to operate under those conditions for a defined period of time [32]. On the other hand, failure can be defined as any condition that causes a device or circuit to cease to operate in a desired manner [32]. A failure can appear instantly after a shock or grow slowly and decrease the device functionality over time until arriving at a failure condition. Each failure mode is the result of a certain failure mechanism in which specific combinations of material properties and the surrounding environment act together.

Interconnects can mechanically fail due to three main mechanisms [32]: tensile rupture (fracture due to mechanical overloading), creep failure (damage caused by a long-lasting permanent load or stress), and fatigue (damage caused by cyclical loads or stresses). These mechanisms affect the interconnection simultaneously. The thermomechanical stress is the main source of mechanical failure (fatigue, delamination, creep, etc.). However other factors can also affect the failure of a device, such as electrical and chemical actions. Interconnections exposed to high electrical current densities are subject to electromigration-induced voiding. Corrosion phenomena metals can accelerate fatigue and delamination failure. In the list below the most frequent mechanisms leading to failure in devices are outlined [33]:

- **Cracking:** Due to the deposition process and the use of thermal processes, thin films are frequently under a state of biaxial stress. This excess of energy in the film can trigger the propagation of a crack. A defect in the film can act as a source for crack initiation. The crack can run across the film thickness and often stops at the interface, leaving the interface and the substrate intact. In the film, the crack extends laterally until it reaches the film edge or until it connects with another crack. The elongated crack is known as a channel crack and it can be bigger than the film thickness (cf. **Figure 1.7**). The crack generation and propagation lead to the fracture of the film and subsequently to an open circuit failure.

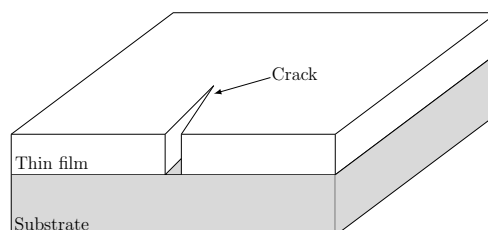


Figure 1.7: Channel crack in a thin film lying on top of a substrate. In this example the substrate and the interface are intact.

- **Delamination:** As described in **Section 1.3.1** the TSV structure is comprised of many different materials. Delamination can evolve at the interface of two materials. Typically, an interface crack nucleates from a site of high stress concentration such as a free edge of the film or a geometric or material junction in a patterned structure. Residual stresses in the films can be the cause of the crack interface propagation. The **Figure 1.8** shows an example of an interface crack.

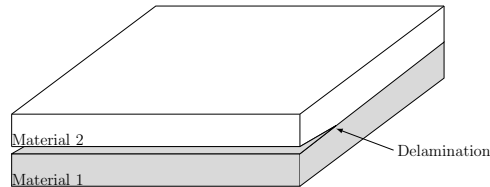


Figure 1.8: Interface crack between two materials. This phenomenon is also known as delamination.

- **Ratcheting:** Interconnect materials under temperature cycling can exhibit failures such as delamination, cracking, or metal film crawling. The cause of these failures is due to the thermal expansion mismatch between the metal and the isolation material or Si, causing a plastic deformation of the metal film. Directed by the shear stresses, generated during various thermal cycles, the metal films introduce a small amount of plastic deformation in each thermal cycle. After many thermal cycles, the accumulated deformation is very large and it can cause a failure in the device. For example, in **Figure 1.9** the gray area indicates a packaging material, the black area an isolating material, the orange area a substrate, and the white area a metal. If we assume that the packaging material has a larger CTE than the other materials, during the thermal cycle a shear stress (τ) will be generated and transmitted to the metal material. It may appear that, after several temperature cycles, the shear stress in the metal vanishes and the structure plastically deforms. Over time this process can lead to a failure due to high material deformation.

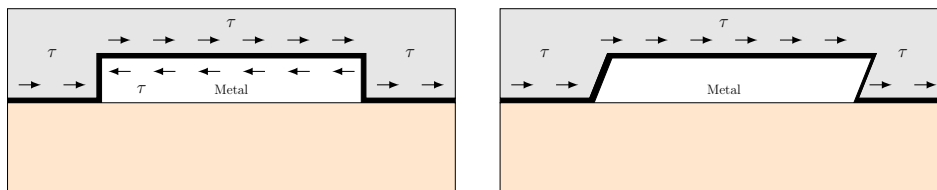


Figure 1.9: Ratcheting. The picture on the left indicates the structure before metal deformation. The picture on the right denotes the deformed structure after many thermal cycles.

- **Electromigration:** During its operation the interconnect line can carry a high electric current. Due to this high current, metal atoms are transported in the direction of electron flow inducing a wear-out of the interconnect metal (cf. **Figure 1.10**). This wear-out mechanism normally leads to the formation of a void which grows and triggers a device failure.

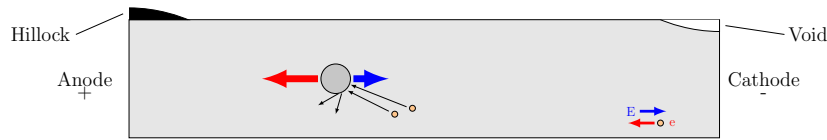


Figure 1.10: Schematic representation of the electromigration phenomenon. The conducting electrons transfer the momentum to the metal ions. This causes the gradual movement of ions and the formation of voids and consequently hillocks in the conductor material.

- **Stress-induced voiding:** This refers to a break in a metal line or a via-hole occurring in the absence of a current flow. As a result of multiple thermal cycles the material is under different stresses which can cause the growth of a void, as presented in **Figure 1.11**. So far, there is not a unanimously accepted theory of the stress-induced voiding phenomenon. However, in copper structures it is thought to be due to the high temperature processing. After the thermal process the copper has a large tensile stress due to a mismatch in the CTEs of the materials involved and therefore the stress relaxes in time through atom diffusion and thus by forming voids.

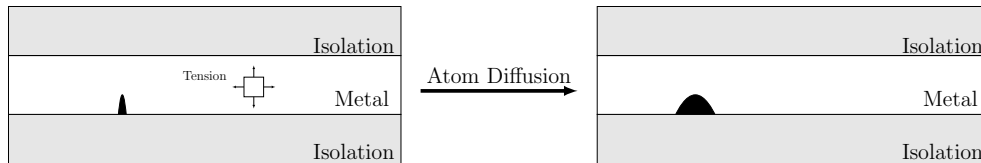


Figure 1.11: Due to a high stress the voids form and can increase in size leading to an open circuit failure.

1.5 FEM Approach for Reliability

The finite element method (FEM) (also called finite element analysis (FEA)) is a numerical method for solving a system of partial differential equations (PDEs). Most physical problems (fatigue, electromigration, thermally induced failure mechanism, delamination, etc.) can be described using a set of PDEs. FEM is employed to solve these PDEs and obtain an accurate analysis of many different physical problems [32].

In a continuum problem of any dimensions an unknown field variable (displacement, potential, etc.) has infinitely many values because it is a continuous function of generic points in the body that generates an infinite number of unknowns. The main idea of FEM is to discretize a domain into a finite number of elements in a way that the entire domain is approximated by the union of these discrete elements (cf. **Figure 1.12**). The discretization procedure permits the study of a field variable by reducing a problem to a finite number of unknowns field variables.

The unknown field variable is expressed by assuming approximating functions (interpolation functions) within each element. At specified nodes or nodal points of the domain, the approximating functions are defined in terms of values of the field variables which are the fundamental unknowns. Nodes are usually located on the element boundaries, where adjacent elements are connected (cf. **Figure 1.12**). The behavior of the field variable within the elements is described by the nodal values of the field variable and the interpolation functions. The nodal values of the field variable are the new unknowns and they represent the finite element problem. When these unknowns are obtained, the interpolation functions define the field variable throughout the aggregated elements. Thus, the

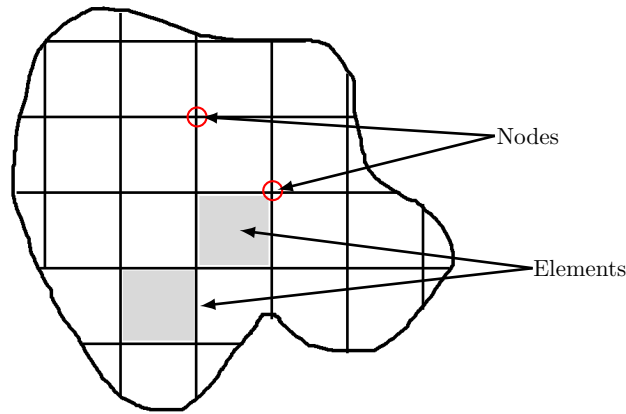


Figure 1.12: Discretized domain and the corresponding elements and nodes.

solutions are initially formulated for individual elements and subsequently assembled to represent the entire problem geometry [34].

FEM is widely employed in microelectronics. A multitude of different physical phenomena can be handled by choosing the desired geometry and using the material data required. The FEM tool permits the determination or prediction of the stress limits, or the lifetime of specific configurations, fundamental for the reliability study.

1.6 Outline of the Thesis

In this document a detailed analysis of the mechanical failure of open TSV is presented. Finite element simulations are employed to investigate the possible causes which lead to mechanical failure. Different simulation schemes, material, and mechanical models are applied. By means of simulations, different scenarios are studied leading to a comprehensive analysis of the mechanical behavior of TSVs. The goal of this work is to improve and analyze the reliability of the TSV interconnections and thus of the entire device leading to a deeper understanding of TSVs. The study can help developers to improve their processes.

The dissertation is divided into six chapters, including this introductory chapter, **Chapter 1**. In **Chapter 2** the elements of the linear elasticity theory are explained, followed by the description of the FEM theory. **Chapter 3**, **Chapter 4**, and **Chapter 5** present the physical models employed and implemented to investigate the failure sources and mechanisms in open TSVs. The stress evolution in an open TSV during 3D IC stacking is analyzed in **Chapter 3**. The results presented in the **Chapter 3** provide description of the critical stress areas in an open TSV due to an external force. In these critical areas a high probability of delamination failure is expected and therefore a study of the delamination between these specific material layers in TSVs is presented in **Chapter 4**. The probability of delamination is high in material films with high residual stress. In **Chapter 5** the generation of the intrinsic stress inside the metal films is investigated. **Chapter 6** summarizes the entire work and presents an outlook for further studies.

2

Overview of Solid Mechanics and the Finite Element Method

Microelectronic devices are complex systems fabricated through the manipulation and integration of many different materials. In order to be able to understand and improve such technology a multidisciplinary approach is necessary.

As explained in **Section 1.4**, mechanical problems in microelectronics are critical issues which may occur during the manufacturing processes or during device operation. In order to improve the devices' lifetime, a deep investigation into potential mechanical issues is essential. In this chapter the fundamental concepts of the solid mechanics theory needed for the analysis of mechanical problems in microelectronics are described.

The finite element method originated from the needs to solve mechanically related problems. In this work a FEM tool is used to calculate the resulting stress/strain in microelectronic components under several loading conditions and therefore an overview of FEM is presented.

2.1 Continuum Mechanics

The continuum mechanics approach ignores the discrete nature of matter, considering materials as uniformly and continuously distributed throughout regions of space. This simplification leads to the definition of material properties such as conductivity, permittivity, yield strength, coefficient of thermal expansion and simulation quantities such as density, displacement, velocity, etc., as continuous functions of position.

Two main types of equations are used in continuum mechanics [35]:

1. General equations applicable equally to all materials and referring to universal physical laws.
2. Equations which describe the mechanical behavior of particular materials known as constitutive equations.

In this section the kinematic and the stress equations are described. Subsequently, a brief description of the constitutive equations concerning elasticity is provided.

2.1.1 Deformation and Strain

This section, which is based on [35, 36], deals with the kinematic relations of a continuous medium. To define the basic deformation and strain concepts we must analyze material kinematics, which refers to the mathematics of motion without considering the masses of objects or the forces which may have caused the motion. Therefore, a kinematic analysis

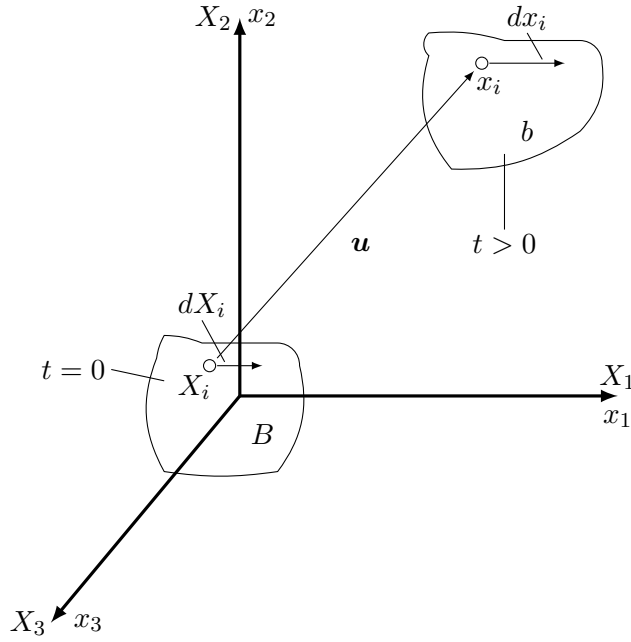


Figure 2.1: Coordinate system. At the reference configuration $t = 0$ the body B is undeformed. The body b is deformed at time $t > 0$. X_1, X_2 and X_3 refer to the material coordinates at $t = 0$. x_1, x_2 and x_3 are spatial coordinates at $t > 0$. \mathbf{u} indicates the displacement vector.

permits to study motion and displacement within a material, without regard to the associated stresses. This permits to analyze the system essentially as a geometric problem. Kinematics is widely applied to solve mechanical problems [36].

In order to describe the motion of a body the definition of a reference coordinate system is necessary (cf. **Figure 2.1**). At time $t = 0$ the body B is unloaded and undeformed. The particle of the body can be identified at all times by the set of coordinates X_i where $i = 1, 2, 3$ refer to fixed Cartesian axes.

At time $t > 0$ the body may have changed its position and shape (we refer to it as b) and its new position is defined by specifying the position x_i of the particle with previous coordinate X_i in the form

$$x_i = x_i(X_p, t), \quad i, p \in \{1, 2, 3\} \quad (2.1)$$

which corresponds to

$$x_1 = x_1(X_1, X_2, X_3, t), \quad x_2 = x_2(X_1, X_2, X_3, t), \quad x_3 = x_3(X_1, X_2, X_3, t). \quad (2.2)$$

In this equation x_i is the occupied coordinate by the body-point X_1, X_2, X_3 at time t . (2.1) is assumed differentiable with respect to X_1, X_2, X_3 and t .

The deformation of the body can be described by only considering two configurations of the body, an initial and a final configuration where the motion of the body can be regarded as a single-parameter sequence of deformations. In (2.1) the mapping has the unique inverse

$$X_i = X_i(x_p, t), \quad i, p \in \{1, 2, 3\} \quad (2.3)$$

or

$$X_1 = X_1(x_1, x_2, x_3, t), \quad X_2 = X_2(x_1, x_2, x_3, t), \quad X_3 = X_3(x_1, x_2, x_3, t). \quad (2.4)$$

From (2.3) the existence of the Jacobian determinant is ensured

$$J := \det \left(\frac{\partial x_i}{\partial X_j} \right), \quad (2.5)$$

which is positive for all points ($J > 0$). The significance of (2.5) is that the material of the body cannot penetrate itself and that a material occupying a finite non-zero volume V at time $t = 0$ cannot be compressed to a point or expanded to infinite volume during its motion ($dV = JdV_0$).

The coordinates X_1, X_2 , and X_3 are known as Lagrangian (or material) coordinates and they refer to distinct material particles at the reference configuration. On the other hand, the coordinates x_1, x_2 , and x_3 are known as Eulerian (or spatial) coordinates and they refer to distinct points of space at the deformed configuration. In continuum mechanics both sets of coordinates can be used.

Lagrangian or Eulerian coordinates can be applied to describe the displacement vector $\mathbf{u} = \mathbf{x} - \mathbf{X}$ of a typical particle from its position \mathbf{X} , in the reference configuration, to its position \mathbf{x} at time t . Using (2.1) as a reference, the displacement vector can be described by

$$\mathbf{u}(\mathbf{X}, t) = \mathbf{x}(\mathbf{X}, t) - \mathbf{X}, \quad \text{or} \quad u_i(X_1, X_2, X_3, t) = x_i(X_1, X_2, X_3, t) - X_i, \quad (2.6)$$

or by using (2.3) as a reference

$$\mathbf{u}(\mathbf{x}, t) = \mathbf{x} - \mathbf{X}(\mathbf{x}, t), \quad \text{or} \quad u_i(x_1, x_2, x_3, t) = x_i - X_i(x_1, x_2, x_3, t). \quad (2.7)$$

The material displacement gradient is obtained by a partial differentiation of the displacement vector (2.6) with respect to the Lagrangian coordinate

$$\frac{\partial u_i}{\partial X_j} = \frac{\partial x_i}{\partial X_j} - \delta_{ij}, \quad (2.8)$$

where δ_{ij} represents the Kronecker symbol. The spatial displacement gradient is determined by partial differentiation of the displacement vector (2.7) with respect to the Eulerian coordinate

$$\frac{\partial u_i}{\partial x_j} = \delta_{ij} - \frac{\partial X_i}{\partial x_j}. \quad (2.9)$$

In a similar way the material deformation gradient is defined by

$$F_{ij} := \frac{\partial x_i}{\partial X_j}, \quad (2.10)$$

and the spatial deformation gradient is defined by

$$F_{ij}^{(-1)} := \frac{\partial X_i}{\partial x_j}. \quad (2.11)$$

From (2.1) and (2.10) the distance differential dx_i (cf. **Figure 2.1**) can be expressed by

$$dx_i = \left(\frac{\partial x_i}{\partial X_j} \right) dX_j = F_{ij} dX_j \quad \text{or} \quad d\mathbf{x} = \mathbf{F} d\mathbf{X}, \quad (2.12)$$

where $d\mathbf{x}$ is the line element vector and \mathbf{F} is the deformation gradient.

\mathbf{F} is a second-rank tensor and it can be interpreted as a linear transformation, where the initial element vector $d\mathbf{X}$ is mapped onto the corresponding vector $d\mathbf{x}$ at time t .

$$\begin{bmatrix} dx_1 \\ dx_2 \\ dx_3 \end{bmatrix} = \begin{bmatrix} 1 + \frac{\partial u_1}{\partial X_1} & \frac{\partial u_1}{\partial X_2} & \frac{\partial u_1}{\partial X_3} \\ \frac{\partial u_2}{\partial X_1} & 1 + \frac{\partial u_2}{\partial X_2} & \frac{\partial u_2}{\partial X_3} \\ \frac{\partial u_3}{\partial X_1} & \frac{\partial u_3}{\partial X_2} & 1 + \frac{\partial u_3}{\partial X_3} \end{bmatrix} \begin{bmatrix} dX_1 \\ dX_2 \\ dX_3 \end{bmatrix} \quad (2.13)$$

An important value is the difference $(dx)^2 - (dX)^2$ for two neighboring particles of a continuum because it can be taken for a suitable measure of strain between the initial and post-displacement configurations. Using (2.10), (2.12), and the summation Einstein's rule, the measure of strain can be written as

$$(dx)^2 - (dX)^2 = (F_{ij}F_{ik} - \delta_{jk})dX_jdX_k \equiv 2\lambda_{jk}dX_jdX_k. \quad (2.14)$$

In the equation above, the second-order tensor with component λ_{ij} is known as the Lagrange finite strain tensor:

$$\lambda_{ij} := \frac{1}{2}(F_{ki}F_{kj} - \delta_{ij}) \equiv \frac{1}{2}(g_{ij} - \delta_{ij}), \quad (2.15)$$

where the tensor

$$g_{ij} = F_{ki}F_{kj} \quad (2.16)$$

is called right Cauchy-Green tensor.

The Lagrange strain tensor (2.15), described in terms of displacement (2.6), takes the form

$$\lambda_{ij} = \frac{1}{2} \left(\frac{\partial u_i}{\partial X_j} + \frac{\partial u_j}{\partial X_i} + \frac{\partial u_k}{\partial X_i} \frac{\partial u_k}{\partial X_j} \right) \quad (2.17)$$

if F_{ij} from (2.10) and (2.8) is substituted into (2.15).

In addition the strain measure can be formulated by employing the spatial coordinate x_i as a set of independent variables

$$(dx)^2 - (dX)^2 = (\delta_{jk} - F_{ij}^{(-1)}F_{ik}^{(-1)})dx_jdx_k \equiv 2\eta_{jk}dx_jdx_k, \quad (2.18)$$

where η_{jk} is the Eulerian finite strain tensor. In terms of displacements (2.7) this tensor takes the form

$$\eta_{ij} = \frac{1}{2} \left(\frac{\partial u_i}{\partial x_j} + \frac{\partial u_j}{\partial x_i} - \frac{\partial u_k}{\partial x_i} \frac{\partial u_k}{\partial x_j} \right). \quad (2.19)$$

If each displacement gradient component $\partial u_i/\partial X_j$ in (2.17) is small compared to δ_{ij} , the product of the derivatives can be neglected since it is much smaller than the linear term. Therefore, the Lagrange infinitesimal strain tensor is obtained:

$$l_{ij} = \frac{1}{2} \left(\frac{\partial u_i}{\partial X_j} + \frac{\partial u_j}{\partial X_i} \right) = \frac{1}{2}(F_{ij} + F_{ji}) - \delta_{ij}. \quad (2.20)$$

Implementing the same methodology for $\partial u_i/\partial x_j \ll \delta_{ij}$ in (2.19) the Eulerian infinitesimal strain tensor is derived

$$\varepsilon_{ij} = \frac{1}{2} \left(\frac{\partial u_i}{\partial x_j} + \frac{\partial u_j}{\partial x_i} \right) = \frac{1}{2}(u_{i,j} + u_{j,i}), \quad (2.21)$$

which is known as the classical strain tensor.

The Eulerian infinitesimal strain tensor is an approximation which is only valid for small changes and can be expressed as [37]

$$\boldsymbol{\varepsilon} = \begin{bmatrix} \frac{\partial u_1}{\partial x_1} & \frac{1}{2} \left(\frac{\partial u_1}{\partial x_2} + \frac{\partial u_2}{\partial x_1} \right) & \frac{1}{2} \left(\frac{\partial u_1}{\partial x_3} + \frac{\partial u_3}{\partial x_1} \right) \\ \frac{1}{2} \left(\frac{\partial u_2}{\partial x_1} + \frac{\partial u_1}{\partial x_2} \right) & \frac{\partial u_2}{\partial x_2} & \frac{1}{2} \left(\frac{\partial u_2}{\partial x_3} + \frac{\partial u_3}{\partial x_2} \right) \\ \frac{1}{2} \left(\frac{\partial u_3}{\partial x_1} + \frac{\partial u_1}{\partial x_3} \right) & \frac{1}{2} \left(\frac{\partial u_3}{\partial x_2} + \frac{\partial u_2}{\partial x_3} \right) & \frac{\partial u_3}{\partial x_3} \end{bmatrix}, \quad (2.22)$$

or using the engineering notation

$$\boldsymbol{\varepsilon} = \begin{bmatrix} \varepsilon_{xx} & \varepsilon_{xy} & \varepsilon_{xz} \\ \varepsilon_{yx} & \varepsilon_{yy} & \varepsilon_{yz} \\ \varepsilon_{zx} & \varepsilon_{zy} & \varepsilon_{zz} \end{bmatrix}. \quad (2.23)$$

The components ε_{xx} , ε_{yy} , and ε_{zz} refer to the normal strain and $\varepsilon_{xy}=\varepsilon_{yx}$, $\varepsilon_{yz}=\varepsilon_{zy}$, and $\varepsilon_{zx}=\varepsilon_{xz}$ are the shear strain components. In some literature [37], also the following notation is used:

$$\gamma_{xy} = 2\varepsilon_{xy} \quad \gamma_{xz} = 2\varepsilon_{xz} \quad \gamma_{yz} = 2\varepsilon_{yz}, \quad (2.24)$$

however we will stick to the notation from (2.23) in this work. The formulation in (2.21) forms a system of six equations for the three displacement components. The strain components must satisfy the compatibility conditions. Because the displacement field u_1 , u_2 and u_3 in any system has to be unique, the strain components are not independent of each other [36]. By eliminating the displacements from (2.21), the compatibility conditions become:

$$\begin{aligned} \frac{\partial^2 \varepsilon_{xx}}{\partial x_2^2} + \frac{\partial^2 \varepsilon_{yy}}{\partial x_1^2} - 2 \frac{\partial^2 \varepsilon_{xy}}{\partial x_1 \partial x_2} &= 0 & \frac{\partial^2 \varepsilon_{xx}}{\partial x_2 \partial x_3} - \frac{\partial}{\partial x_1} \left(-\frac{\partial \varepsilon_{yz}}{\partial x_1} + \frac{\partial \varepsilon_{zx}}{\partial x_2} + \frac{\partial \varepsilon_{xy}}{\partial x_3} \right) &= 0 \\ \frac{\partial^2 \varepsilon_{xx}}{\partial x_3^2} + \frac{\partial^2 \varepsilon_{zz}}{\partial x_1^2} - 2 \frac{\partial^2 \varepsilon_{xz}}{\partial x_1 \partial x_3} &= 0 & \frac{\partial^2 \varepsilon_{yy}}{\partial x_3 \partial x_1} - \frac{\partial}{\partial x_2} \left(-\frac{\partial \varepsilon_{zx}}{\partial x_2} + \frac{\partial \varepsilon_{xy}}{\partial x_3} + \frac{\partial \varepsilon_{yz}}{\partial x_1} \right) &= 0 \\ \frac{\partial^2 \varepsilon_{yy}}{\partial x_3^2} + \frac{\partial^2 \varepsilon_{zz}}{\partial x_2^2} - 2 \frac{\partial^2 \varepsilon_{yz}}{\partial x_2 \partial x_3} &= 0 & \frac{\partial^2 \varepsilon_{zz}}{\partial x_1 \partial x_2} - \frac{\partial}{\partial x_3} \left(-\frac{\partial \varepsilon_{xy}}{\partial x_3} + \frac{\partial \varepsilon_{yz}}{\partial x_1} + \frac{\partial \varepsilon_{zx}}{\partial x_2} \right) &= 0 \end{aligned} \quad (2.25)$$

2.1.2 Stress

When a body is deformed internal forces known as stress arise inside it. The stress generates to restore the undeformed state of the body. At mechanical equilibrium the sum of all acting and internal forces must equal to zero. This section, based on [35, 38], provides the relationships between force and stress.

In order to study how the body exterior interacts with the body interior we imagine a closed surface S within a loaded body Z (**Figure 2.2**). We consider a unit vector \mathbf{n} normal to S with direction outward from the interior of S and a small surface element of area ΔS . Two sides of ΔS according to the direction of \mathbf{n} are distinguished. The part of material Z lying on the positive side of the normal exerts a force $\Delta \mathbf{F}$ on the other part that is situated on the negative side of the normal. $\Delta \mathbf{F}$ is a function of the area and the orientation of surface S . By assuming that $\Delta \mathbf{F}/\Delta S$ approaches a definite limit as ΔS approaches zero the stress vector \mathbf{t} (also referred to as the traction vector) can be defined by

$$\mathbf{t} := \lim_{\Delta S \rightarrow 0} \left(\frac{\Delta \mathbf{F}}{\Delta S} \right) = \frac{d\mathbf{F}}{dS}. \quad (2.26)$$

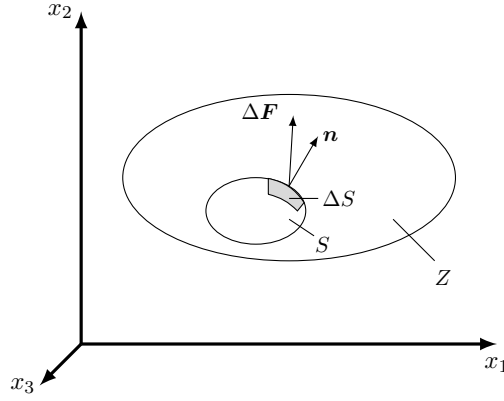


Figure 2.2: Schematic representation of a body subjected to a force $\Delta \mathbf{F}$.

The components of the stress vector are normal stress and shear stress. Normal stress is defined as $\sigma = \mathbf{t} \cdot \mathbf{n}$ and shear stress as $\tau = \sqrt{t^2 - \sigma^2}$.

By considering three specific sections corresponding to the coordinate system x_1 , x_2 , and x_3 (or x , y , and z) three stress vectors are assigned \mathbf{t}_1 , \mathbf{t}_2 , and \mathbf{t}_3 . The Cartesian components of the stress vectors are denoted by σ_{ij} , where the index i correlates to the coordinate direction. If we consider the stress vector \mathbf{t}_1 , it can be expressed by:

$$\mathbf{t}_1 = \sigma_{11}\mathbf{e}_1 + \sigma_{12}\mathbf{e}_2 + \sigma_{13}\mathbf{e}_3 = \sigma_{1j}\mathbf{e}_j, \quad (2.27)$$

where \mathbf{e}_1 , \mathbf{e}_2 , and \mathbf{e}_3 are the unit vectors in the coordinate directions. Similarly the stress vectors \mathbf{t}_2 and \mathbf{t}_3 can also be calculated, leading to the general expression

$$\mathbf{t}_i = \sigma_{ij}\mathbf{e}_j. \quad (2.28)$$

The stress component σ_{ij} contains the magnitude, the direction normal to the reference plane (first subscript) and the direction of action (second subscript). The sign of the stress components can be positive or negative.

The stress components σ_{ij} are usually described by using the engineering notation with a cube, as shown in **Figure 2.3**. The stress components act perpendicular (normal stress) and parallel (shear stress) to the faces of the cube. Normal stresses can pull the cube (tensile normal stress) or push it (compressive normal stress).

The stress tensor (also called Cauchy stress tensor) $\boldsymbol{\sigma}$ is a second order tensor which consists of normal and shear components acting on an infinitesimal element. Considering a 3D system, the stress tensor is described through nine stress components [39]

$$\boldsymbol{\sigma} = \begin{bmatrix} \sigma_{xx} & \tau_{xy} & \tau_{xz} \\ \tau_{yx} & \sigma_{yy} & \tau_{yz} \\ \tau_{zx} & \tau_{zy} & \sigma_{zz} \end{bmatrix}, \quad (2.29)$$

where σ_{xx} , σ_{yy} , and σ_{zz} are the normal stresses and τ_{xy} , τ_{yx} , τ_{yz} , τ_{zy} , τ_{zx} , and τ_{xz} are the shear stress components.

If the stress tensor is symmetric the number of stress components reduces to six because

$$\begin{aligned} \tau_{yx} &= \tau_{xy}, \\ \tau_{yz} &= \tau_{zy}, \quad \text{and} \\ \tau_{zx} &= \tau_{xz}. \end{aligned} \quad (2.30)$$

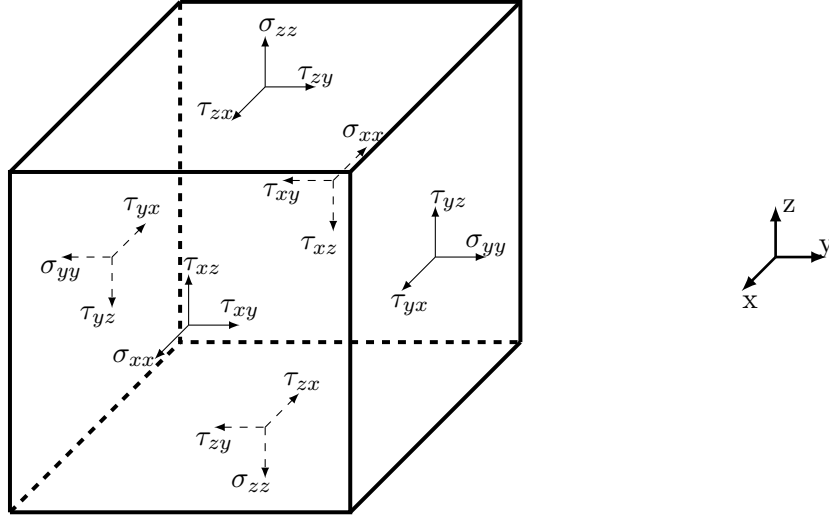


Figure 2.3: Stress components on an infinitesimal cube.

By applying Newton's first law to a solid subjected to body force components represented by F_x , F_y , and F_z , the equilibrium conditions of the stress components can be derived [35, 36, 37]. F_i could be alternatively described as $F_i = \rho b_i$, where ρ is the density of the body and b_i is the force per unit of mass. An equilibrium of an arbitrary volume V of a continuum requires that the resulting moment and force acting on the volume be zero; therefore, the sum of surface and body forces satisfy an integral relation

$$\iint_S t_i dS + \iiint_V F_i dV = 0, \quad (2.31)$$

where F_i represents the component of body force and t_i is the stress component acting on an arbitrarily oriented infinitesimal area $\mathbf{n}dS$ ($t_i = \sigma_{ij}n_j$). By converting the resulting surface integral to a volume integral using the Gauss's divergence theorem, we obtain

$$\iint_S \sigma_{ij}n_j dS = \iiint_V \sigma_{ji,j} dV, \quad (2.32)$$

and then equation (2.31) becomes

$$\iiint_V (\sigma_{ij,j} + F_i) dV = 0, \quad (2.33)$$

where $\sigma_{ij,j} \equiv \partial\sigma_{ij}/\partial x_j$ is the divergence of the stress tensor. Because the volume in (2.33) is arbitrary the integral vanishes and we obtain the equilibrium conditions:

$$\begin{aligned} \frac{\partial\sigma_{xx}}{\partial x_1} + \frac{\partial\tau_{xy}}{\partial x_2} + \frac{\partial\tau_{xz}}{\partial x_3} + F_x &= 0, \\ \frac{\partial\tau_{xy}}{\partial x_1} + \frac{\partial\sigma_{yy}}{\partial x_2} + \frac{\partial\tau_{yz}}{\partial x_3} + F_y &= 0, \quad \text{or} \quad \sigma_{ij,i} + \rho b_i = 0 \\ \frac{\partial\tau_{xz}}{\partial x_1} + \frac{\partial\tau_{zx}}{\partial x_2} + \frac{\partial\sigma_{zz}}{\partial x_3} + F_z &= 0, \end{aligned} \quad (2.34)$$

The Cauchy stress tensor $\boldsymbol{\sigma}$ is used to model small deformations (infinitesimal strain theory) and it is a fundamental concept in the theory of linear elasticity. For large deformations the concept of the Piola-Kirchhoff stress tensor is used [36].

In engineering the concept of the scalar Von Mises effective Stress is commonly used to predict yielding of materials under a loading conditions as well as other physical phenomena [36]

$$\sigma_{mises} = \sqrt{\frac{1}{2} [(\sigma_{xx} - \sigma_{yy})^2 + (\sigma_{xx} - \sigma_{zz})^2 + (\sigma_{yy} - \sigma_{zz})^2]}. \quad (2.35)$$

2.1.3 Constitutive Laws

The equations described above are applicable for all continuous materials. However additional equations, called constitutive equations, are necessary to describe the mechanical behavior of any particular material.

Four theories for material behavior can be distinguished [35]:

- **Elasticity:** Material deformation is reversible and it returns to its original shape and size once loads are removed. For most materials the stress is a linear function of the strain. The strain depends only on the applied stress and does not depend on the history of loading.
- **Plasticity:** If the material is under modest stresses it responds elastically. If the stress exceeds a critical magnitude the specimen is permanently changed in size and shape. During this phase the stress is not a linear function of the strain.
- **Viscoelasticity:** Materials combine elastic and viscous behavior. It is characterized by a time-dependent response and by the load or deformation history.
- **Viscoplasticity:** Material deformation depends on the rate of the applied load. Unlike with plasticity the material is under a creep flow which is a function of time and the applied load.

Creep behavior exists in viscoelasticity and viscoplasticity theories. Creep is the phenomenon where a solid material moves slowly or deforms permanently under stresses.

Materials are additionally described as brittle or ductile [37]. In brittle materials rupture occurs without any noticeable prior deformation, behaving elastically before rupture. For ductile material the rupture arrives after a plastic deformation.

The different material behaviors listed above can be analyzed using stress-strain curves. For each material a unique relationship between stress and strain can be found. Stress-strain curves are obtained by recording the strain at distinct intervals of applied stress. **Figure 2.4** depicts an example of a stress-strain curve with an elastic-plastic behavior for a ductile material. In the plot several characteristic points can be identified: The yield strength point defines the stress where a material starts to plastically deform. Below this value the material behaves elastically. The ultimate strength point defines the maximum stress which a material can withstand during deformation. The fracture strength point represents the stress where the specimen fails or fractures. Usually, in brittle materials the stress-strain curve is only valid until the yield strength is reached, at which point fracture occurs. The yield strength in brittle materials is referred to as the fracture strength.

The stress-strain curve describes the elastic modulus E (also known as Young's modulus). E is a typical mechanical property which defines a reversible, time-independent elastic strain induced by a load. It is calculated by dividing the tensile stress by the strain of the elastic part of the stress-strain curves. On the other hand, ductility is a mechanical property for plastic material and it defines the maximum strain which the material can withstand without breaking.

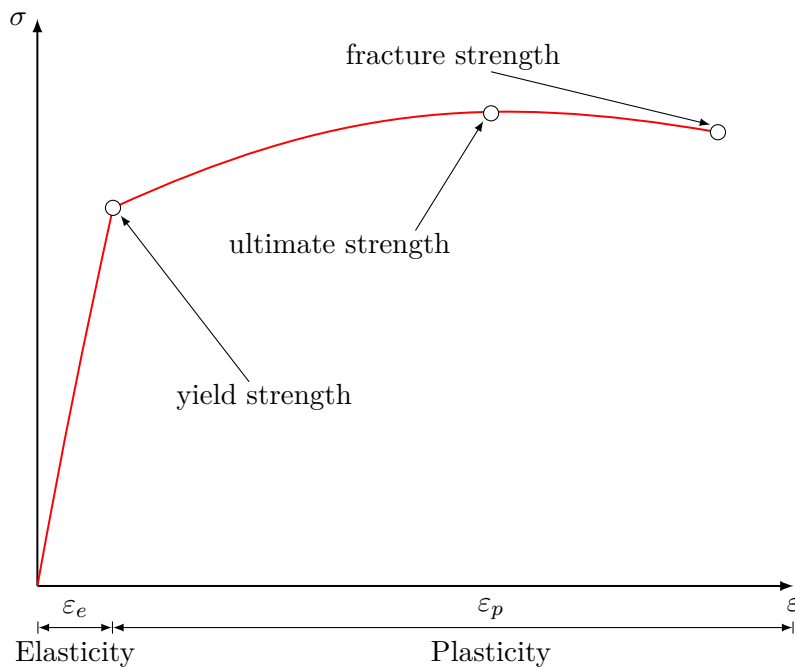


Figure 2.4: Example of stress-strain curve for a ductile material.

The behavior of materials and their properties are correlated to the arrangement of atoms in the material body. Single-crystal is a body where atoms are ordered in a pattern which repeats itself; therefore, only a single crystalline phase is present. Polycrystalline materials are composed of more than one crystal (grains) and often combine different crystalline phases (cf. **Figure 2.5**). At the atomic scale elastic and plastic deformations are significantly different (cf. **Figure 2.6**) [40]. Elastic deformation results in each atom moving under a load. On the other hand, in plastic deformation, only a few atoms move and the phenomenon is anisotropic (even though it is usually considered as an isotropic phenomenon in polycrystalline materials). Plasticity is the phenomenon which moves atoms through many interatomic distances relative to their positions. During plastic deformation the material tends to preserve the crystal structure, therefore this limits the

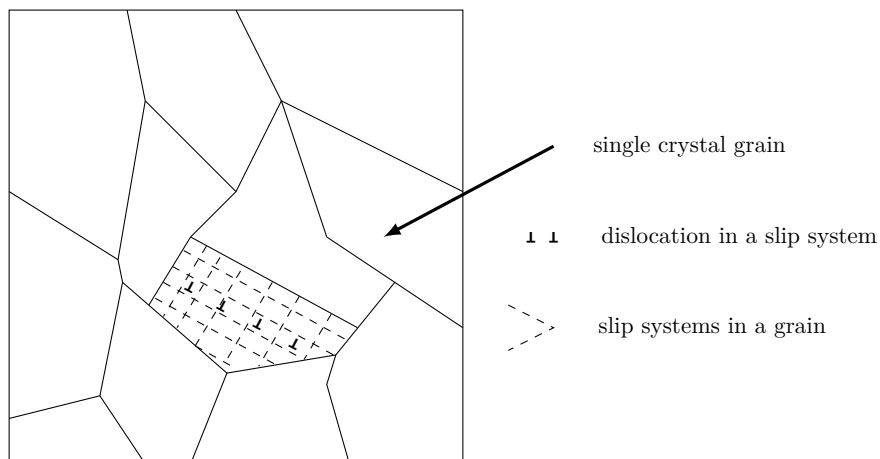


Figure 2.5: Polycrystalline material.

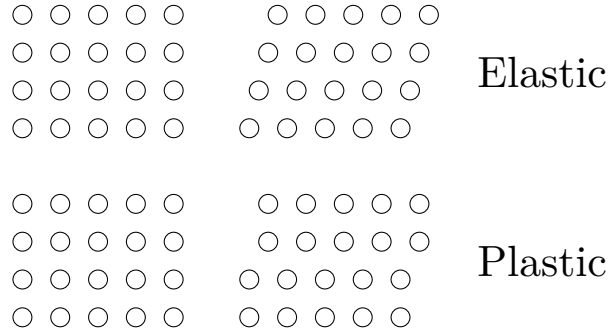


Figure 2.6: Atom movements in elastic and slip deformation.

way in which the plastic deformation can appear. A typical deformation is represented by a slip system containing a particular slip plane in a given slip direction. Slip planes are crystallographic planes with the highest density of atoms. The slip direction and the magnitude of a dislocation in the slip plane are defined by the Burgers vector [41, 42]. Each material has a characteristic slip system, in which dislocations are carriers of plastic deformation [40]. Dislocations are one-dimensional lattice defects where atoms are out of position in the crystal. They move and are generated under the action of high shear stresses because the atoms in the vicinity of the dislocation line rearrange their bonds. During this process the work done is dissipated through lattice vibration, and the dislocation movement results in a relative slip.

It is therefore clear that the plastic mechanism is influenced by the microstructural features such as slip plane, lattice imperfections, alloying, and impurity elements. The plasticity is also influenced by the movement, multiplication, and interaction between dislocations [43]. Therefore, the microstructures of materials define properties such as elasticity, plasticity, and creep.

An elastic-plastic material is usually studied assuming that the strains $\boldsymbol{\varepsilon}$ and strain increments $d\boldsymbol{\varepsilon}$ consist of an elastic and a plastic component [37]:

$$\boldsymbol{\varepsilon} = \boldsymbol{\varepsilon}_e + \boldsymbol{\varepsilon}_p, \quad d\boldsymbol{\varepsilon} = d\boldsymbol{\varepsilon}_e + d\boldsymbol{\varepsilon}_p. \quad (2.36)$$

We take a closer look on the elastic component of a linear stress-strain relationship in the next subsection. For the plastic component a different constitutive law, based on plastic strain increments or total plastic strains, are in use [35, 37].

2.1.3.1 Elasticity

For a linear elastic material, assuming small (infinitesimal) strain ($\partial u_i / \partial x_j \ll 1$), stresses and strains are related [36, 37, 44] through the following constitutive equation:

$$\boldsymbol{\sigma} = \mathbf{C} : \boldsymbol{\varepsilon} \quad \text{or} \quad \sigma_{ij} = C_{ijkl} \varepsilon_{kl}, \quad (2.37)$$

where \mathbf{C} indicates the elasticity tensor. The equation above is known as Hooke's law and the two dots indicates a summation over two index pairs. \mathbf{C} is a fourth-order tensor with 81 components C_{ijkl} . Since the stress and strain tensors are symmetric it follows that

$$C_{ijkl} = C_{jikl} = C_{ijlk} = C_{jilk}, \quad (2.38)$$

which reduces the number of independent components from 81 to 36. Equation (2.37) can be inverted and the elasticity law becomes

$$\boldsymbol{\varepsilon} = \mathbf{M} : \boldsymbol{\sigma} \quad \text{or} \quad \varepsilon_{ij} = M_{ijkl} \sigma_{kl}, \quad (2.39)$$

where \mathbf{M} is the compliance tensor. The components M_{ijkl} have the same symmetry properties as C_{ijkl} .

For an isotropic material, \mathbf{C} is an isotropic tensor which is described by only two independent constant:

$$C_{ijkl} = \lambda\delta_{ij}\delta_{kl} + \mu(\delta_{ik}\delta_{jl} + \delta_{il}\delta_{jk}), \quad (2.40)$$

where λ and μ are the Lamé constants defined as

$$\lambda = \frac{E\nu}{(1+\nu)(1-2\nu)}, \quad \mu = \frac{E}{2(1+\nu)}, \quad (2.41)$$

where E is the Young's modulus, ν is the Poisson's ratio, and μ is the shear modulus. Substituting (2.40) in (2.37), an isotropic material is described as

$$\sigma_{ij} = \lambda\varepsilon_{kk}\delta_{ij} + 2\mu\varepsilon_{ij}. \quad (2.42)$$

2.2 Plane Strain and Plane Stress

Many 3D solid mechanics problems can be treated as 2D problems. Plane strain and plane stress are two idealized stress configurations, which simplify problem analysis [37]. The two approximations are described by using the following engineering notation with coordinates x, y, z , displacements u_x, u_y, u_z , strains $\varepsilon_{xx}, \tau_{xy}, \dots$ and stresses $\sigma_{xx}, \tau_{xy}, \dots$

2.2.1 Plane Strain

The plane strain is defined to be a state which assumes that $u_z, \varepsilon_{zz}, \gamma_{xz}, \gamma_{yz}, \tau_{xz}$, and τ_{yz} are equal to zero. Plane strain can be idealized as long wire where stress components act perpendicular to its length. Therefore, the equilibrium conditions reduce to

$$\frac{\partial\sigma_{xx}}{\partial x} + \frac{\partial\tau_{xy}}{\partial y} = 0, \quad \frac{\partial\tau_{xy}}{\partial x} + \frac{\partial\sigma_{yy}}{\partial y} = 0, \quad (2.43)$$

the kinematic relations to

$$\varepsilon_{xx} = \frac{\partial u_x}{\partial x}, \quad \varepsilon_{yy} = \frac{\partial u_y}{\partial y}, \quad \varepsilon_{xy} = \frac{1}{2} \left(\frac{\partial u_x}{\partial y} + \frac{\partial u_y}{\partial x} \right), \quad (2.44)$$

and compatibility conditions become

$$\frac{\partial^2\varepsilon_{xx}}{\partial y^2} + \frac{\partial^2\varepsilon_{yy}}{\partial x^2} = \frac{\partial^2\varepsilon_{xy}}{\partial x\partial y}. \quad (2.45)$$

This assumption permits to reduce the stress-strain relation to

$$\begin{aligned} \varepsilon_{xx} &= \frac{1-\nu^2}{E} \left(\sigma_{xx} - \frac{\nu}{1-\nu}\sigma_{yy} \right), & \varepsilon_{yy} &= \frac{1-\nu^2}{E} \left(\sigma_{yy} - \frac{\nu}{1-\nu}\sigma_{xx} \right), \\ \varepsilon_{xy} &= \frac{\tau_{xy}}{2\mu}, & \sigma_{zz} &= \nu(\sigma_{xx} + \sigma_{yy}), \end{aligned} \quad (2.46)$$

where μ is the shear modulus.

2.2.2 Plane Stress

On the other hand, in the plane stress approximation, σ_{zz} , τ_{xz} , τ_{yz} , γ_{xz} , and γ_{yz} are zero and the other stress and strain components are independent of z . Here, the problem can be simplified to a 2D thin plate problem where the stress components act along the plane. By applying the plane stress assumption to the equilibrium conditions, kinematic relations, and compatibility conditions as shown in (2.43)-(2.45) the stress-strain relation reduces to

$$\begin{aligned}\varepsilon_{xx} &= \frac{1}{E}(\sigma_{xx} - \nu\sigma_{yy}), & \varepsilon_{yy} &= \frac{1}{E}(\sigma_{yy} - \nu\sigma_{xx}), \\ \varepsilon_{xy} &= \frac{\tau_{xy}}{2\mu}, & \varepsilon_{zz}E &= -\nu(\sigma_{xx} + \sigma_{yy}).\end{aligned}\tag{2.47}$$

2.3 Source of Residual Stress in Thin Films

In microelectronic devices, thin films can have residual stresses, which arise due to two main sources: intrinsic and thermal stress [45]. High values of residual stress can affect the quality and performance of thin films and subsequently of the entire devices. Therefore, the investigation of the origin of the residual stress is a fundamental aspect to examine.

2.3.1 Intrinsic Stress

Intrinsic stress emerges during the deposition processes (e.g. sputtering, spraying, painting, spin coating, CVD, PVD, and electrodeposition). The magnitude of the intrinsic stress depends on the process, deposition temperature, and deposited material. During the deposition process, the microstructure evolves from single atom islands to a uniform film, influencing the magnitude of intrinsic stress [45]. In **Chapter 5** a detailed description of intrinsic stresses in thin films is reported.

2.3.2 Thermal Strain and Thermal Stress

In absence of mechanical loads a body can deform due to temperature changes. This deformation is called thermal deformation, which gives rise to so called thermal strain inside the body [39]. For small temperature changes the thermal strain is linearly proportional to the temperature change and it is described by the Coefficient of Thermal Expansion (CTE). CTE is a material property which describes how a material expands upon heating or contracts upon cooling. For changes in volume the volumetric CTE can be expressed as

$$\alpha_v = \frac{1}{V_0} \left(\frac{\partial V}{\partial T} \right)_p,\tag{2.48}$$

where V_0 is the initial volume, and p indicates a pressure constant. For changes in length, α_v is denoted as α_l , but instead of a change in volume V is substituted by length l

$$\alpha_l = \frac{1}{l_0} \left(\frac{\partial l}{\partial T} \right)_p,\tag{2.49}$$

where l_0 indicates the initial length. For an isotropic material, where $\alpha_v = 3\alpha_l$ the thermal strain can be expressed as

$$\begin{aligned}\varepsilon_{xx}^{th} &= \varepsilon_{yy}^{th} = \varepsilon_{zz}^{th} = \alpha_l(T_f - T_0), \\ \varepsilon_{xy}^{th} &= \varepsilon_{yz}^{th} = \varepsilon_{xz}^{th} = 0,\end{aligned}\tag{2.50}$$

where the change from T_0 to T_f corresponds to the temperature variation. The shear components are all zero because the thermal expansion is volumetric.

Thermal stress is the stress generated in a constrained structure due to a thermal expansion or contraction. Two different set of constraints are possible: external constraint and internal constraint. External constraint can be every external object which obstruct the free expansion or contraction of the system, when temperature changes occur. Internal constraint usually appear in composite systems, formed by different materials, or when a nonuniform temperature distribution is present. Due to the different CTEs every material behaves differently under thermal variation. The thermal strain generated in a material can affect and then generate thermal stress, thereby impacting the system.

The relationships between stress and strain for an isotropic material, including the thermal strain are given as

$$\begin{aligned}\varepsilon_{xx} &= \frac{1}{E}(\sigma_{xx} - \nu\sigma_{yy} - \nu\sigma_{zz}) + \alpha_l(T_f - T_0), & \varepsilon_{xy} &= \frac{\tau_{xy}}{2\mu}, \\ \varepsilon_{yy} &= \frac{1}{E}(-\nu\sigma_{xx} + \sigma_{yy} - \nu\sigma_{zz}) + \alpha_l(T_f - T_0), & \varepsilon_{yz} &= \frac{\tau_{yz}}{2\mu}, \\ \varepsilon_{zz} &= \frac{1}{E}(-\nu\sigma_{xx} - \nu\sigma_{yy} + \sigma_{zz}) + \alpha_l(T_f - T_0), & \varepsilon_{zx} &= \frac{\tau_{zx}}{2\mu}.\end{aligned}\tag{2.51}$$

2.4 Virtual Work

The principle of virtual work is applied to study the mechanics of deformable bodies. The term virtual refers to the implementation of infinitesimal displacements, called virtual displacement, which do not represent a real displacement acting on the system. By considering the equilibrium equations of a system, where all the forces acting on a system in static equilibrium must be equal zero, virtual displacement can be applied and the resulting deformation of the body can be obtained [36, 37].

We consider a body of volume V in equilibrium, where a prescribed traction \mathbf{t} on boundary Γ_t and a prescribed displacement \mathbf{u} on boundary Γ_u are

$$\begin{aligned}\sigma_{ij}n_j &= t_i & \text{on} & \Gamma_t, \\ u_i &= 0 & \text{on} & \Gamma_u.\end{aligned}\tag{2.52}$$

To derive the concept of the virtual work it is necessary to recall the equilibrium condition and the classic strain tensor:

$$\begin{aligned}\frac{\partial\sigma_{ij}}{\partial x_j} + \rho b_i &= 0 & \text{on} & V, \\ \varepsilon_{ij} &= \frac{1}{2} \left(\frac{\partial u_i}{\partial x_j} + \frac{\partial u_j}{\partial x_i} \right) & \text{on} & V.\end{aligned}\tag{2.53}$$

$\delta\mathbf{u}$ is defined as virtual displacement and it has to satisfy the boundary condition on Γ_u . By employing $\delta\mathbf{u}$ a virtual strain is defined

$$\delta\varepsilon_{ij} = \frac{1}{2} \left(\frac{\partial\delta u_i}{\partial x_j} + \frac{\partial\delta u_j}{\partial x_i} \right).\tag{2.54}$$

The equilibrium condition is multiplied by the virtual displacement

$$\left(\frac{\partial\sigma_{ij}}{\partial x_j} + \rho b_i \right) \delta u_i = 0.\tag{2.55}$$

By using the product rule

$$\frac{\partial \sigma_{ij}}{\partial x_j} \delta u_i = \frac{\partial \sigma_{ij} \delta u_i}{\partial x_j} - \sigma_{ij} \frac{\partial \delta u_i}{\partial x_j}, \quad (2.56)$$

and the symmetry of (2.54) equation (2.55) can be rewritten as

$$\frac{\partial \sigma_{ij} \delta u_i}{\partial x_j} + \rho b_i \delta u_i = \sigma_{ij} \delta \varepsilon_{ij} \quad (2.57)$$

which, when is integrated over the volume of V becomes

$$\int_V \frac{\partial \sigma_{ij} \delta u_i}{\partial x_j} dV + \int_V \rho b_i \delta u_i dV = \int_V \sigma_{ij} \delta \varepsilon_{ij} dV, \quad (2.58)$$

Gauss's divergence theorem is applied at the first volume integral, becoming a surface integral

$$\int_{\Gamma_t} \sigma_{ij} \delta u_i n_j d\Gamma_t + \int_V \rho b_i \delta u_i dV = \int_V \sigma_{ij} \delta \varepsilon_{ij} dV. \quad (2.59)$$

By using the boundary condition the equation above can be rewritten in a simplified form

$$\int_{\Gamma_t} t_i \delta u_i d\Gamma_t + \int_V \rho b_i \delta u_i dV = \int_V \sigma_{ij} \delta \varepsilon_{ij} dV, \quad (2.60)$$

where the integrals on the left represent the virtual work done by external forces. On the right hand side the integral represents the virtual work done by internal forces. The system is in equilibrium if the entire virtual work of the imposed virtual displacements vanishes, therefore (2.60) is equivalent to (2.34).

2.5 Fracture Mechanics

Fracture is a degradation process which leads to the generation of new surfaces. Fracture develops through cracking, which is the development of displacement discontinuity surfaces within the solid. Previously a continuum-mechanical analysis was presented, however a microscopic approach is necessary to understand the role of the microstructure in fracture mechanics [37]. At the microscopic level, the fracture process consists of breaking the bonds between elements (atoms, ions, molecules, etc.). The bonding force between two elements is described by

$$F = -\frac{a}{r^m} + \frac{b}{r^n}, \quad (2.61)$$

where a , b , m , and n are constants which characterize the bond type and r is the distance between elements. The first term is the attractive force, while the second term describes a repulsive force. During the separation of elements (fracture) a negative material-specific work W^B is performed by the bonding force. This work is the surface energy necessary to form new surfaces in the immediate neighborhood, leading to an instant change of the lattice geometry. From the macroscopic point of view, considering the material as a continuum and neglecting dissipative processes (heat), the work of bonding forces is converted into the surface energy of the body

$$\Gamma^0 = \gamma^0 A, \quad (2.62)$$

where A is the newly created surface and γ^0 is the surface energy density.

In a polycrystalline material the separation of atomic planes (microcracks) is often combined with pronounced microplastic processes (dislocations). The dislocation pile-up at obstacles is an important phenomenon during microcrack formation.

It can cause a high stress concentrations leading to bond breaking along favored lattices places:

- Transcrystalline cleavage occurs when a crack runs through several grains, and the separation surface changes according to local lattice planes.
- Intercrystalline fracture separation between weak grain boundaries occurs on account of dislocation pile-up or grain boundary sliding takes place along these boundaries.

These processes describe fracture in brittle materials. In plastic deformation the load is not enough to break the atomic bonds but it is large enough to produce permanent deformation by shearing atomic planes (dislocations); therefore, the failure is the plastic regime.

Cracks are classified from different phenomenological viewpoints. A stationary crack is a crack which does not change in length. If the crack starts to propagate and it becomes non-stationary a specified load or deformation is called crack initiation. Crack propagation can further be distinguished as stable, when the increase in crack length requires an increases external load, or unstable, when the crack advances without any increase in the external load. In **Chapter 4** the basis of fracture mechanics are described in further details.

2.6 FEM

In **Section 1.5** the basic ideas behind the finite element method are described. In this section some mathematical concepts of FEM are presented [46, 47, 48]. The solution to a problem is obtained by applying a variational method. The weighted residual method and its different approaches are initially described. Subsequently the so called weak formulation is reported. These methods permit to calculate an approximate solution in the form of a linear system by minimizing an associated error function. A description of the spatial discretization is also presented in this section. At the end of the chapter FEM is applied to solve a mechanical problem.

A physical problem can often be described by the following general differential equation

$$\frac{d}{dx} \left[a(x) \frac{du(x)}{dx} \right] + b(x) \frac{du(x)}{dx} + c(x)u(x) - f(x) = 0, \quad (2.63)$$

where $u(x)$ is the unknown function. The coefficient functions $a(x)$, $b(x)$, and $c(x)$ and the source term $f(x)$ describes a physical problem. For example, if we consider an elastic bar, we must solve for $u(x)$ where the parameter a corresponds to the bar stiffness $E \cdot A$ (E is the Young's modulus and A the cross sectional area) and f is the applied body load.

For a well-defined problem set, boundary conditions are required. There are three types of boundary conditions: The first is called Dirichlet boundary condition where a domain Ω has a boundary along which the displacement is a constant, defined by

$$u(x_D) = u_D \quad x_D \in \Gamma, \quad (2.64)$$

where Γ represents the boundary. The second kind is called the Neumann boundary condition where the slope of the boundary value is known

$$a(x_N) \frac{du(x)}{dx} \Big|_{x=x_N} = q_N \quad x_N \in \Gamma, \quad (2.65)$$

where q_N represents a scalar function. The third kind is called the Robin boundary condition

$$\xi_R u(x_R) + \varrho_R \frac{du(x)}{dx} \Big|_{x=x_R} = \gamma_R, \quad x_R \in \Gamma \quad (2.66)$$

where ξ_R , ϱ_R , and γ_R are parameters given by the physical problem. This condition represents a weighted sum of the value and the slope of the function at the boundary.

2.6.1 Weighted Residual Method

In this section we describe the general method of the weighted residual and the derivation of the solution using different approaches.

One-dimensional physical problems in a domain Ω can often be described by the differential equation (2.63); however, to describe mathematical concepts of FEM it is more useful represent a differential equation with the linear operator $L\{\dots\}$

$$L\{u^0(x)\} = \frac{d}{dx} \left[a(x) \frac{du^0(x)}{dx} \right] + b(x) \frac{du^0(x)}{dx} + c(x)u^0(x) = f(x). \quad (2.67)$$

In (2.67) $u^0(x)$ represents the exact or real solution of the problem subject to boundary conditions along the boundary Γ and to the prescribed geometry. The solution $u^0(x)$ solves the differential equation along every point of the domain $x \in \Omega$. To simplify the mathematical equation, in the following derivations we indicate

$$L\{u^0(x)\} = f(x). \quad (2.68)$$

When an exact analytical solution cannot be found, an approximated solution of the problem is obtained by employing numerical methods. The goal is to calculate a useful approximation of the exact solution

$$u_h(x) \approx u^0(x). \quad (2.69)$$

In the case of the weighted residual method [47, 49] an approximation of the solution of the following form is chosen

$$u_h(x) = \alpha_0 + \sum_{a=1}^n \alpha_a \varphi_a(x), \quad (2.70)$$

where α_0 has to satisfy the non-homogeneous boundary conditions, $\varphi_a(x)$ are a set of linear independent basis functions, and α_a are the free parameters of the approximation approach. If the solution has to satisfy homogeneous boundary conditions the variable α_0 can be omitted.

A local error know as residual r is obtained by inserting the approximation function for $u^0(x)$ into the differential equation (2.67)

$$r = L\{u_h(x)\} - f(x). \quad (2.71)$$

Performing an integration over the entire domain Ω the residual r , weighted with a weighting function $W(x)$, gives

$$\int_{\Omega} rW(x)d\Omega = \int_{\Omega} (L\{u_h(x)\} - f(x))W(x)d\Omega = \langle r, W(x) \rangle \stackrel{!}{=} 0, \quad (2.72)$$

which represents an inner product. By choosing the appropriate α_a parameters of the approximated solution, the average r can be forced r to zero over the entire domain.

$W(x)$ is referred to as the test function and it allows for an arbitrary weighting of the error in the domain Ω . Usually, the structure of the test function is defined as the approximation function $u_h(x)$ by a sum of a weighted basis function set:

$$W(x) = \sum_{b=1}^n \beta_b \psi_b(x), \quad (2.73)$$

where β_b are arbitrary coefficients and $\psi_b(x)$ are linear independent shape functions. The choice of the shape functions $\psi_b(x)$ depends on the applied method:

- The Point-Collocation Method is based on the Dirac delta function. The error r vanishes at the n selected points $x_1, x_2, \dots, x_n \in \Omega$. At those so called collocation points the approximated solutions satisfies the differential equation. Thereby, the test function is set as:

$$W(x) = \beta_1 \underbrace{\delta(x - x_1)}_{\psi_1} + \dots + \beta_n \underbrace{\delta(x - x_n)}_{\psi_n} = \sum_{b=1}^n \beta_b \delta(x - x_b), \quad (2.74)$$

where the Dirac delta function is:

$$\delta(x - x_b) = \begin{cases} 0 & \text{for } x \neq x_b \\ \infty & \text{for } x = x_b. \end{cases} \quad (2.75)$$

By applying the test function (2.74) in the inner product (2.72) and considering the property of the Dirac delta function,

$$\int_{\Omega} \delta(x - x_b) dx = 1, \quad (2.76)$$

$$\int_{\Omega} f(x) \delta(x - x_b) dx = f(x_b), \quad (2.77)$$

and choosing $\beta_b = \delta_{ib}$ for $i \in \{1, \dots, n\}$, this results in a system of n linear independent equations. The property of the delta function leads to $\int_{\Omega} r W(x) d\Omega = r = 0$, therefore no integral needs to be calculated within the point-collocation procedure. The parameters α_a can be calculated by solving the system:

$$\begin{aligned} r(x_1) &= L\{u_h(x_1)\} - f(x_1) = 0, \\ &\vdots \\ r(x_n) &= L\{u_h(x_n)\} - f(x_n) = 0. \end{aligned} \quad (2.78)$$

Because $L\{\dots\}$ is linear in this argument these equations can be further derived

$$r(x_i) = L\{u_h(x_i)\} - f(x_i) = L\left\{\sum_{a=1}^n \alpha_a \varphi_a(x_i)\right\} - f(x_i) = \sum_{a=1}^n \alpha_a L\{\varphi_a(x_i)\} - f(x_i) = 0, \quad (2.79)$$

which can be written in matrix form

$$(L\{\varphi_a(x_i)\})_{i,a} (\alpha_a)_a - (f(x_i))_i = 0 \quad \text{or} \quad \mathbf{L}\boldsymbol{\alpha} = \mathbf{f} \quad i, a \in \{1, \dots, n\}. \quad (2.80)$$

The results can be obtained by inverting the matrix:

$$\boldsymbol{\alpha} = \mathbf{L}^{-1} \mathbf{f}. \quad (2.81)$$

By obtaining the parameters α_a and by plugging them in (2.70) the approximated solution is derived.

- The Subdomain-Collocation Procedure is considered to be a variation of the point collocation method. The domain Ω is divided in non overlapping subdomains Ω_b . The shape functions of the test functions are chosen in such a way that $\psi_b(x) = 1$ in Ω_b and zero otherwise:

$$\psi_b(x) = \mathbf{1}_{\Omega_b}(x), \quad (2.82)$$

where the indicator function is defined by

$$\mathbf{1}_{\Omega_b}(x) := \begin{cases} 1 & \text{if } x \in \Omega_b, \\ 0 & \text{if } x \notin \Omega_b. \end{cases} \quad (2.83)$$

Therefore the test function is defined as

$$W(x) = \sum_{b=1}^n \beta_b \mathbf{1}_{\Omega_b}(x). \quad (2.84)$$

The integral of the error becomes zero over the different domains:

$$\int_{\Omega} r(x)W(x)d\Omega = \sum_{b=1}^n \beta_b \int_{\Omega_b} r(x)d\Omega_b \stackrel{!}{=} 0. \quad (2.85)$$

β_b are chosen as in the point-collocation procedure ($\beta_b = \delta_{ib}$ for $i \in \{1, \dots, n\}$) resulting in the following n -equation system:

$$\begin{aligned} r(x_1) &= \int_{\Omega_1} L\{u_h(x)\} - f(x)d\Omega_1 = 0, \\ &\vdots \\ r(x_n) &= \int_{\Omega_n} L\{u_h(x)\} - f(x)d\Omega_n = 0. \end{aligned} \quad (2.86)$$

The parameters α_a can subsequently be calculated as described in the point-collocation method.

- The Least Squares Method has a test function defined as

$$W(x) = \sum_{b=1}^n \beta_b \psi_b = \sum_{b=1}^n \beta_b \frac{\partial r}{\partial \alpha_b}, \quad (2.87)$$

where β_b is chosen as $\beta_b = \delta_{ib}$ for $i \in \{1, \dots, n\}$.

In the method of least squares the weighted integral is written as

$$\int_{\Omega} \frac{\partial(L\{u_h(x)\} - f(x))}{\partial \alpha_b} (L\{u_h(x)\} - f(x))d\Omega = 0, \quad (2.88)$$

where, employing the chain rule, the following form can be derived:

$$\frac{\partial}{\partial \alpha_b} \int_{\Omega} (L\{u_h(x)\} - f(x))^2 d\Omega = 0. \quad (2.89)$$

This finally leads to the minimization of the square residual:

$$\min_{\alpha_b} \int_{\Omega} (L\{u_h(x)\} - f(x))^2 d\Omega. \quad (2.90)$$

In detail, the employed test function is

$$W(x) = \sum_{b=1}^n \frac{\partial r}{\partial \alpha_b} = \sum_{b=1}^n \frac{\partial(\alpha_b L\{\varphi_b\} - f(x))}{\partial \alpha_b} = L\{\varphi_b\}, \quad (2.91)$$

thus this equation can be inserted in (2.88)

$$\int_{\Omega} L\{\varphi_b\} \left(\sum_{a=1}^n \alpha_a L\{\varphi_a\} - f(x) \right) d\Omega = 0. \quad (2.92)$$

The equation can then be rewritten as

$$\sum_{a=1}^n \int_{\Omega} L\{\varphi_b\} L\{\varphi_a\} d\Omega \alpha_a = \int_{\Omega} L\{\varphi_b\} f(x) d\Omega, \quad (2.93)$$

and

$$\begin{aligned} \sum_{a=1}^n \int_{\Omega} L\{\varphi_1\} L\{\varphi_a\} d\Omega \alpha_a &= \int_{\Omega} L\{\varphi_1\} f(x) d\Omega \\ &\vdots \quad \text{or} \quad \mathbf{L}\boldsymbol{\alpha} = \mathbf{f}. \\ \sum_{a=1}^n \int_{\Omega} L\{\varphi_n\} L\{\varphi_a\} d\Omega \alpha_a &= \int_{\Omega} L\{\varphi_n\} f(x) d\Omega \end{aligned} \quad (2.94)$$

From this linear system it is possible to obtain the α_a parameters necessary to describe the approximated function.

- The Petrov-Galerkin Procedure is a method where the set of test functions $\psi_b(x)$ and the set of basis functions $\varphi_a(x)$ are different. The test function is defined as

$$W(x) = \sum_{b=1}^n \beta_b \psi_b(x). \quad (2.95)$$

Equation (2.95) can be plugged into (2.72)

$$\sum_{b=1}^n \sum_{a=1}^n \beta_b \alpha_a \int_{\Omega} \psi_b(x) (L\{\varphi_a\} - f(x)) d\Omega = 0 \quad (2.96)$$

The parameters β_b are chosen as $\beta_b = \delta_{ib}$ for $i \in \{1, \dots, n\}$ and (2.96) is re-written as

$$\sum_{a=1}^n \alpha_a \int_{\Omega} \psi_b(x) L\{\varphi_a\} d\Omega = \int_{\Omega} \psi_b(x) f(x) d\Omega, \quad (2.97)$$

which can be written as system of linear equations:

$$\begin{aligned} \sum_{a=1}^n \int_{\Omega} \psi_1(x) L\{\varphi_a\} d\Omega \alpha_a &= \int_{\Omega} \psi_1(x) f(x) d\Omega \\ &\vdots \\ \sum_{a=1}^n \int_{\Omega} \psi_n(x) L\{\varphi_a\} d\Omega \alpha_a &= \int_{\Omega} \psi_n(x) f(x) d\Omega, \end{aligned} \quad (2.98)$$

from which is possible to obtain the α_a of the approximated function.

- The Galerkin Procedure is a method based on choosing the same set of shape functions for the approximation $\psi_b(x)$ and the weighting $\varphi_a(x)$ function. Therefore the weighting function for this method is defined by

$$W(x) = \sum_{b=1}^n \beta_b \varphi_b(x), \quad (2.99)$$

where β_b are the coefficients which can be chosen arbitrary.

The definition (2.99) can be plugged into (2.72), obtaining

$$\int_{\Omega} \sum_{b=1}^n \beta_b \varphi_b(x) r d\Omega = \sum_{b=1}^n \beta_b \int_{\Omega} \varphi_b(x) r d\Omega = 0. \quad (2.100)$$

By inserting the approximation function (2.70) in the above equation we obtain

$$\sum_{b=1}^n \beta_b \int_{\Omega} \varphi_b(x) (L\{\sum_{a=1}^n \alpha_a \varphi_a(x)\} - f(x)) d\Omega = 0. \quad (2.101)$$

This integral can be separated

$$\sum_{b=1}^n \beta_b \int_{\Omega} \varphi_b(x) L\{\sum_{a=1}^n \alpha_a \varphi_a(x)\} d\Omega - \sum_{b=1}^n \beta_b \int_{\Omega} \varphi_b(x) f(x) d\Omega = 0 \quad (2.102)$$

and due to the linearity of the differential operator the summation can be extracted

$$\sum_{b=1}^n \beta_b \sum_{a=1}^n \alpha_a \int_{\Omega} \varphi_b L\{\varphi_a(x)\} d\Omega - \sum_{b=1}^n \beta_b \int_{\Omega} \varphi_b f(x) d\Omega = 0. \quad (2.103)$$

The weighting functions can be arbitrary chosen and therefore we consider only one $\beta_b = 1$ and the other zero, resulting in

$$\sum_{a=1}^n \alpha_a \int_{\Omega} \varphi_b L\{\varphi_a(x)\} d\Omega = \int_{\Omega} \varphi_b f(x) d\Omega. \quad (2.104)$$

Using this method for all b results in n equations, which leads to a system of linear equations

$$\begin{aligned} \sum_{a=1}^n \int_{\Omega} \varphi_1 L\{\varphi_a(x)\} d\Omega \alpha_a &= \int_{\Omega} \varphi_1 f(x) d\Omega \\ &\vdots \\ \sum_{a=1}^n \int_{\Omega} \varphi_n L\{\varphi_a(x)\} d\Omega \alpha_a &= \int_{\Omega} \varphi_n f(x) d\Omega, \end{aligned} \quad (2.105)$$

which can be expressed in matrix form by

$$\mathbf{L}\boldsymbol{\alpha} = \mathbf{f}, \quad (2.106)$$

with the following definitions:

$$\begin{aligned} \boldsymbol{\alpha} &= (\alpha_a)_{a=1,\dots,n}, \\ \mathbf{L} &= \left(\int_{\Omega} \varphi_b L\{\varphi_a(x)\} d\Omega \right)_{b=1,\dots,n; a=1,\dots,n}, \\ \mathbf{f} &= \left(\int_{\Omega} \varphi_b(x) f(x) d\Omega \right)_{b=1,\dots,n}, \end{aligned} \quad (2.107)$$

where $\boldsymbol{\alpha}$ is the vector of the unknown α_a coefficients, \mathbf{f} is the load vector, and \mathbf{L} is called stiffness matrix. Many FEM implementations are based on this procedure together with the weak formulation described in the next subsection.

2.6.2 Weak Formulation

A solution to (2.63), which is called the strong formulation, is very difficult or impossible for typical engineering problems. It requires continuity on the dependent field variables and that the approximation function be differentiable up to the order of the differential equations. For such problems, the weak formulation can be used, which mathematically corresponds to the strong formulation. Usually the weak formulation has an integral form and it requires a weaker continuity on the field variables. It also allows for a reduction in the necessity for the differentiability of the approximation function by one order and permits a native incorporation of the Neumann boundary condition [50]. Here the transition from the strong formulation to the weak formulation is described [48].

In a 3D system a differential equation in domain Ω can be defined by:

$$\nabla \cdot a(\mathbf{x})\nabla u(\mathbf{x}) + \mathbf{b}(\mathbf{x}) \cdot \nabla u(\mathbf{x}) + c(\mathbf{x})u(\mathbf{x}) = f(\mathbf{x}), \quad (2.108)$$

where $f(\mathbf{x})$ is the source term. This equation corresponds to the strong formulation. Furthermore the problem must fulfill boundary conditions, which could be given in the following way.

$$\begin{aligned} u(x_D) &= u_D & \text{on} & \Gamma_D \\ \frac{\partial u(\mathbf{x})}{\partial \mathbf{n}} &= q_N & \text{on} & \Gamma_N, \end{aligned} \quad (2.109)$$

where \mathbf{n} is the normal. The union $\Gamma = \Gamma_D \cup \Gamma_N$ is at the boundary Γ of the domain Ω . On Γ_D the Dirichlet boundary condition and on Γ_N the Neumann boundary condition are implemented. The function $u(\mathbf{x})$ has to be solved on the entire simulation domain Ω .

The weak formulation is obtained by multiplying (2.108) by (2.73) and integrating over the entire domain Ω (cf. inner product)

$$\int_{\Omega} W(\mathbf{x}) (\nabla \cdot a(\mathbf{x})\nabla u(\mathbf{x}) + \mathbf{b}(\mathbf{x}) \cdot \nabla u(\mathbf{x}) + c(\mathbf{x})u(\mathbf{x}) - f(\mathbf{x})) d\Omega = 0. \quad (2.110)$$

Subsequently, the *Green's* first integration theorem is applied

$$\begin{aligned} & - \int_{\Omega} a(\mathbf{x})\nabla W(\mathbf{x}) \cdot \nabla u(\mathbf{x})d\Omega + \int_{\Gamma_N} a(\mathbf{x})W(\mathbf{x}) \underbrace{\frac{\partial u(\mathbf{x})}{\partial \mathbf{n}}}_{q_N} d\Gamma_N + \\ & + \int_{\Omega} W(\mathbf{x}) (\mathbf{b}(\mathbf{x}) \cdot \nabla u(\mathbf{x}) + c(\mathbf{x})u(\mathbf{x})) d\Omega = \int_{\Omega} f(\mathbf{x})W(\mathbf{x})d\Omega. \end{aligned} \quad (2.111)$$

Therefore, the weak formulation for the initial boundary problem becomes:

$$\begin{aligned} & - \int_{\Omega} a(\mathbf{x})\nabla W(\mathbf{x}) \cdot \nabla u(\mathbf{x})d\Omega + \int_{\Gamma_N} a(\mathbf{x})W(\mathbf{x})q_N d\Gamma_N + \\ & + \int_{\Omega} W(\mathbf{x}) (\mathbf{b}(\mathbf{x}) \cdot \nabla u(\mathbf{x}) + c(\mathbf{x})u(\mathbf{x})) d\Omega = \int_{\Omega} f(\mathbf{x})W(\mathbf{x})d\Omega. \end{aligned} \quad (2.112)$$

by setting $u(\mathbf{x}) = u_D$ on Γ_D .

The Neumann boundary conditions are incorporated in (2.112), while the Dirichlet boundary condition u_D must be explicitly enforced. Equation (2.112) is mathematically equivalent to (2.108) in the case that the solution is sufficiently smooth.

The approximated solution can be obtained by plugging the equations (2.73) and (2.70) into (2.112) and by choosing $\beta_b = \delta_{ib}$ for $i \in \{1, \dots, n\}$,

$$\begin{aligned} \sum_a \alpha_a \left[- \int_{\Omega} a(\mathbf{x})\nabla \varphi_b \cdot \nabla \varphi_a d\Omega + \int_{\Omega} \varphi_b b(\mathbf{x}) \cdot \nabla \varphi_a d\Omega + \int_{\Omega} c(\mathbf{x})\varphi_b \varphi_a d\Omega \right] \\ = - \int_{\Gamma_N} a(\mathbf{x})\varphi_b q_N d\Gamma_N + \int_{\Omega} f(\mathbf{x})\varphi_b d\Omega, \end{aligned} \quad (2.113)$$

where for $b \in \{1, \dots, n\}$ the solution results in a system of n equations which can be expressed in matrix form by

$$\mathbf{L}\boldsymbol{\alpha} = \mathbf{f} \quad (2.114)$$

with values

$$\begin{aligned} \boldsymbol{\alpha} &= (\alpha_a)_{a=1, \dots, n}, \\ \mathbf{L} &= - \left(\int_{\Omega} a(\mathbf{x}) \nabla \varphi_b \cdot \nabla \varphi_a d\Omega + \int_{\Omega} \varphi_a b(\mathbf{x}) \cdot \nabla \varphi_a d\Omega + \int_{\Omega} c(\mathbf{x}) \varphi_b \varphi_a d\Omega \right)_{a=1, \dots, n; b=1, \dots, n} \\ \mathbf{f} &= \left(- \int_{\Gamma_N} a(\mathbf{x}) \varphi_b u_N d\Gamma_N + \int_{\Omega} f(\mathbf{x}) \varphi_b d\Omega \right)_{b=1, \dots, n}. \end{aligned} \quad (2.115)$$

The α_a parameters for the approximated function can subsequently be obtained.

2.6.3 Spatial Discretization

FEM is based on splitting complex domains or subdomains into geometrically simple shapes called finite elements. These elements, forming a mesh, are defined in 1D by intervals, in 2D usually by triangles or quadrilaterals, and in 3D usually by tetrahedrals or hexahedras. The size of these elements is a crucial parameter, as a finer mesh results in a more accurate approximation of the solution, while a coarser mesh reduces the computational time.

All the single elements Ω_h together form assembly Ω_t . Due to the simple shape of the elements Ω_t does not perfectly correspond to the real domain Ω , creating an inaccuracy in the final approximated solution, which depends once again on the meshing density.

In each subdomain, due to the meshing, a number of nodal points are defined. These nodal points are the supporting points of the basis functions $\varphi_a(x)$. The basis functions $\varphi_a(x)$, implemented for the approximated functions, are low order polynomials and the order is chosen according to the desired accuracy.

As an example, we consider a 1D domain divided into elements of small intervals $[x_{n-1}, x_n]$ with $n = 1, \dots, M$, where x_n are the nodes. The following properties have to be satisfied [48]:

- Nodal point are ordered

$$x_{n-1} < x_n \quad \text{for} \quad n = 1, \dots, M. \quad (2.116)$$

- The domain is completely covered

$$[a, b] = \bigcup_{n=1}^M [x_{n-1}, x_n] \quad x_0 = a, x_M = b. \quad (2.117)$$

- Each interval is unique

$$[x_{n-1}, x_n] \cap [x_{k-1}, x_k] = \emptyset \quad \text{for} \quad n \neq k. \quad (2.118)$$

In order to simplify the example we use an equidistant discretization

$$x_n = a + nh \quad n = 0, \dots, M,$$

where the mesh size h is defined by

$$h = \frac{a - b}{M}. \quad (2.119)$$

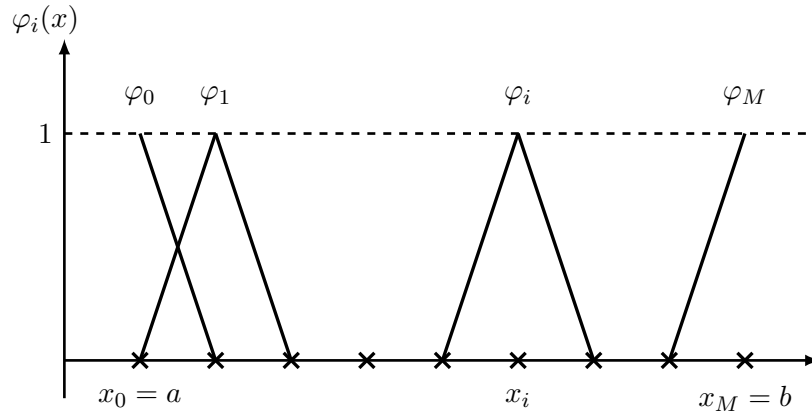


Figure 2.7: Piecewise linear hat-functions

The approximation function $u_h(x)$ is then composed of a combination of linear functions that are non zero in a small interval. For example, if we consider piecewise linear hat-functions (**Figure 2.7**), defined by

$$\varphi_n(x) = \begin{cases} 0 & a \leq x \leq x_{n-1} \\ \frac{x - x_{n-1}}{h} & x_{n-1} < x \leq x_n \\ \frac{x_{n+1} - x}{h} & x_n < x \leq x_{n+1} \\ 0 & x_{n+1} < x \leq b, \end{cases} \quad (2.120)$$

then, on the nodal points, the chosen basis functions fulfill the conditions

$$\varphi_n(x_k) = \delta_{nk} = \begin{cases} 1 & n = k \\ 0 & n \neq k \end{cases} \quad (2.121)$$

and the approximate function $u_h(x)$ is defined by

$$u_h(x) = \sum_{n=1}^{M-1} \varphi_n(x) \alpha_n + \varphi_0(x) \alpha_a + \varphi_M(x) \alpha_b. \quad (2.122)$$

This allows the calculation of the unknown parameters α_n by applying one of the methods previously described (cf. **Section 2.6.1**).

The chosen polynomial functions have to be continuous over the entire domain.

2.7 FEM for Solid Mechanics

A typical application for FEM are solid mechanics problems. Here, a general derivation and implementation for a linear elastic solid is presented [36]. The description follows a general framework used to find solutions for problems in solid mechanics. Different approaches to construct the weak form, as well as expressions for the strain and the constitutive law, can be found in [36, 49].

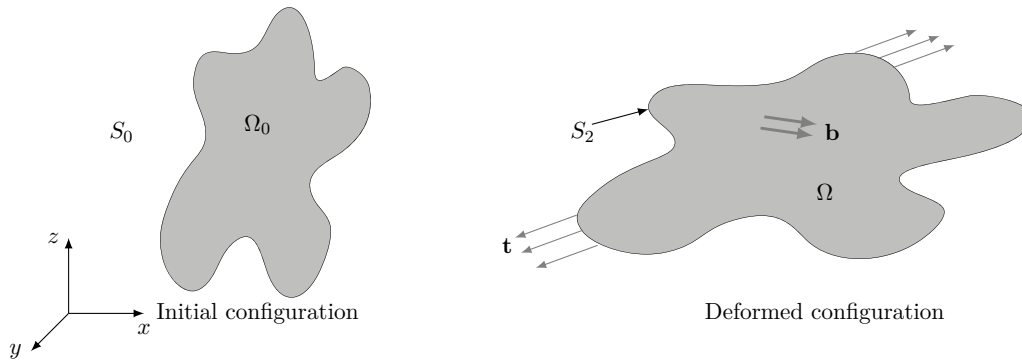


Figure 2.8: An unformed body (left) and a deformed body (right).

The system depicted in **Figure 2.8** is used as an example. The following properties and equations of linear elastic bodies have to be considered:

- The shape of the body at the deformed configuration Ω .
- The initial stress field in the body (zero in this FEM setting).
- The elasticity tensor \mathbf{C} (cf. (2.38)).
- The coefficients of thermal expansion (2.48) for the body as well as the temperature distribution (to simplify the FEM derivation they are neglected).
- A body force distribution \mathbf{b} (force per unit volume) acting on the body.
- Boundary conditions: displacement $u(x_D)$ on a section Γ_D of the boundary Ω or tractions t_i on a section Γ_t of the boundary Ω .

The coefficients u_i , ε_{ij} , and σ_{ij} are calculated by satisfying the governing equations of static linear elasticity:

- The Eulerian infinitesimal strain tensor (2.21).
- The elastic stress-strain relation (2.37).
- The equation of static equilibrium for stress (cf. (2.34)), given by $\partial\sigma_{ij}/\partial x_i + \rho b_i = 0$.
- Boundary conditions of the stress and the displacement: $\sigma_{ij}n_i = t_i$ on Γ_t and $u_i = u(x_D)$ on Γ_D .

In **Section 2.4** we demonstrated how the virtual work is used to replace the stress equilibrium equations. The principle was expressed by defining a virtual displacement field $\delta\mathbf{u}(\mathbf{x})$. The principle of virtual work corresponds to the weak formulation of the equilibrium condition.

If σ_{ij} satisfies

$$\int_{\Omega} \sigma_{ij} \delta\varepsilon_{ij} d\Omega - \int_{\Omega} \rho b_i \delta u_i d\Omega - \int_{\Gamma_t} t_i \delta u_i d\Gamma_t = 0, \quad (2.123)$$

for all virtual displacement fields and virtual strains, the equation of stress equilibrium $\partial\sigma_{ij}/\partial x_i + \rho b_i = 0$ and the boundary condition $\sigma_{ij}n_i = t_i$ on Γ_t are automatically satisfied (cf. **Section 2.4**). By employing the principle of virtual work the displacement field in a linear elastic solid in an integral form (weak form) can be derived.

To better explain the FEM procedure the first integral in (2.123) can be rewritten. In fact, by employing the symmetry of the stress tensor $\sigma_{ij} = \sigma_{ji}$ for the *virtual strain* definition (2.54) we can write

$$\sigma_{ij}\delta\varepsilon_{ij} = \frac{1}{2}\left(\sigma_{ij}\frac{\partial u_i}{\partial x_j} + \sigma_{ji}\frac{\partial \delta u_j}{\partial x_i}\right) = \sigma_{ij}\frac{\partial \delta u_i}{\partial x_j}. \quad (2.124)$$

Furthermore for linear elastic solids we recall $\sigma_{ij} = C_{ijkl}\varepsilon_{kl} = C_{ijkl}(\partial u_k/\partial x_l + \partial u_l/\partial x_k)/2$ and $C_{ijkl} = C_{ijlk}$, leading to $\sigma_{ij} = C_{ijkl}(\partial u_k/\partial x_l)$. This allows us to write

$$\sigma_{ij}\delta\varepsilon_{ij} = C_{ijkl}\frac{\partial u_k}{\partial x_l}\frac{\partial \delta u_i}{\partial x_j}. \quad (2.125)$$

The expression (2.125) can be plugged into the first term of (2.123) and the virtual work can be rewritten as

$$\int_{\Omega} C_{ijkl}\frac{\partial u_k}{\partial x_l}\frac{\partial \delta u_i}{\partial x_j}d\Omega - \int_{\Omega} \rho b_i\delta u_i d\Omega - \int_{\Gamma_t} t_i\delta u_i d\Gamma_t = 0, \quad u_i = u(x_D) \quad \text{on} \quad \Gamma_D. \quad (2.126)$$

The displacement field $u_k(\mathbf{x})$ is solved if it satisfies (2.126) for all virtual velocity fields δu_i fulfilling $\delta u_i = u(x_D)$ on Γ_D .

The strain components can be obtained from $\varepsilon_{ij} = 1/2(\partial u_i/\partial x_j + \partial u_j/\partial x_i)$. By using the stress-strain relation $\sigma_{ij} = C_{ijkl}\varepsilon_{kl}$ the stresses can be calculated. In this procedure no partial differential equations need to be solved; instead, equivalent integrals are present making the problem solvable using FEM.

The integral form of (2.126) can be approximated by discretizing the displacement field, which can be calculated as a set of n discrete points in the body, known as nodes. We denote them as x_i^a with $a = 1, \dots, n$; therefore, the unknown displacement vector at each node is denoted as $u_k(x_i^a)$.

The FEM procedure specifies the displacement field at an arbitrary point within the solid by interpolating between nodal values. The interpolation function can be defined as

$$u_k(\mathbf{x}) = \sum_{a=1}^n \alpha_{ai}\varphi_a(\mathbf{x}). \quad (2.127)$$

The same procedure can be used for the virtual displacement, which represents the test function

$$\delta u_i(\mathbf{x}) = \sum_{b=1}^n \beta_{bi}\varphi_b(\mathbf{x}). \quad (2.128)$$

Now (2.127) and (2.128) are substituted in (2.126). By choosing $\beta_{bi} = \delta_{bb'}$, $\delta_{ii'}$ for $b' \in \{1, \dots, n\}$ and $i' \in \{1, \dots, 3\}$, the virtual work equation can be expressed in a system of linear equations

$$\begin{aligned} \sum_{a=1}^n \int_{\Omega} C_{1jkl}\frac{\partial \varphi_a(\mathbf{x})}{\partial x_l}\frac{\partial \varphi_1(\mathbf{x})}{\partial x_j}d\Omega \alpha_{ak} - \int_{\Omega} \rho b_1\varphi_1(\mathbf{x})dV - \int_{\Gamma_t} t_1\varphi_1(\mathbf{x})d\Gamma_t &= 0 \\ \vdots & \\ \sum_{a=1}^n \int_{\Omega} C_{3jkl}\frac{\partial \varphi_a(\mathbf{x})}{\partial x_l}\frac{\partial \varphi_n(\mathbf{x})}{\partial x_j}d\Omega \alpha_{ak} - \int_{\Omega} \rho b_3\varphi_n(\mathbf{x})dV - \int_{\Gamma_t} t_3\varphi_n(\mathbf{x})d\Gamma_t &= 0. \end{aligned} \quad (2.129)$$

The system of equations in (2.129) can be rewritten in matrix form as

$$\begin{bmatrix} K_{1111} & K_{1112} & K_{1113} \\ K_{1211} & K_{1212} & K_{1213} \\ K_{1311} & K_{1312} & K_{1313} \\ \vdots & \vdots & \vdots \\ K_{n1n1} & K_{n1n2} & K_{n1n3} \\ K_{n2n1} & K_{n2n2} & K_{n2n3} \\ K_{n3n1} & K_{n3n2} & K_{n3n3} \end{bmatrix} \begin{bmatrix} \alpha_{11} \\ \alpha_{12} \\ \alpha_{13} \\ \vdots \\ \alpha_{n1} \\ \alpha_{n2} \\ \alpha_{n3} \end{bmatrix} = \begin{bmatrix} f_{11} \\ f_{12} \\ f_{13} \\ \vdots \\ f_{n1} \\ f_{n2} \\ f_{n3} \end{bmatrix} \quad \text{or} \quad \mathbf{K}_{bika} \boldsymbol{\alpha}_{ak} = \mathbf{f}_{bi}, \quad (2.130)$$

where the notations indicate

$$\mathbf{K}_{bika} = \left(\int_{\Omega} C_{ijkl} \frac{\partial \varphi_a(\mathbf{x})}{\partial x_l} \frac{\partial \varphi_b(\mathbf{x})}{\partial x_j} d\Omega \right)_{b=1,\dots,n; i=1,\dots,3; k=1,\dots,3; a=1,\dots,n} \quad \boldsymbol{\alpha}_{ak} = (\alpha_{ak})_{a=1,\dots,n; k=1,\dots,3} \quad (2.131)$$

$$\mathbf{f}_{bi} = \left(\int_{\Omega} \rho b_i \varphi_b(\mathbf{x}) d\Omega + \int_{\Gamma_t} t_i \varphi_b(\mathbf{x}) d\Gamma_t \right)_{b=1,\dots,n; i=1,\dots,3}.$$

Therefore, the α_{ak} parameters for the displacement $u_k(\mathbf{x})$ can be obtained and, by using the elastic strain relations, the stress in the deformed body can be calculated.

3

Stress Evolution during 3D IC Stacking using Open TSVs

In open TSVs the presence of high levels of mechanical stress is critical to the mechanical stability of the structure. During 3D IC stacking external mechanical stress acting on the TSV can be generated leading to accelerated circuit failure.

In this work an external force applied on an open TSV was reproduced using a model, which was implemented using FEM. The implemented model was calibrated using experimental data from an industrial partner. Subsequently the areas in the structure, in which a mechanical failure due to an external force is most likely, were localized. In these critical areas the probability of cracking or delamination is highest.

In the first part of this chapter a brief description of the approach used to reproduce an external force acting in open TSVs is provided. In the second part the results obtained from the FEM simulations are discussed.

3.1 Stress Generation during 3D IC Stacking

During the 3D IC stacking, dies and wafers are bonded to each other, either as die-to-die, die-to-wafer, or wafer-to-wafer [14]. Different sources of mechanical stress can be identified during stacking:

- For bonding thermo-compression technology is commonly employed [51]. During this process, the bonding pressure and temperature [52] have to be controlled to limit the high generation of mechanical stress in the structures. As described in **Section 2.3.2** during temperature changes thermal strain is generated and therefore during stacking the temperature has to be controlled to limit the develop of thermal stress [53].
- Unintentional indenters and loads, for example due to the presence of dust particles in a contaminated environment, can appear during the stacking process. These particles can apply extra mechanical stress at the structures. In the adhesive/polymer bonding the adhesive materials could be thought as a potential contaminant developing extra mechanical stress [54].

In this work, these stresses are considered as an external load acting on an open TSV. During the stacking process mechanical stress evolves in the TSV structure, generating mechanical instability.

3.2 Nanoindentation

The approach used in order to treat the potential presence of unintentional indenters during bonding with open TSVs was the nanoindentation. Usually, nanoindentation is

employed to evaluate the elastic modulus, the strain-hardening exponent, the fracture toughness, and the viscoelastic properties [38, 55]. However, in this study, nanoindentation was differently used. It was employed to reproduce an external load acting in an open TSV. This external load can result in additional mechanical stress during the 3D IC stacking. Nanoindentation is a simple method which consists of contacting the material of interest (open TSV) with another material (indenter). In one of these two materials, the mechanical properties, such as elastic modulus and hardness, are unknown. In the other, the material properties are known.

The main goal of this work was to estimate the areas in which mechanical failure due to an external load can be expected. From the results, a better understanding of how to increase the mechanical stability of the system can be obtained.

During nanoindentation, an indenter is placed in contact with the surface of a sample in which a steadily increasing load is applied. This causes the indenter to penetrate into the sample. Indenters can be adapted to suit the parameters under investigation and can therefore have different shapes and can be composed of different materials. Indenters are identified as spherical, conical, Vickers, or Berkovich [38, 56]. The applied force at the indenter is usually in the millinewton range, and the depth of penetration is on the order of micrometers.

During nanoindentation experiments, both load and depth of penetration are recorded at each load increment, resulting in load-displacement curves. Following the measurement of the maximum load, the indenter is steadily removed and the penetration depth is recorded again. If a residual impression is left on the surface of the specimen, a plastic deformation in the material has occurred. In contrast, if the removal of the indenter does not leave an impression, the material has behaved elastically.

Figure 3.1 (a) depicts an example of a load-displacement curve. The top line represents the loading while the indenter is penetrating the sample. The bottom line, on the other hand, depicts the unloading during which the indenter is extracted from the sample. Since the unloading curve does not follow the loading curve the sample deforms plastically. The plastic response is detectable because the unloading curve does not return to its initial displacement value. Therefore, a residual impression due to plastic deformation of the material remains. Usually, the loading portion of the indentation cycle consists of an elastic response of the material at lower loads followed by plastic flow, or yield, within the sample at higher loads [38]. Generally speaking the indentation stress-strain response

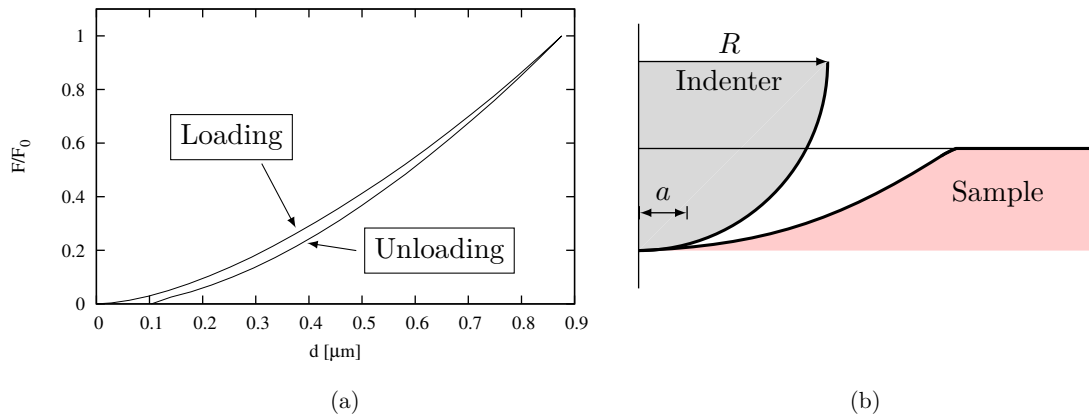


Figure 3.1: (a) A sample of load displacement curve. (b) An indenter penetrating into a sample.

of an elastic-plastic solid can be divided into three regimes. These regimes are defined by considering the mean contact pressure of the indenter p_m , and the uniaxial compressive yield (or flow) stress Y of the sample. The contact pressure of the indenter is defined by

$$p_m = \left(\frac{4E^*}{2\pi} \right) \frac{a}{R}, \quad (3.1)$$

where E^* is the reduced modulus that combines the Young's modulus of the indenter E and that of the specimen E'

$$\frac{1}{E^*} = \frac{(1 - \nu^2)}{E} + \frac{(1 - \nu'^2)}{E'}. \quad (3.2)$$

If the contacting bodies are two spheres, the indenter radius R is defined by

$$\frac{1}{R} = \frac{1}{R_1} + \frac{1}{R_2}, \quad (3.3)$$

where R_1 indicates the indenter radius and R_2 the sample radius [57]. R and a are depicted in **Figure 3.1** (b).

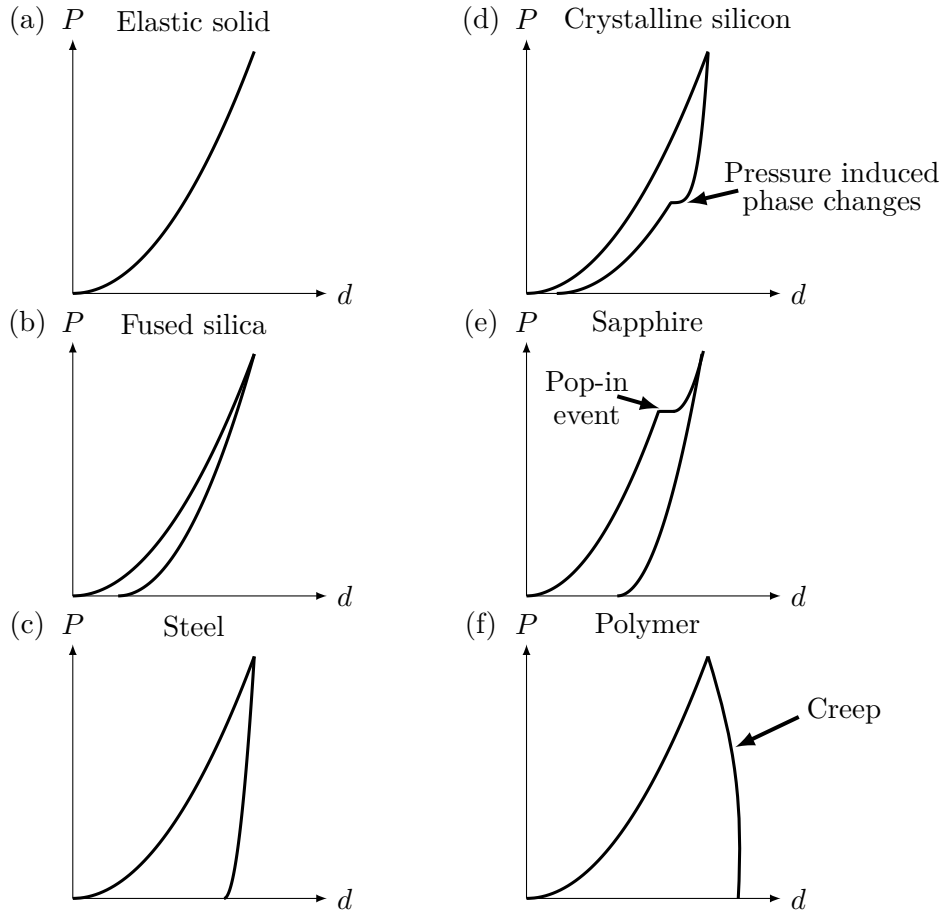


Figure 3.2: Examples of load-displacement (P - d) curves for different material responses and properties. The pop-in event in (e) indicates cracking or delamination.

The three regimes during the nanoindentation are defined as [58]:

- $p_m < 1.1 \cdot Y$: The sample has a full elastic response.
- $1.1 \cdot Y < p_m < C \cdot Y$: Plastic deformation appears at the initial surface of the sample. (C is a constant that depends on the sample material and indenter geometry)
- $p_m = C \cdot Y$: The plastic deformation area extends and grows in size as the indentation contact area increases.

During these three regimes different physical phenomena may occur in the sample. Non-linear events, such as phase transformation (**Figure 3.2** (d)), cracking, and delamination (**Figure 3.2** (e)) are identifiable in the load displacement curves. The presence of discontinuities in the load displacement curves suggest the appearance of cracks or delamination (**Figure 3.2**).

3.3 FEM Approach

The mechanical reliability of TSVs is strongly connected to the material properties and the size of the device. Materials behave differently under mechanical stress, which affects the mechanical stability of the entire system. The bottom portion of an open TSV can be composed of different material layers. During the deposition processes and subsequent fabrication steps (die bonding, etc.), new mechanical stresses can be generated leading to mechanical instability. Mechanical stresses, in turn, determine the formation of new defects or the propagation of existing defects in the structure. Therefore, the material properties and the device geometry must be optimized in order to minimize mechanical stresses and to improve reliability [59].

FEM was used to simulate the application of an external load on an open TSV, as shown in **Figure 3.3**. From the simulation results, information regarding the development of mechanical stress in the device are obtained. In these simulations the bottom part of the open TSV was mechanically fixed laterally at the Si sidewall. The bottom area was thereby “free” to bend in the y -axis direction (red arrow in **Figure 3.3**). The figure corresponds to a structure used for optical sensor applications [29, 60] at the step in the fabrication process prior to die bonding. During the fabrication process, a critical mechanical stress can be generated. High concentrations of mechanical stress can cause failure in the form of cracking and delamination in the layers which make up the bottom of the TSV.

The bottom of the TSV under consideration consists of a multilayer structure which corresponds to the Al based interconnect structure for CMOS technology [29]. These layers are materials with different thicknesses and mechanical properties. In the following, this many-layered structure is diagrammatically depicted as a single layer, denoted as “multilayer” in **Figure 3.3** and it corresponds to oxide, nitride, and aluminium layers.

The mechanical and electromechanical properties of the materials play an important role for the reliability of devices. Mechanical properties of thin films should be accurately measured at the length scale of the devices under consideration, since their properties are different from those of bulk materials. These differences can be due to size effects, grain structures, and processing [61]. Unfortunately material properties for thin materials employed in open TSV are not available in literature.

3.3.1 Simulation Setup

In an open TSV, the indenter can be placed at two different locations, either internal or external to the TSV. These two locations will produce a different distribution of mechanical

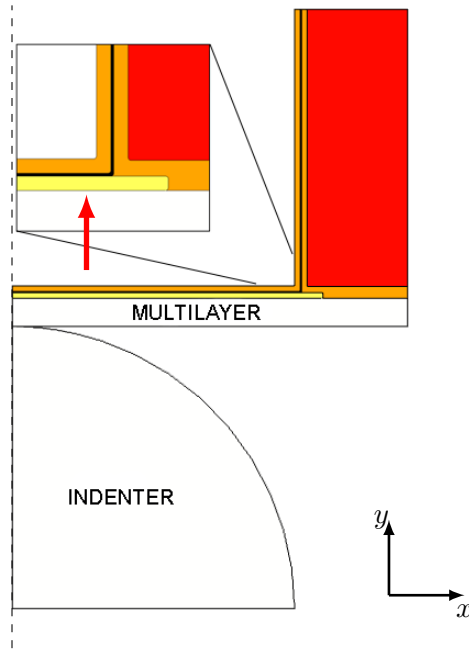


Figure 3.3: Two-dimensional representation of a TSV structure and an indenter. The dashed line indicates the axis of symmetry. Only a quarter of the system is represented. Al is shown in yellow, W in black, SiO₂ in orange, and Si in red. The multilayer consists of different materials. The indenter is spatially external to the TSV (the via height and width of the TSV in the figure do not represent the real size, under consideration).

stress inside the TSV. In this work an indenter acting external to an open TSV, as shown in **Figure 3.3**, was considered. A spherical diamond indenter with a radius of 50 μm , a Young's modulus of 1100 GPa, and a Poisson's ratio of 0.07 was used. The TSV aspect ratio is 1:2.5 and the TSV diameter is 100 μm [29]. The layers which line the inside of the TSV have thicknesses of 1 μm for SiO₂, 1 μm for the Al layer, and 0.2 μm for W.

The simulations were performed by accounting for each material of the multilayer, rather than considering a single artificial one (**Figure 3.3**). The materials used in an open TSV have a polycrystalline or amorphous structure. An isotropic behavior can therefore be assumed which leads to a simplification of the simulation, such as allowing to use a two-dimensional axis-symmetric simulation environment. Because of the location of the indenter, the mechanical stress is mainly generated in the multilayer area and not along the Si in the sidewall. Therefore it is assumed that Si is isotropic and that it does not significantly influence the mechanical stability of the multilayer. Only a negligible influence of the anisotropy of the Si on the final results is expected.

FEM simulation requires a contact condition between indenter and sample to recreate the interaction between TSV bottom and indenter during penetration. In the implemented model, this condition was reproduced by employing the contact pressure penalty method [38, 62].

Accurate results are obtainable by modeling the contact areas of the indenter and the TSV with a very fine mesh. In general, all geometries would benefit from a fine mesh, but this would lead to excessively long simulation times. A mapped mesh with a minimum element size of 0.5 μm was employed for the layer in contact with the indenter. Along the edge of the indenter in contact with the TSV, a maximum element size of 0.06 μm was used.

A stationary parametric sweep study was performed. The movement of the indenter was emulated using the prescribed displacement as variable. This was repeated for increasing displacement, until the maximum measured displacement from the experimental data was reached.

The TSV structure was mechanically fixed at a single point, the top of the TSV sidewall. For the outer-rightmost Si region, a so-called roller constraint was chosen, which allows the material to move tangential to the boundary but not perpendicular to it. On the other edges, the TSV was free to move, allowing for a reproduction of the real conditions of the device.

3.3.2 Plasticity Simulation

In the implemented model, the elastic-plastic behavior of the materials was considered. The elastic behavior was reproduced with Hooke's law (2.37). The plastic behavior was described by employing an isotropic hardening law [62, 63].

An elastic-plastic material is usually modeled under the assumption that the strains $\boldsymbol{\varepsilon}$ and strain increments $d\boldsymbol{\varepsilon}$ formed by the elastic and plastic part can simply be added together (2.36). By coupling the elastic part $\boldsymbol{\varepsilon}_e$, described by Hooke's law, and the plastic part $\boldsymbol{\varepsilon}_p$ in (2.36), the stress $\boldsymbol{\sigma}$ in a material can be described as [36, 37, 44]

$$\boldsymbol{\sigma} = \mathbf{C} : \boldsymbol{\varepsilon}_e = \mathbf{C} : (\boldsymbol{\varepsilon} - \boldsymbol{\varepsilon}_p), \quad (3.4)$$

where \mathbf{C} is the elasticity tensor.

When considering an isotropic plastic material, the strain increment is studied by using the plastic potential Q_p , which is a function of the three invariants of the Cauchy stress tensor

$$Q_p(\boldsymbol{\sigma}) = Q_p(I_1(\boldsymbol{\sigma}), J_2(\boldsymbol{\sigma}), J_3(\boldsymbol{\sigma})), \quad (3.5)$$

where the three invariants are defined by

$$\begin{aligned} I_1 &= \sigma_{xx} + \sigma_{yy} + \sigma_{zz}, \\ J_2 &= \frac{1}{2}(\sigma_{ii}\sigma_{jj} - \sigma_{ij}\sigma_{ji}), \text{ and} \\ J_3 &= \sigma_{xx}\sigma_{yy}\sigma_{zz} + 2\sigma_{xy}\sigma_{yz}\sigma_{zx} - \sigma_{xy}^2\sigma_{zz} - \sigma_{yz}^2\sigma_{xx} - \sigma_{zx}^2\sigma_{yy}. \end{aligned} \quad (3.6)$$

An increment of the plastic strain tensor $\dot{\boldsymbol{\varepsilon}}_p$ can therefore be decomposed as

$$\dot{\boldsymbol{\varepsilon}}_p = \lambda \frac{\partial Q_p}{\partial \boldsymbol{\sigma}} = \lambda \left(\frac{\partial Q_p}{\partial I_1} \frac{\partial I_1}{\partial \boldsymbol{\sigma}} + \frac{\partial Q_p}{\partial J_2} \frac{\partial J_2}{\partial \boldsymbol{\sigma}} + \frac{\partial Q_p}{\partial J_3} \frac{\partial J_3}{\partial \boldsymbol{\sigma}} \right), \quad (3.7)$$

where λ is the plastic multiplier, which depends on the current state of the stress and the load history. The "dot" in $\dot{\boldsymbol{\varepsilon}}_p$ does not indicate a true time derivative, but rather it indicates the rate at which the plastic strain tensor changes with respect to $\partial Q_p / \partial \boldsymbol{\sigma}$. The employed measure of the plastic deformation is the effective plastic strain rate $\dot{\boldsymbol{\varepsilon}}_{pe}$, which is defined as

$$\dot{\boldsymbol{\varepsilon}}_{pe} = \sqrt{\frac{2}{3} \dot{\boldsymbol{\varepsilon}}_p : \dot{\boldsymbol{\varepsilon}}_p}. \quad (3.8)$$

In the theory of plasticity, it is possible to describe yielding in the terms of $\boldsymbol{\sigma}$ only by means of a yield function. Therefore, a yield function can be used to define the onset of the plastic behavior. Given a yield function $F_y(\boldsymbol{\sigma}, \boldsymbol{\sigma}_{ys})$, which defines the limits of the elastic regimes, when $F_y(\boldsymbol{\sigma}, \boldsymbol{\sigma}_{ys}) < 0$ the material reacts elastically and when $F_y(\boldsymbol{\sigma}, \boldsymbol{\sigma}_{ys}) \geq 0$ it begins to deform plastically [63].

$\sigma_{ys}(\varepsilon_{pe})$ is the current yield stress which evolves during plastic flow and is described by an isotropic hardening law. The isotropic hardening law under consideration is a linear equation described by

$$\sigma_{ys}(\varepsilon_{pe}) = \sigma_{ys0} + \frac{E_{Tiso}}{1 - \frac{E_{Tiso}}{E}} \varepsilon_{pe}, \quad (3.9)$$

where σ_{ys0} is the initial yield stress (a material property), which indicates the stress level at which plastic deformation occurs. As can be seen in (3.9) $\sigma_{ys}(\varepsilon_{pe})$ is determined by the isotropic tangent modulus E_{Tiso} and the effective plastic strain ε_{pe} . The yield level increases proportionally with the effective plastic strain ε_{pe} [62, 63]. In **Figure 3.4** the σ_{ys0} and E_{Tiso} necessary to describe the plastic behavior are represented in a stress-strain plot.

The yield function is defined as

$$F_y = \sigma_{mises} - \sigma_{ys}(\varepsilon_{pe}), \quad Q_p = F_y, \quad (3.10)$$

where σ_{mises} is the Von Mises stress.

Not only do the material parameters influence the load-displacement curves, but nanoindentation is also sensitive to the level of residual stress in the layers. The results of experimental indentation are therefore the sum of two contributions: plastic deformation and residual stress.

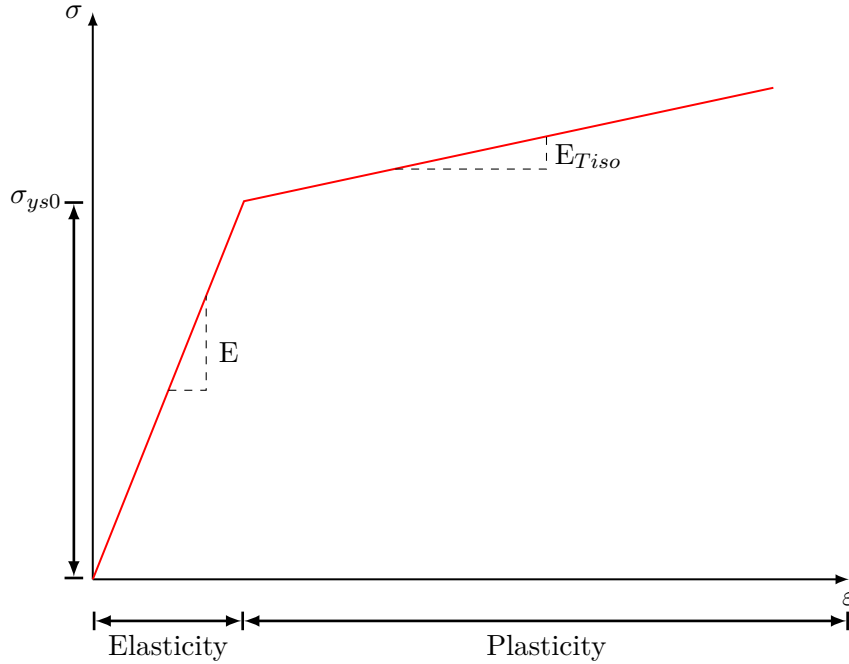


Figure 3.4: Stress-strain curve showing the elastic part before reaching the σ_{ys0} . At σ_{ys0} the plastic deformation begins.

3.4 Results and Discussions

The model calibration can permit to understand how mechanical stress develops within the different layers (multilayer) as the force applied by the indenter increases. The presented model was calibrated using experimental data from an industrial partner. The

experimental data were obtained for a displacement of the indenter into the surface up to approximately $3 \mu\text{m}$. During the experiment, the process of unloading was not recorded.

In **Figure 3.5** the simulation result shows the indenter at the highest prescribed indentation displacement. The movement of the indenter causes it to penetrate approximately $3 \mu\text{m}$ into the multilayer, which results in the displacement and deformation of the materials therein. The highest displacement is found at the center of the device. The deformation of the sample develops around the contact point between indenter and sample, and increases as the load is applied.

From the experimental data it was possible to obtain the load-displacement curve. The loading plot provides information about the mechanical properties, as well as the failure of the device.

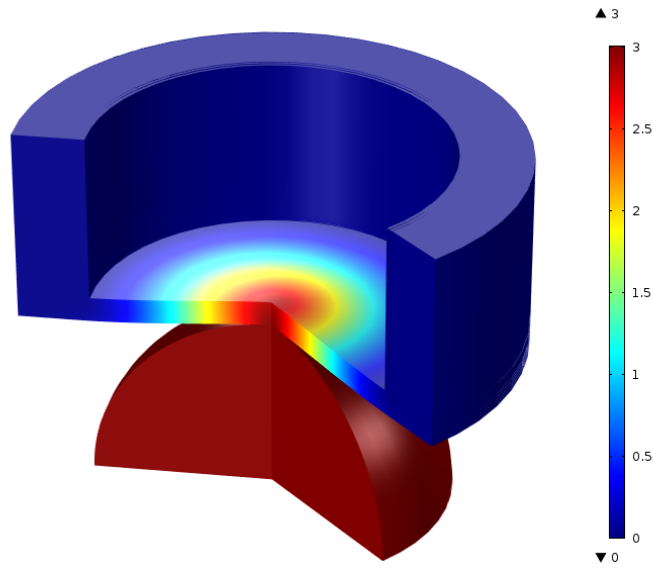


Figure 3.5: FEM result, illustrating the displacement (μm) of the indenter inside of the TSV. The displacement peaks at about $3 \mu\text{m}$.

In **Figure 3.6** the red and black lines indicate the experimental and simulation, respectively. Due to the complex, multilayered architecture of TSVs, the experimental results do not represent the behavior of only one material, but rather the behavior of a multilayer structure. In the experimental data shown in **Figure 3.6** we can identify an initial elastic regime which corresponds to an indentation displacement between 0 and $0.25 \mu\text{m}$, followed by a plastic regime for indentation displacements above $0.25 \mu\text{m}$. An aberration is notable around an indentation displacement of $2.5 \mu\text{m}$, assumed to be due to a failure in the device, such as cracking or delamination [38].

The results of the simulation are in good agreement with experimental data, as can be seen in **Figure 3.6**. It is particularly important to have a good fit for low loads of the indenter, in the range of 0 to $0.1 \times F/F_0$ because, in this range, only the elastic behavior of the materials influences the result. The fitting of the plastic regime requires much more effort because the bottom of the TSV consists of different materials. Each material could exhibit plasticity, which can occur when different sufficiently high loads are applied. Furthermore, the plastic properties of thin layers employed in TSV structures are not reported in the literature. The plastic response of plastic materials during loading was described in (3.9), where the yield stress and isotropic tangent modulus are the fitting parameters [64, 65, 66]. The results of the simulation depend on the values of the yield stress and the

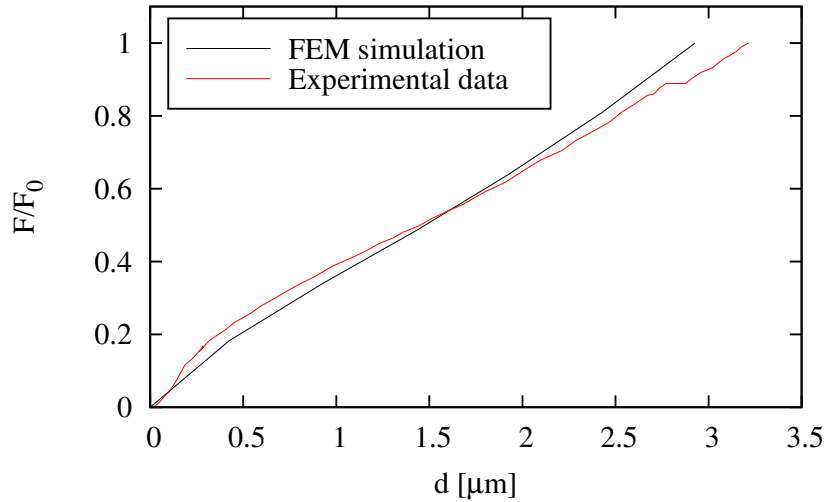


Figure 3.6: The loading part of the nanoindentation process is plotted and it illustrates a comparison between the FEM simulation and experimental data.

isotropic tangent modulus of the materials. To fit the model with the experimental data, the values of the yield stress and the isotropic tangent modulus of the plastic materials of the multilayer which were in contact with the indenter during indentation were modified. By changing these parameters, a good match with the experimental data was found. The deviation between the experimental results and the simulations is due to the multilayer structure for which the composition between layers and the non-bulk character can have an influence on the plastic behavior, which the model does not take into account.

During the deposition processes, residual stresses develop in the layers of the multilayer structure. These stresses can influence the nanoindentation test [38]. Different values of residual stress [67] were attempted in thin films of the multilayer in order to assist the calibration process. However, these tests did not improve the fitting; therefore, the influence of the residual stress was not considered.

Figure 3.7 depicts the normalized Von Mises stress due to the penetration of the indenter in the TSV. Two locations with high mechanical stress can be seen. The first is above the indenter and the second is located at the bottom corner around the TSV sidewall. The first interaction with the indenter generates a critical mechanical stress only at this location. As the indenter penetrates into the TSV, the mechanical stress develops and becomes high at the bottom corner around the TSV sidewall. An increase in the displacement of the indenter increases the stress in the TSV. The inset in **Figure 3.7** depicts in detail the distribution of the Von Mises stress in the W layer.

From the simulations stress values at different locations were determined allowing to deduce which mode of failure is most likely to occur. The highest stresses were found at the corner of the TSV sidewall, in particular:

- In the SiO_2 layer.
- At the interface between SiO_2 and W.

The **Figure 3.8** illustrates the Von Mises stress development in the SiO_2 layer and at the interface between SiO_2/W at the corner of the TSV sidewall. This result indicates a continuous increase in the SiO_2 . The stress behaves differently in the SiO_2 layer and at the SiO_2/W interface. The stress at the SiO_2/W interface initially grows continuously, but at

a smaller slope than the stress at the SiO₂ surface. After an indentation of approximately 0.5 μm, the slope is further reduced. This does not indicate that the failure will be confined to the SiO₂ layer; the SiO₂/W interface could be experiencing a reduced stress behavior due to defects or a small interface fracture toughness, which can strongly contribute the failure at the interface.

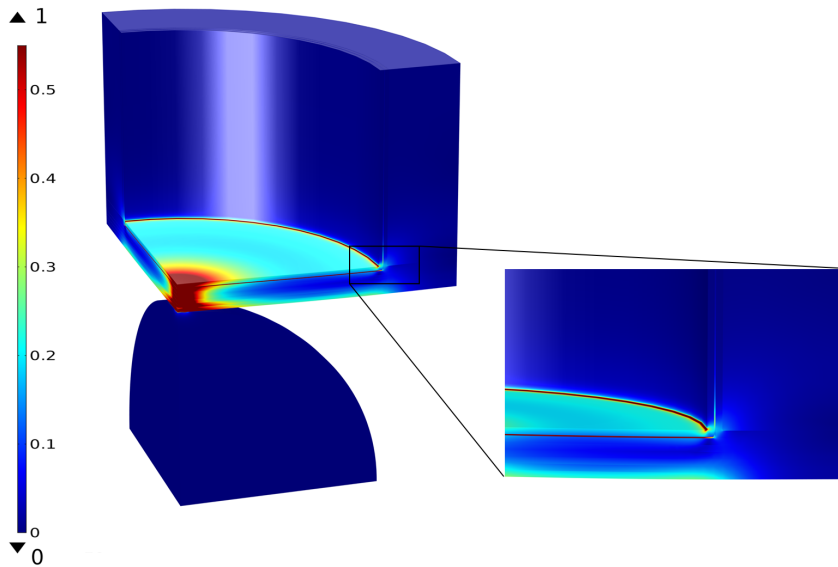


Figure 3.7: This image depicts normalized Von Mises stress development in the TSV. Two physical regions with high mechanical stress can be identified. The first is located in the TSV area above the indenter and the second is at the corner of the TSV. This perspective of the structure differs from **Figure 3.3** in order to highlight those areas with a high concentration of mechanical stress.

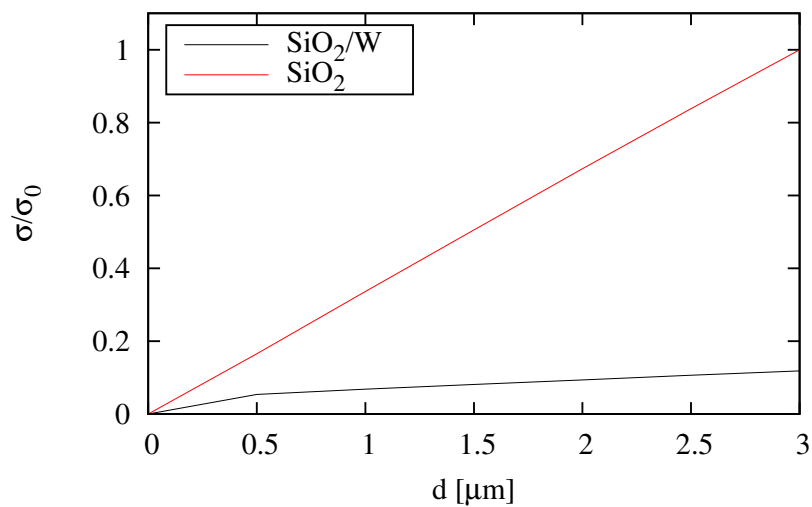


Figure 3.8: Normalized Von Mises stress versus displacement into surface.

3.5 Summary

In this chapter the stress development in the layers of open TSVs, during the application of an external force, was investigated. The implemented model permits to simulate the penetration of an indenter into the bottom of the TSV, reproducing the extra mechanical stress which might appear during the 3D IC stacking. The simulations were calibrated with experimental data, provided by an industrial partner. The model was fitted qualitatively by altering the plasticity parameters of the material under test. The simulations can predict the areas of the device in which there is increased stress and thereby a higher probability of failure. The following scenarios were found:

- Initially, only the area of the TSV, directly above the indenter, appears to be problematic. During indentation, the concentration of stress can increase, until a failure occurs. The presence of defects can facilitate delamination or cracking.
- At higher indentations, the increased stress becomes an issue at the corners of the TSV. In this area we can expect cracking of the SiO₂ layer. The cracks can then propagate and, upon reaching an interface, cause delamination.

The model can be used to identify the way in which geometric and material properties influence the mechanical stability of TSVs during 3D IC stacking.

4

Fracture Mechanics and Delamination in Open TSVs

In **Chapter 3** the nanoindentation technique was applied in order to locate the areas with a high concentration of mechanical stress in an open TSV. In these areas the probability of device failure, such as cracking or delamination, is high. The bottom of the TSV under consideration, which saw the highest stress build-up, consists of a multilayer structure which represents the Al-based interconnection used in CMOS technology. In this section we investigate how external forces, layer thicknesses, and the residual stress in the layers can induce delamination at the interfaces which form the bottom of an open TSV.

4.1 Basis of Fracture Mechanics

In order to understand the delamination failure it is first necessary to explain the theory of cracks in bodies. The following theories are based on and described in detail in [37, 68, 69, 70, 71]. In continuum mechanics a crack is defined as a cut in a body which has its end inside the body volume. This end of the crack is referred to as a crack-tip. Crack surfaces are defined as the two opposite boundaries formed by the cutting plane and are generally treated as traction-free. The crack-tip and crack surfaces are illustrated in **Figure 4.1**.

In a solid material a crack can propagate in three different modes:

- **Mode I:** Opening the crack opens normal to the crack plane due to a load perpendicular to the crack surface.
- **Mode II:** Sliding the crack faces are displaced parallel to the crack surface and perpendicular to the crack-tip due to a shear loading.
- **Mode III:** Tearing the crack faces are displaced parallel to the crack surface and parallel to the crack-tip due to a shear loading acting in parallel to the crack tip.

These propagation modes can occur independently or in combination. To fully understand the crack propagation modes it is necessary to analyze the crack-tip field within a small region of radius R around the crack tip. Therefore the description of the crack-tip field demands the specification of a hybrid Cartesian and polar coordinate system as shown in **Figure 4.2**.

4.1.1 Crack-Tip Field

The mechanical analysis of the crack-tip field under mode I (cf. **Figure 4.1** (a)) will be explained in the following and it is based on [37, 70, 71].

The derivation of the crack-tip field is achieved by employing the Airy stress function and the Westergaard approach which are described in **Appendix A** and **Appendix B**,

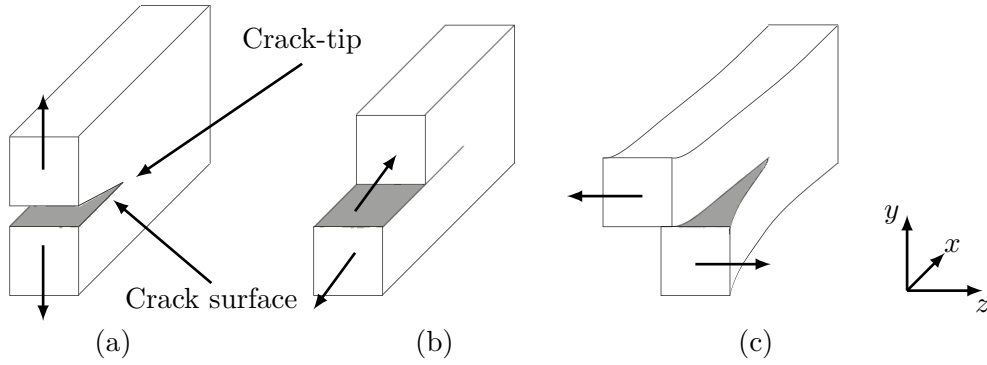


Figure 4.1: The three crack opening modes. (a) indicates mode I (opening), (b) mode II (sliding) and (c) mode III (tearing).

respectively. The system analyzed is illustrated in **Figure 4.2**, where a set of in-plane Cartesian coordinates x and y , and polar coordinates r or φ at the crack tip are chosen. A complex representation $z = x + iy$ of the coordinates is employed in the derivations.

A line crack with the following boundary conditions is considered:

1. Very large stresses at the crack tip.
2. Traction free crack surfaces.

The stresses σ_{xx} and σ_{yy} along the $y = 0$ plane can be expressed as

$$\sigma_{xx} = \sigma_{yy} = \text{Re}\{Z_I(z)\}, \quad (4.1)$$

where $Z_I(z)$ is the Westergaard function described in **Appendix B** and is employed to analyze crack problems [70, 71]. The Westergaard function permits to analyze the stress field at the crack tip by using a complex potential, as the Airy stress function, related to boundary condition of the system. In the following derivations the argument of Z is omitted for better readability and the subscript of Z indicates the crack mode. Because the strain energy in the body has to be finite, the order of the singularity of stresses at the crack has to be of higher order than $z^{-1/2}$. Therefore the solution of the crack problem can be written in the form

$$Z_I = \frac{g(z)}{\sqrt{z}}, \quad (4.2)$$

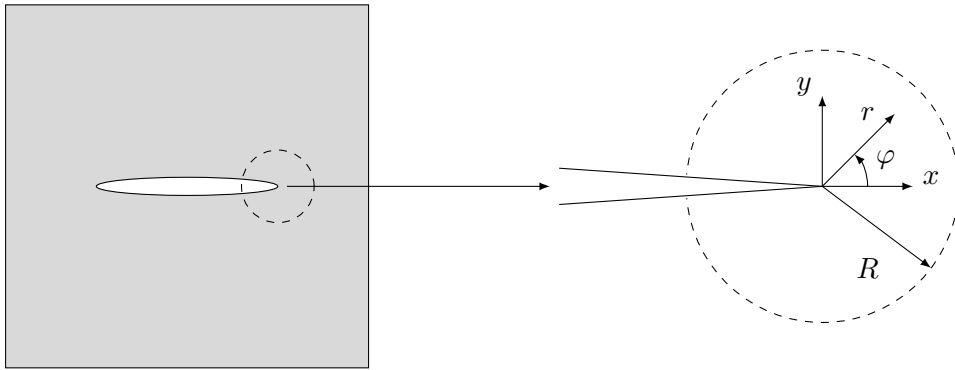


Figure 4.2: Coordinate at the crack-tip.

where $g(z)$ is a function which does not diverge at the crack tip ($z \rightarrow 0$). In this way the solution permits to obtain $\sigma_{yy} \rightarrow \infty$ for $z \rightarrow 0$, satisfying the first boundary condition. The second boundary condition $\sigma_{yy} = 0$ for $x < 0$ and $y = 0$, is defined by

$$\sigma_{yy} = \operatorname{Re} \left\{ \frac{g(z)}{\sqrt{x}} \right\} = \operatorname{Re} \left\{ \frac{g(x)}{\sqrt{x}} \right\} = 0, \quad (4.3)$$

which is satisfied if $g(x)$ is real along $y = 0$.

The function $g(z)$ close to the origin of the crack-tip can be represented by a Taylor series

$$g(z) = g(0) + z \left. \frac{dg(z)}{dz} \right|_{z=0} + \frac{1}{2!} z^2 \left. \frac{d^2g(z)}{dz^2} \right|_{z=0} + \dots \quad (4.4)$$

Close to the crack-tip the function $g(z)$ is real and constant. This constant $g(0)$ is related to the stress intensity factor K_I by

$$g(0) \equiv \frac{K_I}{\sqrt{2\pi}}, \quad (4.5)$$

which gives

$$Z_I = \frac{K_I}{\sqrt{2\pi z}} \quad (4.6)$$

close to the crack tip. The subscript of the stress intensity factor K_I indicates the crack mode. K represents the magnitude of the crack tip stress.

The functions Z_I and Z'_I necessary to describe the stresses near the tip can be expressed by employing the polar coordinate representation of $z = re^{i\varphi}$

$$\begin{aligned} Z_I &= \frac{K_I}{\sqrt{2\pi z}} = \frac{K_I}{\sqrt{2\pi r}} e^{-i\frac{\varphi}{2}} = \frac{K_I}{\sqrt{2\pi r}} \left[\cos\left(\frac{\varphi}{2}\right) - i \sin\left(\frac{\varphi}{2}\right) \right], \\ Z'_I &= \frac{d}{dz} \frac{K_I}{\sqrt{2\pi z}} = -\frac{1}{2} \frac{K_I}{\sqrt{2\pi}} z^{-\frac{3}{2}} = -\frac{K_I}{\sqrt{2\pi r}} \frac{1}{2r} e^{-i\frac{3\varphi}{2}} = -\frac{K_I}{\sqrt{2\pi r}} \frac{1}{2r} \left[\cos\left(\frac{3\varphi}{2}\right) - i \sin\left(\frac{3\varphi}{2}\right) \right]. \end{aligned} \quad (4.7)$$

Therefore the real and imaginary parts of the Westergaard function are

$$\begin{aligned} \operatorname{Re}\{Z_I\} &= \frac{K_I}{\sqrt{2\pi r}} \cos\left(\frac{\varphi}{2}\right), \\ \operatorname{Im}\{Z_I\} &= -\frac{K_I}{\sqrt{2\pi r}} \sin\left(\frac{\varphi}{2}\right), \\ \operatorname{Im}\{Z'_I\} &= \frac{K_I}{\sqrt{2\pi r}} \frac{1}{2r} \sin\left(\frac{3\varphi}{2}\right), \\ \operatorname{Re}\{Z'_I\} &= -\frac{K_I}{\sqrt{2\pi r}} \frac{1}{2r} \cos\left(\frac{3\varphi}{2}\right). \end{aligned} \quad (4.8)$$

The stresses at the crack-tip can be described by using the Westergaard function (more detail in **Appendix B**)

$$\begin{aligned} \sigma_{xx} &= \operatorname{Re}\{Z_I\} - y \operatorname{Im}\{Z'_I\} + 2A, \\ \sigma_{yy} &= \operatorname{Re}\{Z_I\} + y \operatorname{Im}\{Z'_I\}, \\ \tau_{xy} &= -y \operatorname{Re}\{Z'_I\}, \end{aligned} \quad (4.9)$$

where A is an uniaxial stress that does not add singularity at the crack tip. If we do not consider the higher-order terms, the stresses at the crack tip are given by plugging (4.8)

into (4.9) (A is set to 0)

$$\begin{aligned}\sigma_{xx} &= \frac{K_I}{\sqrt{2\pi r}} \cos\left(\frac{\varphi}{2}\right) \left[1 - \sin\left(\frac{\varphi}{2}\right) \sin\left(\frac{3\varphi}{2}\right)\right], \\ \sigma_{yy} &= \frac{K_I}{\sqrt{2\pi r}} \cos\left(\frac{\varphi}{2}\right) \left[1 + \sin\left(\frac{\varphi}{2}\right) \sin\left(\frac{3\varphi}{2}\right)\right], \\ \tau_{xy} &= \frac{K_I}{\sqrt{2\pi r}} \cos\left(\frac{\varphi}{2}\right) \sin\left(\frac{\varphi}{2}\right) \cos\left(\frac{3\varphi}{2}\right),\end{aligned}\tag{4.10}$$

where $y = r \sin \varphi = 2r \sin\left(\frac{\varphi}{2}\right) \cos\left(\frac{\varphi}{2}\right)$.

The displacements at the crack-tip are obtained by following the same procedure (cf. **Appendix B**)

$$\begin{aligned}u_x &= \frac{K_I}{8\mu\pi} \sqrt{2\pi r} \left[(2\kappa - 1) \cos\left(\frac{\varphi}{2}\right) - \cos\left(\frac{3\varphi}{2}\right)\right], \\ u_y &= \frac{K_I}{8\mu\pi} \sqrt{2\pi r} \left[(2\kappa + 1) \sin\left(\frac{\varphi}{2}\right) - \sin\left(\frac{3\varphi}{2}\right)\right],\end{aligned}\tag{4.11}$$

where for the plane strain, κ and σ_{zz} are defined by

$$\kappa = 3 - 4\nu, \quad \sigma_{zz} = \nu(\sigma_{xx} + \sigma_{yy}),\tag{4.12}$$

and for the plane stress, they are defined by

$$\kappa = (3 - \nu)/(1 + \nu), \quad \sigma_{zz} = 0,\tag{4.13}$$

where μ denotes the shear modulus.

With (4.10) and (4.11) stresses and displacements at the crack-tip for mode I have been derived. These equations are valid for any cracked body under mode I, where if the stress σ_{yy} is known, the stress intensity factor for mode I can be obtained as

$$K_I = \lim_{r \rightarrow 0} \sqrt{2\pi r} \sigma_{yy}(\varphi = 0).\tag{4.14}$$

Since the approach is analogous for the other two modes only the end results are given in the following. During mode II the stresses near the crack-tip are defined by [37, 70, 71]

$$\begin{aligned}\sigma_{xx} &= -\frac{K_{II}}{\sqrt{2\pi r}} \sin\left(\frac{\varphi}{2}\right) \left[2 + \cos\left(\frac{\varphi}{2}\right) \cos\left(\frac{3\varphi}{2}\right)\right], \\ \sigma_{yy} &= \frac{K_{II}}{\sqrt{2\pi r}} \sin\left(\frac{\varphi}{2}\right) \cos\left(\frac{\varphi}{2}\right) \cos\left(\frac{3\varphi}{2}\right), \\ \tau_{xy} &= \frac{K_{II}}{\sqrt{2\pi r}} \cos\left(\frac{\varphi}{2}\right) \left[1 - \sin\left(\frac{\varphi}{2}\right) \sin\left(\frac{3\varphi}{2}\right)\right],\end{aligned}\tag{4.15}$$

and the displacements by

$$\begin{aligned}u_x &= \frac{K_{II}}{8\mu\pi} \sqrt{2\pi r} \left[(2\kappa + 3) \sin\left(\frac{\varphi}{2}\right) + \sin\left(\frac{3\varphi}{2}\right)\right], \\ u_y &= -\frac{K_{II}}{8\mu\pi} \sqrt{2\pi r} \left[(2\kappa - 3) \cos\left(\frac{\varphi}{2}\right) + \cos\left(\frac{3\varphi}{2}\right)\right].\end{aligned}\tag{4.16}$$

If the stress τ_{xy} is known the stress intensity factor for mode II can be obtained as:

$$K_{II} = \lim_{r \rightarrow 0} \sqrt{2\pi r} \tau_{xy}(\varphi = 0).\tag{4.17}$$

For mode III the stresses near the crack-tip are

$$\begin{aligned}\tau_{yz} &= \frac{K_{\text{III}}}{\sqrt{2\pi r}} \cos\left(\frac{\varphi}{2}\right), \\ \tau_{xz} &= -\frac{K_{\text{III}}}{\sqrt{2\pi r}} \sin\left(\frac{\varphi}{2}\right),\end{aligned}\tag{4.18}$$

and the corresponding displacement is

$$u_z = \sqrt{\frac{2}{\pi}} \frac{K_{\text{III}}}{\mu} \sqrt{r} \sin\left(\frac{\varphi}{2}\right).\tag{4.19}$$

Also here a stress intensity factor can be derived if the stress τ_{yz} is known

$$K_{\text{III}} = \lim_{r \rightarrow 0} \sqrt{2\pi r} \tau_{yz}(\varphi = 0).\tag{4.20}$$

4.1.2 Delamination

In this section the fundamental equations required to describe cracks in the interface between two materials with different material properties, also referred to as delamination, are given. The reported theory is based on [37, 70].

The concept of the intensity factor K , described in the previously section, cannot be easily applied, because the crack-tip in the case of delamination field has a different form compared to a crack in a single homogeneous material.

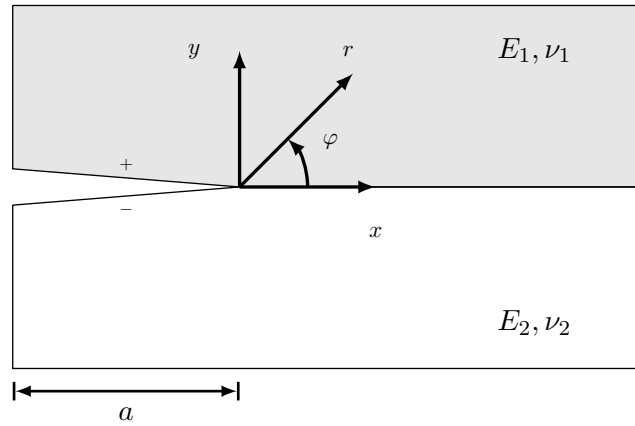


Figure 4.3: Tip of a bimaterial crack.

Delamination is illustrated in **Figure 4.3**. A bimaterial crack lies at the interface between two materials with elastic constants E_1, ν_1 and E_2, ν_2 . This particular problem is analyzed by using an eigenfunction expansion method [37, 70]. For the description of the crack-tip field, a plane strain condition is considered, the complex variable method is employed (cf. **Appendix A**), and polar coordinates at the crack-tip are defined. The first boundary condition of the problem is that the crack surfaces ($\varphi = \pm\pi$) are traction-free

$$\begin{aligned}(\sigma_{\varphi\varphi})_1 &= 0 \quad \text{for } \varphi = \pi, \\ (\sigma_{r\varphi})_1 &= 0 \quad \text{for } \varphi = \pi, \\ (\sigma_{\varphi\varphi})_2 &= 0 \quad \text{for } \varphi = -\pi, \\ (\sigma_{r\varphi})_2 &= 0 \quad \text{for } \varphi = -\pi.\end{aligned}\tag{4.21}$$

The second boundary condition is the continuity of the stress field and the displacement field at the interface ($\varphi = 0$)

$$\begin{aligned}(\sigma_{\varphi\varphi})_1 &= (\sigma_{\varphi\varphi})_2 & \text{for } \varphi = 0, \\(\sigma_{r\varphi})_1 &= (\sigma_{r\varphi})_2 & \text{for } \varphi = 0, \\(u_r)_1 &= (u_r)_2 & \text{for } \varphi = 0, \\(u_\varphi)_1 &= (u_\varphi)_2 & \text{for } \varphi = 0.\end{aligned}\tag{4.22}$$

These boundary conditions represent a system of equations where a general solution has to be obtained. One possible approach is to describe the problem through the Airy stress function ϕ for Material 1 and for Material 2. The Airy stress function satisfies the equilibrium equations (2.43) and therefore the compatibility equation (2.45) is given as

$$\nabla^2 \nabla^2 \phi_j = 0 \quad \text{where } j = 1, 2\tag{4.23}$$

with the Nabla operator ∇^2 defined as

$$\nabla^2 = \frac{\partial^2}{\partial r^2} + \frac{1}{r} \frac{\partial}{\partial r} + \frac{1}{r^2} \frac{\partial^2}{\partial \varphi^2}.\tag{4.24}$$

To obtain the solution of the boundary conditions the variables of the stress function have to be separated in the following way

$$\phi_j = r^{\lambda+1} F_j(\varphi) \quad \text{where } j = 1, 2,\tag{4.25}$$

where λ is the eigenvalue to be determined and $F_j(\varphi)$ are the eigenfunctions of the biharmonic operator in (4.23) [70].

If we insert (4.25) into (4.23), we obtain

$$\frac{d^4 F_j(\varphi)}{d\varphi^4} + 2(\lambda^2 + 1) \frac{d^2 F_j(\varphi)}{d\varphi^2} + (\lambda^2 - 1)^2 F_j(\varphi) = 0, \quad j = 1, 2,\tag{4.26}$$

where the solution of the differential equations (4.23) can be obtained by using an Ansatz leading to [72]

$$F_j(\varphi) = a_j \sin(\lambda+1)\varphi + b_j \cos(\lambda+1)\varphi + c_j \sin(\lambda-1)\varphi + d_j \cos(\lambda-1)\varphi, \quad j = 1, 2\tag{4.27}$$

where a_j, b_j, c_j, d_j are unknown constants.

By using (4.25) and the Airy stress in polar coordinates [70], the stress components are described by

$$\begin{aligned}(\sigma_{rr})_j &= \frac{1}{r^2} \frac{\partial^2 \phi_j}{\partial \varphi^2} + \frac{1}{r} \frac{\partial \phi_j}{\partial r} = r^{\lambda-1} \left[F_j''(\varphi) + (\lambda+1)F_j(\varphi) \right], \\(\sigma_{\varphi\varphi})_j &= \frac{\partial^2 \phi_j}{\partial r^2} = r^{\lambda-1} \lambda(\lambda+1)F_j(\varphi), \\(\sigma_{r\varphi})_j &= -\frac{1}{r} \frac{\partial^2 \phi_j}{\partial r \partial \varphi} + \frac{1}{r^2} \frac{\partial \phi_j}{\partial \varphi} = -\lambda r^{\lambda-1} F_j'(\varphi),\end{aligned}\tag{4.28}$$

and the displacements in polar coordinates [70] by

$$\begin{aligned}(u_r)_j &= \frac{1}{2\mu_j} r^\lambda \{ -(\lambda+1)F_j(\varphi) + (1+\kappa_j)[c_j \sin(\lambda-1)\varphi + d_j \cos(\lambda-1)\varphi] \}, \\(u_\varphi)_j &= \frac{1}{2\mu_j} r^\lambda \{ -F_j'(\varphi) - (1+\kappa_j)[c_j \cos(\lambda-1)\varphi - d_j \sin(\lambda-1)\varphi] \}.\end{aligned}\tag{4.29}$$

Equations (4.28) and (4.29) are further plugged into the boundary conditions (4.21) and (4.22)

$$\begin{aligned}
a_1 \sin(\lambda + 1)\pi + b_1 \cos(\lambda + 1)\pi + c_1 \sin(\lambda - 1)\pi + d_1 \cos(\lambda - 1)\pi &= 0, \\
-a_2 \sin(\lambda + 1)\pi + b_2 \cos(\lambda + 1)\pi - c_2 \sin(\lambda - 1)\pi + d_2 \cos(\lambda - 1)\pi &= 0, \\
a_1(\lambda + 1) \cos(\lambda + 1)\pi - b_1(\lambda + 1) \sin(\lambda + 1)\pi \\
+c_1(\lambda - 1) \cos(\lambda - 1)\pi - d_1(\lambda - 1) \sin(\lambda - 1)\pi &= 0, \\
a_2(\lambda + 1) \cos(\lambda + 1)\pi + b_2(\lambda + 1) \sin(\lambda + 1)\pi \\
+c_2(\lambda - 1) \cos(\lambda - 1)\pi + d_2(\lambda - 1) \sin(\lambda - 1)\pi &= 0, \\
b_1 + d_1 &= b_2 + d_2, \\
a_1(\lambda + 1) + c_1(\lambda - 1) &= a_2(\lambda + 1) + c_2(\lambda - 1), \\
(1 + \kappa_1)c_1 &= \frac{\mu_1}{\mu_2}(1 + \kappa_2)c_2 + \left(\frac{\mu_1}{\mu_2} - 1\right) [(\lambda + 1)a_2 + (\lambda - 1)c_2], \\
(1 + \kappa_1)d_1 &= \frac{\mu_1}{\mu_2}(1 + \kappa_2)d_2 - \left(\frac{\mu_1}{\mu_2} - 1\right) (\lambda + 1)[b_2 + d_2].
\end{aligned} \tag{4.30}$$

A non-trivial solution of the system of equations (4.30) for the unknown coefficients a_j, b_j, c_j , and d_j exists if the determinant of the system 8×8 vanishes. The solution of the system of equations leads to

$$\cot^2 \lambda \pi + \left[\frac{\frac{\mu_1}{\mu_2}(1 + \kappa_2) - (1 + \kappa_1) - 2\left(\frac{\mu_1}{\mu_2} - 1\right)}{\frac{\mu_1}{\mu_2}(1 + \kappa_2) + (1 + \kappa_1)} \right]^2 = 0, \tag{4.31}$$

where this equation only has complex solutions for λ (real solution results only if a homogeneous material is considered Material 1 = Material 2). Therefore a physically solution [70] is obtained for the set of eigenvalues:

$$\begin{aligned}
\lambda_{n-} &= (n - 1/2) - i\varepsilon \\
\lambda_{n+} &= (n + 1/2) + i\varepsilon \quad n = 0, 1, 2, \dots
\end{aligned} \tag{4.32}$$

where

$$\varepsilon = \frac{1}{2\pi} \ln \frac{\mu_2 \kappa_1 + \mu_1}{\mu_1 \kappa_2 + \mu_2}, \tag{4.33}$$

with $\mu_i = E_i/2(1 + \nu_i)$, $\kappa_i = 3 - 4\nu_i$ and ε the bimaterial constant.

The field which dominates as $r \rightarrow 0$ (forming a singularity of the stress at the crack-tip) corresponds to the eigenvalue with the smallest real part

$$\lambda = 1/2 + i\varepsilon. \tag{4.34}$$

Taking into account

$$r^{i\varepsilon} = e^{i\varepsilon \ln r} = \cos(\varepsilon \ln r) + i \sin(\varepsilon \ln r), \tag{4.35}$$

and using (4.28) and (4.29), and considering (4.34) the stresses and displacements can be approximated to

$$\sigma_{rr}, \sigma_{\theta\theta}, \sigma_{r\theta} \sim r^{-1/2} [\cos(\varepsilon \ln r) + i \sin(\varepsilon \ln r)], \quad u_r, u_\theta \sim r^{1/2} [\cos(\varepsilon \ln r) + i \sin(\varepsilon \ln r)]. \tag{4.36}$$

It is clear that the typical $1/\sqrt{r}$ -type singular behavior for the stresses and the displacements is present at the bimaterial crack-tip. Unlike for a homogeneous body, these quantities oscillate, with increasing amplitude, while approaching the crack-tip.

The crack tip stresses (in Cartesian coordinates) can be expressed by introducing the stress intensity factors [37, 73] as:

$$\begin{aligned}
(\sigma_{yy} + i\tau_{xy})_{\varphi=0} &= \frac{K(r/2a)^{i\varepsilon}}{\sqrt{2\pi r}}, \\
(u_y^+ - u_y^-) + i(u_x^+ - u_x^-) &= \frac{c_1 + c_2}{2 \cosh \pi \varepsilon} \frac{K(r/2a)^{i\varepsilon}}{1 + 2i\varepsilon} \sqrt{\frac{r}{2\pi}},
\end{aligned} \tag{4.37}$$

where $2a$ indicates an arbitrary reference crack length, the sign $+$ and $-$ are the upper and lower surface of the crack tip, respectively (**Figure 4.3**), and K is the stress intensity factor which can be separated in a real and an imaginary part:

$$K = K_1 + iK_2, \quad (4.38)$$

and

$$c_1 = (1 + \kappa_1)/\mu_1, \quad c_2 = (1 + \kappa_2)/\mu_2. \quad (4.39)$$

The stress intensity factors and the length $2a$ are weighted by the material constant ε and therefore a decomposition into purely mode I and mode II is not possible. This can be seen if using relation (4.35) we write the stresses at the interface from (4.37) in the following form

$$\begin{aligned} \sigma_{yy} &= \frac{1}{\sqrt{2\pi r}} \{K_1 \cos[\varepsilon \ln(r/2a)] - K_2 \sin[\varepsilon \ln(r/2a)]\}, \\ \tau_{xy} &= \frac{1}{\sqrt{2\pi r}} \{K_1 \cos[\varepsilon \ln(r/2a)] + K_2 \sin[\varepsilon \ln(r/2a)]\}. \end{aligned} \quad (4.40)$$

The stress intensity factor K_1 is associated with the normal and the shear stresses in the interface, which is also true for K_2 since during delamination both modes are inseparably connected to each other. In the homogeneous material case K_1 and K_2 correspond to K_I and K_{II} , respectively.

4.2 Energy Release Rate

The energy release rate G is a fundamental concept in fracture mechanics [37, 70, 71]. This quantity is the released energy $d\Pi$ during an infinitesimally small crack advance dA (A indicates a crack area in 3D and a crack length in 2D)

$$G = -\frac{d\Pi}{dA}. \quad (4.41)$$

The total potential energy Π is composed of the strain energy U and the potential of external forces V

$$\Pi = U + V, \quad (4.42)$$

where U is defined by

$$U = \int_{A_0} W dA, \quad (4.43)$$

where A_0 is the initial area of the crack. V is defined by

$$V = - \int_{\Gamma_t} T_i u_i d\Gamma. \quad (4.44)$$

W in (4.43) is the strain energy density given by

$$W = \int_0^{\varepsilon_{kl}} \sigma_{ij} d\varepsilon_{ij}, \quad (4.45)$$

where σ_{ij} denotes the components of the stress tensor and ε_{ij} the components of the strain tensor [74]. In (4.44) T_i indicates a prescribed traction on Γ_t and u_i the corresponding displacements (cf. **Figure 4.4**). If the body is not subjected to external tractions the potential energy is equal to the strain energy $\Pi = U$.

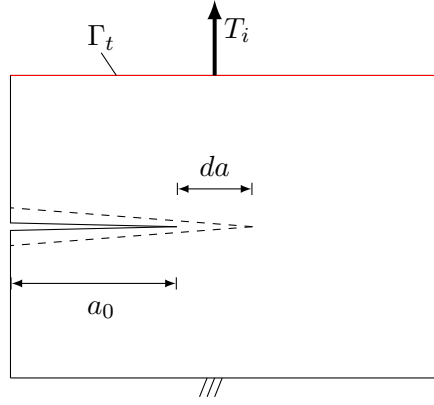


Figure 4.4: Example of crack advance in two-dimensional.

In two-dimensional problems, $d\Pi$ is related to the crack extension and therefore by considering an infinitesimally small crack extension da , G is defined by

$$G = -\frac{d\Pi}{da}. \quad (4.46)$$

For a homogeneous material and assuming the linear elastic case G can be expressed in terms of stress intensity factors, where G can describe a single mode or a combination of modes.

We derive G for mode I (cf. **Figure 4.1** (a)), where the stress before the crack elongates is given by σ_{yy} and the displacement after the crack has elongated is given by u_y along $y = 0$. The strain energy generated over an increment of crack extension of length Δa is given by

$$-2 \int_0^{\Delta a} \frac{1}{2} \sigma_{yy} u_y dx = \left(\frac{d\Pi}{da} \right) \Delta a, \quad (4.47)$$

where the minus sign indicates that the stresses and displacements act in opposite directions during relaxation and the factor of 2 refers to the two crack surfaces. By using the definition of G (cf. (4.46)) and by considering a crack extension of a small length Δa in the limit $\Delta a \rightarrow 0$, the energy release rate for mode I is calculated

$$G = -\frac{d\Pi}{da} = \lim_{\Delta a \rightarrow 0} \frac{2}{\Delta a} \int_0^{\Delta a} \frac{1}{2} \sigma_{yy} u_y dx. \quad (4.48)$$

In the current problem, (4.6) is employed to describe the stress and displacement of interest

$$\begin{aligned} \sigma_{yy} &= \text{Re}\{Z_I\} = \frac{K_I}{\sqrt{2\pi x}} \quad \text{for } x > 0, y = 0, \\ u_y &= \frac{2}{E} \text{Im}\{\overline{Z_I}\} = \frac{2}{E} \text{Im}\left\{ \frac{2K_I \sqrt{z}}{\sqrt{2\pi}} \right\} \quad \text{along } y = 0. \end{aligned} \quad (4.49)$$

It is necessary to consider the displacement of interest which corresponds to the new crack length. Therefore $x = \Delta a$ and $z = -(x - \Delta a) + iy, y = 0$; therefore, the displacement of interest is

$$u_y = \frac{2}{E} \text{Im}\left\{ \frac{2K_I \sqrt{-(\Delta a - x)}}{\sqrt{2\pi}} \right\} = \frac{4K_I \sqrt{\Delta a - x}}{E \sqrt{2\pi}}. \quad (4.50)$$

By plugging the stress (4.49) and the displacement (4.50) into (4.48) G can be obtained

$$\begin{aligned} G &= \frac{K_I^2}{E} && \text{plane stress,} \\ G &= \frac{(1-\nu^2)K_I^2}{E} && \text{plane strain.} \end{aligned} \quad (4.51)$$

For modes II and III the same derivation can be carried out, leading to

$$G = \frac{\kappa + 1}{8\mu} K_{II}^2, \quad (4.52)$$

for mode II and to

$$G = \frac{1}{2\mu} K_{III}^2, \quad (4.53)$$

for mode III. If a general crack loading is taken in consideration, all three modes are present and G is described by

$$G = \frac{(1-\nu^2)}{E} (K_I^2 + K_{II}^2) + \frac{1}{2\mu} K_{III}^2. \quad (4.54)$$

For delamination, G can be derived by applying the same approach resulting in

$$G = \frac{(c_1 + c_2)(K_1^2 + K_2^2)}{16 \cosh^2(\pi\varepsilon)}, \quad (4.55)$$

where c_1 and c_2 are described by (4.39), and ε by (4.33). Here G is uniquely determined by both stress intensity factors K_1 and K_2 .

4.2.1 Failure Criterion

During the fracture process new surfaces are generated [37, 71]. During the crack process the material is separated along the fracture surface dA , which can be divided into the upper dA^+ and lower dA^- surface of the crack. During the creation of a crack expansion of dA , the energy required to generate the fracture is given by $d\Gamma$. During the material separation due to cracking $d\Gamma$ is given by

$$d\Gamma = 2\gamma dA, \quad (4.56)$$

where γ is the fracture surface energy usually considered to be constant and the factor of 2 stands for the two surfaces of the crack.

If we consider a quasi static fracture process of an elastic body the balance of the energy in play reads

$$\frac{d\Pi}{dA} + \frac{d\Gamma}{dA} = 0, \quad (4.57)$$

thus during the fracture process the change of the potential Π due to an external or internal force and the fracture energy Γ sum up to zero. Using (4.56) and (4.41) we can write

$$G = G_c \quad (4.58)$$

with $G_c = 2\gamma$. Expression (4.58) can be understood as a condition for crack propagation. If the released energy is equal to the energy needed for the fracture process the crack will advance. This fracture criterion is known as *Griffith's fracture criterion* [69] and it is

applicable for homogeneous materials. For the relation between G and K_i (i indicates the crack mode) this criterion can be used for any combination of crack modes.

The fracture criterion can also be described for bimaterial cracks. In **Section 4.1.2** it was shown that during delamination mode I and mode II always act together. G depends on K_1 and K_2 and therefore the fracture criterion is based on both modes. The phase angle Ψ of the mixed mode characterizes G ; therefore, the fracture criterion is described as

$$G(\Psi) = G_c^{(i)}(\Psi) \quad \tan \Psi = \frac{K_{II}}{K_I}. \quad (4.59)$$

The term $G_c^{(i)}(\Psi)$ is the fracture toughness and is a function of the phase angle Ψ . The fracture resistance of the interface has to be experimentally measured.

4.3 Energy Release Rate Calculation

The evaluation of the energy release rate G can be used to predict the crack or delamination propagation. In this section the various procedures to calculate G are described. These methodologies are then applied to the TSV structure in **Section 4.4** and **Section 4.5**.

4.3.1 J -Integral

In linear fracture mechanics the value G can be obtained by applying the J -Integral method [74, 75, 76].

The value of the J -Integral is equal to the energy which is dissipated by the fracture. The J -Integral method is applicable for systems obeying linear-elastic fracture mechanics as well as for materials with an inelastic behavior. The J -Integral is evaluated along a path Γ around the crack-tip of the cracked body. The path can be arbitrary chosen as long as the crack-tip is inside the region surrounded by the path [76].

The definition of the J -Integral is given by

$$J = \int_{\Gamma} \left(W dy - T_i \frac{\partial u_i}{\partial x} ds \right) = \int_{\Gamma} \left(W n_x - T_i \frac{\partial u_i}{\partial x} \right) ds, \quad (4.60)$$

where W is the strain energy density, T_i are the components of the traction vector, u_i are the components of the displacement vector, and n_i are the components of the unit vector perpendicular to the integration path (**Figure 4.5**). The strain energy density is the work per unit volume done during the elastic deformation of a material and is defined by (4.45).

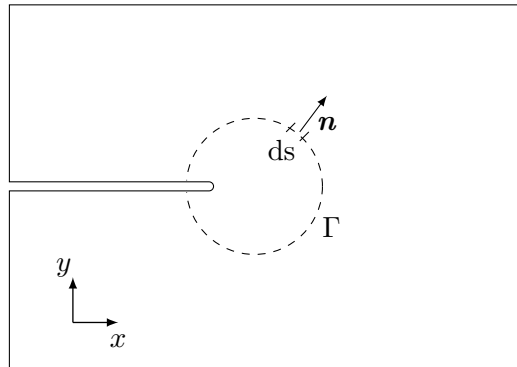


Figure 4.5: A possible (arbitrary) path around the crack-tip for the J -integral.

For linear elastic materials, introducing (2.37) into (4.45), W is defined by

$$W = \frac{1}{2} \sigma_{ij} \varepsilon_{ij}. \quad (4.61)$$

The traction vector is defined by

$$T_i = \sigma_{ij} n_j. \quad (4.62)$$

Considering a straight bond line, the standard J -Integral, primarily developed for problems of single homogeneous materials, can also be applied to bi-material interfaces [37, 76].

4.3.2 Regression Analysis

The energy release rate G can be calculated by determining the values K_1 and K_2 from (4.55). These values are obtained by regression analysis fitting. Regression analysis permits to obtain unknown parameters by employing fitting functions. One of the most common approaches is the least squares method, where through the minimization of the sum of squared residuals (residual is the difference between an observed value and the fitted value provided by a model) the fitting parameters can be obtained [77].

The stress intensity factors are obtainable by using the stress at the head of the right side of the crack-tip (cf. **Figure 4.3**) which is described by (4.40). The equation for σ_{yy} is multiplied by $\cos[\varepsilon \ln(r/2a)]$ and added to the equation for τ_{xy} previously multiplied by $\sin[\varepsilon \ln(r/2a)]$ [78]. The resulting equation is denoted as σ_1 and represents the combined stress

$$\sigma_1 = \sigma_{yy} \cos[\varepsilon \ln(r/2a)] + \tau_{xy} \sin[\varepsilon \ln(r/2a)] = \frac{K_1}{\sqrt{2\pi r}}. \quad (4.63)$$

An additional combined stress σ_2 can be obtained by multiplying τ_{xy} with $\cos[\varepsilon \ln(r/2a)]$. An addition to the product of σ_{yy} and $\sin[\varepsilon \ln(r/2a)]$ leads to

$$\sigma_2 = -\sigma_{yy} \cos[\varepsilon \ln(r/2a)] + \tau_{xy} \sin[\varepsilon \ln(r/2a)] = \frac{K_2}{\sqrt{2\pi r}}. \quad (4.64)$$

The values σ_1 and σ_2 can be calculated using σ_{yy} and τ_{xy} , which can be obtained from FEM simulations. The stress intensity factors K_1 and K_2 are calculated by a regression of σ_1 versus r and σ_2 versus r [68, 78]. The values K_1 and K_2 can be further used to calculate G using (4.55).

4.4 Delamination Prediction at TSV Bottom

In this section the J -Integral method was employed to predict delamination failure at the TSV bottom. The study was carried out by means of simulation, which is based on the evaluation of the J -Integral at different interfaces. These simulations enable the determination of the structures with the lowest failure probability.

The study of delamination in TSVs is necessary, because the delamination can increase the probability of cracking or corrosion of the conducting layer (W) or lead to rupture of sidewall oxide isolation. To limit these problems different factors were analyzed to understand how they can influence delamination, and the mechanical stability of the device.

4.4.1 Studied System

The existence of mechanical stress can be sufficient to degrade the performance and to induce crack or delamination in the TSVs [79]. In **Section 3** the critical areas where a mechanical failure of the TSV can be assumed were found. One of these areas is the bottom of the TSV sidewall which consists of various interfaces between different material films with different thicknesses and mechanical properties. At these interfaces the possibility of delamination leading to failure of the device needs to be considered.

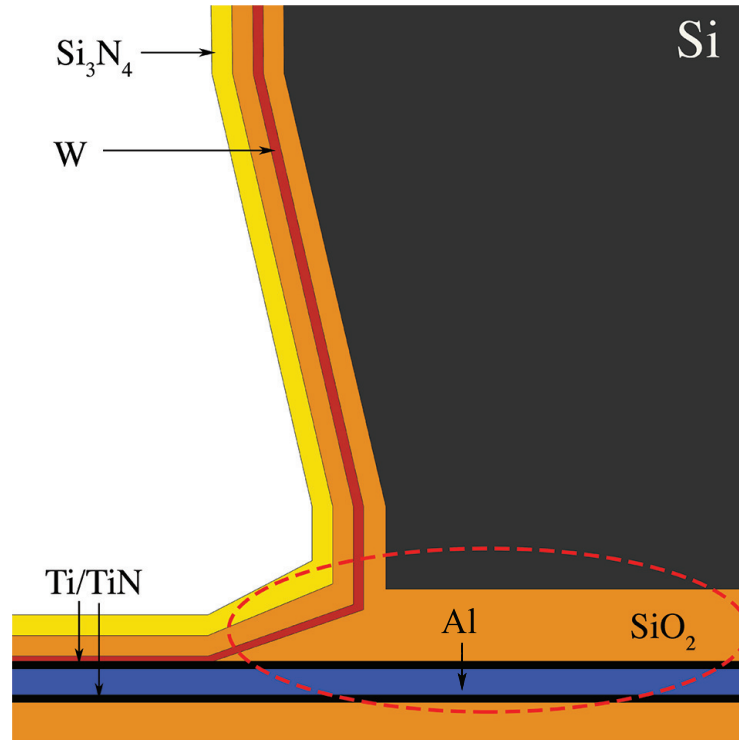


Figure 4.6: Schematic of the Open TSV geometry under consideration. The open TSV is integrated in the silicon of the wafer. The alternating layers with different thickness are located at the bottom. There are the interfaces where a failure of the device due to delamination is expected.

Figure 4.6 depicts the open TSV studied [29, 80, 81]. Different factors such as the residual stress of the films, the film thicknesses, and the external forces influence the failure of the device. By analyzing these factors the critical mechanical and geometrical conditions which influence G , and thereby the probability of delamination, can be studied.

4.4.2 Approach

The energy release rate G was calculated for the different interfaces at the bottom of the TSV by using COMSOL Multiphysics [62]. Considering the bottom of an open TSV as free to bend, cracking or delamination of the layers has to be expected under the sidewall (cf. red circled region **Figure 4.6**).

Two-dimensional simulations for the structure shown in **Figure 4.7** were carried out. All the layers have a length w of 20 μm and the thicknesses of the layers were varied according to the values given in **Table 4.1**.

All the materials were assumed to be linear elastic and isotropic. The failure of the interconnection in the area under the sidewall was studied; therefore, the top layer of the

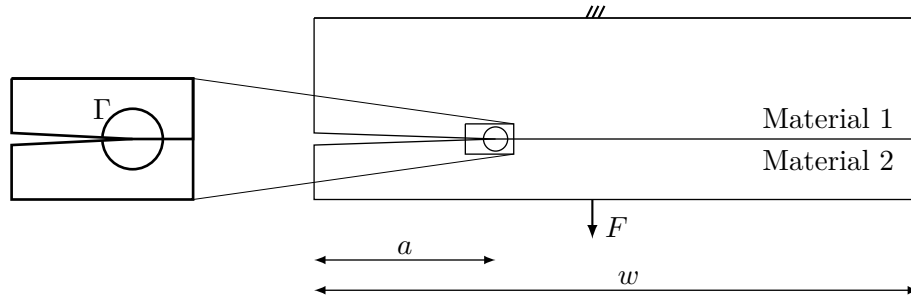


Figure 4.7: Schematic representation of the studied system. In the inset the path Γ for the J integral calculation is shown. The variable a indicates the crack length and w the width of the layer.

simulation space was assumed mechanically fixed as the sidewall of the TSV was fixed. Furthermore, a downward force was applied on the bottom of the system and the bottom of the TSV was considered free to bend (cf. **Figure 4.7**). The simulations were started with a small initial crack length a and gradually increased until a predefined value was reached.

The four interface systems found in the open TSV are Ti/Al, SiO₂/TiN, SiO₂/W, and Si/SiO₂. For the prediction of failure due to delamination, the values G are compared to critical values G_c taken from [82, 83, 84, 85] and showed in the **Table 4.2**.

Calculations were carried out for different ratios of crack length a and layer width w . All simulations start with a crack of length 0.5 μm which was gradually increased by steps of 0.5 μm until 3 μm was reached.

By varying the following factors their influence on G was investigated:

- **Residual stress:** The stress was simulated by adding an initial stress in each considered layer. It was introduced by setting σ_{xx} and σ_{yy} to the assumed stress values. The residual stress in the layer is due to the combination of the film deposition process and thermal processes. Small changes in residual stress influence the value of G .
- **Thicknesses of the layers:** The thickness of the layers influence G and different values were employed to find the critical condition for the delamination.
- **External force:** It can represent extra mechanical stress during the fabrication processes (for example, during bonding between dies or between the interposer layer and die [14]), or an accidental load, for example due to the presence of dust particles.

Layer	Ti/TiN	SiO ₂	Al	W	Si
Thickness (μm)	0.05-0.2	0.3-1.4	0.3-0.6	0.04-0.16	5

Table 4.1: Thickness of layers employed.

Interface	SiO ₂ /TiN	Si/SiO ₂	SiO ₂ /W
G_c (J/m ²)	1.9	1.8	0.2-0.5

Table 4.2: Critical values G_c for the considered interface.

G was calculated by employing the J -Integral method (**Section 4.3.1**) where the integral path Γ is displayed in **Figure 4.7**. Because the experimental critical values of G_c found in literature have a larger range of phase angles Ψ and because the main mode which acts in the considered structure is unknown, only G was evaluated in this study, without investigate the value of Ψ . Therefore, the failure prediction is made by comparing G from the simulations with G_c .

4.4.3 Results

In all the plots shown (**Figures 4.8-4.23**), the x -axis represents the ratio a/w , the y -axis the considered factors, and the z -axis the calculated G . For the residual stress and thickness analyses a downward force of 110 mN was applied (F in **Figure 4.7**).

4.4.3.1 Residual Stress Analysis

In **Figure 4.8** the G values for the interface between Ti and Al are plotted. The initial stress in the Al was assumed to be compressive. Inside the Ti a constant compressive initial stress σ_{Ti} of 50 MPa was used. For the Ti a thickness h_{Ti} of 0.15 μm and for the Al a thickness h_{Al} of 0.5 μm were set. The effect of the ratio a/w on G is small compared to the influence of the initial stress. This shows that the probability of a failure is effectively reduced by a decrease in the initial stress in the Al layer.

Figure 4.9 depicts the G value for an interface between Ti and Al where the initial stress in the Ti was varied. For the Ti a thickness h_{Ti} of 0.15 μm and for the Al a thickness h_{Al} of 0.5 μm were set. A compressive stress σ_{Al} of 100 MPa was set in the Al layer. A reduction in the initial stress in Ti leads to an increase in the energy release rate; therefore, in contrast to **Figure 4.8** the decrease in the initial stress in the Ti layer can lead to a delamination propagation. The increase of the crack length does not significantly influence G . For this interface no value of G_c to compare with our values were available in literature. Nevertheless the G values are very small thus we can assume no delamination failure for this interface.

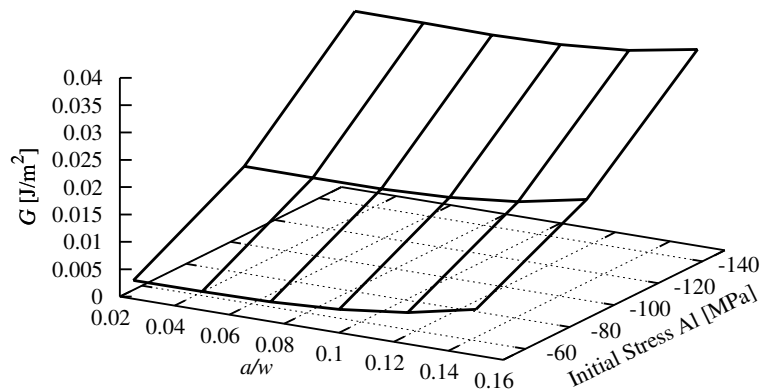


Figure 4.8: The energy release rate G for different initial stresses (Al) and crack lengths in the interface Ti/Al. Simulation conditions were $\sigma_{Ti} = -50$ MPa, $h_{Ti} = 0.15$ μm , and $h_{Al} = 0.5$ μm .

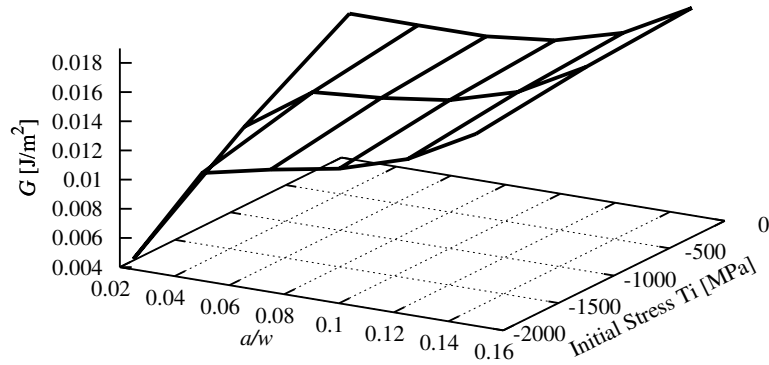


Figure 4.9: The energy release rate G for different initial stresses (T_i) and crack lengths in the interface Ti/Al. Simulation conditions were $\sigma_{Al}=-100$ MPa, $h_{Ti}=0.15$ μm , and $h_{Al}=0.5$ μm .

Figure 4.10 shows the behavior of G at the interface between Si and SiO₂. Thicknesses of 5 μm and 1.4 μm for Si (h_{Si}) and SiO₂ (h_{SiO_2}) were used, respectively. The critical value G_c was found to be 1.8 J/m^2 [83]. All the points are far below the critical value. A slight decrease of G with an increase of the crack length is observable. This shows the stability of this interface for every crack length and for every initial stress in the SiO₂ layer.

The behavior of G at the SiO₂/W interface is shown in **Figure 4.11** for thicknesses of 0.4 μm and 0.1 μm for the SiO₂ (h_{SiO_2}) and the W (h_W) layers, respectively. In the SiO₂ an initial compressive stress σ_{SiO_2} of 100 MPa was assumed. The simulations were carried out for different tensile initial stresses in the W layer. The G_c according to [84] is in the range of 0.2-0.5 J/m^2 and therefore quite small compared to G obtained for the SiO₂/W

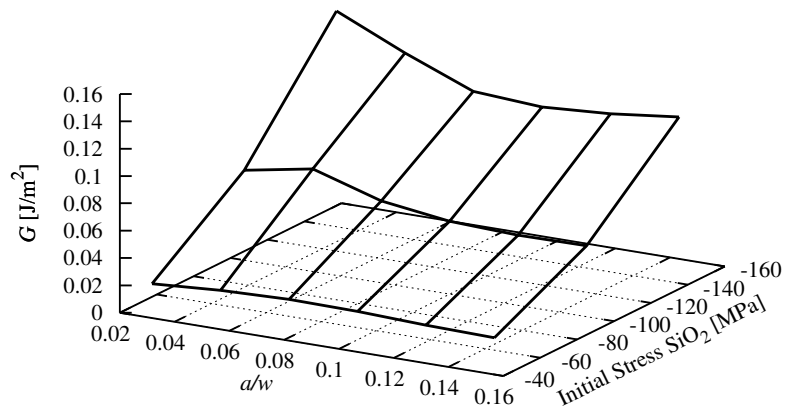


Figure 4.10: The energy release rate G for different initial stresses (SiO₂) and crack lengths in the interface Si/SiO₂. Simulation conditions were $h_{Si}=5$ μm , and $h_{SiO_2}=1.4$ μm .

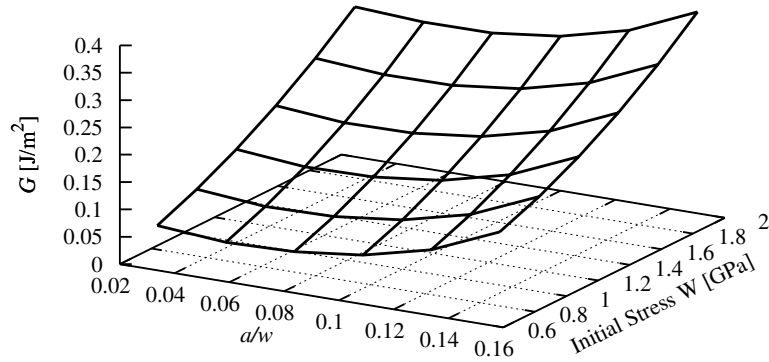


Figure 4.11: The energy release rate G for different initial stresses (W) and crack lengths in the interface SiO_2/W . Simulation conditions were $\sigma_{\text{SiO}_2}=-100$ MPa, $h_{\text{W}}=0.1$ μm and $h_{\text{SiO}_2}=0.4$ μm .

interface. For this system the influence of the a/w ratio variation is small compared to the initial stress variation. There is a constant increase in G with an increase in the initial tensile stress in the W layer. Initial stresses above 1.25 GPa will lead to delamination at all a/w ratios and therefore to the failure of the device.

In **Figure 4.12** the interface SiO_2/W was also taken in consideration. An initial tensile stress σ_{W} of 1.25 GPa and a thickness h_{W} of 0.1 μm were used for the W layer. Different initial compressive stresses in the SiO_2 using a thickness h_{SiO_2} of 0.4 μm were simulated. An increase in G is observable for increasing crack lengths a . In contrast to the behavior of G due to a varying initial stress in the W layer, here the variation of G with

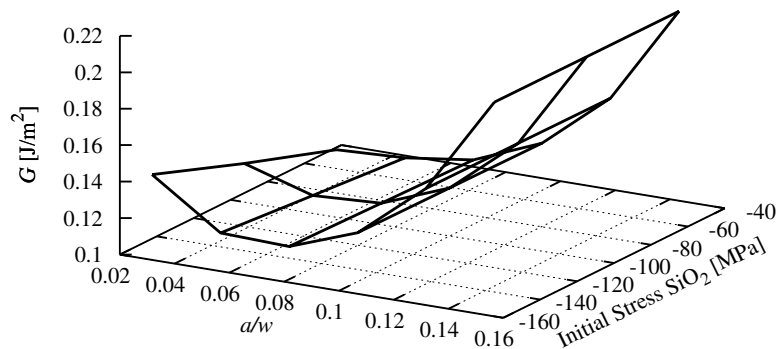


Figure 4.12: The energy release rate G for different initial stresses (SiO_2) and crack lengths in the interface SiO_2/W . Simulation conditions were $\sigma_{\text{W}}=1.25$ GPa, $h_{\text{SiO}_2}=0.4$ μm , and $h_{\text{W}}=0.1$ μm .

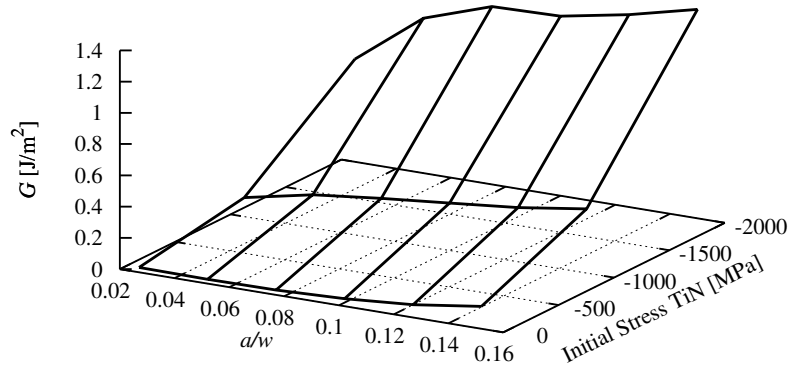


Figure 4.13: The energy release rate G for different initial stresses (TiN) and crack lengths in the interface SiO₂/TiN. Simulation conditions were $\sigma_{\text{SiO}_2} = -100$ MPa, $h_{\text{SiO}_2} = 1$ μm , and $h_{\text{TiN}} = 0.15$ μm .

respect to the variation of the initial stress in the SiO₂ is negligible. Only at high crack lengths is the modeled G value close to the critical G_c . Therefore, the main influence to the stability of this interface is connected to the crack length.

Figure 4.13 shows the behavior of G at the interface SiO₂/TiN. Here thicknesses of 1 μm and 0.15 μm for the SiO₂ (h_{SiO_2}) and TiN (h_{TiN}) were used, respectively. A compressive stress σ_{SiO_2} of 100 MPa was used for the SiO₂ layer. Critical value G_c for this interface was found to be 1.9 J/m^2 [82]. In this configuration the a/w ratio does not cause failure at the interface. The main effect which can be the cause of problems in this

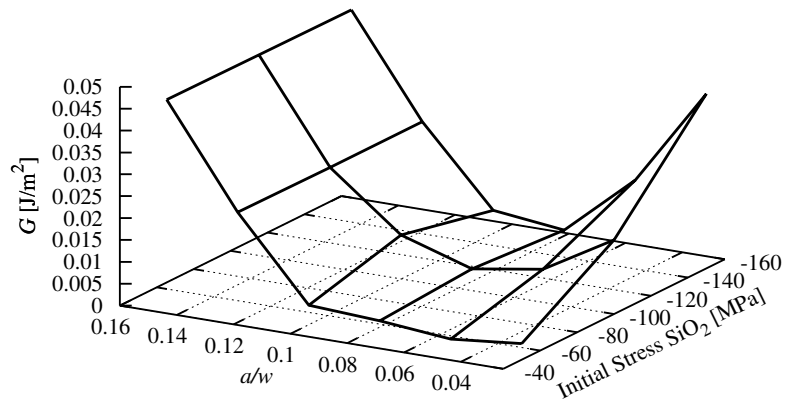


Figure 4.14: The energy release rate G for different initial stresses (SiO₂) and crack lengths in the interface SiO₂/TiN. Simulation conditions were $\sigma_{\text{TiN}} = -50$ MPa, $h_{\text{SiO}_2} = 1$ μm , and $h_{\text{TiN}} = 0.15$ μm .

interface is the initial stress in the TiN. A constant increase of G related to the initial stress can be observed.

In **Figure 4.14** the SiO₂/TiN interface was analyzed. The thickness of 1 μm for the SiO₂ (h_{SiO_2}) layer and 0.15 μm for the TiN (h_{TiN}) layer with a compressive initial stress σ_{TiN} of 50 MPa for the TiN were chosen. By varying the a/w ratio in the range 0.08 to 0.1 a minimum G at high initial stresses is found. This behavior results in a high G for short and long crack lengths. This means that the presence of a crack in the interface does not support the propagation, provided that the length of the initial crack does not exceed a certain critical value. Under the modeled variation configuration and load delamination will not occur as the values of G are below the critical value.

4.4.3.2 Thickness Analysis

In **Figures 4.15-4.19** the calculated G for different layers thicknesses is shown. In this section the influence of the layer thicknesses are investigated. The results for the SiO₂/W interface are presented in **Figure 4.15**. For the SiO₂ layer a thickness h_{SiO_2} of 0.4 μm and a compressive stress σ_{SiO_2} of 100 MPa were used. In the W layer a tensile stress σ_{W} of 1.25 GPa was applied. The effect of the W thickness is highly relevant because a high increase of G is observed at long crack lengths and small thicknesses. For large thicknesses of W the calculated G is in the range of the G_c and for this condition we can expect delamination to take place.

Figure 4.16 shows the behavior of G at the SiO₂/W interface. Here a thickness h_{W} of 0.1 μm for the W was set. A compressive stress of 100 MPa in the SiO₂ (σ_{SiO_2}) layer and a tensile stress of 1.25 GPa in the W (σ_{W}) layer were used. The thickness of the SiO₂ does not appear to have a significant influence on G and the increase in G is only attributed to the a/w ratio.

In **Figure 4.17** the results at the interface between SiO₂ and TiN for different TiN thicknesses are displayed. A layer thickness h_{SiO_2} of 1 μm and a compressive initial stress of 100 MPa for the SiO₂ (σ_{SiO_2}) and a compressive initial stress of 50 MPa in the TiN

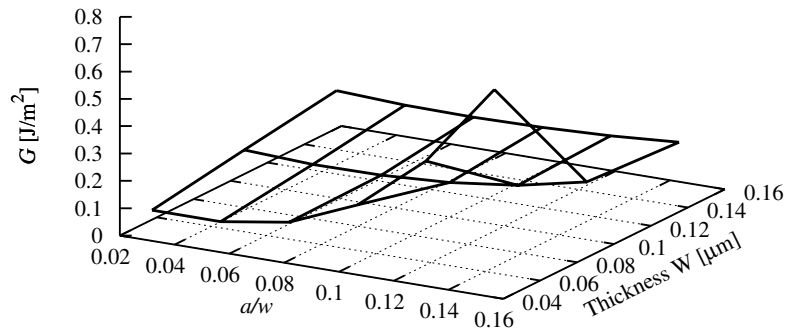


Figure 4.15: The energy release rate G for different thicknesses (W) and crack lengths in the SiO₂/W interface. Simulation conditions were $\sigma_{\text{SiO}_2}=-100$ MPa, $\sigma_{\text{W}}=1.25$ GPa, and $h_{\text{SiO}_2}=0.4$ μm .

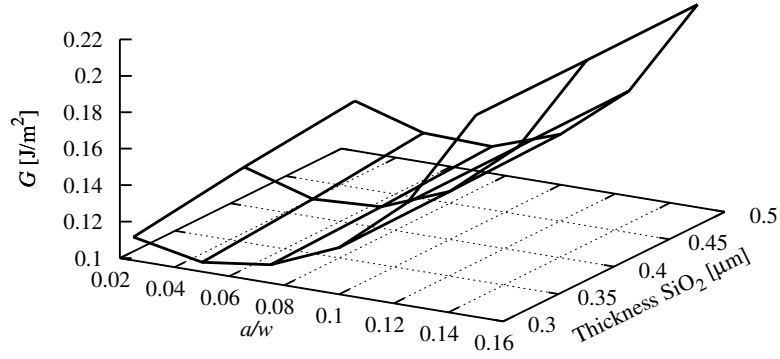


Figure 4.16: The energy release rate G for different thicknesses (SiO_2) and crack lengths in the SiO_2/W interface. Simulation conditions were $\sigma_{\text{SiO}_2}=-100$ MPa, $\sigma_{\text{W}}=1.25$ GPa, and $h_{\text{W}}=0.1$ μm .

(σ_{TiN}) were chosen. For this interface at very small thicknesses and at long crack lengths there is an important increase in G which can exceed the critical G_c of 1.9 J/m^2 [84].

In **Figure 4.18** the interface between the Ti and Al for different thicknesses were studied. A thickness h_{Ti} of 0.15 μm and a compressive initial stress σ_{Ti} of 50 MPa for the Ti was used. A compressive stress σ_{Al} of 100 MPa for the Al was chosen. The critical energy release rate for this interface is not available in literature. We can assume that the delamination will not appear because the calculated values of G are very small. A significant increase in G is noted only at small thicknesses of the Al and at high crack lengths. For the other configurations the G remains almost unchanged.

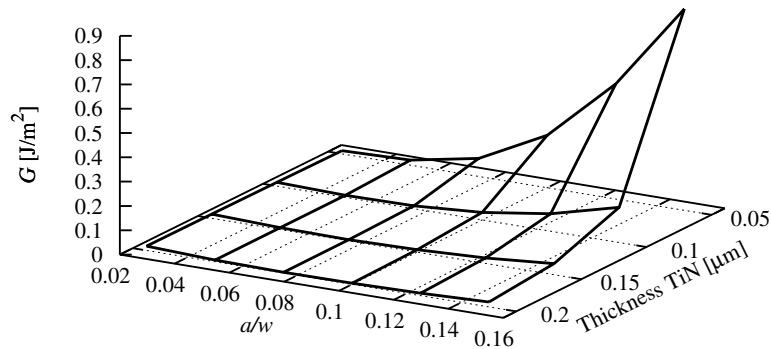


Figure 4.17: The energy release rate G for different thicknesses (TiN) and crack lengths in the SiO_2/TiN interface. Simulation conditions were $\sigma_{\text{SiO}_2}=-100$ MPa, $\sigma_{\text{TiN}}=-50$ MPa, and $h_{\text{SiO}_2}=1$ μm .

In **Figure 4.19** the G values of the interface between Si and SiO₂ are reported. An initial compressive stress σ_{SiO_2} of 100 MPa in the SiO₂ was used. For the Si layer a thickness h_{Si} of 5 μm was set. The thickness variation of the SiO₂ does not produce high value of G .

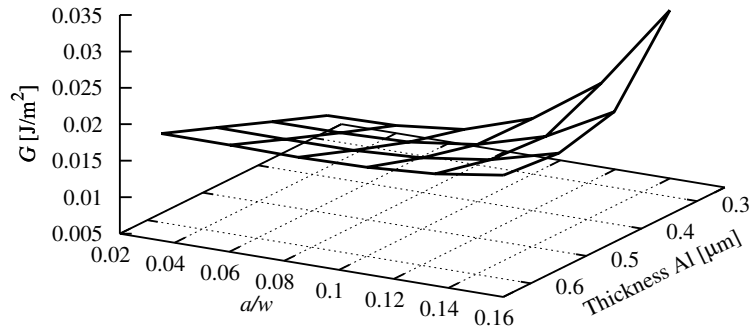


Figure 4.18: The energy release rate G for different thicknesses (Al) and crack lengths in the Ti/Al interface. Simulation conditions were $\sigma_{\text{Ti}}=-50$ MPa, $\sigma_{\text{Al}}=-100$ MPa, and $h_{\text{Ti}}=0.15$ μm .

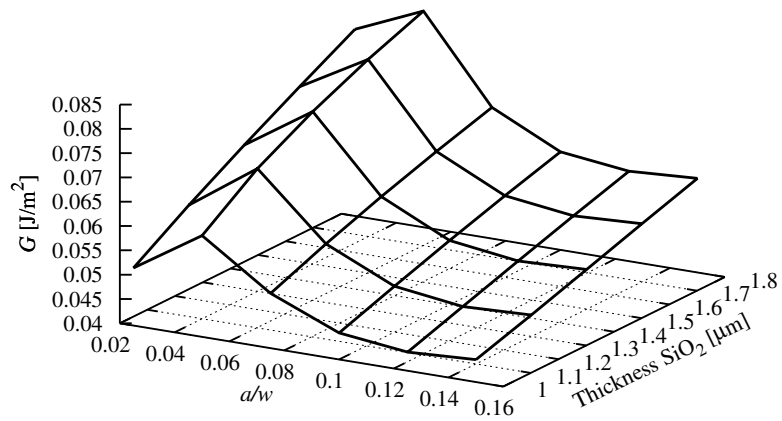


Figure 4.19: The energy release rate G for different thicknesses (SiO₂) and crack lengths in the Si/SiO₂ interface. Simulation conditions were $\sigma_{\text{SiO}_2}=-100$ MPa and $h_{\text{Si}}=5$ μm .

4.4.3.3 Force Analysis

The effects of different forces on the system are presented in **Figures 4.20-4.23**. In these simulations different forces in the range of 10-210 mN were applied.

The behavior of G at the SiO_2/W interface is shown in **Figure 4.20**. A thickness of $0.4 \mu\text{m}$ for the SiO_2 (h_{SiO_2}) layer and a thickness of $0.1 \mu\text{m}$ for the W (h_{W}) layer were employed. In the SiO_2 a compressive initial stress σ_{SiO_2} of 100 MPa and in the W a tensile stress σ_{W} of 1.25 GPa were applied. The simulations were carried out for different forces. The G_c is in the range of $0.2\text{-}0.5 \text{ J/m}^2$ [84] and therefore small in comparison to the values of G obtained for the SiO_2/W interface. For this system delamination is expected only when a force over 100 mN is applied.

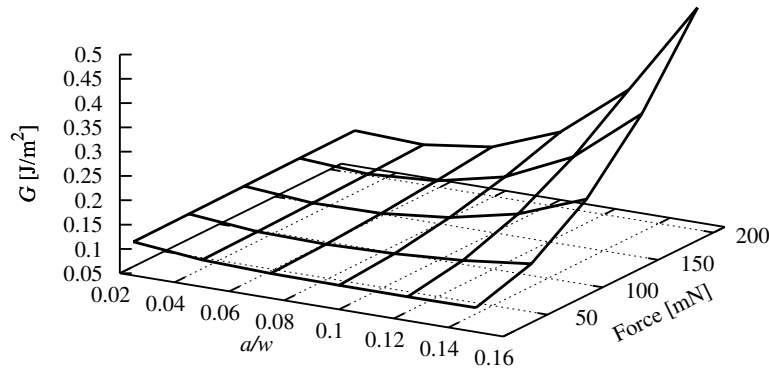


Figure 4.20: The energy release rate G for different force and crack lengths in the SiO_2/W interface. Simulation conditions were $\sigma_{\text{SiO}_2}=-100 \text{ MPa}$, $\sigma_{\text{W}}=1.25 \text{ GPa}$, $h_{\text{SiO}_2}=0.4 \mu\text{m}$, and $h_{\text{W}}=0.1 \mu\text{m}$.

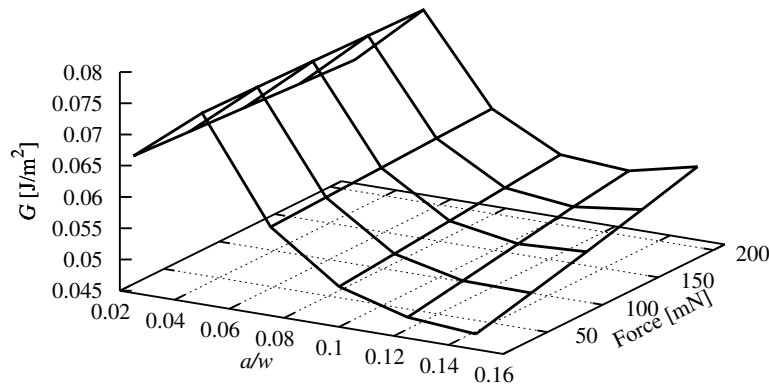


Figure 4.21: The G for different forces and crack lengths in the Si/SiO_2 interface. Simulation conditions were $\sigma_{\text{SiO}_2}=-100 \text{ MPa}$, $h_{\text{SiO}_2}=1.4 \mu\text{m}$, and $h_{\text{Si}}=5 \mu\text{m}$.

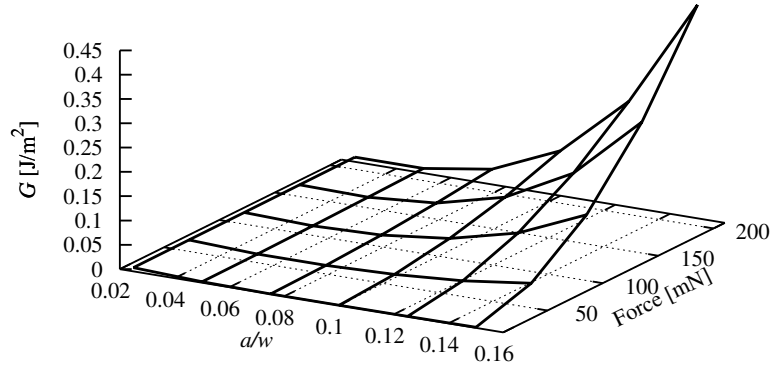


Figure 4.22: The G for different forces and crack lengths in the SiO_2/TiN interface. Simulation conditions were $\sigma_{\text{SiO}_2}=-100$ MPa, $\sigma_{\text{TiN}}=-100$ MPa, $h_{\text{SiO}_2}=1$ μm , and $h_{\text{Ti}}=0.15$ μm .

In **Figure 4.21** the G values of the interface between Si and SiO_2 are plotted against the a/w ratio. An initial compressive stress σ_{SiO_2} of 100 MPa in the SiO_2 with a thickness h_{SiO_2} of 1.4 μm were used. For Si a layer thickness h_{Si} of 5 μm was set. The effect of a force variation is small compared to the influence of the a/w ratio. In this interface for smaller crack lengths the values of G are larger than for long crack lengths. The critical G_c value of 1.8 J/m^2 [83] for this interface is much larger than those calculated in the given simulations.

The G values of the interface between the SiO_2/TiN are shown in **Figure 4.22**. Thicknesses of 1 μm and 0.15 μm for the SiO_2 (h_{SiO_2}) and TiN (h_{Ti}) were used, respectively. A compressive stress of 100 MPa for the SiO_2 (σ_{SiO_2}) and 100 MPa for the TiN (σ_{TiN}) were applied. Here G increases with the increase in the crack length and the applied force. The

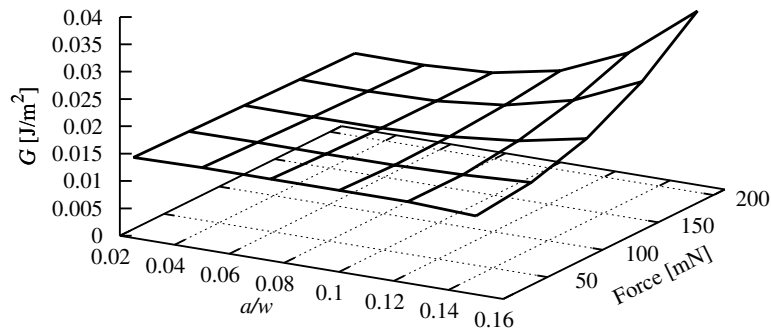


Figure 4.23: The G for different forces and crack lengths in the Ti/Al interface. Simulation conditions were $\sigma_{\text{Ti}}=-50$ MPa, $\sigma_{\text{Al}}=-100$ MPa, $h_{\text{Ti}}=0.1$ μm , and $h_{\text{Al}}=0.5$ μm .

calculated values of G are much lower than G_c , therefore we can expect delamination only for large applied forces.

In **Figure 4.23** the G values obtained for the interface between the Ti/Al are reported. For the Ti layer a thickness h_{Ti} of $0.1 \mu\text{m}$ and initial compressive stress σ_{Ti} of 50 MPa were employed. The Al layer was assumed to have a thickness h_{Al} of $0.5 \mu\text{m}$ and an initial compressive stress σ_{Al} of 100 MPa. The G values obtained are very small therefore no delamination can be supposed for this interface.

4.4.4 Discussion

The impact of the layer thicknesses, the residual stresses, and the applied forces on the energy release rate G were investigated and are summarized in **Table 4.3**.

In **Section 4.4.3.1** the effects of the films' residual stresses on G were investigated. In the SiO_2/W interface, a high probability of delamination propagation occurs when, due to the deposition process and thermal processes, the W layer exhibits high values of residual stress. In addition, the presence of defects, generated during film deposition and resulting in the presence of cracks at the interface, increase the probability of delamination failure. The SiO_2/TiN interface shows the possibility of delamination propagation only for high values of compressive initial stress in the TiN layer. The variation of initial stress in the SiO_2 does not produce high G values decisive for mechanical failure. The Si/ SiO_2 interface remains stable for every crack length and residual stress. Although the critical energy release rates are not available in literature for the Ti/Al interface, a qualitative estimation of the delamination can be given. As the obtained energy release rate is very small, no delamination propagation in this interface is anticipated. In the SiO_2/W interface the most critical condition that lead to delamination propagation is obtained when high values of residual stress in the W layer are noted.

In **Section 4.4.3.2** the effects of the layer thicknesses were investigated. Different values of thicknesses of the layer change the value of G . From simulations it is possible to conclude that for long crack lengths the thickness of the layer has an important effect on the stability of the interface. Usually a thickness decrease strongly increases G . This is not applicable for the SiO_2/W interface, where also at high thicknesses a high G was obtained.

In **Section 4.4.3.3** the effects of an external load were studied. The increased applied force leads to an evident increase in G . This effect is not valid at every interface. The force has a stronger effect at the SiO_2/TiN interface than at the Si/ SiO_2 interface, where a small increase in G as a function of the load is observed. The stability of these interfaces was demonstrated up to a force of 210 mN.

The main influencing factor is the residual stress of the W film which has a strong impact on the stability of the interfaces, which are part of the TSV. By reducing the residual stress of the W film the probability of delamination propagation can be reduced in open TSV. In this study the energy release rate was calculated at different interfaces. The values of the critical energy release rate G_c found in the literature were used to predict the probability of delamination under the varied conditions.

The applied model enables the simulation of different boundary conditions (e.g. thicknesses, initial stresses, applied force) and the determination of TSV structures which are less prone to delamination.

		Interfaces			
		Ti/Al	SiO ₂ /TiN	SiO ₂ /W	Si/SiO ₂
Factors	Residual stresses	No delamination for the investigated conditions. G values very small	G increases as σ_{TiN} increases. G values far below G_c	Delamination for σ_W over 1.25 GPa and for long crack lengths	G increases as σ_{SiO_2} increases. G values far below G_c
	Layer thicknesses	No delamination for the investigated conditions. G values very small	G increases for thin TiN layers and for long crack lengths. G values far below G_c	Delamination for thin W film and for long crack lengths	No delamination for the investigated conditions. G values far below G_c
	Applied forces	No delamination for the investigated conditions. G values very small	G increases as the applied force increases. G values far below G_c	Delamination for applied force over 100 mN and for long crack lengths	No delamination for the investigated conditions. G values far below G_c

Table 4.3: Summary of the conditions for delamination propagation.

4.5 Experimental Analysis

Experimental measurements were used to calculate the critical energy release rate G_c at the interface between SiO₂ and W. SiO₂ and W are building materials of Open TSVs and these materials are fundamental for the reliability of the full integrated circuit. W is the conducting material and its mechanical stability is essential to avoid an open circuit failure. In this section a developed model to calculate the energy release rate G is presented and the results are compared with experimental data.

4.5.1 Experiment - Four Point Bend Technique

In microelectronics, the fracture at interfaces between adjoining materials is a critical phenomenon for device reliability and different techniques are available for reliability analysis. As seen previously, in an Open TSV a typical conductor material is W (**Section 1.3.2**). Due to deposition and thermal processes the conductor has a high value of intrinsic tensile stress [86]. The stress in the layers can be sufficiently high to degrade the performance and to induce crack or delamination in the TSV.

There are several methods for measuring G_c which employ different sample geometries. Thin film delamination can initiate as a result of a driving force or stored energy in the films [82].

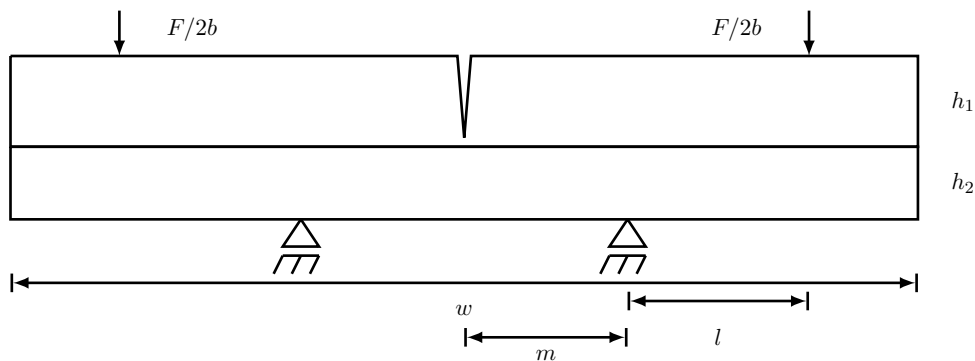


Figure 4.24: Schematic representation of the studied system. On the top a force (F) was applied, and at the bottom two fixed points were used as bearings.

Sample	h_1 [μm]	h_2 [μm]	% Del.	Comments
1	726.3	684.6	28	CVD-TiN with Ti
2	725.7	684.4	7	CVD-TiN without Ti
3	725.5	688.3	78	CVD-TiN with Ti
4	726	698.7	89	CVD-TiN without Ti
5	724.7	683.3	84	PVD-TiN with Ti

Table 4.4: Geometry of the samples used in the simulation study. The thickness h_2 includes the thickness of the adhesive. The comments indicate the type of deposition process and the presence or absence of the Ti layer.

The four point bend (4PB) technique is the most popular adhesion test employed to characterize interface cracks. For such fractures, normal and shear stresses act along the crack and the mixed mode condition prevails (**Section 4.1**). The 4PB setup was used to determine the experimental values of the critical energy release rate G_c . G_c was measured at different interfaces, relevant to the Open TSV structures. In the present work COMSOL Multiphysics [62] was used to simulate the 4PB technique and to calculate G .

The Fraunhofer Institute for Electronic Nano System (Fraunhofer-ENAS) used a 4PB specimen [87] to determine the experimental G_c . In **Figure 4.24** the 4PB setup is illustrated. The technique consists of a bimaterial flexural beam with a notch in the top layer. For the bimaterial beam two Si wafers were used to sandwich the film of interest. Under the Si top layer, indicated with h_1 in **Figure 4.24**, a SiO_2 layer with a thickness of 500 nm was placed. Subsequently, at the SiO_2 film a TiN layer with a thickness of 11 nm and a W layer with a thickness of 200 nm were placed. On the top of the h_2 Si layer an adhesive was laid in order to link to the top h_1 layer. At the interfaces of three samples an additional Ti layer with a thickness of 25 nm was deposited between the SiO_2 and TiN. The deposition process of the TiN layer, the thickness of the layers, and the samples including are presented in **Table 4.4**. At the end of the experimental measurements the percentage of delamination in the sample was measured (cf. % Del. in **Table 4.4**). All the samples have a length w of 44 mm and a depth b of 3.5 mm. In the 4PB method a constant

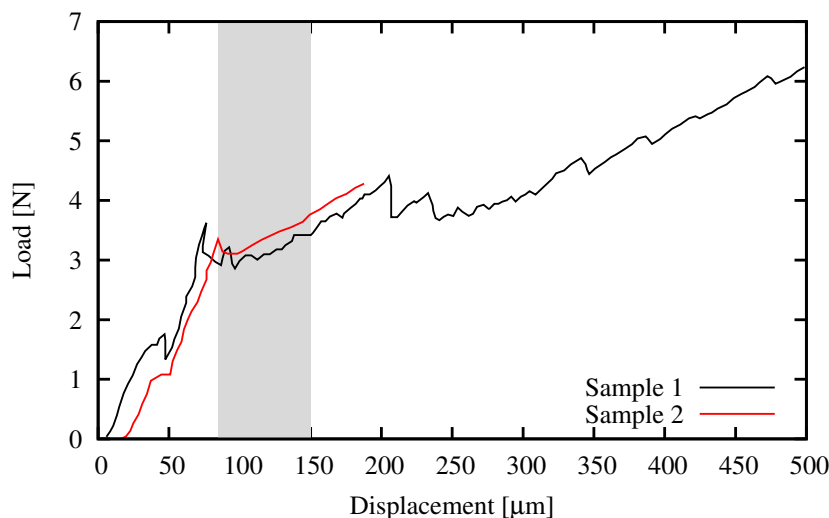


Figure 4.25: Experimental results for Sample 1 and Sample 2. The gray area indicates the steady state region where delamination appears.

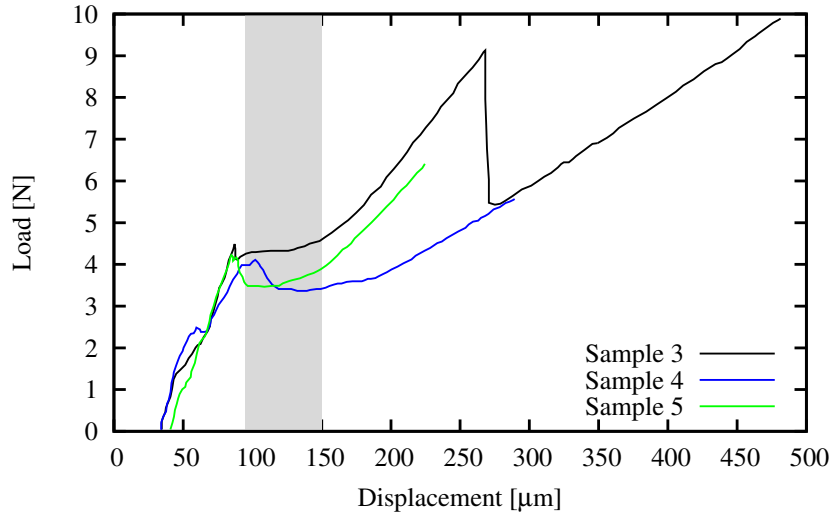


Figure 4.26: Experimental results for Sample 3, Sample 4, and Sample 5. The gray area indicates the steady state region where delamination appears.

load F and two fixed points are applied at the sample as shown in the **Figure 4.24**. By recording the load as a function of displacement a plateau was obtained when the crack interface reached the steady state. In this regime G is independent of the crack length and indicates the G_c value [87].

In the 4PB technique the Euler-Bernoulli beam theory in plane strain condition is applied [87] and the critical energy release rate G_c is calculated using

$$G_c = \frac{3F_c^2 l^2}{2E_{Si} b^2} \left[\frac{1}{h_2^3} - \frac{1}{h_1^3 + h_2^3 + 3h_1 h_2 (h_1 + h_2)} \right], \quad (4.65)$$

where F_c is the force measured at the steady state of the plots in **Figure 4.25** and **Figure 4.26**, E_{Si} is the Young modulus of Si, and the remaining parameters are indicated in **Figure 4.24**.

4.5.2 Simulation

The 4PB technique was simulated using the finite element method. The geometry used for the experiment has been reproduced in two-dimensional simulations. Due to the symmetry conditions in the 4PB test, it is sufficient to consider only half of the structure as depicted in **Figure 4.27**. All the materials are assumed to be linear elastic. On the left side of the **Figure 4.27** a symmetry condition was applied and a fixed point and a load point were applied as in the experiment. Near the crack tip, a very fine triangular mesh was used. The initial conditions for the simulations include an interface crack with a length of 1 mm, which has been increased by 1 mm steps during the simulation until the desired value is reached.

In **Figure 4.27** the results of a simulation with $a=5$ mm are shown. Due to the boundary condition the Von Mises Stress is mainly generated at the h_2 layer. The stress distribution at the interface crack opening is described by (4.37). For every crack length the σ_{yy} and τ_{xy} values were extracted as a function of r . **Figure 4.28** and **Figure 4.29** show an example of the obtained results, where the cross dots are the values of the stresses obtained from the FEM simulations. The x -axis indicates the interface distance at the

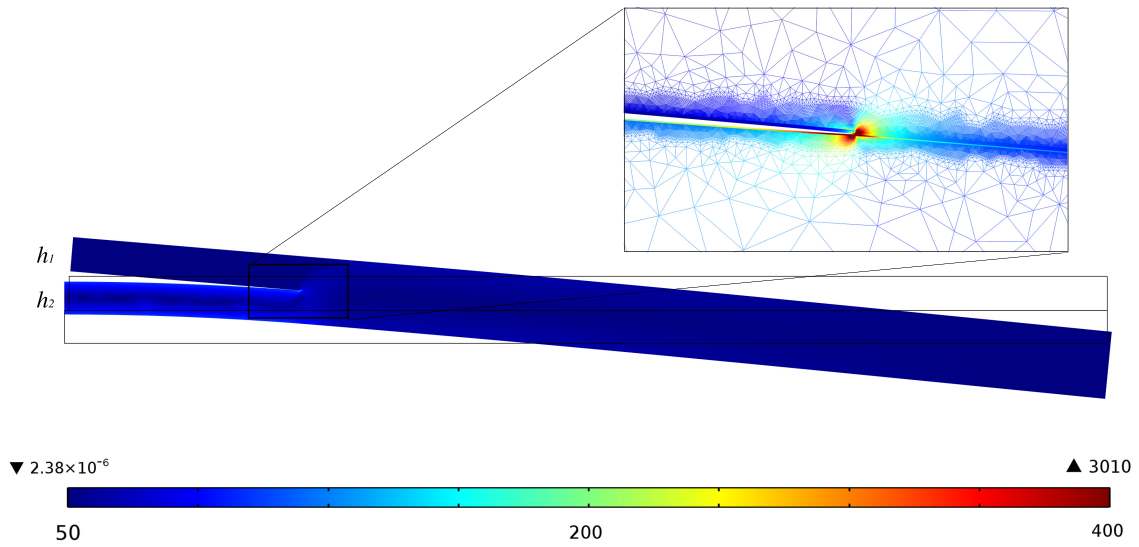


Figure 4.27: FEM simulation of the 4PB test. The legend indicates the Von Mises Stress (10^6 N/m^2). Due to the boundary condition the stress development in the bottom layer can be observed. In the inset a zoomed-in section of the crack, with the mesh used is shown.

right side of the crack-tip (r) and the y -axis the stress value. Here, the singularity described in **Section 4.1.2** can be observed for both stresses.

4.5.3 Simulation Results

The simulation results are obtained by using the approach described in **Section 4.3.2** where the values of σ_{yy} and τ_{xy} were extracted from the FEM simulations. The G values are calculated by applying the approach for every simulated crack length in the range from 1 mm to 10 mm.

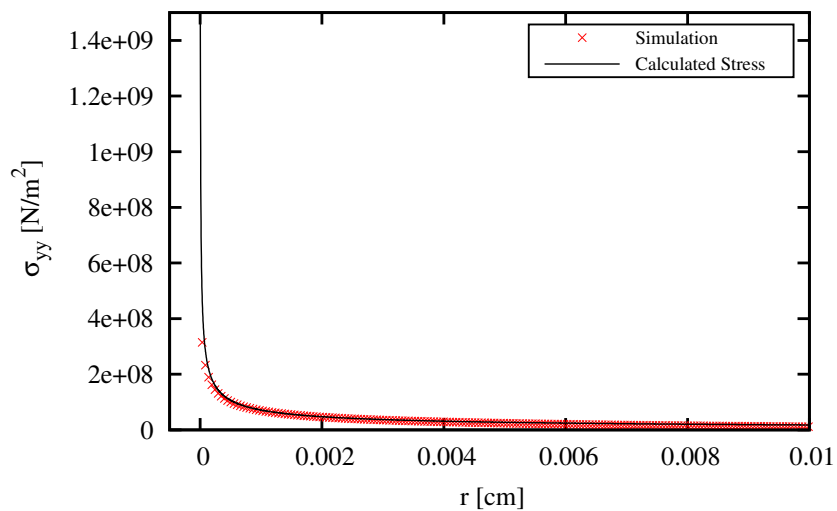


Figure 4.28: Example of the obtained FEM results compared with the stresses calculated using (4.40). Here σ_{xx} as a function of r is shown.

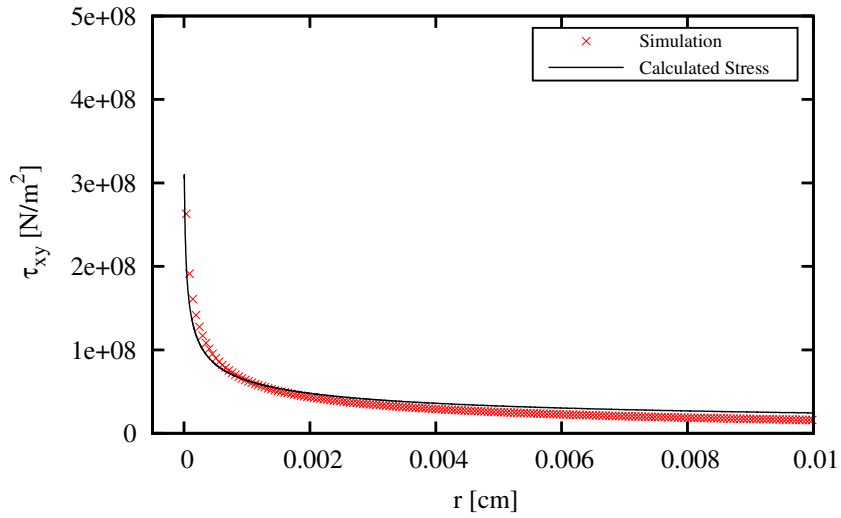


Figure 4.29: Example of the obtained FEM results compared with the stresses calculated using (4.40). Here τ_{xy} as a function of r is shown.

In **Figure 4.28** and **Figure 4.29** the results of the regression analysis are compared with the FEM simulation results. By using the approach described in **Section 4.3.2** the values of K_1 and K_2 were obtained; by subsequently inserting them in (4.40) the stresses at the interface can be reproduced. The reproduced stresses qualitatively and quantitatively match the FEM simulation results very closely.

Figure 4.30 displays the G values calculated at every crack length a for the Sample 1 and Sample 2 (**Table 4.4**). As the crack approaches the fixed point of the 4PB test (4 mm from the center of the samples, m in **Figure 4.24**) the G value decreases [88].

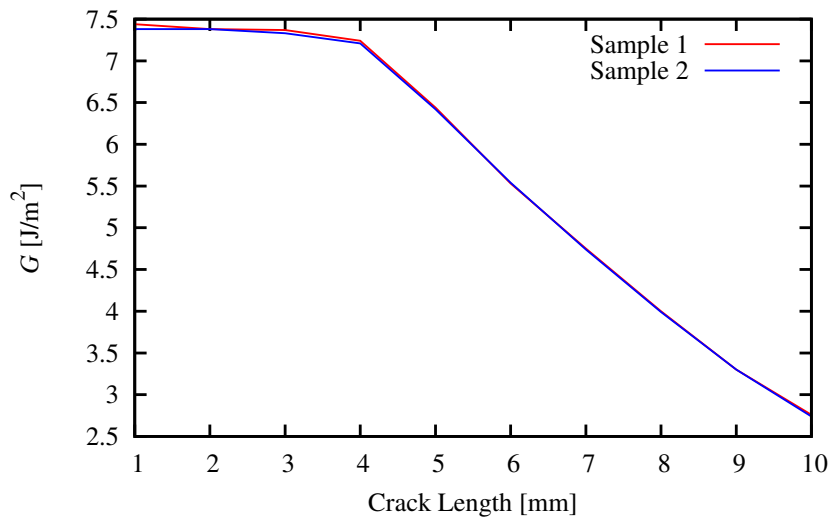


Figure 4.30: G obtained from FEM simulations. Crack length in the range from 1 mm to 10 mm was simulated.

The simulated value G at every crack length a for Sample 3, Sample 4, and Sample 5 (**Table 4.4**) is shown in **Figure 4.31**. Here the decrease in G is less pronounced than in Sample 1 and Sample 2. The value $m=10$ mm (same as in the experiment) was used

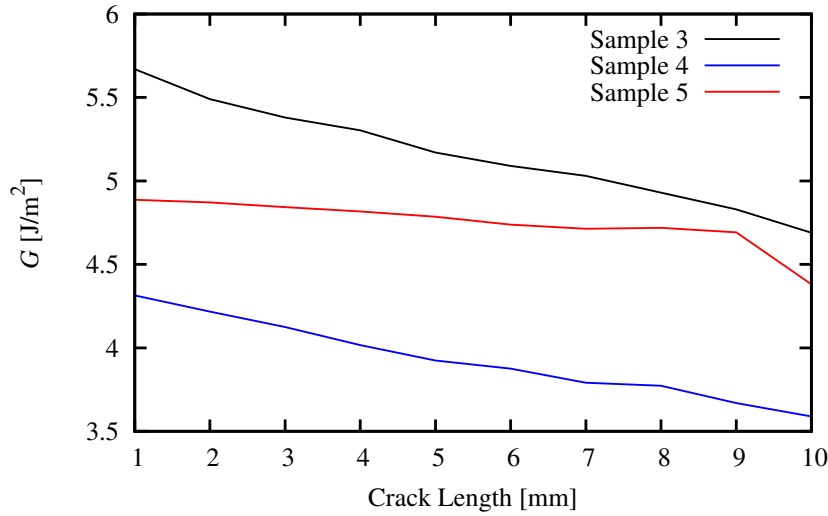


Figure 4.31: G obtained from FEM simulations. The crack length in the range from 1 mm to 10 mm was simulated.

and the simulations were executed until the crack length of $a=10$ mm was reached. The different line slopes are due to the different thicknesses and interfaces of the analyzed sample.

The experimental G_c was determined by using the average of the loads in a steady state range. In addition, for the FEM simulation results an average value for G_c was determined. In particular for Sample 1 and Sample 2 G_c was calculated in a range of crack lengths from 1 mm to 4 mm and for Sample 3, Sample 4 and Sample 5 in a range of crack lengths from 3 mm to 9 mm.

In **Table 4.5** the G_c values obtained from experimental and simulation data are compared. For Samples 1 and 2 the FEM simulation results differ from the experiments results. This difference is attributed to the behavior observed in **Figure 4.25**. In these load-displacement plots no clean steady state regions can be observed. The discontinuous sections of the load plots are a result of an unstable crack propagation. It is quite possible that due to some defects or imperfect adhesion between the layers the delamination propagates unevenly. This is also understandable considering the percent of delamination in these two samples (cf. **Table 4.4**). For Sample 1 and Sample 2 the percentage of delamination is 28 % and 7 %, respectively. For Sample 3, Sample 4, and Sample 5 the percentage of delamination is over 75 % that indicates a stable crack propagation. The FEM simulation results for Sample 3, Sample 4, and Sample 5 appear closer, as given in

Sample	Experimental G_c [J/m²]	Simulation G_c [J/m²]	% Error
1	5.95	7.36	19,2
2	5.9	7.33	19,5
3	4.6	5.10	9,8
4	3.5	3.88	9,8
5	3.9	4.75	17,9

Table 4.5: G_c values measured from experimental data and calculated using FEM simulations. The G_c values calculated for Sample 3, Sample 4, and 5 are in good agreement with the experimentally measured G_c values.

Table 4.5. The G_c values for Sample 3 and Sample 4 are very close to the experimental values. This is again due to a better adhesion in a longer region and thus a more pronounced steady state load area. In **Figure 4.26** a distinguishable constant load created as a result of the delamination is observed. The FEM simulation results the Sample 5 is less accurate but still in an acceptable range (cf. % Err. in **Table 4.5**).

Simulation results and experimental data imply that the influence of the additional Ti layer (**Table 4.4**) is negligible.

4.5.4 Discussion

A FEM simulation method to calculate the energy release rate G at the interface between two materials was presented. The 4PB technique can be simulated by considering a simplified structure. From the FEM simulations, the stress at the interface was obtained and used to calculate the energy release rate G . The results of FEM simulations strongly depend on the quality of the experimental data. For the calculation of G_c it is necessary to start with a load-displacement plot, where a steady state load is clearly observable and distinguishable. This study demonstrated the efficiency of the FEM simulation and how it can be used to calculate G for different boundary conditions and geometries of the TSV structure, where the delamination is a potential reliability issue.

The results obtained are in good agreement with experimental measurements. Therefore, the developed model provides a convenient tool for the study of delamination issues in TSVs.

4.6 Comparison between J -Integral and Regression Analysis

In the previous sections two different methods for the calculation of the energy release rate G were presented, namely J -Integral and regression analysis. The results in **Section 4.5** show good agreement between experimental data and simulations. Therefore, the developed method correctly represent the physical delamination behavior.

A comparison between the two methods is given in this section. Using an identical structure G was calculated with the two methods. The results of the two methods are compared to verify their quality with respect to the G value.

4.6.1 Structure

Figure 4.32 depicts the structure under simulation. At the left side of the structure a symmetric condition was set. Layer 1 indicates Si and layer 2 indicates SiO₂ films. Si has a thickness of 70 μm and SiO₂ of 72.6 μm . The length w was set to 2.22 mm and the applied force F has a value of 0.2 N. The fixed point was positioned at $m=1$ mm from the left side of the structure.

As used previously in the other simulations also here a stationary simulation was performed. Crack lengths in the range from 0.1 mm to 0.9 mm were simulated.

4.6.2 Results and Discussion

In **Figure 4.33** the simulation results are presented. There is a clear agreement between the two methods. The black crosses indicate the results obtained from the J -Integral method and the red crosses are the results obtained from the regression analysis. Both methods give a constant G for every simulated crack length.

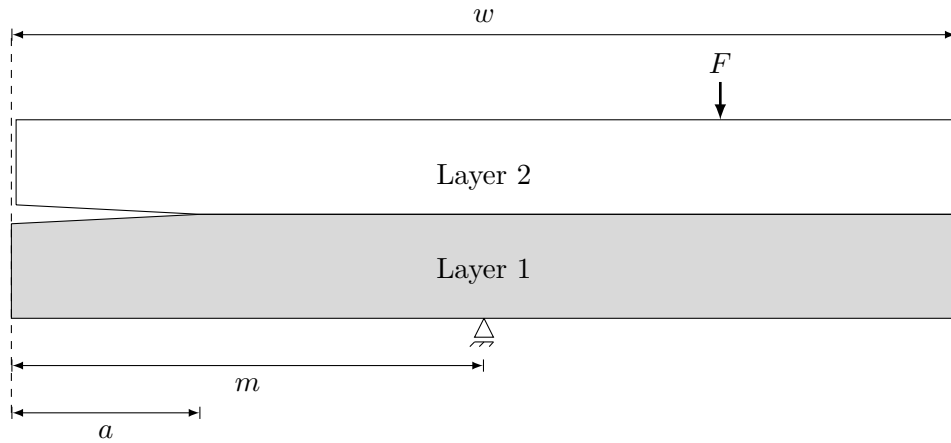


Figure 4.32: Structure used for a comparison between the two methods.

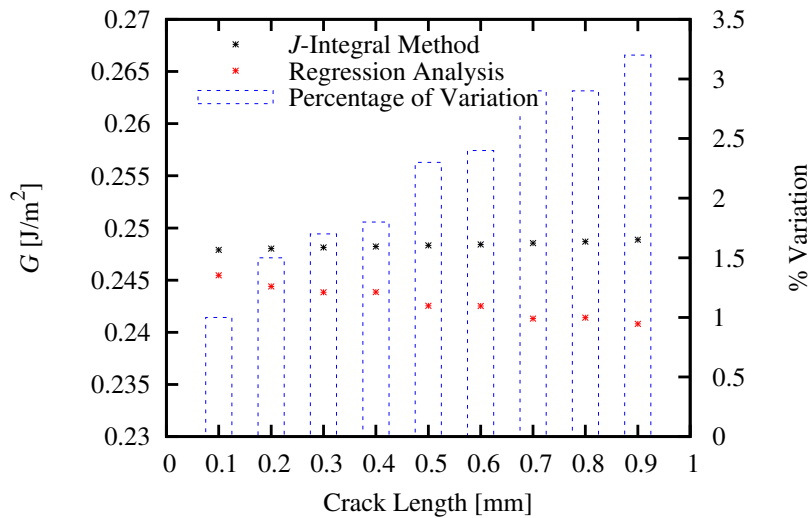


Figure 4.33: G values obtained using the J -Integral method and the linear regression method. Crack lengths in the range from 0.1 mm to 0.9 mm were simulated. The percentage of variation between the two methods is reported.

The two methods were verified for the same structure. The results are effectively identical. As shown in **Figure 4.33** the variation in percentage between the two methods varies from 1% at small crack lengths to 3.2% at long crack lengths. The regression analysis becomes less accurate as the simulated crack lengths approach the fixed point m of the structure [87]. The J -Integral method is implemented in a FEM tool. This method permits to calculate the G value directly at the end of the simulation. The method needs to calculate an integral over a path between the two materials. If the material thickness of one layer or both is too thin, the inability of defining a path for the integral can be encountered.

The regression analysis can be applied when thin films are taken in account. It produces the same results, but the evaluation time necessary to calculate G is higher, as the results have to be post processed. After the simulation, the stress at the interface needs to be collected and used in a statistical analysis software, which is used to perform the post-processing fitting.

4.7 Summary

In this chapter the delamination theory was explained and the probability of delamination at several material interfaces, essential for the fabrication of an open TSV was investigated.

The energy release rate G , which is an important measure for delamination prediction, was calculated at different interfaces. By comparing G with the critical energy release rate G_c predictions about the probability of delamination can be made. Two different methods used in calculations of G were implemented using FEM. The J -Integral method permits to obtain G at the end of the FEM simulation. The regression analysis method, however requires two post-processing steps. In the first step the obtained stress values at the interface between the two materials need to be extracted. In the second step, through a regression analysis of the collected stress values K_1 and K_2 , necessary to calculate G are determined.

The second method was verified by replicating experiments and the obtained results sufficiently reproduce the measured results. Therefore, the two methods were employed to calculate G for the same structure. The results obtained from the two methods are in good agreement.

While investigating the material interfaces present in open TSVs using the J -Integral method, it was found that the most critical conditions were at the SiO₂/W interface. For this interface the G_c was determined experimentally (**Section 4.5**) and the simulated value (3.5-5.95 J/m²) was higher than that found in literature (0.2-0.5 J/m² [84]). This difference is caused by a particular configuration of the film/substrate geometry. The thickness of the layers, the residual stress of the layers, and the employed method to calculate G_c produce different results. Open TSVs have sophisticated structures which do not permit to know the critical condition for the failure. Therefore we are able to qualitatively predict the most unstable condition for delamination by comparing G with the lowest G_c found in literature.

The SiO₂/W interface is fundamental for the mechanical stability of open TSVs. G was calculated by investigating the influence of factors such as residual stresses in the films, thicknesses of the layers and, force applied to the system. It was determined, that the most unstable system is one where the residual stress in the W layer is very high, a high external force is applied, or the W film is very thin. Therefore, in the next chapter the origin of the residual stress in solid films is studied.

5

Simulation of Intrinsic Stress Build-Up in Thin Metal Films

Thin films in microelectronics exhibit residual stress which can affect the performance and reliability of devices. In **Chapter 4** it was demonstrated how high values of residual stress in thin films can be problematic for the mechanical stability of 3D interconnect structures, such as open TSVs. A high value of residual stress in the W layer of the TSV structure can increase the probability of delamination at the interface between W and SiO₂.

In this chapter, the mechanism behind stress development during film growth is investigated. This study is needed for the understanding of the reduction of film stress which is necessary to increase the mechanical reliability of TSVs. Usually metal films are used in TSVs to electrically connect the integrated circuit in the 3D structure. Typically, the growth process of metal films in TSVs follows the Volmer-Weber mechanism. A FEM-based model describing the stress evolution during the three steps of Volmer-Weber growth was implemented. In general, stress in the film evolves from compressive to tensile and can then return to compressive. The stress generated in the film strongly depends on processing and material properties. Results obtained from the model were compared with different experimental data. The implemented model helps to predict the intrinsic stress in thin films during the growth process and enables an analysis of the influence of fabrication conditions on the thin film stress. The presence of scallops, which appear as a consequence of deep reactive ion etching, results in reduced intrinsic stress. Film growth on a scalloped substrate was simulated. When the scallops were more pronounced, i.e. a larger height/width ratio, the intrinsic stress was further reduced. In addition film growths at different deposition temperatures and different growth rates were simulated.

5.1 Introduction

Thin films are utilized in microelectronics to build functional devices such as interconnects. The properties of a film and its applications are determined by the choice of material and its geometry. The mechanical properties of thin films with a thickness in the range of several atomic layers differ from those of bulk materials. These differences are caused by the diverse microstructures of the film, which depend greatly on the deposition technique. Most films used for microelectronics are polycrystalline materials composed of a large number of small crystallites. In order to understand the microstructure of the film and its mechanical properties, the deposition process must be studied in detail. Significant stress may develop in the film during the deposition process and during the subsequent cooling to room temperature, due to a large mismatch in the thermal expansion coefficients between the material used in the film and the surrounding layers. Stress can lead to reliability issues such as cracking and delamination within a device structure, resulting in poor reliability and ultimately early device failure. Understanding the mechanisms which generate stress

in films during the deposition processes is therefore essential in order to decrease the probability of an interconnect failure.

In this chapter the intrinsic stress build-up during the deposition process using simulation methods is analyzed. The deposition process of a given film is modeled by employing well-established theories and physical models which describe film growth [89, 90, 91, 92]. Each material has different properties and consequently a different impact on the growth process of the film. The analysis is focused on W and Cu, which are the materials typically used for TSV interconnects [28, 29] (**Section 1.3.2**).

Although this study deals with stress build-up during deposition, for TSVs the etching step cannot be avoided. In order to fabricate the TSV structure, etching of the silicon wafer is required. This step can be performed either by ion-enhanced plasma etching or by deep reactive ion etching (DRIE) [93]. Both methods have their own reliability concerns: Problems specific to DRIE are scallop formation along the sidewall, notch formation at the bottom of the TSV, and potential step coverage concerns [94]. Etching using ion-enhanced plasma, such as SF_6/O_2 , results in noticeable sidewall tapering, resulting in a significant limitation in the aspect ratio of the etched hole [95].

5.2 Theoretical Background

The mechanical properties of a thin film are highly dependent on the conditions under which the film deposition takes place. Different deposition processes are used during integrated circuit fabrication where metals, dielectrics, and semiconductors are grown. Due to thermodynamical reasons, there are three different modes describing film growth during deposition, namely Volmer-Weber (V-W), Frank-Van der Merwe, and Stranski-Krastanov [92]. Film stress development in polycrystalline metal films deposited onto polycrystalline or amorphous substrates is investigated. The atoms of the polycrystalline metal film are more strongly bound to each other than to the substrate, and this situation is well described by the V-W growth mode [42, 90]. The film growth of these materials is therefore investigated with the basic assumption that the film growth proceeds according to the V-W mode.

The stress build-up during the growth process is also influenced by the layer on top of which the deposition takes place, such as SiO_2 or the barrier layer. The geometry along the sidewalls of TSVs on top of which metal liner is deposited can have scalloped features. These features are a result of the wafer etching process, mainly the deep reactive ion etching (Bosch process [14, 24]). In this study, the effects of the scallops on the stress build-up during film growth are also analyzed.

5.2.1 Volmer-Weber Growth

In the **fourth processing step** (**Section 1.3.1**) of TSV fabrication a metal film is deposited. Polycrystalline metal films deposited onto polycrystalline or amorphous substrates are described by the V-W growth mode [42, 90]. During the V-W mode three unique growth steps can be distinguished. Each step affects the film microstructure and consequently the physical properties of the film. The initial stage of film growth is the nucleation of islands onto the substrate. During the deposition process, atoms arrive on the surface and initiate the nucleation step. The minimum nucleus, formed by the atoms on the surface, has a characteristic size associated with a critical initial radius R_i . Beyond this size, the nucleus is stable and begins to grow [90]. The microstructure of a growing film is influenced by the deposition rate v_d , the substrate temperature T_s , and the material

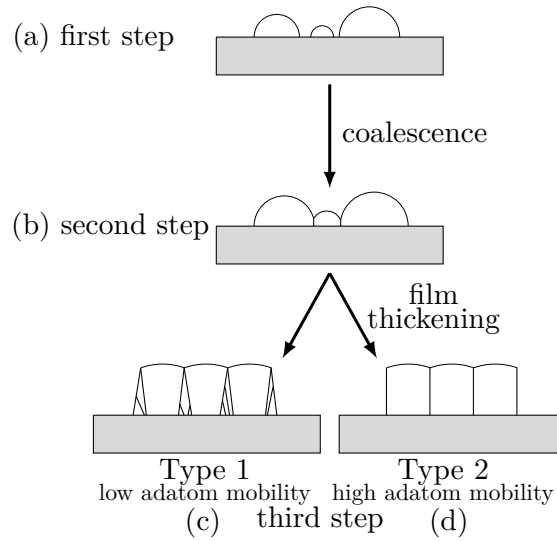


Figure 5.1: Three steps of the V-W growth process. (a) indicates the nucleation of the islands where compressive stress occurs, (b) indicates the coalescence process where the islands impinge upon each other, and (c)-(d) is the thickening process where a homogeneous film is formed. The properties of the deposited material distinguish two kinds of microstructure, Type 1 (for low adatom mobility materials) or Type 2 (for high adatom mobility materials).

properties. Nucleation events continue to occur during deposition as long as there exists a substrate area exposed to the atoms [42, 90]. The first growth step consists of the nucleation of islands in the film deposition process as shown in **Figure 5.1** (a). During the second growth step the islands grow larger in size and start to impinge on each other, forming a continuous polycrystalline film. This step is commonly referred to as the island coalescence process (illustrated in **Figure 5.1** (b)) After island coalescence film thickening takes place.

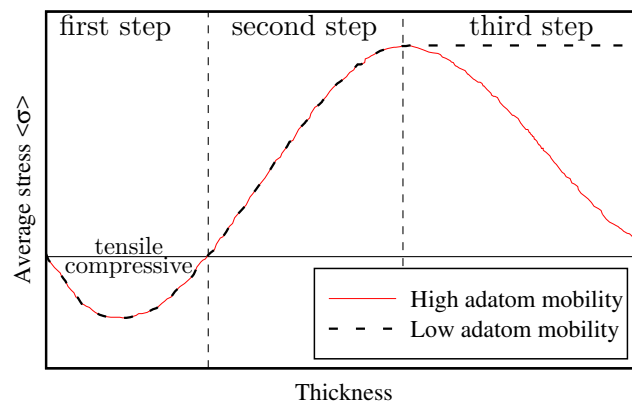


Figure 5.2: Stress evolution during the deposition process for both kinds of materials.

In this third step the formed film continues to thicken and gain volume until the deposition process is interrupted; this step is shown in **Figure 5.1** (c)-(d). During the thickening process the structure of the grains and their evolution are strongly influenced by the adatom diffusivity of the material employed in the deposition process. There

are two different types of grain-structure evolution. Materials with low adatom mobility (high melting temperature) exhibit a columnar grain structure with increasing grains during thickening referred to as Type 1; this type is depicted in **Figure 5.1** (c). In these materials (e.g. Si, W, Fe), the adatom diffusivity is relatively low even at high processing temperature. In materials with high adatom mobility (low melting temperature), the microstructure forms equiaxed grains which continue to evolve during film thickening. This process is typically found in Al, Ag, Au, and Cu, depicted in **Figure 5.1** (d), and is referred to as Type 2.

The three V-W growth steps generate stress within the film as shown in **Figure 5.2**. This stress evolves from compressive to tensile and can then develop further in one of two different ways. It can either become compressive again or remain tensile [96], depending on the adatom mobility of the material used in the deposition process.

5.2.2 DRIE Scallop Formation

An essential step in TSV fabrication is the etching of silicon, previously described as the **first processing step** (**Section 1.3.1**). Most often this proceeds using DRIE which is a combination of multiple cycles of the isotropic deposition of a polymer and an ion-enhanced plasma etching of the polymer and underlying silicon wafer. The polymer protects the

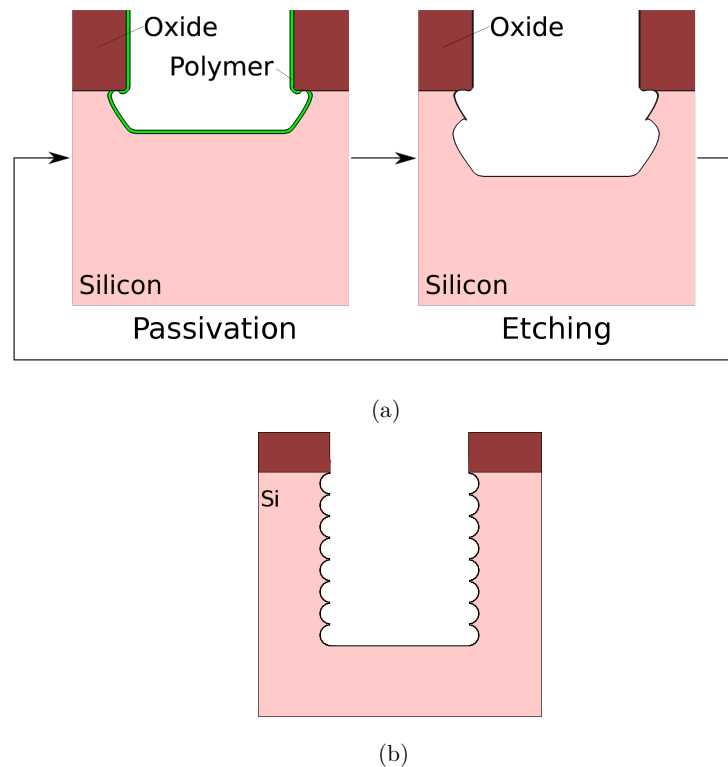


Figure 5.3: (a) A schematic illustration of the DRIE process, where a passivation layer protects the sidewalls during the subsequent etching cycle. (b) Etched trench structure after 8 deposition/etch cycles.

sidewalls from the chemical etch, while it is removed from the trench bottom. As the bottom becomes exposed, chemical etching proceeds there. This ensures a vertical etch, but with the presence of a rough, scalloped sidewall. In **Figure 5.3** (a) a simple schematic

of the DRIE process is depicted, while **Figure 5.3** (b) shows the resulting trench with scalloped sidewalls after 8 cycles.

The deposition of the thin polymer layer is usually performed in a C_xF_y gas environment, while the subsequent etching step is performed in an ion-enhanced plasma environment, usually using SF_6 gas [97]. By controlling the individual times for the deposition and etch steps of the cycles, the geometry of the resulting scallops can be manipulated. In this work several scallop structures are examined in order to determine which factors have the greatest influence on the intrinsic stress generation. With these results the process sequence proceeds in a way to minimize the resulting stress in the thin film can be ensured.

5.3 Volmer-Weber Model for Thin Films

During the V-W growth of the film the produced stress plays an important role in the growth process itself. In the following sections the stress-generation mechanisms is described. First, the geometric conditions used for the simulation of the growth mechanism, followed by a theoretical model implemented with the FEM are described.

The model is capable of simulating V-W growth for materials with both high and low adatom mobility. Although the grain size in films is not uniform, in this work layers having only a single grain size which corresponds to the average grain size of the deposited film are considered. This assumption does not correspond to the real condition; however, a negligible influence of the other grain sizes on the final stress generation is expected. The main purpose of this study is to analyze the interaction between single grains.

Further, it is important to note that the crystal orientation, the elastic anisotropy, and the possible plastic relaxation were not taken into account. These material properties can influence the stress generation during film growth; however, the intent of the developed model is to describe qualitative trends of growth in confined geometries and to describe the effects of fabrication conditions on the stress evolution.

The cylindrical geometry of TSVs could impact and influence the magnitude and concentration of the film stress. A cause of the complexity to simulate the 3D TSV geometry only two-dimensional geometries are considered. Further studies are necessary to understand the impact of the cylindrical geometry of TSV.

5.3.1 Geometry

The growth process is analyzed for material islands with a hemicylindrical shape [90]. The material island is represented as a half-cylindrical cut along the z -axis, which lies on a substrate (**Figure 5.4**). The length l of the cylinder with a circular-cap cross section is assumed to be infinite. This assumption is implemented by using the plane strain condition (i.e. strains in z -direction are zero) in two-dimensional simulations. A thin film as a periodic array of islands is modeled, and therefore the symmetry boundary condition is imposed on outward normals of the geometry. A non-slip interface condition between the islands and the substrate is employed. A schematic representation of the islands is shown in **Figure 5.4**. FEM model to simulate V-W film growth is implemented in COMSOL Multiphysics [62] and described in the sections which follow. A stationary parametric sweep is used to simulate the growth steps. With the radius parameter R (**Figure 5.5**) the island geometry is modified as it grows. At each value of the parameter R a new geometry is created and the stress generated due to island growth is computed. The stress calculated for every value of R is used as the initial stress condition (in terms of the stress tensor component σ_{xx} and σ_{yy}) for the subsequent simulation step. It is assumed that

all materials behave elastically and that all islands are of the same size. Furthermore, an initial island with a critical radius (corresponding to a small R_i value) already nucleated on the substrate is considered. For every simulation step, R is assumed to increase linearly in time t according to

$$R(t) = R_i + tv_g = h_f, \quad (5.1)$$

where R_i is the initial radius of the island and h_f is the film thickness. In this way R progressively grows as a function of v_g .

The average grain size of a film depends on the deposition parameters. In the implemented model, r is the radius of the island at the coalescence point which corresponds to the average grain size of the film.

The comparison with experimental data is carried out by computing the average stress in the film $\langle \sigma_{xx} \rangle$ using a FEM simulation, followed by the evaluation of the stress-thickness product $\langle \sigma_{xx} \rangle \times h_f$ [90]. The stress-thickness product $\langle \sigma_{xx} \rangle \times h_f$ is often called the “force/width” and is frequently used in measurements of stresses through thin films in order to highlight that the stress can have a through-the-thickness variation which cannot be determined solely by post-deposition curvature measurement [98].

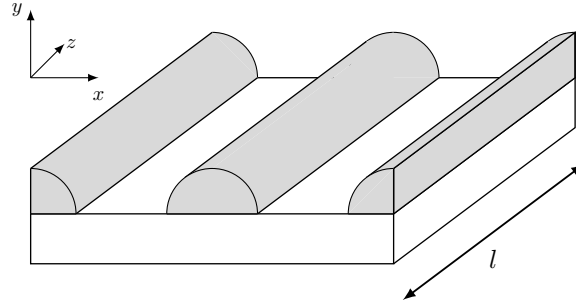


Figure 5.4: Half-cylindrical islands which lie on the substrate.

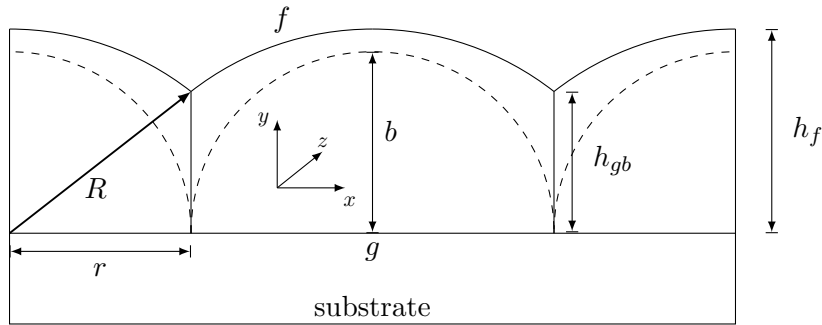


Figure 5.5: Schematic diagram of the impingement of the islands is shown. The dashed lines indicate the island before the coalescence process and the solid lines depict the homogeneous film (after the coalescence of the islands).

5.3.2 First Step: Compressive Stress

In the first step of V-W growth (cf. **Figure 5.1** (a)) a compressive stress develops in the islands before the film becomes continuous. The stress subsequently emerging is mainly due to the action of the surface stress [89, 90]. In the solid nucleus the surface atoms have an equilibrium interatomic spacing which differs from those of the interior (bulk)

atoms, due to the different bondings between surface and interior atoms. This difference in equilibrium spacing results in the development of surface stress f (cf. **Figure 5.5**). f is associated with the reversible work per unit area required to elastically strain a solid surface. Because of the surface stress f a Laplace pressure ΔP is generated inside the island. During the deposition process, the island increases in volume dV and some amount of work $\Delta P dV$ is produced. The work available for a volume increase, due to the pressure, must balance the work required for an increase of the surface, due to the surface stress f . For positive surface stress f a compressive stress due to Laplace pressure is present and measurable during the first step of the deposition process. As for a free surface, surface stress can also be associated with the solid-solid interface between island and substrate. The interface stress necessary to stretch an interface by elastically deforming the island and substrate is denoted by g (**Figure 5.5**) [99]. In this analysis the effect of the stress on the island-substrate interface [89, 90] are neglected.

There is a second mechanism concurrently generating a compressive stress. This stress is based on the fact that the island becomes strongly attached (non-slip) to the substrate during the first growth step. The radius size at which the island is frozen-in at the substrate is denoted as R_{fr} which is a function of the strength of the island-substrate bonding. If the radius of the island is less than R_{fr} , this mechanism does not affect the internal stress, since the island is unconstrained [89, 90]. As the volume of the island's nucleus grows further, the internal elastic stress tends to relax due to the Laplace pressure. Since the island is now rigidly bonded to the substrate, the difference between the lattice parameter, corresponding to R_{fr} , and the lattice parameter which it would have due to the Laplace pressure tends to generate a compressive stress in the islands. Considering both effects and the geometry included in the model, the compressive stress is given by

$$\sigma_{comp} = f \left(\frac{1}{R} - \frac{1}{R_{fr}} \right). \quad (5.2)$$

This equation is used in the model to describe the initial compressive stress observed at an early stage of film growth prior to island coalescence.

5.3.3 Second Step: Island Coalescence Process

The tensile stress evolution during film growth is connected to island impingement as depicted in **Figure 5.1** (b). The reason for this process is that the small gaps between adjacent grains are closed by forming grain boundaries with height h_{gb} (**Figure 5.5**). The energy released through the reduction of the surface area of the islands is converted into elastic deformation energy of the participating grains. In recent years, several approaches for the computation of the tensile stress generated by island coalescence have been formulated [90, 100, 101]. In the chosen model's geometry, the approach described by Seel [90] is considered, where the generated average tensile stress in the continuous film is given by

$$\langle \sigma \rangle = \sqrt{\frac{1}{9} \left(\frac{E}{1 - \nu^2} \right) \frac{(2\gamma_s - \gamma_{gb})}{r}}, \quad (5.3)$$

where E is the Young's modulus, ν is the Poisson's ratio, γ_s is the surface energy, γ_{gb} is the grain boundary energy, and r is the radius of the island R at the coalescence point. In the derivation of (5.3) the islands are considered to have a circular shaped cross section [90]. In this study (5.3) is used to describe the tensile stress generated during the island coalescence process. The equation can be applied to predict the average film stress by using parameters γ_s and γ_{gb} available in the literature [102].

5.3.4 Third Step: Thickening

In this section the third growth step for low and high adatom mobility materials is described. Usually, materials with low adatom mobility exhibit a large tensile stress which remains constant throughout the thickening process [89, 92]. For these materials, the third step under the assumption that the stress generated during the second step remains constant throughout is considered.

For high adatom mobility materials, on the other hand, compressive stress can re-emerge. Different theories have been developed to describe compressive stress generation during the third step of V-W growth. Compressive stress development can be due to the movement of atoms toward the edges of the film [103], excess adatom concentration on the surface [104], capillarity effects [105], or movement of atoms into the grain boundaries [91]. The compressive stress generation by the diffusion of atoms into the grain boundaries during film growth is considered. This kinetic model for the evolution of residual stress was validated with measurements in several studies [1, 2, 91]. The theory assumes that the film during its deposition is composed of multiple thin layers. The film is thereby represented by parallel atomic layers in the grains with a grain boundary between them. During the deposition process, the grain boundary height h_{gb} changes as the atoms fill the edge in between the grains. For this process islands are considered with circular arcs between the grain boundaries with the same center for all thicknesses as shown in **Figure 5.6**. $h_{gb,i}$ denotes the grain boundary height, where the i th layer is grown. The atoms can move into the grain boundary, changing the grain boundary height from $h_{gb,i}$ to $h_{gb,i+1}$ [91]. Film stress therefore changes as a function of the grain boundary velocity v_{gb} . The value of v_{gb} is not constant, as it does not only depend on the constant growth velocity v_g , but also on the geometrical transformation of the islands. **Figure 5.7** shows that a higher v_g results in higher grain boundary velocities and consequently changes the magnitude of the generated compressive stress due to the shorter time required for the atoms to move into the grain boundary.

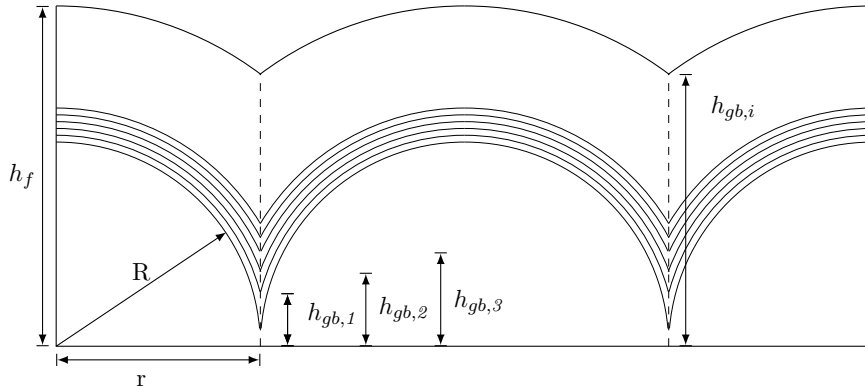


Figure 5.6: $h_{gb,i}$ during film growth.

The atoms can move into the grain boundary, because the film surface is not in equilibrium during the deposition process, which leads to an atomic flux. The chemical potentials on the surface and in the grain boundaries are different from their equilibrium [2, 91].

The increase in the chemical potential on the surface due to non-equilibrium conditions is defined as $\delta\mu_s$. The non-equilibrium condition is caused by the flux of impinging atoms, leading to a supersaturation of adatoms or to a change in surface morphology. The non-equilibrium value of the chemical potential in the grain boundary is a cause of the stress in the layer. It is defined as $-\sigma_i\Omega$ where σ_i is the stress in the i th layer and Ω is the atomic

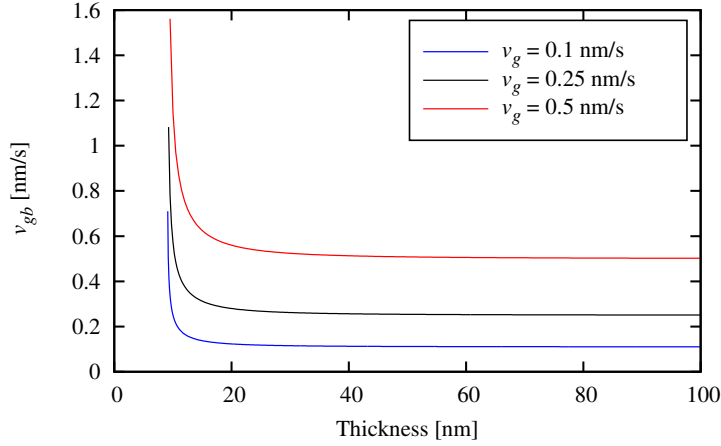


Figure 5.7: Behavior of v_{gb} as a function of thickness for different v_g .

volume. The chemical potential is negative, because the chemical potential is lower than the equilibrium value in the presence of tensile stress. The stress in the layer, and therefore the chemical potential in the grain boundary, changes with time due to the diffusion of atoms into the grain boundary. The difference in the chemical potential between the surface μ_s and the grain boundary μ_{gb} is given by

$$\Delta\mu = \mu_s - \mu_{gb} = \delta\mu_s + \sigma_i\Omega. \quad (5.4)$$

The chemical potential depends on growth conditions and on the stress in the film. The difference in the chemical potential $\Delta\mu$ is the driving force behind the necessary movement of atoms N_{gb} from the surface to the grain boundary. When there is no growth, the chemical potential on the surface and at the grain boundary are identical, therefore no atom moves into the grain boundary. The rate of insertion of atoms into the grain boundary is defined as [1, 2, 91]

$$\frac{\partial N_{gb}}{\partial t} = 4C_s \frac{D}{a^2} (1 - e^{-\Delta\mu/kT}) \cong 4C_s \frac{D\Delta\mu}{a^2kT}, \quad (5.5)$$

where C_s is the fractional coverage, D is the effective diffusivity, a is the height of an atomic step ($\Omega^{1/3}$), k is the Boltzmann constant, and T is the deposition temperature. The atomic step is the amount of space necessary to close two adjacent layers, forming a bond and an additional grain boundary. The atoms can only migrate after a grain boundary is formed, after which a tensile stress, generated by the island coalescence process, is already present. The insertion of atoms into the grain boundary decreases the tensile stress in the film. Thus, the generated stress σ_i at the i th layer can be described as [1, 2]

$$\sigma_i = \sigma_T - \frac{aEN_{gb}}{(1-\nu)L}, \quad (5.6)$$

where σ_T is the tensile stress generated due to island coalescence, ν is the Poisson ratio, and L is the grain size (equal to $2 \cdot r$ (cf. **Figure 5.5**)). The second term in the right-hand-side of (5.6) represents the compressive stress generated by the movement of atoms into the grain boundary.

The stress evolution for the i th layer is obtained by differentiating (5.6) with respect to time. Using (5.5), the rate of stress change is given by

$$\frac{\partial \sigma_i}{\partial t} = -\frac{4EC_s D \Delta\mu}{aLkT(1-\nu)}. \quad (5.7)$$

By solving (5.7), Chason *et al.* [1, 2] evaluated the stress in the i th layer to

$$\sigma_i = \sigma_C + (\sigma_T - \sigma_C)e^{-\frac{\Delta t_i}{\tau}}, \quad (5.8)$$

where Δt_i is the time period in which the atoms can move into the grain boundary. The other terms are defined as

$$\sigma_c = -\frac{\delta\mu_s}{\Omega}, \quad (5.9a)$$

$$\frac{1}{\tau} = \frac{4C_s E \Omega D}{a L k T (1 - \nu)}. \quad (5.9b)$$

The time increment Δt_i is defined [1, 2] by

$$\Delta t_i = \frac{a}{\frac{\partial h_{gb,i}}{\partial t}}. \quad (5.10)$$

When the layer forms ($t = t_i$), only the term σ_T , which is due to coalescence, is relevant.

The velocity v_{gb} has an important influence on compressive stress release. At the beginning, v_{gb} is high and the atoms have a short time in which to migrate into the grain boundary. The stress in the layer therefore becomes more tensile. When the thickness increases, v_{gb} decreases and converges to the average deposition rate; consequently the tensile stress in the film decreases.

To include (5.8) in the model, a reformulation is performed. The velocity v_{gb} can be obtained from the geometry; therefore, the stress for discrete layers can be replaced by a continuum description. By using (5.1), the term $h_{gb,i}$ can be written as:

$$h_{gb,i} = \sqrt{h_f^2 - r^2} = \sqrt{(R_i + tv_g)^2 - r^2}. \quad (5.11)$$

The grain boundary velocity is given by

$$v_{gb} = \frac{\partial h_{gb,i}}{\partial t} = \frac{v_g(R_i + tv_g)}{\sqrt{(R_i + tv_g)^2 - r^2}} = \frac{v_g h_f}{\sqrt{h_f^2 - r^2}}. \quad (5.12)$$

In [1, 2] the stress-thickness product of the film was calculated by summing the stress contributions from each layer and multiplying by the layer thickness

$$\langle \sigma \rangle h_f = a \sum_{i=1}^{N_{layers}} \left[\sigma_C + (\sigma_T - \sigma_C)e^{-\frac{\Delta t_i}{\tau}} \right]. \quad (5.13)$$

In this model the average stress is calculated as a function of film thickness h_f with (5.8) and (5.12) integrating over the interval $[h_{gb,1}, h_{gb,i}]$

$$\langle \sigma \rangle = \frac{1}{h_f} \int_{h_{gb,1}}^{h_{gb,i}} \sigma_C + (\sigma_T - \sigma_C)e^{-\frac{\beta}{(v_g h_f)/\sqrt{h_f^2 - r^2}}} dh, \quad (5.14)$$

where

$$\beta = \frac{4C_s E \Omega D}{L k T (1 - \nu)}. \quad (5.15)$$

The parameter β has the dimension of a velocity, and its value influences the exponential term in (5.14). The average stress generated in the film depends on the number of mobile atoms adjusted by the parameters β and v_g . The value σ_T can be calculated theoretically

using the stress generated at the coalescence point [90] or by fitting to experimental data [1, 2].

Equation (5.14) is implemented in the model and enables to simulate growth processes for different boundary conditions. At every film thickness the integral (5.14) is calculated and its value is used as the initial stress in the film for the next simulation step. Using experimental data, the model can be calibrated and evaluated for different boundary and geometric conditions.

5.4 Results

W and Cu are materials frequently used for TSV interconnects [28, 29]. W is a material with a low adatom mobility, and it exhibits a high value of intrinsic tensile stress. Cu is a material with high adatom mobility and can exhibit compressive or tensile stress depending on the film thickness and the conditions of deposition. For open TSVs, W [29] or Cu [28] are usually used for metalization.

The development of compressive or tensile stress in the thin film in an open TSV can induce delamination or cracking (**Chapter 4**). Usually, tensile stress can generate surface cracking, channeling, spalling, and debonding of the substrate. If the stress in the film is compressive, the dominant failure modes are buckling-driven interface or edge delamination [45]. In the following sections an investigation of the factors which influence the evolution of stress in the film in order to ascertain how to reduce the probability of mechanical failure is studied. The capabilities of the model are demonstrated for W and Cu films.

As described in **Section 5.2.1** during the first step and the second step of the V-W growth, materials with low and high adatom mobility exhibit the same physical behavior. Therefore, it is important to clarify that in this work the results regarding the first and second step are valid for both types of materials. A complete analysis of the three steps of the V-W for low adatom mobility is reported. In contrast only the third step of the V-W for high adatom mobility is presented, since the first two steps are identical to the low adatom mobility. During these two steps proper material parameters have to be used in (5.2) and (5.3) [89, 90].

5.4.1 Low Adatom Mobility Analysis

5.4.1.1 Sample Description

In the following sections the mechanical effects of the V-W growth on a full plate sample and at the sidewall area of an open TSV structure are examined.

Residual stress measurements of W layers, either deposited as blanket films or grown along the sidewall of TSVs etched in silicon, were investigated in [86]. In the full plate sample described in [86], a specific stack was deposited on the silicon substrate. The stack was composed of SiO₂ (500 nm), Ti (40 nm), TiN (55 nm) and W (200 nm). The layer sequence of Ti/TiN/W was repeated twice. In the W layer on the top of the sample structure a grain size of 300 nm ($2 \cdot r$ in **Figure 5.5**) was measured. Since the V-W growth impacts mainly only the first layers, the implement model was simplified by considering one Ti/TiN/W stack.

For the full plate sample the residual stress measured [86] at room temperature was 1.6 GPa. In the TSV sidewall it was four times smaller 0.4 GPa. This large difference could be caused by delamination, difference in the residual stress, non equi-biaxial state of stress or by the presence of rippled sidewalls in the TSV [86]. The measured residual

stress is basically thermal stress generated from the different thermal expansion coefficients between film and substrate (cf. **Section 2.3.2**). The V-W growth occurs during the deposition process where the film stress is different than the value measured at room temperature. Therefore, a FEM elastic thermo-mechanical simulation was performed to obtain the value of intrinsic stress during the deposition process. By considering a deposition process at 400 °C, the obtained film stress was 0.64 GPa. In the following simulations the calibration of the full plate sample with a grain size of 300 nm was performed by using an intrinsic film stress of 0.64 GPa.

5.4.1.2 Island Nucleation and Expansion

During the first step of the V-W growth (5.2) was applied to simulate the growth of W islands already nucleated on a Ti/TiN substrate.

The stress σ_{xx} distribution due to the Laplace pressure during the first step of the V-W growth is shown in **Figure 5.8**. A low tensile stress acts on the surface of the islands and a compressive stress at the center of the islands.

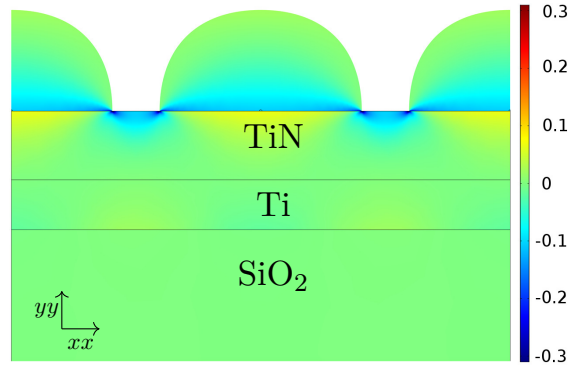


Figure 5.8: σ_{xx} (in GPa) during the initial nucleation of W isolated islands. Development of compressive stress is observable at the W islands.

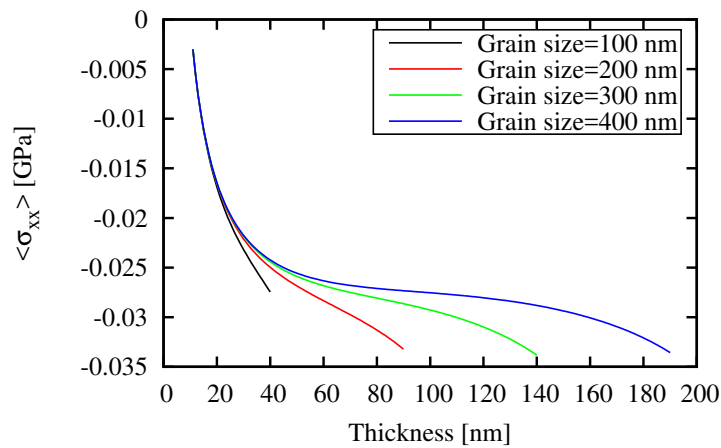


Figure 5.9: Behavior of the compressive stress due to the Laplace pressure for different grain sizes before coalescence. For all the samples $R_{fr}=10$ nm was assumed.

The islands exhibit a compressive average stress $\langle \sigma_{xx} \rangle$ (negative value) which is reported as a function of the film thickness in **Figure 5.9** for different grain sizes. The

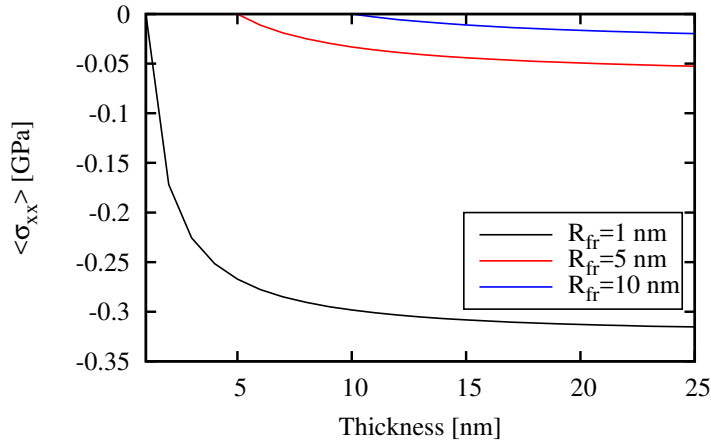


Figure 5.10: Behavior of the compressive stress for different values of R_{fr} .

magnitude of the generated stress is influenced by the grain sizes of the islands. Thin films having big grain size produce less compressive stress compared to small grain size. Because $R_{fr}=10$ nm was set the compressive stress starts from the thickness of 10 nm (cf. **Figure 5.9**).

The generated stress during this first step of the V-W growth can influence the substrate (**Figure 5.8**). If the substrate is thin and the generated stress is high, the probability of crack or delamination at the interface increases (**Chapter 4**).

R_{fr} is a function of the strength of the island-substrate bonding and in this configuration it was assumed to be in a range between 1 nm and 10 nm [90]. In **Figure 5.10** results for three different R_{fr} values and an island grain size of 300 nm are shown. The compressive stress decreases with increasing R_{fr} , and the smallest R_{fr} produces a compressive stress around 300 MPa. Stress in this range can influence the mechanical stability of the system and in particular in the thin layers.

The magnitude of the generated compressive stress is determined by the surface stress f , the frozen-in radius R_{fr} , and the island radius R . Due to the simulation conditions, islands having a large grain size do not impinge rapidly. At the initial simulation step, the distance between islands corresponds at the simulated grain size ($2 \cdot r$ in **Figure 5.5**). When a large grain size is considered, the initial distance between islands is wide. Therefore, islands of a depositing film whose expected grain size is large do not impinge rapidly. The substrate is therefore exposed to compressive stress for an extended period of time. If R_{fr} is small, the strength of the island-substrate bonding is strong and compressive stress can reach a high value, critical to the mechanical stability of the system. In this study the model was applied for a low adatom mobility material. It should be clarified that the model can also be adapted to suit high adatom mobility materials by adjusting the parameters f and R_{fr} in (5.2).

5.4.1.3 Island Coalescence and Grain Formation

During the coalescence process the film stress is gradually changing from compressive to tensile. (5.3) was used at the first contact point between islands where the tensile stress is generated due to the impinge of them. During the coalescence process grain boundaries are formed due to the reduction of the surface area of the islands.

The simulation was calibrated by using the intrinsic stress value of 0.64 GPa (cf. **Sec-**

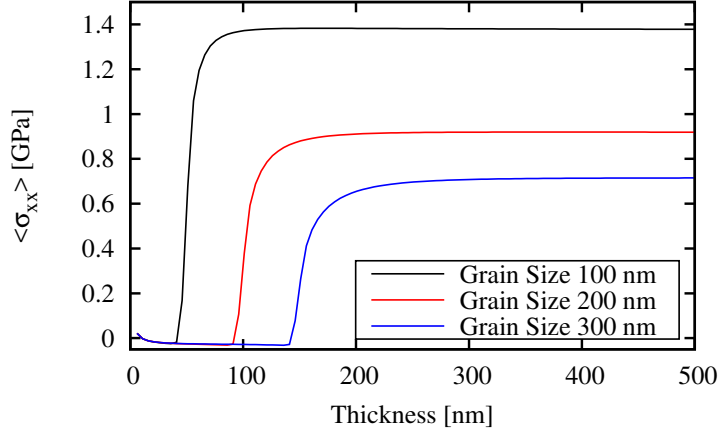


Figure 5.11: $\langle \sigma_{xx} \rangle$ dependence on film thickness for different grain size during V-W growth. After the coalescence, the stress becomes tensile and constant.

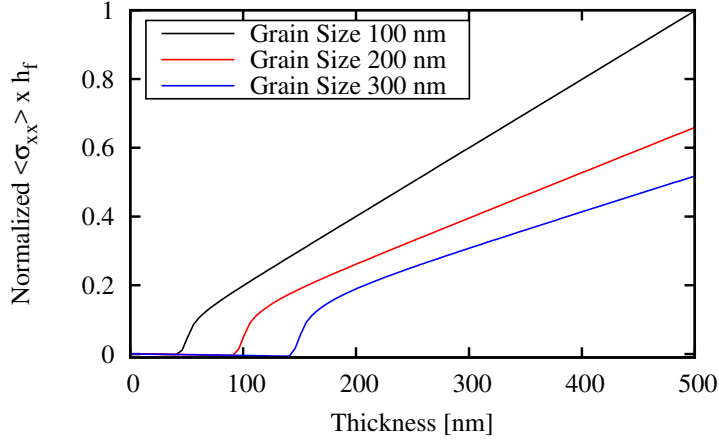


Figure 5.12: Normalized $\langle \sigma_{xx} \rangle \times h_f$ for different grain size during growth.

tion 5.4.1.1). The term $(2\gamma_s - \gamma_{gb})$ in (5.3) was varied until the desired average $\langle \sigma_{xx} \rangle$ at the film thickness of 200 nm was obtained. The values used are shown in **Table 5.1**.

The film stress $\langle \sigma_{xx} \rangle$ as a function of the film thickness is shown in **Figure 5.11**. The simulations were carried out until a thickness of 500 nm was reached. Initially, the film stress is compressive when coalescence starts the compressive stress decreases until it changes its sign and becomes tensile. Subsequently, the film stress increases until it saturates and reaches a constant value. The end of the coalescence process corresponds to the first peak value of the tensile stress. In **Figure 5.11** the influence of the grain size on the film stress is reported. Small grain size produces high stress in the film, on the other hand big grain size produces a small film stress [90] as described in **Section 5.3.3**.

f [J/m ²]	R_{fr} [nm]	$(2\gamma_s - \gamma_{gb})$ [J/m ²]
2.833 [99]	10	7.6

Table 5.1: Parameters used for the simulations. The value $(2\gamma_s - \gamma_{gb})$ was used as fitting parameter.

The stress-thickness $\langle \sigma_{xx} \rangle \times h_f$ is mainly tensile and increases nearly linearly with film thickness. The normalized stress-thickness for different grain size is displayed in **Figure 5.12**. The constant slopes for thicknesses above 50 nm (grain size=50 nm), 100 nm (grain size=100 nm), and 150 nm (grain size=150 nm) indicate the independence of the film stress on the film thickness.

5.4.1.4 Effects of the Island Shapes

The island coalescence process assuming three different nuclei shapes was investigated. In this analysis, stress forms in the film due only to the island coalescence process.

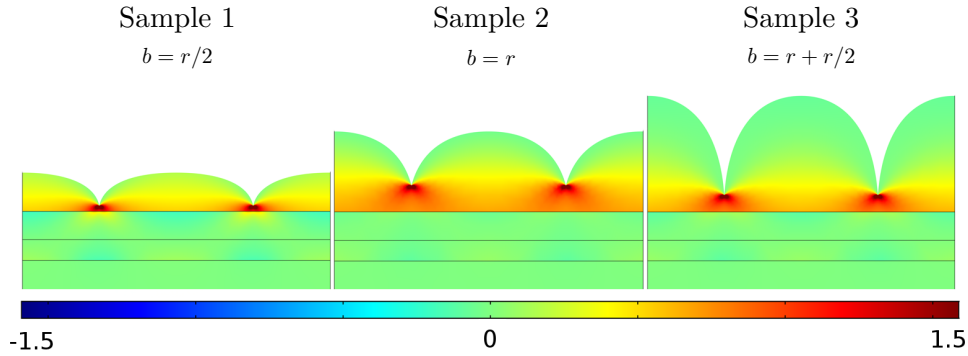


Figure 5.13: Distributions of σ_{xx} stress (GPa) at the point of coalescence for three different samples are shown.

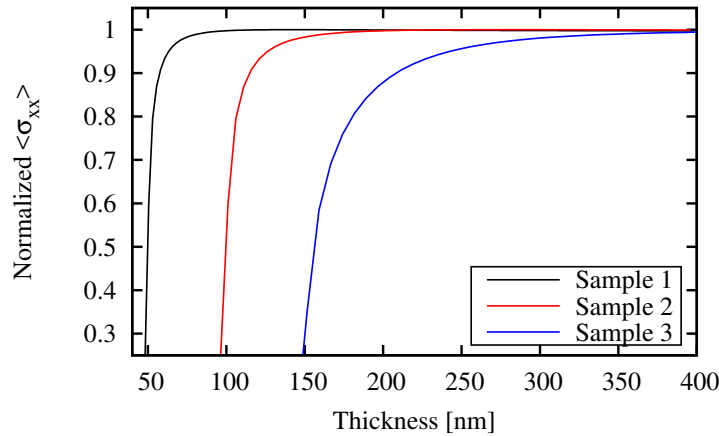


Figure 5.14: Normalized average stress as a function of film thickness measured for the three different samples is shown. As the films thicken, their stress reach a steady value. All the stresses are normalized at the steady value.

The three samples studied are shown in **Figure 5.13**. Sample 2 shows an island with a circular shape, whereas Sample 1 and Sample 3 depict islands of elliptical shape. The island height b is a function of the grain radius (cf. **Figure 5.5**). For all three samples (5.3) was applied at the first contact point between the islands. With the exception of the grain height, all parameters were kept constant for the simulations of all three samples.

The difference in island geometries leads to a different stress evolution during V-W growth. **Figure 5.13** shows the stress components σ_{xx} generated, when coalescence takes

place. Due to the different height to width ratio, coalescence is initiated at different film thicknesses. The stress increase associated with film coalescence therefore starts at different times for Sample 1, 2, and 3 (**Figure 5.14**).

When the film converges to a homogeneous height, the surface irregularity reduces, and the islands' initial shapes have no influence on the intrinsic stress in the film. This phenomenon can be observed in **Figure 5.14**, where the normalized average stress $\langle\sigma_{xx}\rangle$ as a function of film thickness is shown to be constant after film coalescence and equal for all three island shapes.

The maximum stress develops in the film, when the surface roughness is low, specifically when the grain boundary height is equal to the film thickness of a homogeneous film. During the film growth after island collision, the grain boundary height changes as the film thickness increases (h_{gb} in **Figure 5.6**). At the point of coalescence between islands the grain boundary height is small, but as the film becomes thicker the grain boundary height grows reaching approximately the film thickness. Tensile stress develops due to a reduction in the surface areas of the islands [90, 100, 101] and the maximum tensile stress is generated when the grain boundary height is equal to the film thickness. This process is consistent with the results reported in [106], which suggests that tensile stress due to coalescence evolves during grain boundary formation and reaches its maximum value, when the film develops into a homogeneous film. From this analysis, it is possible to see how the microstructure influences $\langle\sigma_{xx}\rangle$ at different film thicknesses. In particular, the grains' size influences stress as well as the thickness of the film and the islands' shapes.

5.4.1.5 Influence of Scallops

For low adatom mobility materials the stress generated at the end of the coalescence process remains constant during the third step of V-W growth. The model was verified for W V-W growth on a full plate sample and at the sidewall of an open TSV. The V-W growth simulation of W on a full plate sample was calibrated using corresponding experimental results **Section 5.4.1.1**. Subsequently, the calibrated model was used to simulate the V-W growth of W at the sidewall of an open TSV.

The third simulation step is dominated by the film-thickening. The deposited metal (W) is a low-mobility material, therefore the generated intrinsic stress remains tensile during the growth [89]. In **Figure 5.11** the results of the V-W growth on a full plate sample are shown. The mechanical stress in the film is constant and tensile after the end of the coalescence process. As the grain size of the film decreases the intrinsic film stress increases.

The formation of surface roughness along the TSV sidewall, called scallops, due to the etch process is characteristic of open TSVs. This particular structure modifies the distribution of stress in the W layer. The CVD growth process was reproduced on a scalloped surface. As reported in [86] the film stress measured at room temperature along the sidewall of an open TSV was four times smaller than the stress in a full plate sample. To understand the possible effects of the TSV geometry a more detailed investigation on the influence of a scalloped substrate on the intrinsic film stress was carried out.

In **Figure 5.15** the $1\ \mu\text{m}/0.1\ \mu\text{m}$ structure is depicted, where w_s and h_s indicate the width and the height of the scallops, respectively. The W layer is grown on top of a 40 nm TiN layer which sits on top of a SiO₂ substrate; this structure corresponds to the sidewall of an open TSV before W deposition [29]. During V-W growth the generated stress also influences the substrate where the thin film is grown. In order to investigate how the mechanical stress affects the substrate, a compressive residual stress of 1GPa was set in the TiN layer [67]. Usually the SiO₂ substrate contains inconsequential amounts of residual

stress [67] and it was therefore considered stress free in this study. In all simulations the same material properties were used and the grain size of the W islands $2 \cdot r$ was set to 200 nm.

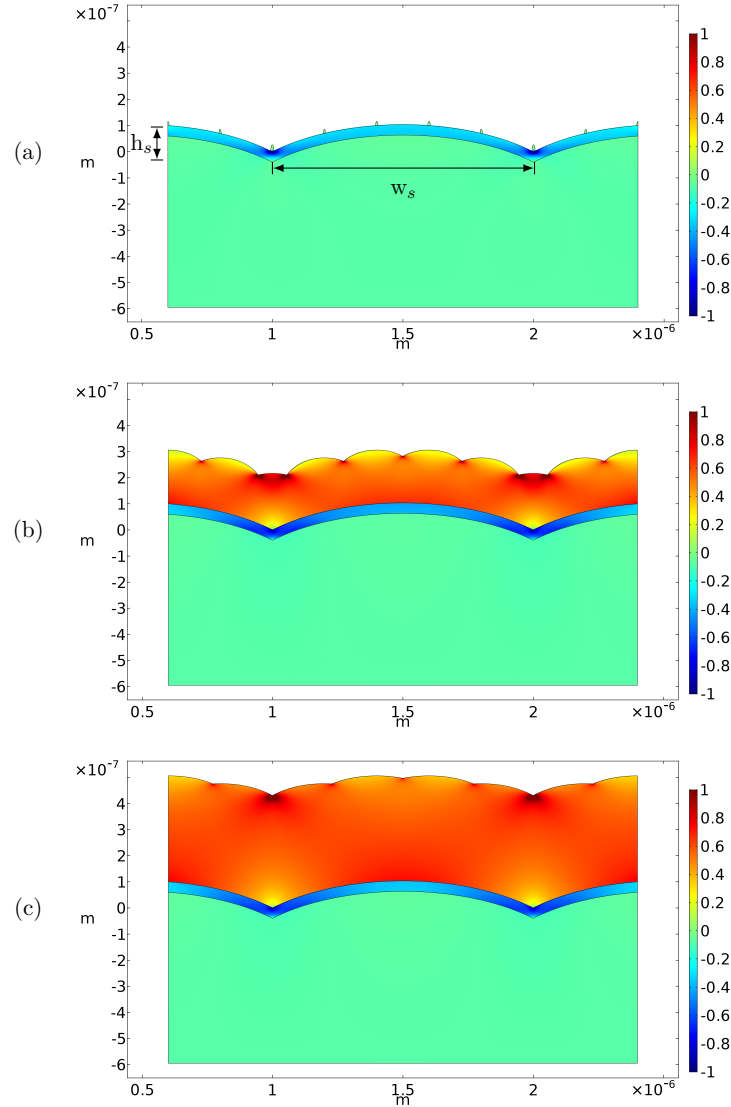


Figure 5.15: Normalized $\langle \sigma_{xx} \rangle$ distribution in a scalloped structure ($h_s=0.1 \mu\text{m}$ and $w_s=1 \mu\text{m}$) for three different film thicknesses (~ 0 nm (a), 200 nm (b), and 400 nm (c)).

The W layer exhibits a low adatom mobility; therefore (5.3) was used to describe the film growth. The effects of the scalloped structure on the normalized average stress were investigated (cf. **Figure 5.15**). This particular structure can produce a high concentration of stress during film thickening, which leads to mechanical failure. In **Figure 5.15** the normalized stress distributions at film thicknesses of ~ 0 nm, 200 nm, and 400 nm are displayed. The highest tensile stress is observed at the intersection points of the grains. In turn, the highest compressive stress is observed at the intersection points of the scallops. These locations are the critical areas in which a crack in the film or delamination can occur.

The compressive stress in the TiN layer is influenced by the film growth. Initially high values of compressive stress are concentrated only at the intersection points of the scallops.

However, when the film is formed, the compressive stress in the TiN layer spreads toward the center of the scallops.

5.4.1.6 Effects of the Scallop Geometry (Width & Height)

By simulating different scallop sizes important information about the stress generation during film growth on a confined geometry was obtained. The etch process can be designed in order to produce scallops with different geometries. Scallops with a width/height of $0.75 \mu\text{m} / 0.1 \mu\text{m}$, $1 \mu\text{m} / 0.2 \mu\text{m}$, and $1.25 \mu\text{m} / 0.3 \mu\text{m}$ were considered. As previously reported the average film stress is strongly dependent on the film thickness. In the scalloped structure, compared to the full plate sample, the tensile stress due to coalescence increases at a reduced rate as the thickness increases.

Figure 5.16, **Figure 5.17**, and **Figure 5.18**, are the simulation results of a W film grown on scalloped geometries with height/width of $0.75 \mu\text{m} / 0.1 \mu\text{m}$, $1 \mu\text{m} / 0.2 \mu\text{m}$, and $1.25 \mu\text{m} / 0.3 \mu\text{m}$, respectively. In all the figures the green line indicates the normalized average stress during the V-W growth on a full plate sample. The other lines represent the normalized average stress during V-W growth for different scalloped structures where h_s and w_s were varied. For the full plate sample, during the third V-W growth step, the average stress remains constant, as is characteristic of low adatom mobility materials.

In **Figure 5.16** (a), **Figure 5.17** (a) and **Figure 5.18** (a) the width w_s of the scallops was kept constant at $0.75 \mu\text{m}$, $1 \mu\text{m}$, and $1.25 \mu\text{m}$, respectively, and the height h_s of the scallops was varied between $0.1 \mu\text{m}$, $0.2 \mu\text{m}$, and $0.3 \mu\text{m}$ at every width. In all samples the same stress evolution is observable. The width w_s of the scallops influences the stress at small thicknesses; subsequently, as the thickness increases, the film stress evolves similarly for all samples. In **Figure 5.16** (a) it is evident that the width of the scallops affects the film stress evolution until a thickness around 200 nm is reached. Similar is the case in **Figure 5.17** (a) and in **Figure 5.18** (a), where the film stress evolution is unaffected by scallops until thicknesses of 225 nm and 250 nm are reached, respectively. In all figures it is evident that a sharp stress increase takes place during thickening. This increase is connected to the overtaking of grains by neighboring grains. As the scallop width w_s increases this process is delayed, leading to the sharp stress increase at different film thicknesses. This phenomenon of overtaking grains is further described in the next subsection.

In all the samples with $h_s=0.1 \mu\text{m}$ and a varied w_s the normalized average stress does not significantly vary with the scallop width. This is depicted in **Figure 5.16** (b), where in all the scalloped structures the tensile stress evolves similarly and converges at the same maximum value for all samples. In this configuration the scallop heights do not significantly change the film geometry which is still essentially flat and therefore no extreme stress variations are observable.

In **Figure 5.17** (b) h_s was set to $0.2 \mu\text{m}$ and w_s was varied. Here, between film thicknesses of 125 nm to 250 nm different stress behaviors are observed. In this thickness range the film assumes the scalloped shape and its stress is influenced by the geometry. In all the results a sharp stress increase is evident due to grains which are overtaken by neighboring grains. The smallest generated stress is in the structure having $w_s=0.75 \mu\text{m}$ due to the scallop curvatures. In general, as the curvature of the scallops increases (big h_s and small w_s), the film stress decreases.

In **Figure 5.18** (b) the scallop structures have $h_s=0.3 \mu\text{m}$ and the width w_s was varied. These samples correspond to the structures having the most curved scallops. In particular the sample with $w_s=0.75 \mu\text{m}$ has the most pronounced scallop curvature and a small average film stress develops before finally reaching the maximum stress. Also

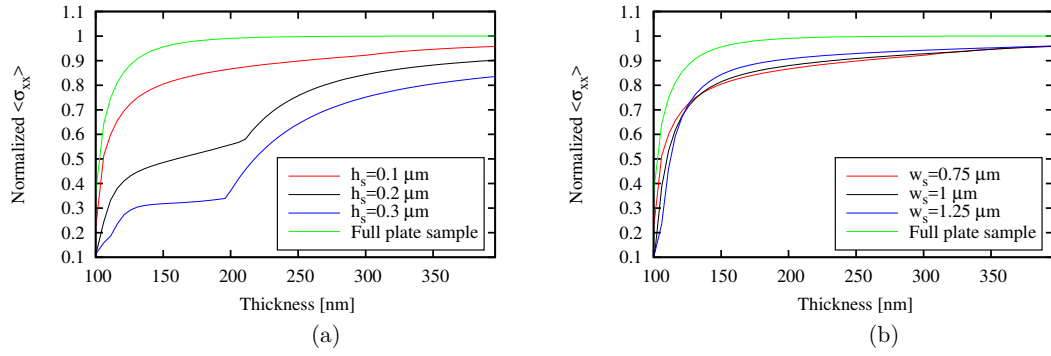


Figure 5.16: Normalized average stress as a function of film thickness measured for different samples. In (a) the height of the scallops was varied, keeping constant the width of 0.75 μm . In (b) the height of 0.1 μm was fixed and the weight of the scallops was varied.

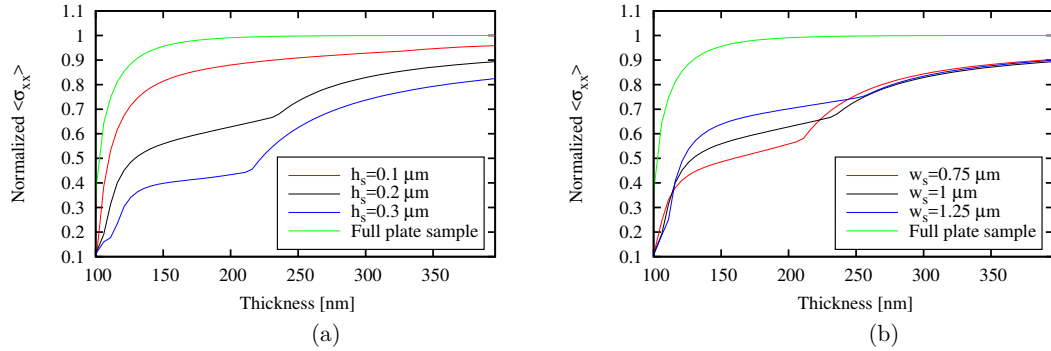


Figure 5.17: Normalized average stress as a function of film thickness measured for different samples. In (a) the height of the scallops was varied, keeping constant the width of 1 μm . In (b) the height of 0.2 μm was fixed and the width of the scallops was varied.

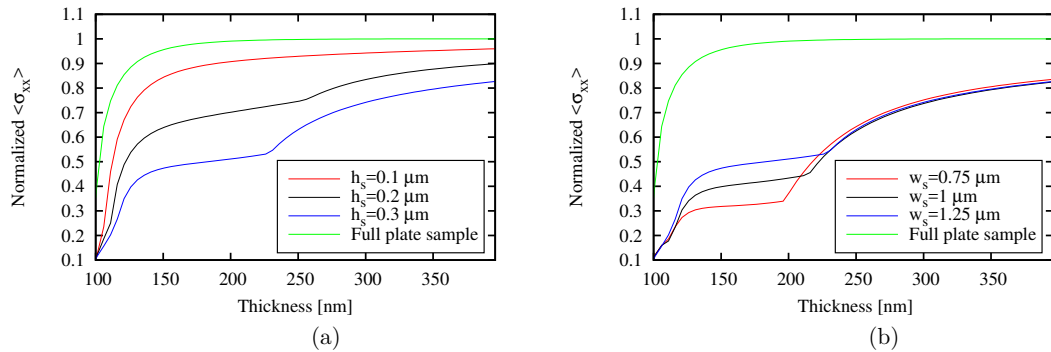


Figure 5.18: Normalized average stress as a function of film thickness measured for different samples. In (a) the height of the scallops was varied, keeping constant the width of 1.25 μm . In (b) the height of 0.3 μm was fixed and the width of the scallops was varied.

here the sharp stress increase at a thickness between 200 nm and 250 nm is due to the overtaking of grains by neighboring grains. This stress behavior is related to the curvature of the scallops that influence the grain growth during film thickening. The grain boundary height h_{gb} increases slowly, unlike in a full plate sample. During the deposition process the film stress build-up evolves. The maximum tensile stress is reached only when the

grain boundary height is equal to the film thickness [106]. Due to the scallop curvatures a homogeneous film (for low roughness the grain boundary height corresponds to the film thickness) is formed at high thicknesses; therefore, at small thicknesses the grain boundary height is small and a low amount of intrinsic tensile stress is generated.

In all samples a stress decrease was observed for thin films (below $\sim 200\text{-}250$ nm), when a notable curvature is present in the scallops, such as at high h_s or at small w_s . The generated stress in these samples is less than that produced in a full plate sample. When the grains are grown on curved surfaces, they have less contact area, thereby producing less stress.

This simulation approach can be used to investigate the stress evolution for arbitrary geometries.

5.4.1.7 Overtaking of Grains

The sharp stress increase observed in **Figure 5.16**, **Figure 5.17**, and **Figure 5.18** of the previously subsection can be described by considering the overtaking of grains. As the film thickness increases a grain can be overtaken by the neighboring grains as depicted in **Figure 5.19**. As described previously the intrinsic stress build-up is an evolving process dependent on the grain boundary height. During overtaking the contact area (grain boundary height) between grains rapidly increases and the film starts to be homogeneous, leading to a rapid stress increase.

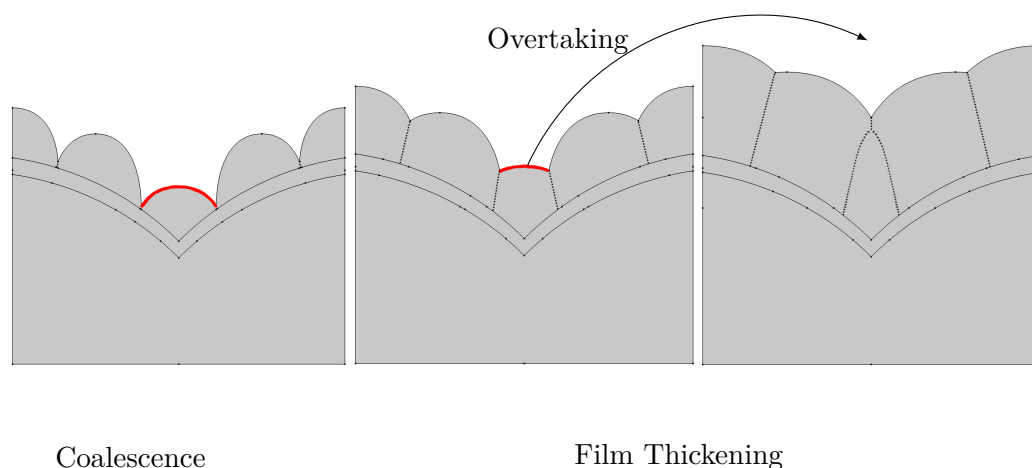


Figure 5.19: Schematic representation of grain overtaking. As the film thickness increases the grain which grows between scallops (indicated in red) is overtaken by the neighboring grains.

The stress in low adatom mobility films grown on a full plate sample stays constant during the third step of the V-W growth. However, when films are grown on a scalloped structure this is no longer the case and two phases of film thickening can be clearly identified:

- The first phase identifies the stage before the overtaking of grains. The film stress has a small value compared to a film grown on a full plate sample. In this phase the intrinsic stress is significantly lower than that in flat samples. This explains the reduced stress in thin films from published experiments [86].

- The second phase indicates the stage after the overtaking of grains. A homogeneous film is forming and a rapid stress increase in the film increase characterizes this stage is observed. As thickening proceeds, the stress approaches the value found in flat samples.

The two-phase stress development during thickening suggests that the scallops only help reduce stress in thin films. For thick films the stress eventually reaches the levels observed in flat samples.

5.4.2 High Adatom Mobility Analysis

5.4.2.1 Temperature Effects

The implemented model, which simulates the generation of compressive stress during the third V-W growth step for high adatom mobility materials, was verified by using stress measurements of Ag films grown on SiO₂. In [1, 2] the stress-thickness product as a function of thickness was measured by changing the deposition temperature. Since the adatom mobility depends on temperature, the shape of the curve at higher temperatures becomes less tensile (i.e. more compressive) as the thickness increases. This experimentally derived behavior [1, 2] is shown in **Figure 5.20**. All samples were grown using a fixed growth rate of $v_g = 0.2$ nm/s.

With the FEM model the experimental data were reproduced by using (5.14), where $\sigma_T = 1550$ MPa and $\sigma_C = -200$ MPa. All simulations were started with an assumed film thickness of 20 nm. The model reproduces the experimental results at different temperatures by varying β (the employed β values are in the inset of **Figure 5.20**).

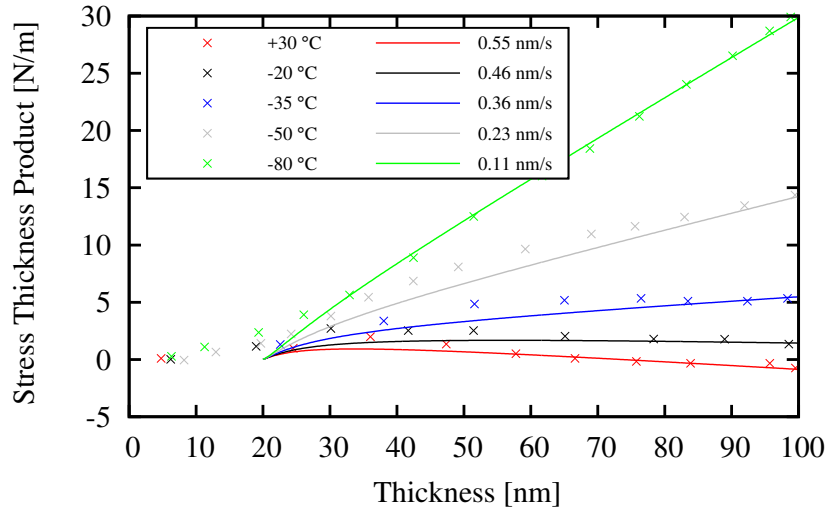


Figure 5.20: The crossed data points are the experimental data from [1, 2], and the lines are the results of the FEM simulations.

In the stress-thickness versus thickness plot (cf. **Figure 5.20**) a tensile behavior is only observable at low temperatures (green line), and at high temperatures the transition from tensile to compressive stress can be seen clearly (red line). In these simulations is assumed that the generated compressive stress is driven only by adatom mobility, allowing the atom to move into the grain boundary. This suggests to vary the atom diffusivity with β . Higher values of β correspond to higher adatom mobilities, whereas smaller values stand for lower adatom mobilities. The simulations produced results with qualitatively

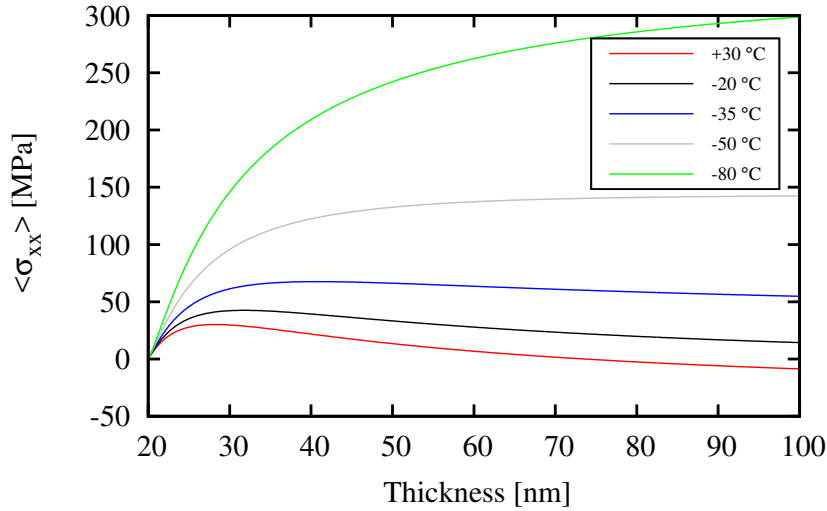


Figure 5.21: Average stress obtained from FEM simulations for different deposition temperatures.

good agreement to experimental data and it provided an understanding of the transition from tensile to compressive stress. The best fittings are obtained at low deposition temperatures. This observation is ascribed to a constant distribution of grain sizes under these growth conditions. At higher temperatures the simulation results of the model fit quantitatively better to experimental results at high film thickness. Especially for temperatures between $-20\text{ }^{\circ}\text{C}$ and $30\text{ }^{\circ}\text{C}$ (cf. black and red lines in **Figure 5.20**) the simulations are in quantitatively good agreement for thicker films, where the model predicts the generation of compressive stress. For small thicknesses the model underestimates the generation of tensile stress. It is supposed that the film roughness and the different sizes of the islands for small film thicknesses have a significant influence on the stress. These effects are not included in the model, due to the impossibility of tracking them experimentally.

$\langle \sigma_{xx} \rangle$ was calculated in the film as a function of film thickness and the results are depicted in **Figure 5.21**. The magnitude of the stress is strongly dependent on the deposition temperature. The transition from tensile to compressive stress at high temperatures is clearly observable. Therefore, the model can be used for the simulation at different deposition temperatures.

As far as interconnect design is concerned, the knowledge of $\langle \sigma_{xx} \rangle$ as function of film thickness can be used to reduce the probability of mechanical failure. In this study the capability of the model to reproduce the deposition process for different temperatures were verified.

5.4.2.2 Growth Rate Effects

In [3] stress measurements during Cu electrodeposition on an Au substrate were carried out. Cu was deposited at room temperature with different growth rates v_g . In order to create a consistent starting layer with respect to grain size for all the considered deposition processes, 100 nm of Cu was deposited with a growth rate of 9.1 nm/s in the first phase. The resulting grains had an average size of $L = 200\text{ nm}$ [3]. After reaching 100 nm thickness, the second phase was initiated by changing the electrical potential, thereby producing different growth rates. Unlike the situation described in the previous section,

the model applied here was verified by changing the growth rate and keeping the other parameters constant.

The electrical potential at the electrodes influences the nucleation density and the growth rate in the electrodeposition process. The experimental stress-thickness product as a function of thickness was reproduced by simulation. The parameters $\sigma_T = 230$ MPa, $\sigma_c = -195$ MPa, and $\beta = 4.125$ nm/s were utilized in the simulation. In **Figure 5.22**, the obtained experimental values for the stress-thickness product between -0.45 V to -0.65 V were compared with the simulation results. An average grain size of 200 nm was used as it fits well to experimental data, even though the grain size for thicknesses over 100 nm was not measured for this experiment [3]. A change in the average grain size during growth may alter the film stress, however, the model qualitatively reproduces the experimental results well with the assumed grain size. The model accurately fits

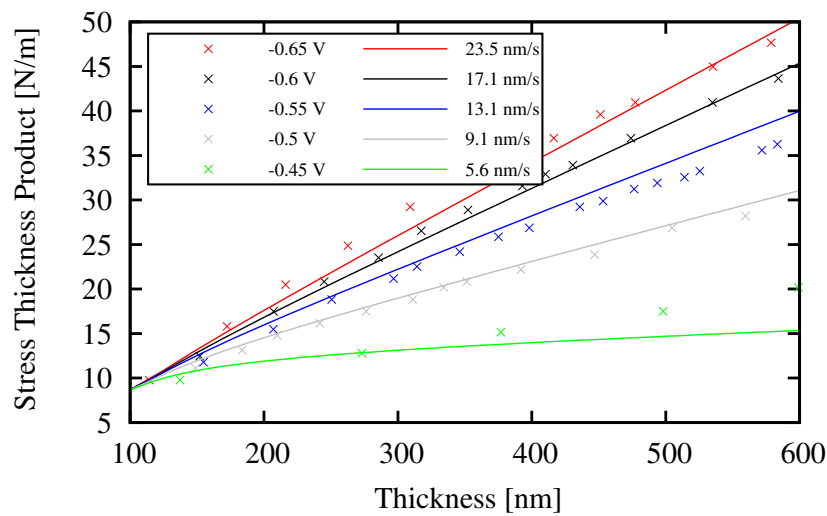


Figure 5.22: The crossed data points are the experimental data from [3] and the lines represent the FEM simulations.

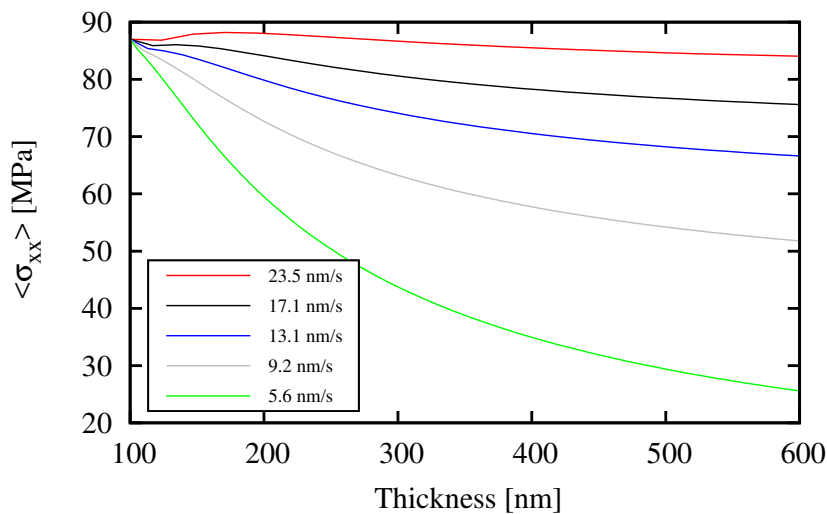


Figure 5.23: Average stress measured from FEM simulations for different thicknesses is shown.

the experimental results for growth rates between 9.1 and 23.5 nm/s. For this range of deposition rates the grain sizes generated by the initial deposition process for all samples were kept constant in the subsequent process phases as the growth rates are increased. At a growth rate of 5.6 nm/s the model does not properly predict the stress for high material thicknesses possibly due the fact that the growth rate in the initial phase surpasses the growth rate of the thickening phase. This can lead to the generation of additional grains leading to a higher roughness of the film. These effects, which might influence the stress in the film, are not included in the model. The growth rate has a significant influence on the residual stress in the film (cf. **Figure 5.23**). For all the simulated deposition conditions, as the growth rate decreases, the film stress reduces. Slow growth rates correspond to a low grain boundary velocity and therefore the film stress becomes less tensile and more compressive. At slow growth rates the adatoms have ample opportunity to move into the grain boundary, generating compressive stress, while at high growth rates the stress remains almost constant throughout thickening.

5.5 Summary

The intrinsic stress generated during the deposition processes of thin metal films was investigated. Since the metalization of wafers in microelectronics is usually performed at the "back end" of the production line, it is important to understand the origin and behavior of stress during film deposition in order to increase reliability and to prevent mechanical failure of the interconnects. The three growth steps responsible for the evolution of stress were identified, and each of them was simulated by FEM.

By applying the concepts of Laplace pressure and of the frozen-in radius, compressive stress generation in the islands during the first growth step was simulated. The estimation of the magnitude of the stress is a very challenging task due to the lack of experimentally confirmed parameters. Nevertheless, the model helps to understand, how stress caused by volume increase develops at the substrate and inside the islands. Information regarding stress distribution in the substrate is useful, when it comes to adjusting the deposition process in order to limit mechanical failures (e.g. delamination, cracks, etc.).

By using Seel's approach the second step regarding the process of island coalescence was examined. At small thicknesses of the film, the shape of the island, grain sizes, and film roughness are factors which influence the stress build-up in a film. For thick films the film is homogeneous (low roughness) and the stress is equally distributed. During the growth process, the maximum stress is reached, when a homogeneous film is formed. For a thin film the island shapes change the stress distribution and thereby the average stress in the film. Therefore, different stress values can be obtained in thin films. Smaller grains exhibit higher stresses, whereas bigger grains produce lower stress in the film.

The stress behavior due to low adatom mobility was analyzed during W growth on a scalloped structure and on a full plate sample. The results demonstrated that the substrate shape influences the film stress for thin films. Thin films grown on a scalloped surface with a high curvature develop a small intrinsic stress. Due to the curved substrate the thickness necessary to reach a homogeneous film increases leading to a small intrinsic stress generation. The grain boundary height on a scalloped structure grows differently than in a flat sample. During the film grows, height and width of the scallops influence the contact areas between islands and consequently the tensile stress generated. As film thickness increases the film becomes homogeneous (when the grain boundary height correspond to film thickness) and the tensile stress converges at the stress value found in a full plate. A new phase in the stress evolution during film thickening on scalloped surfaces was

identified. The first phase indicates thin film growth at the stage before the overtaking of grains, while the second phase occurs after grain overtaking and is similar to the traditional V-W thickening during deposition on flat surfaces. This information can be used during deep reactive ion etching for TSV fabrication. By controlling the etching parameters, the appropriate scallop size necessary to minimize mechanical failure can be achieved. Scallop geometry permits to reduce considerably the film stress. Deposition on scallops having the largest height/width ratio ($h_s=0.3 \mu\text{m} / w_s=0.75 \mu\text{m}$) produce $\sim 70\%$ less film stress compared to a full plate sample. On the other hand, films grown on scallops having the smallest height/width ratio ($h_s=0.1 \mu\text{m} / w_s=1.25 \mu\text{m}$) produce $\sim 20\%$ less of stress compared to a full plate sample. Scallops influence the stress evolution between the coalescence process and the overtaking of islands. As the film becomes thicker the scallop geometry does not impact the stress evolution.

A high adatom mobility model was implemented on the basis of the theory described by Chason. Compressive stress in a film is generated due to the movement of atoms into the grain boundary. The implemented model is able to reproduce measured data from two different experiments. In the first, the effects of the deposition temperature on film stress and in the second the effects of different growth rates were replicated. High deposition temperatures and slow growth rate produce small intrinsic tensile stress. The calibrated model can be applied to investigate the stress evolution for future applications. In open TSVs, Cu is still deposited by electrodeposition. This process often shows an abnormal grain growth. For such cases the described model is not able to properly handle the deposition process. Future technologies generations demanding higher aspect ratio TSVs might require a CVD Cu deposition. However, Cu films deposited by CVD are still not worthy manufacturing [107].

6

Summary and Outlook

One of the key paradigms to enhance and improve the capabilities and performance of ICs is 3D integration. The work presented in this thesis advances the understanding of the mechanical reliability of open TSVs, which are one of the central components in 3D integration. The TSV is essentially a vertical conductor connecting the top and the bottom of a silicon substrate in a stacked die. Because TSVs have the task of electrically connecting components in an IC, its reliability is a fundamental aspect to examine. The TSV reliability deals with the tolerable thermal budget, mechanical stability, process variability, and electromigration. Each of these aspects can seriously impact and compromise the performances of the IC. Therefore, all reliability aspects have to be thoroughly investigated. The work presented here is focused on the mechanical stability of open TSVs. TSV interconnects can mechanically fail due to tensile rupture, creep failure, and fatigue causing an open circuit in the conducting line.

Before mass production is viable, a variety of experimental, modeling, and analysis techniques must be employed in order to investigate all potential failure conditions. Using experimental analysis and simulation techniques, TSVs under different scenarios can be examined and the most reliable configuration of the TSV structure for a desired application can be obtained.

In this thesis FEM, a numerical method which permits to analyze different multiphysical problems, has been employed. Mechanical simulations have been performed for open TSVs, which frequently use conducting materials based on W or Cu metalization technology. The presented work is focused on open W-lined TSVs, which are already used in mass production in image sensors to transport the sensor signal between vertically-stacked dies. W is used when the IC is subjected to many temperature cycles because it has a smaller thermal expansion coefficient compared to Cu. Therefore a smaller stress variation at the interfaces between W and Si under thermal cycling results in a higher structure stability. However, during the deposition process the W develops a very high intrinsic stress, which can be problematic for the stability of the TSV and, furthermore, for the entire IC. For this reason the potential mechanical problems in open W-lined TSVs have been investigated. Results of this investigation extend the state-of-the-art knowledge about the failure modes in such structures.

External forces applied on the structure during 3D IC stacking can generate stress, leading to rupture, in the form of cracking or delamination, in the device. An experimental setup, provided by an industrial partner, was replicated in a FEM environment in order to simulate the effects of an external force acting on the open TSV. By comparing the simulations with measurement data two critical areas with high concentrations of mechanical stress were identified; one located above the applied external force and the other at the bottom corner of the TSV. In these areas different material layers are stacked and a high concentration of mechanical stress can generate mechanical failure such as cracking or delamination. The chosen approach is useful to identify a TSV geometry (re-enforcement

materials and layer thicknesses), necessary to improve the mechanical stability of the structure.

The identified critical areas serve as potential candidates for delamination and were investigated in further detail. The critical conditions necessary for delamination propagation at the high stress locations were predicted. The critical locations are situated at the material interfaces, found in the multilayer structure at the bottom of the TSV. The delamination propagation was determined by calculating the energy release rate at the interfaces. Critical energy release rates for those interfaces are used as a criterion for the delamination propagation. The energy release rates have been calculated using FEM in combination with two different methods. For the first method the energy release rate is calculated using the *J*-Integral approach. For the second method the energy release rate is derived in two steps: in the first step the stress values of the FEM simulation at the interfaces between the materials are gathered, and in the second step the necessary parameters to calculate the energy release rate are fitted through regression analysis of the collected stress values. The first method has been applied to the interfaces present at the bottom of the TSV. The results have shown a critical instability at the SiO₂/W interface. The highest energy release rate is found when the W layer was assumed to carry a high intrinsic tensile stress. The first method is realized by calculating an integral over the crack tip. However, if the considered material layers are very thin, as is the case in our study a suitable integral path around the delamination tip, with respect to the meshing density, can not be defined. Therefore the second method has been implemented and verified with data found in thin layer experiments. The two methods have been further employed to calculate the energy release rate for thicker layers in the same structure producing results with good agreement. These two methods can be used to investigate the critical factors which lead to delamination propagation.

When thin material films are stacked, as in TSVs, the mechanical stability of the system can be compromised by the presence of a high intrinsic stress. In the scope of this thesis a model for the simulation of the stress build-up during deposition of thin films was implemented by using FEM. Due to thermodynamical reasons, polycrystalline metal films deposited onto polycrystalline or amorphous substrates grow according to the Volmer-Weber mode. During the Volmer-Weber mode, three unique growth steps can be distinguished: nucleation, coalescence, and film thickening. In the two first steps the film stress evolves from compressive to tensile. In the third step, which is film thickening, the stress can return to compressive or stays tensile, depending on the continued grain-structure evolution during growth. Materials with a low adatom mobility (high melting temperature) exhibit a columnar grain structure which results in a constant stress during film thickening. For materials with a high adatom mobility (low melting temperature) the microstructure forms equiaxed grains which continue to evolve during film thickening, resulting in a possible compressive stress generation. Models were developed which are useful for the simulation of low and high adatom mobility materials. Stress behavior of low adatom mobility materials was analyzed during W growth onto a scalloped structure and onto a flat sample. Due to the deep reactive ion etching process a scalloped structure can form along the TSV sidewall. The simulation and measurement results have shown that the substrate shape influences the stress in thin films. Thin films grown on a scalloped surface, with a pronounced curvature, develop a small intrinsic stress. The scalloped geometry permits to reduce the film stress considerably. In addition, the implemented model was verified for high adatom mobility materials. The model is able to reproduce the measured data from two different experiments, where in the first Ag was deposited on a SiO₂ layer and in the second Cu was deposited on a Au layer. For the first experimental

results the effects of the deposition temperature on the film stress were replicated and for the second the effects of different growth rates were reproduced. High deposition temperatures and slow growth rates result in small intrinsic film stress. The implemented model for low adatom mobility materials can be applied to investigate the stress evolution in any geometry. The model for high adatom mobility can be used for the analysis of the fabrication effects in complex structures, such as metal deposition in open Cu-TSVs.

The aim of the simulations and models presented here help to understand the potential mechanical problems occurring during IC fabrication, while also enabling a physical prediction of the mechanical stability of open metal-lined TSVs. However, as the 3D integration technology evolves further studies and model improvements will be essential.

The employed methodology and the implemented model, which mimics external forces during the 3D stacking of ICs are used to analyze the stress behavior in the TSV structure. This simulation approach can be used to find alternative geometries and fabrication methods in order to limit the resulting mechanical failure in TSVs. This gives chip designers the possibility to reduce the necessity for expensive and time-consuming experimental tests. Nevertheless, the simulations can be further improved by considering the plastic behavior of the individual materials, but also of the entire multilayer structure. Stress-strain curves of thin films provide the necessary information to describe plasticity of a single material. However, the interaction between layers in a stacked structure can differ from the single layer material behavior. Further studies must be carried out to understand how the plasticity of the materials evolves inside the TSV structure.

The implemented model used to predict delamination has been implemented to investigate the factors which influence delamination. However, more experimental measurements of the critical energy release rate for interfaces which are present in the open TSV are necessary. Measurements of the SiO_2/W interface have been performed by our industrial partner and they found that these results differ from those found in literature. The technique, the size of the samples, and the microstructure of the materials are all factors which influence the critical energy release rate. Therefore, new and different experimental methods to measure the critical energy release rate in open TSVs are essential.

The developed method used to simulate stress build-up in thin films has provided interesting results, in particular about deposition on scalloped substrates. Films grown on a scalloped structure develop less stress compared to a flat alternative. Stress measurements during film growth on different scalloped substrate geometries (different heights and widths of the scallops) should be performed to compare and validate the obtained results against measurements. The model for low adatom mobility materials is suitable to analyze the stress evolution in the IC fabrication processes.

A

Kolosov-Muskhelishvili Formulas

The Kolosov-Muskhelishvili formulas provide the most convenient method to treat two-dimensional crack problems. This formulation allows us to consider stresses and displacements in terms of analytic functions of complex variables. Here, this formulation is derived for two-dimensional problems [70, 71].

A.1 Airy Stress Function

To derive the Kolosov-Muskhelishvili formulation it is necessary to introduce a new function, known as the Airy stress function. By using the stress-strain relations (2.46) together with the equilibrium equations (2.43) and the compatibility equations (2.45) described in **Section 2.2** we can rewrite the compatibility condition as

$$\nabla^2 (\sigma_{xx} + \sigma_{yy}) = 0, \quad (\text{A.1})$$

where the ∇^2 is the Laplace operator defined by

$$\nabla^2 = \frac{\partial^2}{\partial x^2} + \frac{\partial^2}{\partial y^2}. \quad (\text{A.2})$$

The Airy stress function ϕ is defined as

$$\sigma_{xx} = \frac{\partial^2 \phi}{\partial y^2}, \quad \tau_{xy} = -\frac{\partial^2 \phi}{\partial x \partial y}, \quad \sigma_{yy} = \frac{\partial^2 \phi}{\partial x^2}. \quad (\text{A.3})$$

By using the relationships (A.3) in the equilibrium equations (2.43) it is possible to demonstrate that the equilibrium conditions are automatically satisfied by ϕ and (A.1) can be rewritten

$$\nabla^4 \phi = \nabla^2 \nabla^2 \phi = 0, \quad (\text{A.4})$$

where ∇^4 is the biharmonic operator and any function ϕ satisfying this equation is biharmonic.

A.2 Analytic Function and Complex Variable

Secondly, the Kolosov-Muskhelishvili method is formulated by describing two-dimensional elastic problems using analytic functions of complex variables. We define the position representation by the complex variable z , which in polar coordinates (r, θ) is given by

$$\begin{aligned} z &= r(\cos \theta + i \sin \theta) = r e^{i\theta}, \\ \bar{z} &= r(\cos \theta - i \sin \theta) = r e^{-i\theta}, \end{aligned} \quad (\text{A.5})$$

where \bar{z} stands for the complex conjugation. (A.5) can also be described using the Cartesian coordinate system (x, y) :

$$\begin{aligned} z &= x + iy, \\ \bar{z} &= x - iy. \end{aligned} \tag{A.6}$$

A function of the complex variable z ,

$$f(z) = f(x + iy) = f(x + iy) = \text{Re}f(z) + i\text{Im}f(z), \tag{A.7}$$

is said to be analytic at a point z_0 , if it has a derivative at z_0 and at its neighborhood.

A.3 Complex Representation of the Airy Stress Function

To obtain the complex potential representation of the Airy stress function we introduce a function P

$$\nabla^2\phi = P \quad \text{and} \quad \nabla^2P = \nabla^2\nabla^2\phi = 0, \tag{A.8}$$

where

$$\nabla^2\nabla^2 = \frac{\partial^4}{\partial x^4} + 2\frac{\partial^4}{\partial x^2\partial y^2} + \frac{\partial^4}{\partial y^4}. \tag{A.9}$$

Due to the definition (A.4) P is harmonic. We define

$$P = \text{Re}\{f(z)\}, \tag{A.10}$$

where $f(z)$ is an analytic function defined by

$$f(z) = P + iQ. \tag{A.11}$$

The complex representation of the Airy stress function requires a further function

$$\psi(z) = \frac{1}{4} \int f(z)dz = p + iq, \tag{A.12}$$

which is also analytic and its derivative corresponds to

$$\psi'(z) = \frac{1}{4}f(z). \tag{A.13}$$

By considering the *Cauchy-Riemann* equations we can describe $\psi'(z)$ by

$$\psi'(z) = \frac{\partial p}{\partial x} + i\frac{\partial q}{\partial x} = \frac{\partial q}{\partial y} - i\frac{\partial p}{\partial y}, \tag{A.14}$$

which allows us to obtain a relation between P and the functions p and q

$$P = 4\frac{\partial p}{\partial x} = 4\frac{\partial q}{\partial y}. \tag{A.15}$$

By using these relations we can rewrite (A.8) as

$$\nabla^2[\phi - (xp + yq)] = 0, \tag{A.16}$$

where $\phi - (xp + yq)$ is harmonic and can be written as the real part of some analytic function. Therefore $\chi(z)$ can be chosen and is defined as

$$\phi - (xp + yq) = \text{Re}\{\chi(z)\}. \tag{A.17}$$

By employing the relation

$$xp + yq = \operatorname{Re}\{\bar{z}\psi(z)\}, \quad (\text{A.18})$$

the complex potential representation of the Airy stress function is obtained

$$\phi = \operatorname{Re}\{\bar{z}\psi(z) + \chi(z)\}. \quad (\text{A.19})$$

If we define

$$\Theta(z) = \bar{z}\psi(z) + \chi(z), \quad \text{and} \quad \bar{\Theta}(\bar{z}) = z\bar{\psi}(\bar{z}) + \bar{\chi}(\bar{z}), \quad (\text{A.20})$$

summing these equations, we obtain

$$\Theta(z) + \bar{\Theta}(\bar{z}) = \bar{z}\psi(z) + \chi(z) + z\bar{\psi}(\bar{z}) + \bar{\chi}(\bar{z}) = 2\operatorname{Re}\{\Theta(z)\} = 2\phi. \quad (\text{A.21})$$

Equation (A.21) is employed in the next section to derive the Kolosov-Muskhelishvili formulas.

A.4 Stress and Displacement described by Airy Stress Function

By using the definition of the Airy stress function (A.19), the stresses can be described by

$$\begin{aligned} \sigma_{xx} + i\tau_{xy} &= \frac{\partial^2 \phi}{\partial y^2} - i \frac{\partial^2 \phi}{\partial x \partial y} = -i \frac{\partial}{\partial y} \left(\frac{\partial \phi}{\partial x} + i \frac{\partial \phi}{\partial y} \right), \\ \sigma_{yy} - i\tau_{xy} &= \frac{\partial^2 \phi}{\partial x^2} + i \frac{\partial^2 \phi}{\partial x \partial y} = \frac{\partial}{\partial x} \left(\frac{\partial \phi}{\partial x} + i \frac{\partial \phi}{\partial y} \right). \end{aligned} \quad (\text{A.22})$$

For an analytic function $f(z)$ the following relations are valid [70, 71]

$$\begin{aligned} \frac{\partial f(z)}{\partial x} &= f'(z) \frac{\partial z}{\partial x} = f'(z), \\ \frac{\partial f(z)}{\partial x} &= \overline{\left(\frac{\partial f(z)}{\partial x} \right)} = \overline{f'(z)}, \\ \frac{\partial f(z)}{\partial y} &= f'(z) \frac{\partial z}{\partial y} = if'(z), \\ \frac{\partial f(z)}{\partial y} &= \overline{\left(\frac{\partial f(z)}{\partial y} \right)} = -i\overline{f'(z)}. \end{aligned} \quad (\text{A.23})$$

The differentiation of (A.21) with respect to x and y gives

$$\begin{aligned} 2 \frac{\partial \phi}{\partial x} &= \bar{z}\psi'(z) + \psi(z) + \chi'(z) + z\bar{\psi}'(\bar{z}) + \bar{\psi}(\bar{z}) + \bar{\chi}'(\bar{z}), \\ 2 \frac{\partial \phi}{\partial y} &= i \left[\bar{z}\psi'(z) - \psi(z) + \chi'(z) - z\bar{\psi}'(\bar{z}) + \bar{\psi}(\bar{z}) - \bar{\chi}'(\bar{z}) \right], \end{aligned} \quad (\text{A.24})$$

where the second equation multiplied by i and summed to the first gives:

$$\frac{\partial \phi}{\partial x} + i \frac{\partial \phi}{\partial y} = \psi(z) + z\bar{\psi}'(\bar{z}) + \bar{\chi}'(\bar{z}). \quad (\text{A.25})$$

The equations from (A.22) can be rewritten using (A.25)

$$\begin{aligned} \sigma_{xx} + i\tau_{xy} &= \psi'(z) + \bar{\psi}'(\bar{z}) - z\bar{\chi}''(\bar{z}) - \bar{\chi}''(\bar{z}), \\ \sigma_{yy} - i\tau_{xy} &= \psi'(z) + \bar{\psi}'(\bar{z}) + z\bar{\chi}''(\bar{z}) + \bar{\chi}''(\bar{z}). \end{aligned} \quad (\text{A.26})$$

The sum of these two equations results in

$$\sigma_{xx} + \sigma_{yy} = 2 \left[\psi'(z) + \overline{\psi'(z)} \right] = 4\text{Re} [\psi'(z)] \quad (\text{A.27})$$

and the subtraction of the first equation from the second produces

$$\sigma_{yy} - \sigma_{xx} - 2i\tau_{xy} = 2z\overline{\psi''(z)} + 2\overline{\chi''(z)}. \quad (\text{A.28})$$

Taking its complex conjugated results in

$$\sigma_{yy} - \sigma_{xx} + 2i\tau_{xy} = 2 \left[\overline{z}\psi''(z) + \chi''(z) \right]. \quad (\text{A.29})$$

The two equations (A.27) and (A.29) are the complex potential representation of the stresses.

Further we derive the complex potential of the displacements. (2.44) and (A.3) can be substituted in (2.46) to give

$$\begin{aligned} 2\mu \frac{\partial u_x}{\partial x} &= \frac{\partial^2 \phi}{\partial y^2} - \frac{\lambda^*}{2(\lambda^* + \mu)} \nabla^2 \phi, \\ 2\mu \frac{\partial u_y}{\partial y} &= \frac{\partial^2 \phi}{\partial x^2} - \frac{\lambda^*}{2(\lambda^* + \mu)} \nabla^2 \phi, \\ \mu \left(\frac{\partial u_x}{\partial y} + \frac{\partial u_y}{\partial x} \right) &= -\frac{\partial^2 \phi}{\partial x \partial y}, \end{aligned} \quad (\text{A.30})$$

where

$$\lambda^* = \frac{3 - \kappa}{\kappa - 1} \mu \quad (\text{A.31})$$

and κ is defined by

$$\kappa = \begin{cases} 3 - 4\nu & \text{for plane strain} \\ \frac{3-\nu}{1+\nu} & \text{for plane stress} \end{cases} \quad (\text{A.32})$$

and μ is the shear modulus.

By plugging

$$\nabla^2 \phi = P = 4 \frac{\partial p}{\partial x} = 4 \frac{\partial q}{\partial y}, \quad (\text{A.33})$$

into (A.30) we obtain

$$\begin{aligned} 2\mu \frac{\partial u_x}{\partial x} &= -\frac{\partial^2 \phi}{\partial x^2} + \frac{2(\lambda^* + 2\mu)}{\lambda^* + \mu} \frac{\partial p}{\partial x}, \\ 2\mu \frac{\partial u_y}{\partial y} &= -\frac{\partial^2 \phi}{\partial y^2} + \frac{2(\lambda^* + 2\mu)}{\lambda^* + \mu} \frac{\partial q}{\partial y}, \end{aligned} \quad (\text{A.34})$$

which by integrating leads to

$$\begin{aligned} 2\mu u_x &= -\frac{\partial \phi}{\partial x} + \frac{2(\lambda^* + 2\mu)}{\lambda^* + \mu} p + f_1(y), \\ 2\mu u_y &= -\frac{\partial \phi}{\partial y} + \frac{2(\lambda^* + 2\mu)}{\lambda^* + \mu} q + f_2(x), \end{aligned} \quad (\text{A.35})$$

where $f_1(y)$ and $f_2(x)$ represent rigid body displacements and can be neglected. This equation can be rewritten in complex form

$$2\mu(u_x + iu_y) = -\left(\frac{\partial \phi}{\partial x} + i \frac{\partial \phi}{\partial y} \right) + \frac{2(\lambda^* + 2\mu)}{\lambda^* + \mu} \psi(z), \quad (\text{A.36})$$

and recalling (A.25) we obtain

$$2\mu(u_x + iu_y) = \kappa\psi(z) - z\overline{\psi'(z)} - \overline{\chi'(z)}, \quad (\text{A.37})$$

which represent the complex potential of the displacements.

The Kolosov-Muskhelishvili formulas are given by the equations set (A.27), (A.29), and (A.37).

B

Westergaard Approach

The three crack modes described in **Section 4.1** have symmetric and antisymmetric properties. The Westergaard approach permits to easily treat and analyze these kinds of crack problems [70, 71].

The Westergaard approach is derived for a crack that propagates in Mode I, therefore $\tau_{xy}=0$ along $y=0$.

Using this condition and employing (A.29) we can write

$$\text{Im}\{\bar{z}\psi''(z) + \chi''(z)\} = 0 \quad \text{at} \quad y = 0, \quad (\text{B.1})$$

which can be satisfied only if

$$z\psi''(z) + \chi''(z) + A = 0, \quad (\text{B.2})$$

where A is a real constant.

As it is possible to express the stresses and displacements by a single analytic function we write

$$\chi''(z) = -z\psi''(z) - A, \quad (\text{B.3})$$

which can be plugged into (A.27) using (A.37). Solving the resulting equation leads to the stresses

$$\begin{aligned} \sigma_{xx} &= 2\text{Re}\{\psi'(z)\} - 2y\text{Im}\{\psi''(z)\} + A, \\ \sigma_{yy} &= 2\text{Re}\{\psi'(z)\} + 2y\text{Im}\{\psi''(z)\} - A, \\ \tau_{xy} &= -2y\text{Re}\{\psi''(z)\}, \end{aligned} \quad (\text{B.4})$$

and the displacements

$$\begin{aligned} 2\mu u_x &= (\kappa - 1)\text{Re}\{\psi(z)\} - 2y\text{Im}\{\psi''(z)\} + Ax, \\ 2\mu u_y &= (\kappa + 1)\text{Im}\{\psi(z)\} - 2y\text{Re}\{\psi''(z)\} - Ay. \end{aligned} \quad (\text{B.5})$$

If we define

$$\psi'(z) = \frac{1}{2}(Z_I(z) + A) \quad \text{thus} \quad \psi(z) = \frac{1}{2}(\hat{Z}_I(z) + Az) \quad \text{and} \quad \psi'' = \frac{1}{2}Z_I'(z) \quad (\text{B.6})$$

where the hat in $Z_I(z)$ indicates the integral $\hat{Z}_I'(z) \equiv Z_I(z)$. These equations are further used with (B.4) and (B.5), resulting in

$$\begin{aligned} \sigma_{xx} &= \text{Re}\{Z_I(z)\} - y\text{Im}\{Z_I'(z)\} + 2A, \\ \sigma_{yy} &= \text{Re}\{Z_I(z)\} + y\text{Im}\{Z_I'(z)\}, \\ \tau_{xy} &= -y\text{Re}\{Z_I'(z)\}, \\ 2\mu u_x &= \frac{(\kappa - 1)}{2}\text{Re}\{\hat{Z}_I(z)\} - y\text{Im}\{Z_I(z)\} + \frac{1}{2}(\kappa + 1)Ax, \\ 2\mu u_y &= \frac{(\kappa + 1)}{2}\text{Im}\{\hat{Z}_I(z)\} - y\text{Re}\{Z_I(z)\} + \frac{1}{2}(\kappa - 3)Ay, \end{aligned} \quad (\text{B.7})$$

where A is a uniform uniaxial stress and does not add to the singularity of the stress at the crack tip (usually it is set to 0).

Therefore, the stresses and displacements (B.7) can be derived by choosing the following Airy stress function

$$\phi = \operatorname{Re}\{\hat{Z}_I(z)\} + y\operatorname{Im}\{\hat{Z}_I(z)\} + Ay^2, \quad (\text{B.8})$$

where the derivatives of the function \hat{Z}_I are defined as

$$\hat{Z}_I(z) = \frac{\partial \hat{Z}_I(z)}{\partial z}, \quad Z_I(z) = \frac{\partial \hat{Z}_I(z)}{\partial z}, \quad Z_I'(z) = \frac{\partial Z_I(z)}{\partial z}, \quad (\text{B.9})$$

and $Z_I(z)$ is known as Westergaard function.

Bibliography

- [1] E. Chason, “A Kinetic Analysis of Residual Stress Evolution in Polycrystalline Thin Films,” *Thin Solid Films*, vol. 526, pp. 1–14, 2012.
- [2] E. Chason, J. W. Shin, S. J. Hearne, and L. B. Freund, “Kinetic Model for Dependence of Thin Film Stress on Growth Rate, Temperature, and Microstructure,” *Journal of Applied Physics*, vol. 111, no. 8, p. 083520, 2012.
- [3] E. Chason, A. Engwall, F. Pei, M. Lafouresse, U. Bertocci, G. Stafford, J. A. Murphy, C. Lenihan, and D. N. Buckley, “Understanding Residual Stress in Electrodeposited Cu Thin Films,” *Journal of The Electrochemical Society*, vol. 160, no. 12, pp. D3285–D3289, 2013.
- [4] C. Lécuyer, D. C. Brock, and J. Last, *Makers of the Microchip: A Documentary History of Fairchild Semiconductor*. MIT Press, 2010.
- [5] J. S. Kilby, “Invention of the Integrated Circuit,” *IEEE Transactions on Electron Devices*, vol. 23, no. 7, pp. 648–654, 1976.
- [6] R. R. Schaller, “Moore’s Law: Past, Present and Future,” *IEEE Spectrum*, vol. 34, no. 6, pp. 52–59, 1997.
- [7] A. N. Saxena, *Invention Of Integrated Circuits: Untold Important Facts*. River Edge, NJ, USA: World Scientific Publishing Co., Inc., 2009.
- [8] E. M. Moore, “Cramming More Components Onto Integrated Circuits,” *Electronics*, pp. 114–117, 1965.
- [9] G. E. Moore, “Progress in Digital Integrated Electronics,” in *Electron Devices Meeting*, vol. 21, pp. 11–13, 1975.
- [10] M. Dalmau, *Les Microprocesseurs*. <http://www.iutbayonne.univ-pau.fr/~dalmau/documents/cours/archi/MICROPancien.pdf>.
- [11] J. D. Meindl, “Ultra-Large Scale Integration,” *IEEE Transactions on Electron Devices*, vol. 31, no. 11, pp. 1555–1561, 1984.
- [12] G. Bose, “IC Fabrication Technology,” 2014.
- [13] K. Reinhardt and W. Kern, *Handbook of Silicon Wafer Cleaning Technology*. Elsevier Science, 2008.
- [14] P. Garrou, C. Bower, and P. Ramm, *Handbook of 3D Integration*. No. v. 1, Wiley-VCH-Verlag, 2008.

- [15] R. H. Bruce, W. P. Meuli, and J. Ho, "Multi Chip Modules," in *Proc. Conference on Design Automation*, pp. 389–393, 1989.
- [16] R. S. Patti, "Three-Dimensional Integrated Circuits and the Future of System-on-Chip Designs," *Proceedings of the IEEE*, vol. 94, no. 6, pp. 1214–1224, 2006.
- [17] K. L. Tai, "System-in-Package (SIP): Challenges and Opportunities," in *Proc. of the 2000 Asia and South Pacific Design Automation Conference*, pp. 191–196, 2000.
- [18] A. Papanikolaou, D. Soudris, and R. Radojicic, *Three Dimensional System Integration: IC Stacking Process and Design*. Springer US, 2010.
- [19] S. W. Yoon, D. W. Yang, J. H. Koo, M. Padmanathan, and F. Carson, "3d TSV Processes and its Assembly/Packaging Technology," in *Proc. IEEE 3D System Integration (3DIC)*, pp. 1–5, 2009.
- [20] P. Ramm, J. J. Q. Lu, and M. M. V. Taklo, *Handbook of Wafer Bonding*. Handbook of Wafer Bonding, Wiley, 2012.
- [21] W. Arden, M. Brillouët, P. Coge, M. Graef, B. Huizing, and R. Mahnkopf, "More than-Moore white paper," *Version*, vol. 2, p. 14, 2010.
- [22] J. Burghartz, *Ultra-Thin Chip Technology and Applications*. Springer New York, 2010.
- [23] M. Puech, J. M. Thevenoud, J. M. Gruffat, N. Launay, N. Arnal, and P. Godinat, "Fabrication of 3D Packaging TSV using DRIE," in *Symposium on Design, Test, Integration and Packaging of MEMS/MOEMS*, pp. 109–114, 2008.
- [24] F. Laermer and A. Schilp, "Method of Anisotropically Etching Silicon," 1996.
- [25] K. H. Lu, X. Zhang, S. K. Ryu, J. Im, R. Huang, and P. S. Ho, "Thermo-Mechanical Reliability of 3-D ICs Containing Through Silicon Vias," in *Proc. IEEE Electronic Components and Technology Conference (ECTC)*, pp. 630–634, 2009.
- [26] I. D. Wolf, K. Croes, O. V. Pedreira, R. Labie, A. Redolfi, M. V. D. Peer, K. Vanstreels, C. Okoro, B. Vandeveld, and E. Beyne, "Cu Pumping in TSVs: Effect of Pre-CMP Thermal Budget," *Microelectronics Reliability*, vol. 51, no. 9–11, pp. 1856–1859, 2011.
- [27] M. J. Wolf, B. Dretschkow, T. and Wunderle, N. Jurgensen, G. Engelmann, O. Ehrmann, A. Uhlig, B. Michel, and H. Reichl, "High Aspect Ratio TSV Copper Filling with Different Seed Layers," in *Proc. IEEE Electronic Components and Technology Conference (ECTC)*, pp. 563–570, 2008.
- [28] D. Malta, E. Vick, S. Goodwin, C. Gregory, M. Lueck, A. Huffman, and D. Temple, "Fabrication of TSV-Based Silicon Interposers," in *Proc. IEEE International 3D Systems Integration Conference (3DIC)*, pp. 1–6, 2010.
- [29] J. Kraft, F. Schrank, J. Teva, J. Siegert, G. Koppitsch, C. Cassidy, E. Wachmann, F. Altmann, S. Brand, C. Schmidt, and M. Petzold, "3D Sensor Application with Open Through Silicon Via Technology," in *Proc. IEEE Electronic Components and Technology Conference (ECTC)*, pp. 560–566, 2011.

- [30] K. Kondo, M. Kada, and K. Takahashi, *Three-Dimensional Integration of Semiconductors: Processing, Materials, and Applications*. Springer International Publishing, 2016.
- [31] Toshiba, *Toshiba Develops World's First 16-die Stacked NAND Flash Memory with TSV Technology*, 2015. <http://www.businesswire.com/news/home/20150805006880/en/>.
- [32] J. Liu, O. Salmela, J. Sarkka, J. Morris, P. E. Tegehall, and C. Andersson, *Reliability of Microtechnology: Interconnects, Devices and Systems*. Springer New York, 2011.
- [33] Z. Suo, "Reliability of Interconnect Structures," *Interface and Nanoscale Failure*, vol. 8, pp. 265–324, 2003.
- [34] Y. M. Desai, *Finite Element Method with Applications in Engineering*. Dorling Kindersley, 2011.
- [35] J. Betten, *Creep Mechanics*. Springer Berlin Heidelberg, 2008.
- [36] A. F. Bower, *Applied Mechanics of Solids*. CRC Press, 2009.
- [37] D. Gross and T. Seelig, *Fracture Mechanics: With an Introduction to Micromechanics*. Mechanical Engineering Series, Springer Berlin Heidelberg, 2011.
- [38] A. C. Fischer-Cripps, *Nanoindentation*. Mechanical Engineering Series, Springer, 2004.
- [39] G. Q. Zhang, W. D. van Driel, and X. J. Fan, *Mechanics of Microelectronics*. Solid Mechanics and Its Applications, Springer Netherlands, 2006.
- [40] J. Schröder and K. Hackl, *Plasticity and Beyond: Microstructures, Crystal-Plasticity and Phase Transitions*. CISM International Centre for Mechanical Sciences, Springer Vienna, 2013.
- [41] D. Hull and D. J. Bacon, *Introduction to Dislocations*. Elsevier Science, 2001.
- [42] L. B. Freund and S. Suresh, *Thin Film Materials: Stress, Defect Formation and Surface Evolution*. Cambridge University Press, 2004.
- [43] D. Rees, *Basic Engineering Plasticity: An Introduction with Engineering and Manufacturing Applications*. Elsevier Science, 2012.
- [44] A. R. A. Ragab and S. E. A. Bayoumi, *Engineering Solid Mechanics: Fundamentals and Applications*. Taylor & Francis, 1998.
- [45] J. W. Hutchinson, "Stresses and Failure Modes in Thin Films and Multilayers," *Notes for a Dcamm Course. Technical University of Denmark, Lyngby*, pp. 1–45, 1996.
- [46] A. Oechsner and M. Merkel, *One-Dimensional Finite Elements: An Introduction to the FE Method*. Springer Berlin Heidelberg, 2012.
- [47] J. N. Reddy, *An Introduction to the Finite Element Method*. McGraw-Hill series in Mechanical Engineering, McGraw-Hill, 2006.

- [48] M. Kaltenbacher, *Numerical Simulation of Mechatronic Sensors and Actuators: Finite Elements for Computational Multiphysics*. Springer Berlin Heidelberg, 2015.
- [49] O. C. Zienkiewicz, R. L. Taylor, and J. Z. Zhu, *The Finite Element Method: Its Basis and Fundamentals*. Elsevier Science, 2005.
- [50] G. R. Liu and S. S. Quek, *The Finite Element Method: A Practical Course*. Elsevier Science, 2013.
- [51] B. Swinnen, W. Ruythooren, P. D. Moor, L. Bogaerts, L. Carbonell, K. D. Munck, B. Eyckens, S. Stoukatch, D. S. Tezcan, Z. Tokei, J. Vaes, J. V. Aelst, and E. Beyne, “3D Integration by Cu-Cu Thermo-Compression Bonding of Extremely Thinned Bulk-Si Die Containing 10 μm Pitch Through-Si Vias,” in *Proc. International Electron Devices Meeting*, pp. 1–4, 2006.
- [52] S. Hashmi, *Comprehensive Materials Processing*. Elsevier Science, 2014.
- [53] V. Cherman, G. V. der Plas, J. D. Vos, A. Ivankovic, M. Lofrano, V. Simons, M. Gonzalez, K. Vanstreels, T. Wang, R. Daily, W. Guo, G. Beyer, A. L. Manna, I. D. Wolf, and E. Beyne, “3D Stacking Induced Mechanical Stress Effects,” in *Proc. IEEE Electronic Components and Technology Conference (ECTC)*, pp. 309–315, 2014.
- [54] C. Ko and K. Chen, “Wafer-Level Bonding/Stacking Technology for 3D Integration,” *Microelectronics Reliability*, vol. 50, no. 4, pp. 481–488, 2010.
- [55] X. Li and B. Bhushan, “A Review of Nanoindentation Continuous Stiffness Measurement Technique and its Applications,” *Materials Characterization*, vol. 48, no. 1, pp. 11–36, 2002.
- [56] N. K. Mukhopadhyay and P. Paufler, “Micro- and Nanoindentation Techniques for Mechanical Characterisation of Materials,” *International Materials Reviews*, vol. 51, no. 4, pp. 209–245, 2006.
- [57] H. Hertz, “On the Contact of Elastic Solids,” *J. Reine Angew. Math*, vol. 92, no. 110, pp. 156–171, 1881.
- [58] D. Tabor, *The Hardness of Metals*. Monographs on the Physics and Chemistry of Materials, OUP Oxford, 2000.
- [59] A. P. Karmarkar, X. Xiaopeng, and V. Moroz, “Performanace and Reliability Analysis of 3D-Integration Structures Employing Through Silicon Via (TSV),” in *Proc. IEEE International Reliability Physics Symposium (IRPS)*, pp. 682–687, 2009.
- [60] L. Hofmann, S. Dempwolf, D. Reuter, R. Ecke, K. Gottfried, S. Schulz, R. Knechtel, and T. Geßner, “3D Integration Approaches for MEMS and CMOS Sensors Based on a Cu Through-Silicon-Via Technology and Wafer Level Bonding,” in *Proc. SPIE Microtechnologies*, pp. 951709–951709, 2015.
- [61] O. Tabata, T. Tsuchiya, O. Brand, G. K. Fedder, C. Hierold, and J. G. Korvink, *Reliability of MEMS: Testing of Materials and Devices*. Advanced Micro & Nanosystems, Wiley, 2013.
- [62] COMSOL, “COMSOL Multiphysics® v. 5.1., COMSOL AB, Stockholm, Sweden,” 2016. <http://www.comsol.com>.

- [63] J. Lubliner, *Plasticity Theory*. Dover Books on Engineering, Dover Publications, 2013.
- [64] H. D. Espinosa, B. C. Prorok, and M. Fischer, “A Methodology for Determining Mechanical Properties of Freestanding Thin Films and MEMS Materials,” *Journal of the Mechanics and Physics of Solids*, vol. 51, no. 1, pp. 47–67, 2003.
- [65] H. D. Espinosa, B. C. Prorok, and B. Peng, “Plasticity Size Effects in Free-Standing Submicron Polycrystalline FCC Films Subjected to Pure Tension,” *Journal of the Mechanics and Physics of Solids*, vol. 52, no. 3, pp. 667–689, 2004.
- [66] H. Pelletier, J. Krier, A. Cornet, and P. Mille, “Limits of Using Bilinear Stress–Strain Curve for Finite Element Modeling of Nanoindentation Response on Bulk Materials,” *Thin Solid Films*, vol. 379, no. 1–2, pp. 147–155, 2000.
- [67] L. Filipovic, A. P. Singulani, F. Roger, S. Carniello, and S. Selberherr, “Intrinsic Stress Analysis of Tungsten-Lined Open TSVs,” *Microelectronics Reliability*, vol. 55, no. 9–10, pp. 1843–1848, 2015.
- [68] M. Kuna, *Finite Elements in Fracture Mechanics: Theory - Numerics - Applications*. Solid Mechanics and Its Applications, Springer Netherlands, 2013.
- [69] A. A. Griffith, “The Phenomena of Rupture and Flow in Solids,” *Philosophical Transactions of the Royal Society of London. Series A, Containing Papers of a Mathematical or Physical Character*, vol. 221, pp. 163–198, 1921.
- [70] C. T. Sun and Z. Jin, *Fracture Mechanics*. Boston: Academic Press, 2012.
- [71] R. P. Wei, *Fracture Mechanics: Integration of Mechanics, Materials Science and Chemistry*. Cambridge University Press, 2010.
- [72] E. Zeidler, *Springer-Taschenbuch der Mathematik*. Springer Spektrum, 2013.
- [73] B. M. Malyshev and R. L. Salganik, “The Strength of Adhesive Joints Using the Theory of Cracks,” *International Journal of Fracture*, vol. 26, no. 4, pp. 261–275, 1984.
- [74] J. R. Rice, “A Path Independent Integral and the Approximate Analysis of Strain Concentration by Notches and Cracks,” *J. Appl. Mech.*, vol. 35, no. 2, pp. 379–386, 1968.
- [75] B. Budiansky and J. R. Rice, “Conservation Laws and Energy-Release Rates,” *J. Appl. Mech.*, vol. 40, no. 1, pp. 201–203, 1973.
- [76] R. E. Smelser and M. E. Gurtin, “On the J-Integral for Bi-Material Bodies,” *Int. J. Fract.*, vol. 13, no. 3, pp. 382–384, 1977.
- [77] R. H. Myers, D. C. Montgomery, G. G. Vining, and T. J. Robinson, *Generalized Linear Models: with Applications in Engineering and the Sciences*. Wiley Series in Probability and Statistics, Wiley, 2012.
- [78] R. A. Naik and J. Crews, J. H., “Determination of Stress Intensity Factors for Interface Cracks Under Mixed-Mode Loading,” *Paper presented at the ASTM National Symposium on Fracture Mechanics*, 1992.

- [79] K. H. Lu, S.-K. Ryu, Q. Zhao, X. Zhang, J. Im, R. Huang, and P. S. Ho, "Thermal Stress Induced Delamination of Through Silicon Vias in 3-D Interconnects," in *Proc. IEEE Electronic Components and Technology Conference (ECTC)*, pp. 40–45, 2010.
- [80] F. Roger, J. Kraft, K. Molnar, and R. Minixhofer, "TCAD Electrical Parameters Extraction on Through Silicon Via (TSV) Structures in a 0.35 μm Analog Mixed-Signal CMOS," in *Proc. of the 2012 International Conference on Simulation of Semiconductor Processes and Devices (SISPAD)*, pp. 380–383, 2012.
- [81] L. Filipovic and S. Selberherr, "The Effects of Etching and Deposition on the Performance and Stress Evolution of Open Through Silicon Vias," *Microelectron. Reliab.*, vol. 54, no. 9, pp. 1953–1958, 2014.
- [82] A. A. Volinsky, N. R. Moody, and W. W. Gerberich, "Interfacial Toughness Measurements for Thin Films on Substrates," *Acta Mater.*, vol. 50, pp. 441–466, 2002.
- [83] P. J. Wei, W. L. Liang, C. F. Ai, and J. F. Lin, "A New Method for Determining the Strain Energy Release Rate of an Interface Via Force–Depth Data of Nanoindentation Tests," *Nanotechnology*, vol. 20, no. 2, p. 025701, 2009.
- [84] M. S. Kennedy, D. F. Bahr, and N. R. Moody, "The Effect of Nonuniform Chemistry on Interfacial Fracture Toughness," *Metall. Mater. Trans. A*, vol. 38, no. 13, pp. 2256–2262, 2007.
- [85] M. J. Cordill, D. F. Bahr, N. R. Moody, and W. W. Gerberich, "Recent Developments in Thin Film Adhesion Measurement," *IEEE Transactions on Device and Materials Reliability*, vol. 4, no. 2, pp. 163–168, 2004.
- [86] C. Krauss, S. Labat, S. Escoubas, O. Thomas, S. Carniello, J. Teva, and F. Schrank, "Stress Measurements in Tungsten Coated Through Silicon Vias for 3D Integration," *Thin Solid Films*, vol. 530, pp. 91–95, 2013.
- [87] P. G. Charalambides, J. Lund, A. G. Evans, and R. M. McMeeking, "A Test Specimen for Determining the Fracture Resistance of Bimaterial Interfaces," *Journal of Applied Mechanics*, vol. 56, no. 1, pp. 77–82, 1989.
- [88] I. Hofinger, M. Oechsner, H.-A. Bahr, and M. V. Swain, "Modified Four-Point Bending Specimen for Determining the Interface Fracture Energy for Thin, Brittle Layers," *International Journal of Fracture*, vol. 92, no. 3, pp. 213–220, 1998.
- [89] R. C. Cammarata, T. M. Trimble, and D. J. Srolovitz, "Surface Stress Model for Intrinsic Stresses in Thin Films," *Journal of Materials Research*, vol. 15, pp. 2468–2474, 2000.
- [90] S. C. Seel, *Stress and Structure Evolution During Volmer-Weber Growth of Thin Films*. PhD thesis, Massachusetts Institute of Technology, 2002.
- [91] E. Chason, B. W. Sheldon, L. B. Freund, J. A. Floro, and S. J. Hearne, "Origin of Compressive Residual Stress in Polycrystalline Thin Films," *Phys. Rev. Lett.*, vol. 88, p. 156103, 2002.
- [92] R. Koch, "The Intrinsic Stress of Polycrystalline and Epitaxial Thin Metal Films," *Journal of Physics: Condensed Matter*, vol. 6, no. 45, p. 9519, 1994.
- [93] I. Committee *et al.*, "International Technology Roadmap for Semiconductors," 2013.

- [94] N. Ranganathan, D. Y. Lee, L. Youhe, G. Q. Lo, K. Prasad, and K. L. Pey, "Influence of Bosch Etch Process on Electrical Isolation of TSV Structures," *IEEE Transactions on Components, Packaging and Manufacturing Technology*, vol. 1, no. 10, pp. 1497–1507, 2011.
- [95] L. Filipovic, R. L. de Orio, and S. Selberherr, "Process and Reliability of SF₆/O₂ Plasma Etched Copper TSVs," in *Proc. IEEE Thermal, mechanical and multi-physics simulation and experiments in microelectronics and microsystems (EUROSIME)*, pp. 1–4, 2014.
- [96] J. A. Floro, E. Chason, R. C. Cammarata, and D. J. Srolovitz, "Physical Origins of Intrinsic Stresses in Volmer–Weber Thin Films," *MRS Bulletin*, vol. 27, pp. 19–25, 2002.
- [97] F. Roger, A. Singulani, S. Carniello, L. Filipovic, and S. Selberherr, "Global Statistical Methodology for the Analysis of Equipment Parameter Effects on TSV Formation," in *Proc. IEEE International Workshop on CMOS Variability (VARI)*, pp. 39–44, 2015.
- [98] J. A. Floro and E. Chason, "Curvature Based Techniques for Realtime Stress Measurements During Thin Film Growth," *In-Situ Characterization of Thin Film Growth Processes*, p. 191, 2001.
- [99] R. C. Cammarata, "Surface and Interface Stress Effects in Thin Films," *Progress in Surface Science*, vol. 46, no. 1, pp. 1–38, 1994.
- [100] W. D. Nix and B. M. Clemens, "Crystallite Coalescence: A Mechanism for Intrinsic Tensile Stresses in Thin Films," *Journal of Materials Research*, vol. 14, no. 08, pp. 3467–3473, 1999.
- [101] L. B. Freund and E. Chason, "Model for Stress Generated Upon Contact of Neighboring Islands on the Surface of a Substrate," *Journal of Applied Physics*, vol. 89, no. 9, pp. 4866–4873, 2001.
- [102] L. Vitos, A. V. Ruban, H. L. Skriver, and J. Kollár, "The Surface Energy of Metals," *Surface Science*, vol. 411, no. 1-2, pp. 186–202, 1998.
- [103] F. Spaepen, "Interfaces and Stresses in Thin Films," *Acta Materialia*, vol. 48, no. 1, pp. 31–42, 2000.
- [104] C. Friesen, S. C. Seel, and C. V. Thompson, "Reversible Stress Changes at All Stages of Volmer–Weber Film Growth," *Journal of Applied Physics*, vol. 95, no. 3, pp. 1011–1020, 2004.
- [105] R. Koch, D. Hu, and A. K. Das, "Compressive Stress in Polycrystalline Volmer–Weber Films," *Phys. Rev. Lett.*, vol. 94, p. 146101, 2005.
- [106] A. Rajamani, B. W. Sheldon, E. Chason, and A. F. Bower, "Intrinsic Tensile Stress and Grain Boundary Formation During Volmer–Weber Film Growth," *Applied Physics Letters*, vol. 81, no. 7, pp. 1204–1206, 2002.
- [107] S. Sivaram, *Chemical Vapor Deposition: Thermal and Plasma Deposition of Electronic Materials*. Electrical and Electronics Technology Handbooks, Van Nostrand Reinhold, 1995.

Own Publications

- [1] **S. Papaleo**, L. Filipovic, W. H. Zisser, M. Rovitto, H. Ceric, and S. Selberherr, “Modeling Intrinsic Stress Build-Up during Tungsten Deposition in Open Through Silicon Vias,” *Thin Solid Films*, 2016. *submitted*.
- [2] M. Rovitto, **S. Papaleo**, and H. Ceric, “Diffuse Interface Model for Electromigration Void Evolution in Open Through Silicon Vias,” *IEEE Transactions on Device and Materials Reliability*, 2016. *submitted*.
- [3] **S. Papaleo**, W. H. Zisser, A. P. Singulani, H. Ceric, and S. Selberherr, “Stress Evolution During Nanoindentation in Open TSVs,” *IEEE Transactions on Device and Materials Reliability*, vol. 16, no. 4, pp. 470–474, 2016.
- [4] **S. Papaleo**, M. Rovitto, and H. Ceric, “Mechanical Effects of the Volmer-Weber Growth in the TSV Sidewall,” in *Proc. 2016 Electronic Components and Technology Conference (ECTC)*, pp. 1617-1622, 2016.
- [5] **S. Papaleo** and H. Ceric, “A Finite Element Method Study of Delamination at the Interface of the TSV Interconnects,” in *Proc. IEEE International Reliability Physics Symposium (IRPS)*, pp. PA-2-1-PA-2-4, 2016.
- [6] **S. Papaleo**, W. H. Zisser, and H. Ceric, “Factors that Influence Delamination at the Bottom of Open TSVs,” in *Proc. International Conference on Simulation of Semiconductor Processes and Devices (SISPAD)*, pp. 421–424, 2015.
- [7] **S. Papaleo**, W. H. Zisser, and H. Ceric, “Effects of the Initial Stress at the Bottom of Open TSVs,” in *Proc. IEEE International Symposium on the Physical and Failure Analysis of Integrated Circuits (IPFA)*, pp. 447–450, 2015.
- [8] **S. Papaleo**, W. H. Zisser, and H. Ceric, “Stress Analysis in Open TSVs after Nanoindentation,” in *Abstracts of the GDRI CNRS Mecano General Meeting on the Mechanics of Nano-Objects*, pp. 39–40, 2014.

Curriculum Vitae

August 11th 1988

Born in Novara, Italy

September 2002 - July 2007

Istituto Tecnico Industriale “Omar”, Novara, Italy

Electrical Technician

September 2007 - October 2010

Università degli Studi del Piemonte Orientale, Italy

Bachelor of Materials Science

Bachelor Thesis: “Chemical Recycle of EPS packages post use”

June 2010 - September 2010

AIPE (Associazione Italiana Polistirene Espanso), Milano, Italy

Visiting Researcher

Research of new chemical recycle method for expanded polystyrene

October 2010 - July 2013

Università degli Studi di Milano-Bicocca, Italy

Master of Materials Science

Master Thesis: “Application and validation of a calculation model for epitaxial deformed structures”

May 2012 - January 2013

MEMC Electronics Materials (Now Sunedison), Novara, Italy

Visiting Researcher

Mathematical modeling and experimental validation of mechanical behavior of silicon epitaxial structures

November 2013 - December 2016

Vienna University of Technology, Vienna, Austria

PhD program at the Institute for Microelectronics